

Technische Universität München
TUM School of Natural Sciences

**Experimental and Numerical Methods to Assess the
Thermal Runaway Propagation Behavior in Prismatic
Lithium-Ion Battery Cell Stacks**

Sebastian Hölle

Vollständiger Abdruck der von der TUM School of Natural Sciences der Technischen Universität München zur Erlangung des akademischen Grades eines

Doktors der Ingenieurwissenschaften (Dr.-Ing.)

genehmigten Dissertation.

Vorsitz: Prof. Dr. Tom Nilges

Prüfende der Dissertation: 1. Prof. Dr.-Ing. Kai-Olaf Hinrichsen
2. Prof. Dr.-Ing. Andreas Jossen

Die Dissertation wurde am 07.06.2024 bei der Technischen Universität München eingereicht und durch die TUM School of Natural Sciences am 06.09.2024 angenommen.

Abstract

The ongoing demand for ever increasing energy densities of lithium-ion battery packs for electric vehicles poses major challenges to the automotive industry in terms of geometric integration, economics, customer needs, and particularly in safety. To comply with this demand, efficient tools and methods are required within the design and validation process which allow to integrate safe, high performance battery packs at appealing costs. For this purpose, a multi-stage approach that allows to efficiently assess the thermal propagation behavior in multiple cell arrangements, as can be found in high voltage battery packs of prismatic lithium-ion batteries, is developed and presented in this thesis. A combination of experimental and numerical studies is used to investigate the thermal runaway behavior on single cell level and the thermal propagation behavior on multiple cell level. Due to the nature of a lithium-ion battery thermal runaway and propagation, the focus of this thesis is laid on accounting for all the three major heat transfer mechanisms defining this phenomenon: solid body heat conduction, heat transfer due to vented gas, and heat transfer due to vented particles, i.e. two-phase convection. First, the thermal runaway key characteristics are assessed by analyzing a large database of autoclave calorimetry experiments. The results are subsequently used to develop an empirical numerical model that is capable to reproduce the thermal runaway behavior of a single lithium-ion battery cell within the solid body domain. In order to transfer the model to multiple cell level, both experimental and numerical studies with cell stacks are performed. By comparing the propagation behavior of different cell stack setups, the significant impact of both vented gas and vented particles on thermal propagation characteristics becomes especially apparent for battery packs with an enclosed housing. Therefore, an experiment is designed to evaluate the deposition of vented particles and thus the gas-particle-flow occurring during thermal runaway. The results serve as a basis for the formulation of a model within the gas-particle flow domain. The developed experimental and numerical methods on both single and multiple cell level are finally combined to allow for an efficient assessment of the thermal propagation behavior in cell stacks of prismatic lithium-ion batteries. The potential application of the approach to other cell formats or higher integration levels, such as battery modules or packs, allows to satisfy both range and safety requirements of current and future battery packs for electric vehicles.

Kurzzusammenfassung

Die anhaltende Nachfrage nach immer höheren Energiedichten von Lithium-Ionen-Batteriespeichern für Elektrofahrzeuge stellt die Automobilindustrie in Bezug auf geometrische Integration, Wirtschaftlichkeit, Kundenbedürfnisse, und insbesondere Sicherheit vor große Herausforderungen. Um diesen Anforderungen gerecht zu werden, sind effiziente Tools und Methoden innerhalb des Entwicklungs- und Absicherungsprozesses erforderlich, die die Integration eines sicheren und leistungsstarken Batteriespeichers zu attraktiven Kosten ermöglichen. Zu diesem Zweck wird im Rahmen dieser Arbeit ein mehrstufiger Ansatz entwickelt und vorgestellt, der eine effiziente Bewertung der thermischen Propagation in Mehrzell-Aufbauten ermöglicht, wie sie in Hochvoltspeichern mit prismatischen Lithium-Ionen-Batterien vorkommen. Hierfür werden experimentelle und numerische Studien durchgeführt, die das thermische Durchgehen auf Einzelzell-Ebene und die thermische Propagation auf Mehrzell-Ebene untersuchen. Der Schwerpunkt dieser Arbeit liegt aufgrund der Natur des thermischen Durchgehens einer Lithium-Ionen-Batterie sowie dessen Propagation auf der Betrachtung aller drei Wärmeübertragungsarten dieses Phänomens: Festkörper-Wärmeleitung, Wärmeübertragung durch ausgestoßenes Gas, und Wärmeübertragung durch ausgestoßene Partikel, sprich Zweiphasen-Konvektion. Zunächst werden die Hauptmerkmale des thermischen Durchgehens durch die Analyse einer Datenbank bestehend aus Ergebnissen von Autoklaven-Kalorimetrie-Experimenten charakterisiert. Die Ergebnisse werden anschließend verwendet, um ein empirisches Simulationsmodell abzuleiten, das das thermische Durchgehen einer Lithium-Ionen-Batterie auf Festkörper-Ebene reproduzieren kann. Um das Modell auf die Mehrzell-Ebene zu übertragen, werden sowohl experimentelle als auch numerische Studien mit Mehrzell-Aufbauten durchgeführt. Durch den Vergleich des Propagationsverhaltens verschiedener Aufbauten wird deutlich, dass der Einfluss von ausgestoßenem Gas und ausgestoßenen Partikeln auf den Propagationsprozess insbesondere bei Batteriespeichern mit geschlossenem Gehäuse zum Tragen kommt. Daher wird ein Experiment konzipiert, das in der Lage ist, die Ablagerung der ausgestoßenen Partikel und somit die Gas-Partikel-Strömung während eines thermischen Durchgehens zu bestimmen. Die Ergebnisse dienen als Grundlage für den Aufbau eines Simulationsmodells, das diese Gas-Partikel-Strömung beschreibt. Die sowohl auf Einzel- als auch auf Mehrzell-Ebene entwickelten experimentellen und numerischen Methoden werden schließlich kombiniert, um eine effiziente Bewertung des thermischen Propagationsverhaltens in Zell-Stapeln aus prismatischen Lithium-Ionen-Batterien zu ermöglichen. Der potenzielle Übertrag des Ansatzes auf andere Zellformate oder höhere Integrationsebenen, wie z.B. Batteriemodule oder -speicher, ermöglicht es sowohl die Reichweiten- als auch die Sicherheitsanforderungen aktueller und zukünftiger Batteriespeicher für Elektrofahrzeuge zu erfüllen.

Acknowledgements

During my doctorate, I was accompanied, advised, and supported by numerous people. I would like to take this opportunity to thank everyone involved.

First of all, I would like to thank Prof. Dr.-Ing. Kai-Olaf Hinrichsen, for integrating me as an external doctoral student within his research group at the TC-I chair and thus giving me the wonderful opportunity to pursue this exciting project at BMW. Thank you for all your support, feedback, comments, suggestions for improvement, and encouragement you have given me over the years.

Further thanks go to my BMW supervisors Savo Asanin, Sascha Zimmermann, and Philip Kotter. Thank you, Savo, for initiating the doctoral position at BMW and for accompanying me in the early stages. You were a great help in giving my work the necessary structure. Thank you, Sascha, for taking over the supervision from Savo after you decided to join our battery development team. Even when things got chaotic from time to time, you always took the necessary time for me and my work. Thank you, Philip, for your valuable input from a different perspective and for taking on practically all process aspects within BMW.

I would also like to thank all my BMW colleagues from my team within the battery development department who have accompanied me over the years. Despite the many personal changes and reorganizations, I have always felt like an equal member of the team. Special thanks go to all BMW colleagues that contributed as co-authors to my papers and thus to this work: Sebastian Scharner, Simon Haberl, Alexander Rheinfeld, Patrick Osswald, Felix Dengler, und Hyojeong Kim. In this context, I would also like to thank all TI-323 colleagues from the BCCC who supported me with experiments in the safety lab, in particular Alina Mayer, Sebastian Juen, and Jochen Friedl. Of course, I would also like to thank all the students I was able to supervise in the course of my work: Tobias Busch, David Schaeuble, Benjamin Kanz, Berkin Cakan, Felix Dengler, Yunus Emir, Tobias Urban, Suriya Anantharaman, and Amine Trigui.

A very big thank you also goes, of course, to all my fellow doctoral students with whom I was able to found the “Partyministerium”. Thank you Christoph Zörr, Johannes Brehm, Tobias Hofmann, and Valentin Elender. Without you, I would definitely have struggled to get through the times when things weren’t going so well. Thank you for the great time we spent together (thankfully not only in the office).

Last but not least, I want to thank my family and friends for their unconditional support over the last years. Even though I couldn't always spend enough time with you, you always stood by my side. I am deeply thankful to my parents, Ute and Joachim, and my siblings, Sabrina and Leo. Thank you for years of investment in my education, contributing to my personal development, and your unconditional support.

You all made this document possible.

Contents

Nomenclature	ix
1 Introduction to Automotive Battery Pack Safety	1
1.1 Automotive battery packs: state of the art and trends	3
1.2 Fundamentals of lithium-ion batteries	6
1.2.1 Working principles of lithium-ion batteries	7
1.2.2 Battery cell design	9
1.2.3 Potential hazards of lithium-ion batteries	9
1.2.4 Nature of lithium-ion battery thermal runaway	12
1.3 The propagation problem	17
1.4 Experimental methods in the context of battery safety	20
1.4.1 Single cell level	20
1.4.2 Multiple cell level	27
1.5 Numerical methods in the context of battery safety	31
1.5.1 Single cell level	31
1.5.2 Multiple cell level	35
1.6 Thesis outline	38
2 Thermal Runaway Behavior of Lithium-Ion Battery Cells	41
2.1 Experimental assessment of thermal runaway key characteristics	41
2.2 Modeling approaches for heat release during TR	56
3 Thermal Propagation Behavior of Lithium-Ion Battery Cell Stacks	77
3.1 Thermal propagation in open systems without housing	77
3.2 Thermal propagation in closed systems with housing	98
3.2.1 Experimental comparison of open and closed systems	98
3.2.2 Particle deposition during lithium-ion battery thermal runaway . .	109
4 Predictive Modeling of the Thermal Propagation Behavior	137
4.1 Multi-stage approach for efficient assessment of the thermal propagation behavior	137
4.2 Comparison of simulation and experiment	140
5 Conclusions and Outlook	143
Bibliography	147
Scientific Contributions	175

Nomenclature

Please note that the abbreviations and symbols listed in the following are defined as used within the main part of this thesis and may vary from each individual article included in this work due to unique requirements within the integrated articles or specific standards set by the journal. Therefore, abbreviations and symbols are defined once again within each article individually, if necessary.

Abbreviations

3D	three-dimensional
ARC	accelerating rate calorimetry
BEV	battery electric vehicle
BMS	battery management system
C ₂ H ₄	ethylene
C ₂ H ₆	ethane
C ₃ H ₆	propene
CFD	computational fluid dynamics
CH ₄	methane
CNG	compressed natural gas
CO	carbon monoxide
CO ₂	carbon dioxide
CSBC	copper slug battery calorimetry
DEC	diethyl carbonate
DMC	dimethyl carbonate
DSC	differential scanning calorimetry
EC	ethylene carbonate
EMC	ethyl methyl carbonate
EV	electric vehicle
FCEV	fuel cell electric vehicle
FTRC	fractional thermal runaway calorimeter
H ₂	hydrogen
ICE	internal combustion engine
ICEV	internal combustion engine vehicle
ISC	internal short circuit
LCO	lithium cobalt oxide
LFP	lithium iron phosphate
LiPF ₆	lithium hexafluorophosphate

Symbols

LMO	lithium manganese oxide
NCA	lithium nickel cobalt aluminum oxide
NMC	lithium nickel manganese cobalt oxide
NMP	N-methyl pyrrolidone
OEM	original equipment manufacturer
PE	polyethylene
PP	polypropylene
PVDF	polyvinylidene difluoride
SEI	solid electrolyte interphase
SoC	state of charge
SoH	state of health
TP	thermal (runaway) propagation
TR	thermal runaway
TTW	tank-to-wheel
VSP2 [®]	vent size package 2
WTT	well-to-tank
WTW	well-to-wheel

Symbols

Greek symbols

Δ	referring to a difference	—
λ	thermal conductivity	$\text{W m}^{-1} \text{K}^{-1}$
ρ	density	kg m^{-3}

Roman symbols

A	area	m^2
c_p	specific heat capacity	$\text{J kg}^{-1} \text{K}^{-1}$
e	restitution coefficient	—
m	mass	kg
T	temperature	K
t	time or duration	s
v	velocity	m s^{-1}
x, y, z	axes of coordinate system	m

Subscripts

cell	referring to a quantity measured or estimated on battery cell level
C_i	referring to the cell i of a cell stack
gas	referring to the gases vented during thermal runaway
HS_i	referring to the thermal insulation material (heatshield) i of a cell stack
imp	referring to the state of impingement
init	referring to the initial condition

JR	referring to the jelly roll of a battery cell
max	referring to the maximum value
n	referring to a quantity in wall-normal direction
particles	referring to the particles / droplets vented during thermal runaway
reb	referring to the state of rebound
remains	referring to the remains inside of the battery cell after a thermal runaway
t	referring to a quantity in wall-tangential direction
TR	referring to a thermal runaway event
trigger	referring to the trigger condition of thermal runaway
venting	referring to the venting process during thermal runaway

1 Introduction to Automotive Battery Pack Safety

The European Parliament set the path towards zero CO₂ emissions for new passenger cars and light commercial vehicles in February 2023 by approval of the Regulation EU2023/851, which contains an EU fleet-wide zero-emission target for 2035.^{1,2} In its initial form, this new legislation was a commitment towards battery electric vehicles (BEVs) and intended to create clarity for the car industry.^{2,3} In fact, three quarters of all car manufacturer brands operating in Europe have already announced a 100% BEV sales target for 2035 or earlier, and therefore expressed their consent with the path towards decarbonization of passenger cars.⁴ In a last-minute intervention, however, Germany demanded for an exemption within the regulation that allows potential sales of new cars that run on synthetic fuels only (also called e-fuels), and hence restarted a discussion about the further usage of internal combustion engine vehicles (ICEVs) after 2035.⁵

In order to get further insights into the background of this discussion, an analysis from a functional perspective is performed: the main function of a transportation fuel, such as gasoline or a battery, is to provide the energy that is necessary to move the vehicle with its passengers and cargo. From a chemical and integration point of view, this means that the fuel must have a certain specific energy and energy density.⁶ Figure 1.1a compares these two key properties for batteries and liquid or gaseous fuels that are currently considered for the usage in passenger cars. Circles indicate the raw material, whereas triangles indicate the vehicle application including necessary components, such as a tank.

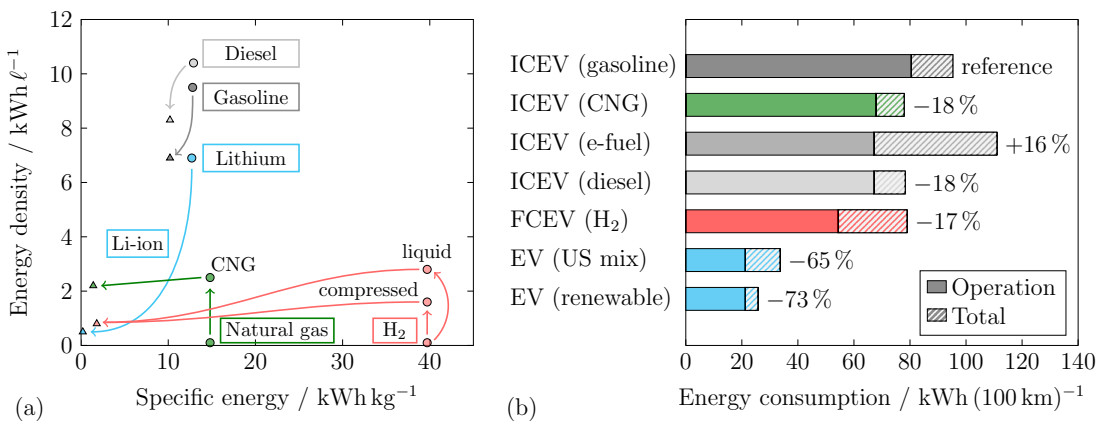


Figure 1.1: (a) Specific energy and energy density of currently used liquid or gaseous fuels for passenger cars compared to batteries. Circles indicate the raw material, whereas triangles indicate the application in a passenger vehicle, such as a tank. Values taken from Refs. [6–8]. (b) Energy consumption of average midsize passenger cars using different powertrain technologies and fuel types. Values taken and converted from Refs. [9–11].

In terms of the raw material's specific energy, the differences between lithium used in batteries for electric vehicles (EVs) (blue circle) and liquid fuels used in ICEVs (gray circles) are negligibly small. Gaseous fuels, such as natural gas (green circles) or hydrogen (red circles), have a higher specific energy than lithium or liquid fuels. Natural gas may be used as alternative fuel for internal combustion engines (ICEs), whereas hydrogen is the propellant of fuel cells. Both natural gas and hydrogen, however, have naturally low energy densities. Therefore, gaseous fuels are either used in a compressed state, e.g. as compressed natural gas (CNG), or must be liquified. Liquid fuels show the highest energy densities, whereas pure lithium lies in-between the gaseous and liquid fuels.⁶⁻⁸

For vehicle applications, though, it is important to also consider the effective properties of fuel together with the necessary fuel storage system. Especially for fuel cell electric vehicles (FCEVs) or vehicles propelled by CNG, the necessity of pressure tanks and other containment structure leads to lower effective specific energies and energy densities compared to ICEVs using diesel or gasoline (indicated by arrows in Fig. 1.1a).⁶⁻⁸ It is exactly this advantage of liquid fuels, that also comes into effect when discussing the usage of synthetic fuels. Synthetic fuels are produced out of hydrogen (preferably generated with renewable energy) and carbon dioxide and form fuels with similar characteristics as their fossil counterparts gasoline or diesel.^{11,12} The main appeal of such synthetic fuels, besides their high specific energy and energy density, is their backward-compatibility with existing ICEs and the liquid fuel distribution system.¹²

The stored potential energy within a fuel, however, is just one of the factors that are relevant for the comparison of different powertrain technologies. The efficiency of the engine or motor is also of high importance, as the stored energy within the fuel must be transformed into kinetic energy in order to eventually move the vehicle. In general, electric motors are capable to perform this conversion more efficiently than ICEs. FCEVs also use electric motors, but due to additional energy conversion steps (fuel cell charges buffer battery which provides power to the electric motor) the overall efficiency of the powertrain is lower compared to BEVs. In this context, it is often referred to the so called tank-to-wheel (TTW) efficiency. A third relevant factor is the energy that is needed to produce and distribute the fuel, also called well-to-tank (WTT) efficiency. The combination of both WTT and TTW efficiency leads to the overall energy efficiency of a powertrain technology/fuel combination, which is referred to as well-to-wheel (WTW) efficiency.^{9-11,13}

Figure 1.1b compares the WTW efficiency in form of energy consumption of average mid-size passenger cars with different powertrain technologies and fuel types. ICEs fueled with gasoline are the least efficient motors within the comparison, which is indicated by the highest energy consumption during operation. Running an internal combustion engine on either CNG, diesel, or e-fuels results in a better TTW efficiency, whereas the operation of electric motors is the most efficient. Adding the WTT energy consumption and hence comparing the WTW efficiency of the different vehicle types underlines the advantages of BEVs regarding energy efficiency, especially when charged from renewable energies in-

stead of the local energy mix. It is worth mentioning, that in particular the production of hydrogen (for FCEVs) or the further processing of hydrogen to e-fuels (for ICEVs) contribute to the high overall energy consumption of such vehicles.^{9–11}

In sum, comparing the overall WTW energy consumption of different powertrain architectures/fuel combinations shows that BEVs are the most efficient option for midsize passenger cars. Therefore, it is not surprising that the electric car market has seen exponential growth in recent years. Against the backdrop of new legislation and ambitious industry targets for decarbonization, a share of 35 % for electric car sales is expected in 2030.¹⁴

One of the main drawbacks of BEVs, however, remains the lower specific energy and energy density of lithium-ion batteries compared to fossil fuels, which currently still poses major challenges in complying with customer demands in terms of driving range despite maximizing battery pack integration space within BEVs. The “range anxiety” is treated as one of the most critical barriers limiting overall customer acceptance.¹⁵ Therefore, car manufacturers aim to continuously increase the specific energy and energy density of their batteries whilst maximizing available integration space in their vehicle architectures. Unfortunately, an increased energy density also bears the risk of safety issues.^{16–18} In order to satisfy both range and safety requirements, efficient experimental and numerical methods are necessary within the design and validation process of lithium-ion batteries for EVs. The scope of this thesis is to develop and apply such methods.

In the following, state of the art and future trends of automotive battery pack design are introduced first (section 1.1), followed by the fundamentals of lithium-ion batteries (section 1.2). The latter includes sections about the working principles, battery cell design, and potential hazards of lithium-ion batteries. These potential hazards of a single battery cell result in potential safety risks on battery pack level, as a battery pack contains a multitude of single battery cells. These risks are discussed in section 1.3, followed by a review of existing experimental (section 1.4) and numerical methods (section 1.5) in the context of battery safety. Finally, the outline of this thesis is presented in section 1.6.

1.1 Automotive battery packs: state of the art and trends

Automotive high voltage battery packs need to fulfill a variety of requirements. First and foremost, the battery serves as a storage that supplies the drivetrain of the vehicle with energy over a certain amount of time or range, respectively. Therefore, the battery has to provide the three primary functions of an electrical energy storage:^{19,20}

1. conversion of electrical power into chemical energy (charge process),
2. storage of chemical energy (storage process), and
3. conversion of chemical energy into electrical power (discharge process).

In addition, the battery must not exceed a certain size and weight in order to account for geometrical and weight constraints of the vehicle. This results in a required **specific**

energy, **energy density**, as well as **power density**. With the main functionality of providing energy being covered, further requirements relate to economic needs. As companies strive for an optimal cost-benefit ratio on the vehicles they sell, the batteries have to meet requirements regarding **manufacturing costs**, **service life** and **quality**. Last but not least, the vehicles and hence the batteries must maintain a certain level of **safety** across the entire operating range, i.e. in addition to intrinsic failures, operational loads and special events such as a crash must also be taken into account.^{19,20}

In this context, the term *battery* can lead to confusion as it is used for several levels of integration. Within this work, the first integration level is the battery *cell*. In the automotive industry, three different formats of such cells have emerged: cylindrical, prismatic and pouch (see Fig. 1.2). The second integration level is the battery *module*, which

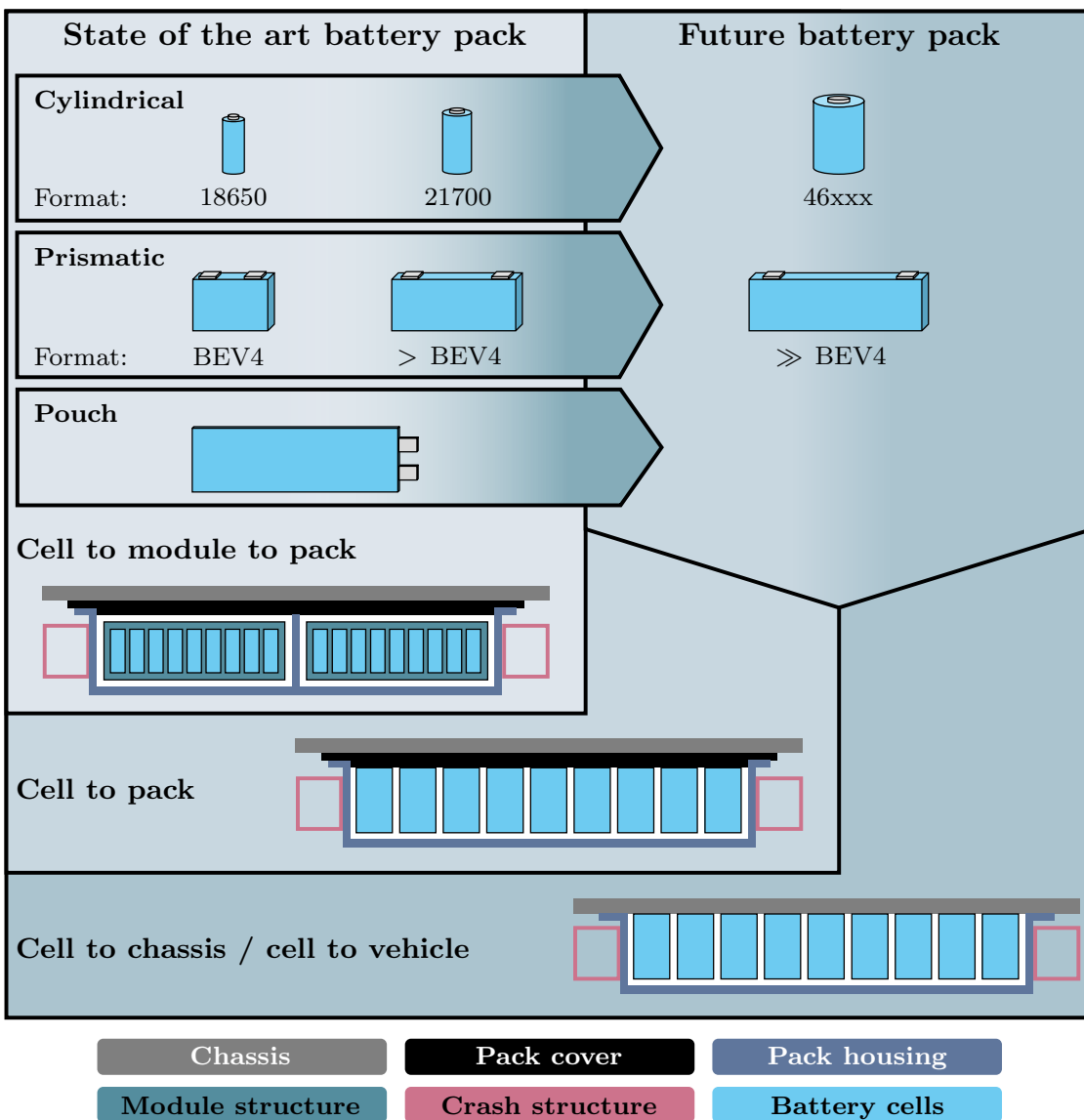


Figure 1.2: Schematic representation of the battery cell formats used in automotive industry and the design concepts of current and future battery packs.

is comprised of several battery cells that are electrically connected in series or parallel. Generally, a frame is used to hold the cells in a fixed position and to protect them from environmental hazards such as external shocks, heat, and vibration. A module may also contain additional components, e.g. parts of the cooling system. The third and last integration level is the battery *pack*. The pack comprises multiple modules, structural components, wiring, the cooling system, the battery management system (BMS), and power electronics, which are all integrated into a housing that is equipped with an over-pressure safety valve.^{21,22}

Most of state of the art battery packs follow the design concept just described. Multiple battery cells are combined to independent modules that are then integrated into a battery pack (**cell to module to pack** concept). Thus, the pack forms an independent component which is attached to the vehicle chassis. In 2008, Tesla designed a battery pack following this design concept and set one of the first milestones in electric mobility by starting regular production of the Roadster.²³ The battery pack comprised a total number of 6831 individual lithium-ion cells housed in eleven modules. Tesla used **cylindrical** battery cells that were 18 mm in diameter by 65 mm in height, leading to the name 18650 (“0” indicates the cylindrical shape).²⁴ After successfully implementing the 18650 cell in the Model S and the Model X battery packs, Tesla introduced a larger cylindrical cell for the production of the Model 3 in 2017. By increasing the cell size to 21700 (21 mm in diameter by 70 mm in height) the cells contained 50 % more energy compared to the 18650 cell.^{25,26} This new cell format was predicted to be the next standardized format of cylindrical batteries,²⁷ leading Rivian Automotive and Lucid Motors, two US-based EV start-ups, to also build their battery packs with this type of battery cell.^{28,29} Tesla, however, announced to further increase the size of its cylindrical cell to 46800 (46 mm in diameter by 80 mm in height). This is predicted to result in five times higher energy, six times higher power, 16 % range increase and 14 % cost reduction.²⁶ With this increase in cell size, it is also possible to renounce the module structure by following the **cell to pack** design concept. The battery cells are directly integrated into the pack structure and therefore, the pack itself is structural. This arrangement results in another 14 % range increase and 7 % cost reduction.^{26,30} A further increase of specific energy and/or energy density will be achieved in future battery packs by the **cell to chassis / cell to vehicle** design concept, i.e. that the vehicle chassis will serve as the pack’s top cover.²⁶

The trend of increasing cell sizes as seen for Tesla cannot be observed in the same way for the second format of automotive lithium-ion cells: the **prismatic** type. The automotive industry rather seems to increase the specific energy and/or energy density on cell level than the size of the cells,³¹ as e.g. done for the BMW i3. Following the cell to module to pack concept, in total eight modules with 12 cells each are combined to a battery pack.³² In the first version, the cells had a nominal capacity of 60 Ah each.³³ Over the years, the capacity of the cells was first increased to 94 Ah and finally to 120 Ah, whilst the cell size and pack design stayed the same.^{34–36} With dimensions of 173 mm in length, 45 mm in width, and 125 mm in height, the cell is built in the “BEV4” format as specified in DIN 91252:2016-11.^{32,37} Taking this cell as a reference, there exists a variety of both smaller

and larger cells nowadays, as the cell dimensions are often adapted in order to optimally fit into the available integration volume of the battery pack. The Chinese battery cell manufacturer SVOLT, for example, announced to sell a cell in the “MEB” format with dimensions of 220 mm in length, 33.4 mm in width, and 102.5 mm in height, as well as a cell in “L6” format with dimensions of 574 mm in length, 21.5 mm in width, and 118 mm in height.³⁸ SVOLT also holds a patent showing large and thin prismatic cells that are used to design battery packs following the cell to pack principle.³⁹ The Chinese battery cell manufacturer BYD holds a similar patent going one step further: the so called “Blade battery” cell is as wide or as long as the whole battery pack with maximum dimensions of up to 2500 mm in length, 13.5 mm in width, and 118 mm in height.⁴⁰ In summary, future battery packs with prismatic cells are expected to be also converted to the cell to pack or cell to chassis concept.⁴¹ As seen in recent patents, both standard size and large cells are used.^{39,40,42,43}

The third cell format used in EVs is the so called **pouch** format. It is characterized by a thin aluminum laminate casing, whereas the cylindrical and prismatic cells have rigid metallic housings made of aluminum or steel.^{44,45} Therefore, pouch cells must be embedded in an outer casing for rigidity, which is usually provided by a module structure.⁴⁵ This results in difficulties when following the cell to pack or cell to chassis design concept using this format type. Still, pouch cells are widely used in battery packs of different original equipment manufacturers (OEMs), such as Audi, Chevrolet, Hyundai, Kia, Nissan, Renault, Volvo or Ford.⁴⁶ Volkswagen also uses pouch cells for the ID.3 or within its “MEB-Platform”.^{47,48} For the latter, Volkswagen designed a standardized interface module that can be equipped with both prismatic and pouch cells.⁴⁸

1.2 Fundamentals of lithium-ion batteries

As shown in the previous section, OEMs focus on increasing the specific energy and energy density of battery packs by either using larger cells, cells that have a higher specific energy and/or energy density itself, and/or highly integrated pack design concepts. This is directly related to the customer experience, as a higher specific energy and energy density lead to longer driving ranges and, hence, a reduced “range anxiety”. In addition, costs can be reduced when using larger cells and/or cell-to-pack or cell-to-chassis designs due to a smaller number of parts.^{26,41} Increasing the amount of energy stored in the battery pack, however, will inevitably lead to a higher risk of hazardous situations in case of an abuse or failure of the system.⁴⁹ This is due to certain hazards and risks that are associated with lithium-ion batteries and their operation, in particular the so called thermal runaway (TR). In the following, the working principles of lithium-ion cells and the potential hazards arising from their operation are summarized, before the nature of a lithium-ion cell TR is characterized.

1.2.1 Working principles of lithium-ion batteries

The lithium-ion technology is based on the reversible intercalation and deintercalation of lithium-ions into and out of respective host lattices.⁴⁴ Since Sony started production and sale of the first commercial lithium-ion battery in 1991, its basic structure has not changed significantly until now.⁴⁵ The electrochemical unit cell of a lithium-ion battery consists out of four main components: a negative (1) and a positive electrode (2), that are electrically isolated by a separator (3) and impregnated with electrolyte (4). The electrodes are composites out of current collectors that are coated with a mixture of electrode active material, binder, solvent, and (conductive) additives.^{44,45} These four main components and the (de)intercalation principle during discharge are illustrated in Fig. 1.3.

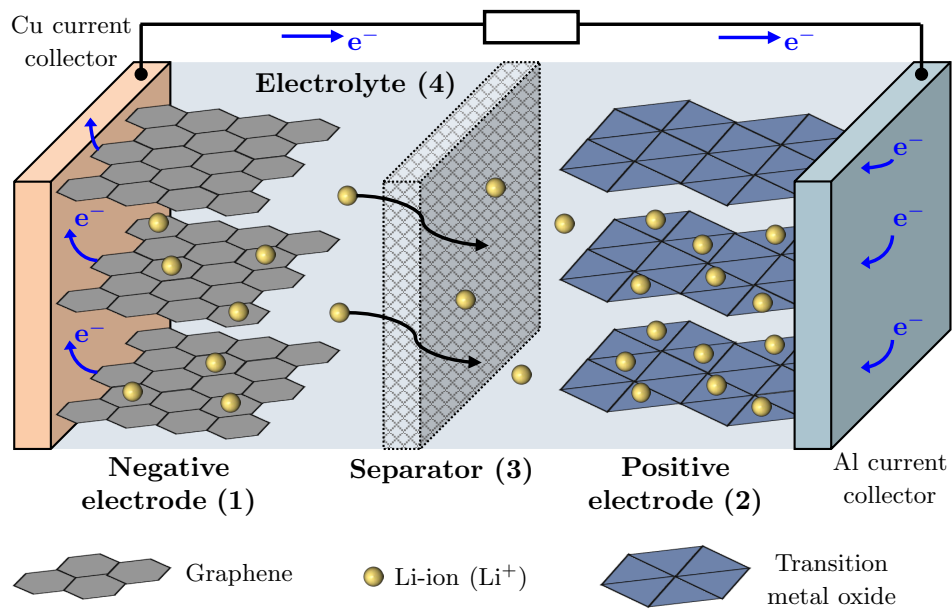
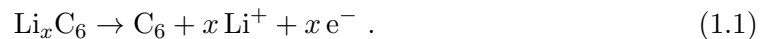


Figure 1.3: Schematic representation of the working principle of a lithium-ion battery during discharge. Figure adapted from Ref. [50]. Reproduced under the terms of the Creative Commons Attribution 4.0 License (CC BY, <https://creativecommons.org/licenses/by/4.0/>), which permits unrestricted reuse of the work in any medium, provided the original work is properly cited.

The following paragraphs summarize the function and commonly used materials of a lithium-ion cell's main components. The information is taken from Refs. [44, 45, 51, 52].

Negative electrode The most common active material of the negative electrode is graphitic carbon that is characterized by carbon atoms in parallel graphene layers. During the charging process, lithium-ions are intercalated between these layers, whereas during discharge, a deintercalation reaction occurs:



In order to increase the electron conductivity, carbon black is used as additive and mixed with the graphitic carbon, which is present as powder. A binder is necessary to ensure

sufficient cohesion between the resulting particle mixture and adhesion to the current collector. Polyvinylidene difluoride (PVDF) is used for this purpose, due to its hair-like structure that efficiently keeps the coating together. N-methyl pyrrolidone (NMP) is used as solvent for PVDF, as the latter is not soluble in water. Eventually, the emerging slurry is applied as coating to a copper foil that forms the current collector of the negative electrode.

Positive electrode The main structure of the positive electrode is comparable to the composite structure of the negative electrode. The main differences are the usage of an aluminum foil as current collector and lithiated transition metal oxides as active material. Sony used lithium cobalt oxide (LCO) in its first version of the lithium-ion battery, but there also exist alternatives that are widely used in commercial applications, such as lithium manganese oxide (LMO), lithium iron phosphate (LFP), lithium nickel manganese cobalt oxide (NMC), or lithium nickel cobalt aluminum oxide (NCA). During discharge, an intercalation reaction into the layered oxides occurs (with M representing e.g. Ni, Co, Mn, Al, and/or Fe):



Separator The separator prevents a physical contact and hence a short circuit between negative and positive electrode. Therefore, microporous membranes made out of polyethylene (PE) and polypropylene (PP) are used. Typically, the structure of the separator is a single PE/PP layer or a PE-PP bilayer, that can additionally be coated with ceramic layers in order to increase the melting temperature and hence battery safety.

Electrolyte The stacked assembly of negative electrode, separator, and positive electrode is soaked with electrolyte in order to fill the electrodes' and separator's pores. The electrolyte is a solution of so called lithium conducting salt in a mixture of organic solvents. Usually, lithium hexafluorophosphate (LiPF_6) is used as lithium salt. The most used organic solvents are ethylene carbonate (EC), dimethyl carbonate (DMC), ethyl methyl carbonate (EMC), and diethyl carbonate (DEC). During normal operation, the electrolyte is not involved in the chemical reactions, but necessary for enabling the lithium-ion exchange between the electrodes through the separator. In the uncharged state of a lithium-ion cell right after production, however, secondary reactions between the lithiated graphite and the electrolyte take place, as the potential of lithiated graphite is beyond the stability window of the electrolyte. Therefore, lithium-ion cells are converted into a stable state by the so called formation, which is the initial charging of the cell. During this process, the solid electrolyte interphase (SEI) builds up on the graphite surface. The SEI is a protective layer that prevents further secondary reactions between the negative electrode and the electrolyte, and is consequently necessary to achieve a stable state of the lithium-ion cell. During the building process of the SEI, however, a part of the lithium is "consumed" and no longer available for further cycling.

1.2.2 Battery cell design

As mentioned in section 1.1, three different cell types are used for the application in an EV battery pack: cylindrical, prismatic, and pouch cells (see Fig 1.4). For **cylindrical** cells, the electrode and separator sheets are wound to a cylindrical shape, forming the so called jelly roll, which is then integrated into a (hardcase) housing, the so called can. The can is commonly used as negative terminal and typically made of steel, but there also exist cylindrical cells built with aluminum cans. For **prismatic** cells, there exist two different types of inner structure: either a flat mandrel is used during the winding process resulting in a flat jelly roll or several electrode/separator sheets are stacked. The flat jelly roll or the stack is then integrated into a cell can, typically made of aluminum or steel. The cover of the (prismatic) can usually incorporates a negative and a positive terminal, an electrolyte fill port, and a rupture disk (the so called vent). The latter is necessary to prevent the build-up of (too) large pressures inside of the sealed can, caused e.g. by a malfunction of the cell. A safety vent is also commonly used in cylindrical cells. The third cell format is the **pouch** cell. For this format type, the stack consisting of electrode/separator sheets is packaged within two aluminum composite films made of several laminated layers (e.g. polyamide, aluminum, and PP). Therefore, the prediction of the venting location in case of a malfunction is difficult for pouch cells due to the nature of the sealed pouch bag. It is possible, however, to design the bag in such a way that the foil fails in certain areas first.^{21,44,52}

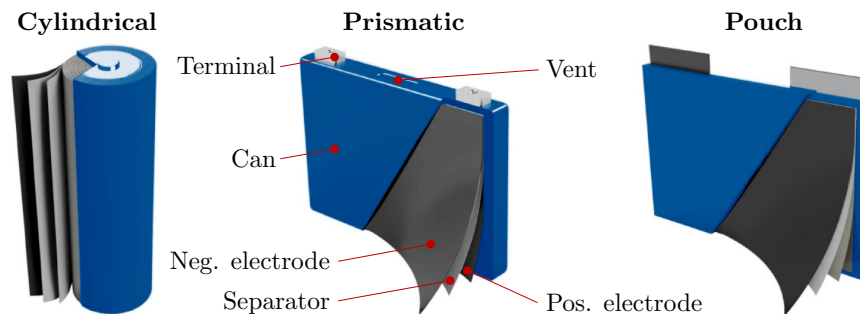


Figure 1.4: Commonly used cell formats of lithium-ion battery cells for EV applications. Figure adapted from Ref. [31]. Reproduced under the terms of the Creative Commons Attribution 4.0 License (CC BY, <https://creativecommons.org/licenses/by/4.0/>), which permits unrestricted reuse of the work in any medium, provided the original work is properly cited.

1.2.3 Potential hazards of lithium-ion batteries

Hazards resulting from a lithium-ion battery failure can be divided into five categories: functional, chemical, kinetic, electrical, and thermal. There also exist failures that do not necessarily cause hazardous situations, such as a defective function that leads to a higher performance degradation over lifetime than expected. In the context of this thesis, however, hazards are defined as failures that can cause human harm or property damage. Some examples for such hazards are summarized in Tab. 1.1.^{53,54}

Failures that explicitly cause safety concerns usually arise from a failure on battery cell level rather than on pack level. The root cause of such failures lies within the materials used within the cell, because lithium-ion cells provide all the three elements that are necessary to trigger and maintain a fire: fuel, an oxidizing agent, and heat.⁵⁵⁻⁵⁷ The electrolyte used in lithium-ion cells is a flammable liquid and consequently can serve as a fuel.^{49,55} As described previously, lithiated transition metal oxides are used as active material for the positive electrode, which can act as an oxidizing agent.^{55,58} Lastly, heat is generated during the operation of a lithium-ion cell due to the internal resistance of the cell. Consequently, lithium-ion cells have the potential to start a combustion inside of a sealed container, which is rarely done - other applications are for example explosives or rocket propellants.⁵⁸

Table 1.1: Potential hazards associated with the failure of a high voltage lithium-ion battery system.^{53,54}

Category	Examples
Functional	<ul style="list-style-type: none"> • Sudden loss of function, e.g. loss of regenerative braking • Defective function, e.g. overcharging due to defective BMS
Chemical	<ul style="list-style-type: none"> • Flammable gas/fluid release • Toxic amount of gas release
Kinetic	<ul style="list-style-type: none"> • Flying parts/debris release • Shock/blast wave release
Electrical	<ul style="list-style-type: none"> • Exposure to high voltage electrical energy
Thermal	<ul style="list-style-type: none"> • Fire/flame or hot gas/fluid release • Exposure to hot parts/surfaces

However, only minimal heat is generated during normal operation of a lithium-ion cell and for EV applications, there are cooling systems that keep the battery cells of the battery pack within a safe temperature range. There are additional systems which ensure that the battery is operated safely within certain voltage and current envelopes.^{49,54,58} On the other hand, Murphy’s law says that anything that can go wrong will go wrong. The probability of a failure is never zero and especially during mass production, defective products will always occur.¹⁶ In addition, a battery cell or pack will be exposed to the risk of abuse like any other product in the hands of a human operator.⁵⁵ Therefore, potential failures or abuse conditions and the resulting hazards have to be considered during the design process of EV battery packs.

In general, a distinction is made between three different abuse conditions that can cause a battery cell failure: mechanical, electrical, and thermal abuse.^{16,17,53-55} However, there are also failures that can occur during the “normal” usage of a battery.^{53,54} These four different failure pathways and exemplary starting conditions are schematically summarized in Fig. 1.5.

All cell failures originate from a damaged separator, leading to direct contact between the electrodes and therefore causing an internal short circuit (ISC). The subsequent resistive joule heating will either lead to an uncritical fault or a critical fault, depending on the heat generation and dissipation rate. If the heat generation rate exceeds the heat dissipation rate, the cell temperature will increase and may eventually trigger the onset of various chemical reactions, which in turn can cause a TR.⁵³ If the generated heat can be dissipated, the fault may be uncritical and result in a functional failure instead of a safety critical failure. Uncritical faults, however, have the potential to lead to a reduced stress tolerance of the battery and hence to trigger safety incidents at a later point in time.⁵⁴ The following paragraphs summarize exemplary causes for each of the four failure pathways.

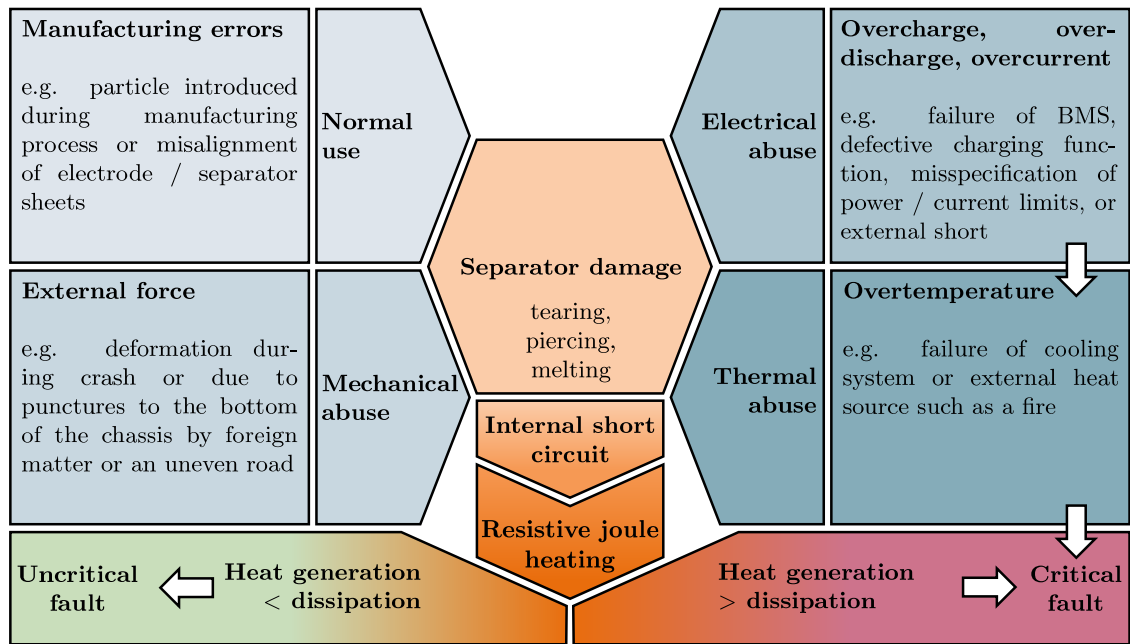


Figure 1.5: Schematic representation of potential triggers with corresponding (ab)use conditions and subsequent phenomena resulting in either an uncritical or critical battery fault. Own representation based on Ref. [59].

Normal use During the manufacturing process, conducting particles may be introduced between the cell layers. If a particle remains undetected during manufacturing, it may start to puncture the separator over multiple charge-discharge-cycles leading to an ISC. Another possible error during manufacturing is the misalignment of electrode or separator layers causing a direct contact between the electrodes and hence an ISC.^{49,53,54}

Mechanical abuse Mechanical abuse occurs if an external force is applied to the battery pack or a battery cell. Driving over an uneven road surface or a foreign object may result in an intrusion to the bottom of the vehicle chassis and hence the battery pack. The applied force can lead to a deformation of the cell, that potentially tears the separator. Furthermore, the penetration of a single or multiple battery cells with an object can occur during a car crash, which may also result in a pierced separator.^{16,53}

Electrical abuse There exist several potential triggers for electrical abuse. If, e.g., a failure of the BMS occurs, the cells in the battery pack (or some of them) may be overcharged. Overcharging of a lithium-ion cell leads to a structurally destabilizing delithiation of the positive electrode material, which eventually triggers an exothermic decomposition reaction as soon as the concentration of lithium decreases below a certain level. The structural change during this reaction releases oxygen and heat, eventually leading to a thermal abuse condition and separator melting. In the same manner, a lithium-ion cell can also be discharged below the lower voltage limits by a failure of the BMS. Overdischarging of a lithium-ion cell leads to dissolution of copper at the negative electrode, which deposits at the positive electrode by forming dendrites. If dendrites grow to a certain size, an ISC is triggered due to a separator puncture by the dendrite, which can become especially critical when the battery is recharged again after deep discharge. A third mechanism of electrical abuse is overcurrent. An overcurrent condition can cause separator damage in two ways: if the current flow exceeds a certain level, resistive joule heating leads to a thermal abuse condition with overtemperature exposure of the jelly roll and, hence, separator melting. This is, e.g., the case for an external short circuit. On the other hand, the current flow can also be below this level when there is, for example, a misspecification of the power or current limits. This can cause an overvoltage condition at the anode surface, leading to the formation of metallic lithium. Over multiple charging cycles, lithium dendrites can reach a size that is big enough to pierce the separator causing an ISC.^{16,49,53}

Thermal abuse Possible causes for a thermal abuse condition are a failure of the cooling system, a poorly designed cooling system and/or insufficient temperature surveillance (e.g. due to poor temperature sensor placement, temperature sensor malfunction, and/or misinterpretation of temperature signals), or an external heat source such as a fire. As soon as the rate of heat generation exceeds the rate of heat dissipation, the temperature of the cells will increase. At elevated temperatures above the operational limits, exothermic chemical reactions occur and act as an additional heat source resulting in a further increase of the cell temperature. This can lead to separator melting, resulting in an ISC.^{49,53}

1.2.4 Nature of lithium-ion battery thermal runaway

Critical faults of lithium-ion battery cells are also known as thermal runaway (TR) - a process of self-sustaining exothermic chemical reactions. As described above, the occurrence of such a fault is linked to the heat generation in a cell (chemical reactions and Joule heat) being larger than the heat dissipation from the cell.⁴⁹ Generally, the TR process can be divided into three stages:^{17,56,58}

- Stage 1: the decomposition of the SEI leads to the onset of electrolyte reduction at the (lithiated) negative electrode material, which increases the cell temperature.
- Stage 2: an increasing temperature leads to an acceleration of the chemical reactions, onset of further reactions, and, eventually, separator melting. Venting and release of smoke may occur.

- Stage 3: Joule heating due to an ISC provides the activation energy that is necessary to trigger strong exothermic decomposition reactions of the positive and/or negative electrode material, which are responsible for the majority of heat release during TR.

Depending on the definition, only the third stage may be referred to as TR. In this case, the first and second stage can be seen as the self-reinforcing trigger mechanism of a TR. In the context of this thesis, this definition shall also apply. As soon as the process enters the third stage, and hence TR, it is not possible to prevent the cell from a complete thermal decomposition,⁵³ which is accompanied by (hot) gas release, potential fire, or even an explosion of the cell.^{49,55} In the following paragraphs, the occurring reactions during a TR are summarized. If not indicated otherwise, the information is taken from Refs. [17, 56].

Reactions at the negative electrode The first reaction that occurs above the operating temperature range (upper value $\sim 60^\circ\text{C}$) is the decomposition of the SEI layer. Starting at around 80°C ,^{60,61} a first exothermic peak locates at $\sim 100^\circ\text{C}$.⁶² Within the temperature range of $120 - 250^\circ\text{C}$, the decomposition reaction of the SEI is overlapped by an endothermic regeneration reaction, maintaining a stabilized SEI thickness. As soon as the SEI begins to fail ($200 - 250^\circ\text{C}$), reactions of the lithiated graphite will occur, such as electrolyte reduction or exfoliation of the graphite structure.⁶² Subsequently, the intercalated lithium starts to react with the PVDF binder at around $250 - 350^\circ\text{C}$, leading to the final decomposition of the binder ($> 350^\circ\text{C}$).^{49,63-65} Note that the reactions just described assume graphite as active material of the negative electrode.

Reactions at the positive electrode Generally, all active materials used for the positive electrode in lithium-ion cells are unstable at elevated temperatures.⁵⁸ However, there are significant differences between the commonly used transition metal oxides regarding thermal stability. In its fully delithiated state, LCO starts reacting with the electrolyte solvents at $130 - 190^\circ\text{C}$.⁶⁵⁻⁷¹ A strongly exothermic structure degradation occurs at around 240°C accompanied by oxygen release.^{66,67,72} A shift of the first heat formation to $210 - 260^\circ\text{C}$ is achieved for the NCA active material by a stabilizing effect of Al.⁷³⁻⁷⁵ The phase degradation with oxygen release starts at around $240 - 280^\circ\text{C}$.^{69,73,74} Others reported earlier onset temperatures of decomposition at $165 - 200^\circ\text{C}$, potentially caused by a higher Ni content.^{69,70,76-78} The phase degradation of NMC occurs at around $260 - 300^\circ\text{C}$.^{73,78,79} As for NCA, however, the onset temperature is shifted to lower temperatures of $135 - 240^\circ\text{C}$ depending on the Ni content.^{71,80,81} For the LMO active material, several exothermic reactions occur between $200 - 325^\circ\text{C}$.^{65,77,79} Some studies also found reactions starting between $150 - 160^\circ\text{C}$.^{64,70} The highest thermal stability is found for LFP with phase degradation and oxygen release starting at temperatures $> 310^\circ\text{C}$,^{71,82-84} but more recent studies also showed onset temperatures of $190 - 245^\circ\text{C}$.^{69,77} Consequently, the order of thermal stability in terms of onset temperature of exothermic reactions can be summarized as $\text{LFP} > \text{LMO} > \text{NMC} > \text{NCA} > \text{LCO}$, whereby it must be noted that the thermal stability of NMC and NCA depends on the Ni content.¹⁷

In addition to onset temperatures, the heat release by the exothermic decomposition reactions must be also taken into account to compare different active materials regarding their behavior during TR. LFP is found to release between $145 - 290 \text{ J g}^{-1}$,^{69,77,85,86} followed by LMO ($439 - 450 \text{ J g}^{-1}$),^{64,77} and LCO ($\approx 450 \text{ J g}^{-1}$).⁶⁴ As already observed for thermal stability, the specific heat release of NMC and NCA also depends on the Ni content. Values between $512 - 971 \text{ J g}^{-1}$ can be found for NMC,⁸⁷ and $793 - 941 \text{ J g}^{-1}$ for NCA with different Ni contents.^{70,77,88}

In conclusion, the LFP active material exhibits a better thermal stability combined with a lower specific heat release compared to the other materials. This is attributed to strong P=O covalent bonds within the LFP octahedral structure and, hence, less oxygen release during decomposition. Materials based on layered oxides (e.g. LCO, NMC, and NCA), in turn, tend to release comparably more oxygen, which reacts with other components within the cell, such as the electrolyte solvents, and contributes to the heat release during TR.¹⁷ In the automotive industry, however, the use of NCA, NMC, and LMO cannot be avoided, since the energy density requirements for certain applications cannot be met with LFP. Even a further increase in energy density is expected within the next years,⁸⁹ that potentially leads to a further reduced thermal stability on active material level.

The melting of the separator As soon as the melting point of the separator material is reached, the separator collapse results in an ISC. This occurs at approximately $125 - 135 \text{ }^\circ\text{C}$ for PE separators and approximately $165 - 170 \text{ }^\circ\text{C}$ for PP separators.^{64,90-94} A further enhancement of the collapse temperature is achieved by adding ceramic coating to either one or both sides of the separator leading to a collapse between $200 - 260 \text{ }^\circ\text{C}$.^{53,92,95,96} Note that the melting of the separator - in contrast to the other reactions - is an endothermic process and hence does not contribute to the self-sustaining character of the TR. In turn, the ISC caused by the separator collapse can contribute significantly to heat generation due to Joule heating (depending on the current state of charge (SoC) of the cell).

Reactions of the electrolyte Electrolyte based on LiPF_6 salt starts to decompose at approximately $195 \text{ }^\circ\text{C}$.⁹⁷⁻⁹⁹ This decomposition reaction is a partly endothermic and partly exothermic multi-stage process that occurs until temperatures of approximately $350 \text{ }^\circ\text{C}$.^{97,99,100} However, the main hazards of the electrolyte arise from the strong gas formation at elevated temperatures. The lowest boiling point is found for DMC ($91 \text{ }^\circ\text{C}$), followed by EMC ($110 \text{ }^\circ\text{C}$), DEC ($126 \text{ }^\circ\text{C}$), and EC ($248 \text{ }^\circ\text{C}$).¹⁰¹ Ultimately, the gas formation is responsible for the cell opening and the release of toxic and/or flammable gases. In combination with the oxygen released by the decomposition of the transition metal oxides and the high temperatures during TR, all three components of the fire triangle are present, resulting in possible fire and explosion of the cell.¹⁰¹⁻¹⁰⁴

In summary, there are different trigger conditions, that either damage the separator directly or lead to the onset of exothermic chemical reactions, eventually resulting in separator melting or collapse (see Fig. 1.5). The originating ISC leads to Joule heat-

ing that acts as additional heat source to the (ongoing) chemical reactions. If the heat generation exceeds the heat dissipation, the self-reinforcing character will trigger further chemical reactions and the TR can no longer be prevented. Potential hazards of this critical fault are (hot) gas release, fire, and even explosion of the lithium-ion battery cell (see Tab. 1.1).

Key characteristics of thermal runaway As shown in the previous paragraphs, much research focused on revealing the TR mechanisms and the underlying chemical processes. Due to the complexity of the phenomenon and the various reactions occurring simultaneously, however, there are still uncertainties and controversial discussions.^{17,105–107} For the further course of this thesis, the TR is therefore considered in a simplified manner as phenomenon defined by the following key characteristics:

- T_{trigger} being the TR trigger temperature,
- dT/dt being the self-heating rate during TR,
- Δm_{TR} being the mass loss during TR, which can be divided into
 - m_{gas} being the mass of vented gas and
 - $m_{\text{particles}}$ being the mass of vented solid particles and liquid droplets,
- t_{venting} being the duration of venting,
- t_{TR} being the TR duration,
- m_{remains} being the mass of the cell after TR, and
- Q_{TR} being the heat released during TR, which can be divided into
 - Q_{remains} being the heat remaining in the cell body and
 - Q_{venting} being the heat that is vented out of the cell body.

Figure 1.6 exemplarily shows the TR sequence induced by penetration of a prismatic lithium-ion cell with a sharp electrically conducting object. In its initial state, the battery cell can be defined by its mass m_{cell} , its temperature T_{cell} , and its specific heat capacity $c_{p,\text{cell}}$. As soon as the object pierces the separator, there is electrical contact between the electrodes and therefore, an ISC occurs. This state is referred to as abuse condition. The resulting Joule heating leads to a temperature increase in the current-carrying components. Depending on SoC, this may result in the (local) jelly roll temperature $T_{\text{JR}}(x, y, z)$ exceeding the TR trigger temperature T_{trigger} . At this point, the triggered chemical reactions release more heat than can be dissipated. Therefore, T_{trigger} is defined as the temperature above which the occurrence of a TR is inevitable and hence marks the begin of TR if exceeded at any point within the jelly roll. The onset of the chemical reactions leads to gas release with the result of increasing pressure inside the cell. This effect is amplified by vaporization of the electrolyte due to the rising temperature. As soon as the burst pressure of the safety vent is exceeded, (hot) gas and solid particles or liquid droplets will be ejected out of the cell, which can be accompanied by fire. During this stage, the TR reaction is defined by the self-heating rate of the cell dT/dt and the mass loss Δm_{TR} , which is composed of a gaseous part m_{gas} and a solid/liquid part $m_{\text{particles}}$. Consequently, a part of the heat released by the TR reaction inside of the cell is transported out of the cell by the vented products for the duration of venting t_{venting} . This heat is referred to as

Q_{venting} and can be divided into Q_{gas} and $Q_{\text{particles}}$ (as for Δm_{TR}). The end of the TR process, and therefore its duration t_{TR} , is defined by the end of the exothermic reactions

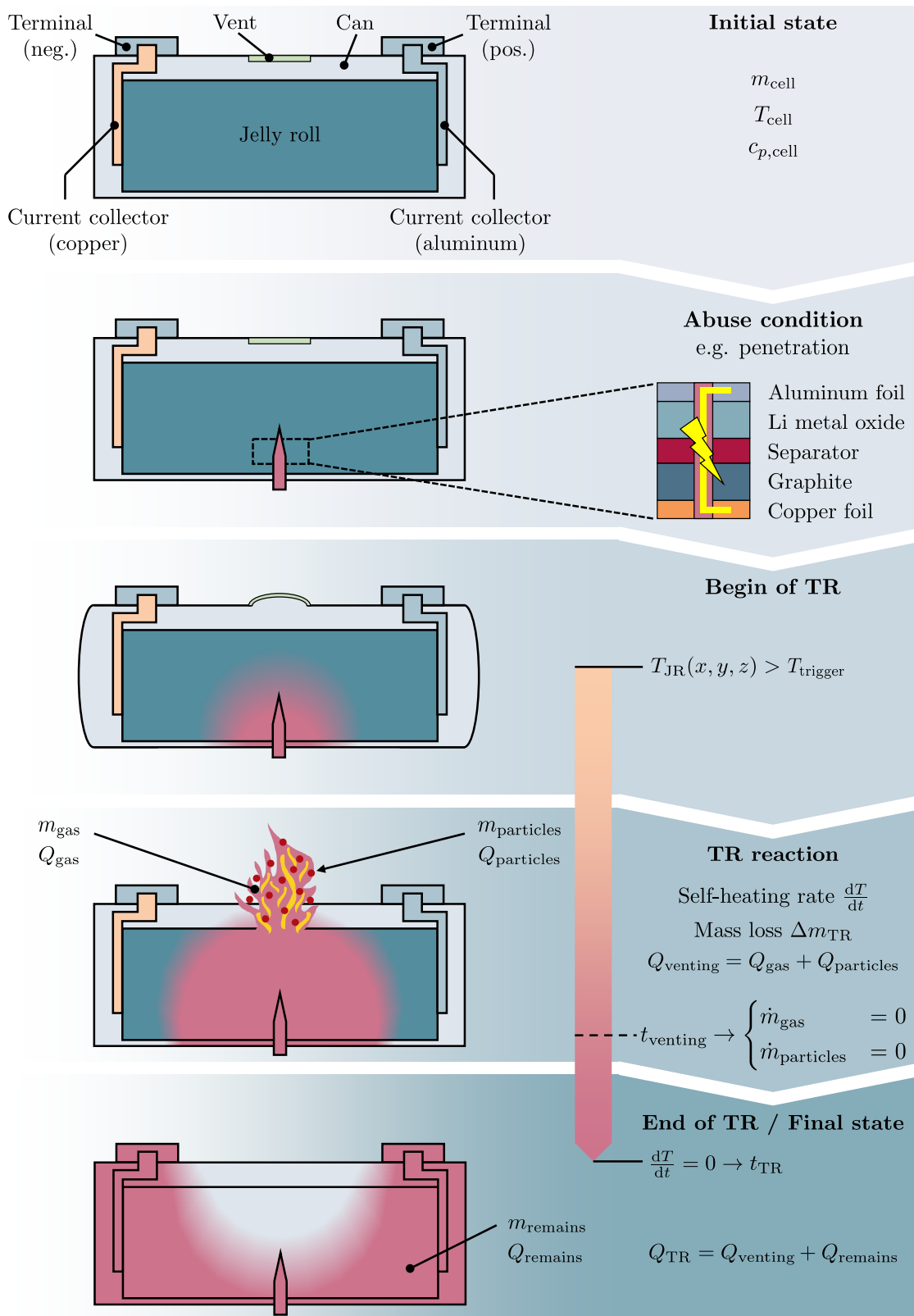


Figure 1.6: Exemplary TR sequence induced by nail penetration of a prismatic lithium-ion cell with key characteristics assigned to different stages.

($dT/dt = 0$). In its final state, the cell's mass is $m_{\text{remains}} = m_{\text{cell}} - \Delta m_{\text{TR}}$. The (total) heat being released during TR Q_{TR} is the sum of Q_{venting} and the heat that remained within the cell body Q_{remains} .

1.3 The propagation problem

As shown in section 1.1, EV pack design is trending towards highly integrated battery packs. On the one hand, this trend results in higher specific energy and energy density, leading to longer driving range as well as reduced costs, which is beneficial for both car manufacturers and customers. On the other hand, the spacing between individual battery cells inside the battery pack as well as protective pack structure is reduced. This is especially challenging as soon as a cell failure occurs. As pointed out in section 1.2, the failure of a single battery cell cannot be completely prevented and therefore, the effects of such a failure have to be considered during the design process. Generally, the heat released by a single cell TR will be transferred to the cell's surroundings. Considering the situation given in a battery pack, these surroundings are often neighboring cells. Consequently, a single cell TR can cause a thermally induced failure in neighboring cells, that may be propagating from one cell to another throughout the battery pack. This phenomenon is the so called thermal (runaway) propagation (TP).^{17,49,53,55,108,109}

With the TP being closely linked to an electro-thermal triggering of further single cell TRs, the TP mechanism is strongly related to heat transfer mechanisms, whilst the single cell TR mechanism is more closely connected to exothermic side reactions that serve as a basis for the TR reaction.¹⁷ Within the course of this thesis, the TP mechanism is divided into two pathways: first, the heat dissipation of Q_{remains} via heat conduction only, and second, the heat dissipation of Q_{venting} via a mixture of heat conduction, convection, and radiation (see Fig. 1.7).

During the TR of a cell within a battery module consisting of prismatic cells, there is the vented matter on the one hand, and the (hot) active material remaining in the cell on the other hand. Within the first seconds of the initial TR, the battery pack can be seen as a closed volume and therefore, the vented gas will spread within the whole pack. As soon as the pressure inside the pack exceeds the release pressure of the pack's safety valve, the gas escapes to the environment and flow paths of the gas evolve. As the vented gas reaches high temperatures, there will be a convective heat transfer between the gas and all surrounding components that are within the flow direction. In addition, during the TR of the initial cell failure, the void volume of the battery pack is usually filled with air. Consequently, there is an additional oxygen source, next to the oxygen released by the TR reaction, that enables the combustion of the flammable venting gas. In this context, the vented particles may act as an ignition source or the gas temperature exceeds the self-ignition temperature. If a combustion occurs, there is significant radiation heat transfer to the surroundings of the flame. The third heat transfer mechanisms is caused by the solid particles and liquid droplets that are carried by the venting gas. The particles

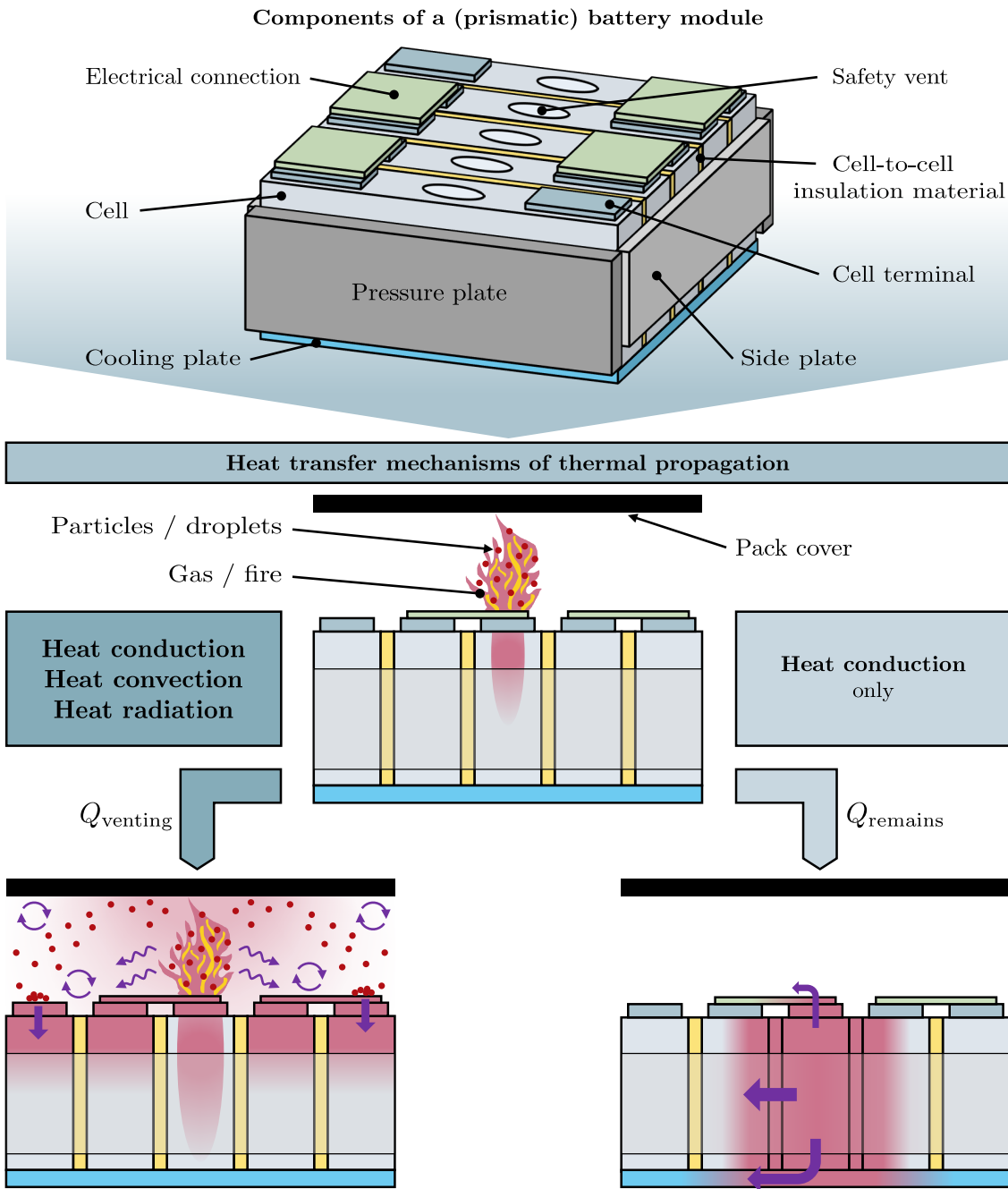


Figure 1.7: Schematic representation of the components of a (prismatic) battery module and the derived heat transfer mechanisms during the TP phenomenon.

and droplets also distribute inside of the battery pack, eventually depositing on the surrounding components. Especially if many particles accumulate at a certain position, the conductive heat transfer can be significant. In conclusion, the heat dissipation of Q_{venting} occurs by all three heat transfer mechanisms and can lead to thermal abuse conditions not only in adjacent cells, but in a larger area around the failed cell.^{108,109}

Considering only Q_{remains} , heat conduction is the primary mechanism of heat transfer. Heat transfer via conduction mainly depends on the temperature difference ΔT between the contacting bodies, the thermal conductivity λ of the contacting bodies, and the con-

tact area A . Looking at the example of Fig. 1.7, the biggest area is directed to adjacent cells and therefore, a large amount of heat can be transferred through this area. A second pathway emerges via the cooling plate. During normal operation, the function of the cooler is to ensure that the battery cells are operated within the designated temperature range. Therefore, an effective thermal coupling between cells and cooler is desirable. This leads, however, to an enhanced heat conduction to adjacent cells in case of a TR. A third pathway is created by the module structure, more precisely the side plates that maintain a certain compression force on the cells. These side plates are often glued to the cells and consequently heat conduction occurs. The fourth and last pathway is caused by the cell connection system. Here, a direct contact between the terminals of adjacent cells enables heat conduction. Usually, materials with high electrical conductivity are used (e.g. aluminum), that also have a high thermal conductivity.¹⁰⁸⁻¹¹¹

There are several factors that have an influence on the TP behavior of a battery pack. Depending on the used cell type (cylindrical, prismatic, pouch), different arrangements of cells can be realized. The main factor that is determining in this context is the cell-to-cell spacing.^{49,108} Minimal distance between cells is often achieved by using thermal insulation materials between adjacent cells.^{49,108,109} The requirements for such thermal barriers are a low thermal conductivity ($< 0.1 \text{ W m}^{-1} \text{ K}^{-1}$) and high working temperatures ($> 600 \text{ }^\circ\text{C}$). Common materials are glass fiber, ceramics, silica aerogels, or phase change materials.¹⁰⁹ Besides blocking or deceleration of the cell-to-cell heat conduction, effective and prompt heat dissipation is also a possible countermeasure against a TP. The latter can be realized, e.g., by an emergency operation mode of the cooling system, as soon as a TR gets detected.^{17,49,109}

Whilst the heat transfer via heat conduction is reliably predictable when assuming that none of the components are melting and the change in geometrical dimensions is negligible, the prediction of heat convection and heat radiation is more challenging.¹⁰⁹ The main source of convective and radiation heat transfer is the vented matter during TR, more precisely the (burnt) gases, solid particles, and liquid droplets which form a kind of “slag”.^{49,108,109} In addition to a thermal failure pathway, the TP might also be caused by mechanical effects, such as pressure increase due to the vented gases or flying parts due to an explosion of a cell.⁴⁹ Within a third - electrical - pathway, a possible trigger is an overcurrent condition. This can be caused in a string of multiple cells that are connected in parallel. If one cell in this string goes into TR, its ohmic resistance can decrease to low values resulting in a discharge of the connected cells into the failed cell.^{49,53,108}

The typical TP process in a battery pack designed following the cell to module to pack concept will show the following failure sequence: starting from the initial cell failure, the TR propagates within the battery module. In the second step, the TR propagates from the failure module to the neighboring modules, eventually resulting in a complete failure of the battery pack accompanied by a vehicle fire.¹⁰⁹ Consequently, the result of a TP can be catastrophic.¹⁰⁸ In order to address this issue, governmental authorities released regu-

lations regarding the safety of EVs and the abuse tolerance of their lithium-ion batteries, respectively. Two examples are the Chinese regulation GB 38031-2020 and the European regulation UN-R 100.03: both require that there is no hazardous situation in the occupant compartment of an EV for 5 minutes after an alarm signal is indicated.^{112,113} In other words, a car manufacturer will only get the type approval for an EV, if the occurrence of a single cell TR does not result in a hazardous situation for at least 5 minutes. Within this context, the propagation time is an important parameter. The propagation time indicates the duration between the occurrence of an initial single cell TR and the occurrence of a second TR within the battery pack.⁴⁹ Naturally, it is desirable to completely prevent the TP phenomenon. If this is not possible, however, the focus is to prolong the propagation time and hence to provide as much time as possible for the occupants to leave the vehicle after the occurrence of a TR.

1.4 Experimental methods in the context of battery safety

Safety testing is generally used to evaluate the behavior of an object of development when exposed to abuse conditions, simulating inadequate use or failure. Such tests are often defined by governmental and non-governmental organizations in order to assure that a system can be safely used in commercial applications.¹¹⁴ For lithium-ion batteries, safety tests can be classified into three main categories: mechanical, electrical and thermal abuse tests.^{114,115} As the individual battery cell plays a crucial role for the safety level of a complete battery pack, much effort in battery safety testing focuses on the single cell.⁵⁵ The TP process, however, can only be investigated on multiple cell level. Consequently, a common approach for the pack design validation is a staged process, in which the results of single cell tests are used to derive design requirements for the module and pack assembly, and subsequent module and/or pack tests are used to validate the final design.⁵³ In the following, an excerpt of most relevant experimental setups on single and multiple cell level is briefly given.

1.4.1 Single cell level

The focus on single cell level is to characterize lithium-ion batteries in terms of their abuse tolerance safety.⁵⁸ During mechanical abuse tests, the cell is exposed to mechanical loads and a potential deformation with its consequences is investigated. Electrical abuse tests evaluate the cell's robustness under critical charging or discharging conditions, such as exceeding voltage and/or current limits. During thermal abuse tests, the cell is exposed to extreme temperature environments.¹¹⁴

Mechanical abuse tests A short description of the most common mechanical abuse tests is given in the following.^{114–117}

- **Crush test:** defined solid bodies such as plates, crushing bars, or spheres are used to compress and deform the cell. The occurring deformation or indentation may lead to an ISC and therefore TR.

- Drop test: the cell is dropped from a certain height onto the floor, which may lead to deformation similar to the crush test.
- Mechanical shock and vibration test: these tests are mainly relevant for automotive applications, as they simulate loads occurring during a vehicle crash or driving on a paved road.
- Penetration test: a sharp object such as a nail or a needle of a given material and diameter is penetrated into the cell to a certain depth with a defined speed. As a consequence, the jelly roll and thus the separator is punctured and an ISC may occur, subsequently leading to TR. The nail penetration is widely used as reproducible TR trigger method.^{118–126}

Electrical abuse tests A short description of the most common electrical abuse tests is given in the following.^{114–116}

- External short circuit test: both terminals of the cell are electrically connected with a low-resistance element, leading to high currents that may cause TR.
- Overdischarge test: the cell is discharged below its lower voltage limit.
- Overcharge test: the cell is charged beyond its upper voltage limit until a TR occurs. Overcharging is widely used as reproducible TR trigger method.^{118,119,124,127–129}

Thermal abuse tests A short description of the most common thermal abuse tests is given in the following.^{114–116}

- Oven test: the cell is exposed to high temperatures above the safety limit for a certain duration.
- Thermal stability test: these tests aim to study the reactive nature of the cell by identifying characteristic temperatures such as the TR trigger temperature. The accelerating rate calorimetry (ARC) is widely used within this context and will be explained in detail further below.
- External heating test: the cell is heated by an external heat source such as a heating wire, a heating pad, or a heat gun. External heating is widely used as reproducible TR trigger method.^{118,124,130–133}

The common TR trigger methods nail penetration, overcharge, and external heating are capable of inducing the TR process with acceptable reliability. However, there are disadvantages using these methods. Researchers observed differences in the TR key characteristics depending on the trigger method. For example, both external heating and overcharging are adding energy to the investigated battery, which may affect the TR reaction.^{124,126} The nail penetration method does not have this disadvantage, but damages the cell can and, hence, potentially causes a can rupture. So there is still the need for a trigger approach that is capable of replicating an ISC as induced during normal use, e.g. by a particle. Therefore, substitute trigger approaches have been developed in recent years as alternative to the established TR trigger methods.^{117,122,126,134} These approaches, however, are based on a modification within the manufacturing process of the cell and consequently complex to implement. In addition, such a modified cell may be impractical as it no longer complies with all transportation regulations.

Additional experimental methods In addition to the standardized mechanical, electrical, and thermal abuse tests, there exist other experimental methods that have been developed for specific purposes related to battery safety. One of these experimental methods are calorimetric techniques. A widely used calorimetry experiment is the ARC, which provides the self-heating rate of a lithium-ion battery during TR as well as the TR trigger temperature. Another frequently used experimental method is abuse testing within an autoclave or sealed reactor, that allows to determine the amount of vented gas, the duration of venting, and/or the venting gas composition. Last but not least, there exist various non-standardized experimental methods to investigate parameters such as the heat released during TR and its distribution into heat remaining in the cell body and heat being vented out of the cell body by ejected matter.^{58,135} All these mentioned quantities represent TR key characteristics as defined in section 1.2.4, which is why an excerpt of the most relevant studies is briefly given in the following.

The **ARC** is widely used to investigate exothermic runaway reactions from hazardous and reactive chemicals.¹³⁶ In the case of lithium-ion batteries, ARC measurements are a common method to determine the thermal stability and self-heating rate on material or electrode level, which also allows to draw conclusions on the single decomposition reactions that occur for certain material combinations.^{60,66,67,70,71,77,137} Nowadays, ARC experiments are additionally performed with full cells in order to assess the interaction of the single decomposition reactions of positive electrode, negative electrode, and electrolyte.^{18,95,107,137–153} On the one hand, it is difficult to make reliable statements about individual reactions in this case. On the other hand, such experiments are necessary to characterize the behavior of a full cell during TR, which is the scope of this subsection. When performing full cell ARC experiments, the investigated cell is placed inside a calorimeter, which is a chamber that is equipped with heaters in its surrounding walls. During the test, the calorimeter aims to match the chamber's temperature with the cell's temperature in order to ensure that there is minimal heat transfer between cell and surroundings. The test procedure follows the so called "heat-wait-see" protocol: first, the calorimeter is heating the test chamber, and thus the investigated cell, by a defined temperature step (e.g. 5 °C). Then, the calorimeter waits for the cell being in isothermal equilibrium with the chamber. After this wait period, there is a seek period to detect a self-heating of the cell. If no self-heating is detected, the next heating step begins. Otherwise, the calorimeter switches to exothermic mode, which means that the calorimeter follows the recorded temperature rise of the cell in order to maintain the adiabatic condition.¹³⁶ The result of an ARC test is the temperature dependent self-heating rate of the investigated cell, which allows to additionally determine the TR trigger temperature. Table 1.2 summarizes and compares an excerpt of most relevant ARC studies with lithium-ion batteries.

One objective of previous ARC studies was to determine the influence of different cell materials on the self-heating rate before and during TR, in particular the influence of

Table 1.2: Excerpt of most relevant ARC studies with lithium-ion batteries.

Author(s)	cell type			chemistry						miscellaneous	
	cylindrical	prismatic	pouch	cell capacity / Ah	TCO	TFP	LMO	NCA	MMC		mixtures
Lamb et al. ¹⁸	✓	✓	✓	1 – 38	✓	✓	✓	✓	✓	✓	database containing 30 experiments
Roth ¹³⁸	✓	✓	✓	0.9 – 1.2	✓	✓	✓	✓	✓	✓	influence of electrolytes
Roth and Doughty ¹³⁹	✓	✓	✓	0.9 – 1.4	✓	✓	✓	✓	✓	✓	influence of SoH, SoC
Hildebrand et al. ¹³⁷	✓	✓	✓	5	✓	✓	✓	✓	✓	✓	influence of SoH, SoC
Ren et al. ¹⁴⁰	✓	✓	✓	24	✓	✓	✓	✓	✓	✓	influence of SoH
Liu et al. ¹⁴¹	✓	✓	✓	1	✓	✓	✓	✓	✓	✓	0% SoC
Abraham et al. ¹⁴²	✓	✓	✓	1	✓	✓	✓	✓	✓	✓	composition of venting gas
Yuan et al. ¹⁴³	✓	✓	✓	1.3 – 3.8	✓	✓	✓	✓	✓	✓	composition of venting gas
Zou et al. ¹⁴⁴	✓	✓	✓	78	✓	✓	✓	✓	✓	✓	composition of venting gas
Golubkov et al. ¹⁴⁵	✓	✓	✓	1.1 – 2.6	✓	✓	✓	✓	✓	✓	composition & amount of venting gas
Golubkov et al. ¹⁴⁶	✓	✓	✓	1.1 – 3.3	✓	✓	✓	✓	✓	✓	composition & amount of venting gas
Feng et al. ⁹⁵	✓	✓	✓	25	✓	✓	✓	✓	✓	✓	thermocouple inside battery cell
Zheng et al. ¹⁴⁷	✓	✓	✓	3 – 25	✓	✓	✓	✓	✓	✓	thermocouple inside battery cell
Xu et al. ¹⁴⁸	✓	✓	✓	4.8 – 37	✓	✓	✓	✓	✓	✓	thermocouple inside battery cell
Liu et al. ¹⁰⁷	✓	✓	✓	25	✓	✓	✓	✓	✓	✓	TR ceasing with liquid nitrogen
Ren et al. ¹⁴⁹	✓	✓	✓	24	✓	✓	✓	✓	✓	✓	TR ceasing with liquid nitrogen
Tang et al. ¹⁵⁰	✓	✓	✓	24	✓	✓	✓	✓	✓	✓	TR ceasing with liquid nitrogen
Yayathi et al. ¹⁵¹	✓	✓	✓	2.4 – 5.3	✓	✓	✓	✓	✓	✓	determination of energy release
Zhao et al. ¹⁵²	✓	✓	✓	2	✓	✓	✓	✓	✓	✓	determination of energy release
He et al. ¹⁵³	✓	✓	✓	1.9	✓	✓	✓	✓	✓	✓	analysis of heat transfer effects

the positive electrode active material or the electrolyte composition.^{18,138,139} Within this context, the influence of the state of health (SoH) or the SoC of lithium-ion cells were also studied.^{137,139–141} Other researchers focused on an additional gas composition analysis.^{142–144} In order to determine the amount of vented gas besides the self-heating rate, Golubkov et al. built a self-made calorimeter with a sealed reactor.^{145,146} As more and more results of ARC tests became available over the years, the research focused on revealing further insights into the TR process, e.g. by implementing temperature sensors within the battery cell in order to track not only cell can temperatures, but also the jelly roll temperature during a TR.^{95,147,148} Another approach was to cease the TR reaction immediately after occurrence by freezing the battery cell with liquid nitrogen.^{107,149,150} In recent years, there were also publications with the aim to improve the experimental method of an ARC, e.g. by additionally measuring the heat released during TR or gaining a better understanding of the heat transfer mechanisms during the test.^{151–153}

The **vent size package 2 (VSP2[®])** is another adiabatic calorimetry experiment that has been used to investigate lithium-ion batteries. In comparison to ARC measurements, the VSP2[®] experiment provides not only the temperature dependent self-heating rate of investigated cells, but also the pressure rise rate within the sealed test chamber.¹⁵⁴ This allows to draw conclusions regarding the release rate of the vented gas. However, there only exist publications of 18650 cylindrical cells due to the geometrical limitations of the test chamber.^{155–159}

Whilst ARC and VSP2[®] experiments are designed to measure the reaction kinetics of a TR, there also exist calorimetric experiments that focus on other parameters such as the heat released during TR. For example, the **copper slug battery calorimetry (CSBC)** introduced by Liu et al. measures the heat remaining in the body of 18650 cells after TR.^{160,161} They also coupled the CSBC with a **cone calorimeter** in order to determine the heat being vented out of the cell body and draw conclusions on the total heat released during TR.¹⁶⁰ The heat release rate during combustion of the venting gases was determined by Liu et al. with a self-made experimental apparatus,¹⁶² but there also exist standardized setups such as the so called **Tewarson calorimeter**.¹⁰² The mentioned experiments, however, are only capable of measuring fractions of the total heat released during TR. Therefore, Lyon and Walters used a **bomb calorimeter** in order to determine the total heat released during TR.¹⁶³ Nevertheless, the distribution between heat remaining in the cell body and heat being vented out of the cell body is of high relevance. The **fractional thermal runaway calorimeter (FTRC)** of Walker et al. is designed to characterize both the fraction of heat that is released through the cell casing via heat conduction and the heat that is transferred via the ejected materials.^{126,164}

Besides calorimetric experiments, **autoclave** experiments or tests conducted in **sealed reactors** are widely used to determine the amount of vented gases, the vent gas composition, as well as the amount and composition of ejected particles. Table 1.3 summarizes and compares an excerpt of most relevant experimental studies using this approach.

Table 1.3: Excerpt of most relevant autoclave / sealed reactor studies with lithium-ion batteries.

Author(s)	cell type	chemistry	setup	quantities	miscellaneous
	prismatic pouch	LCO LMO NMC mixtures	autoclave / volume / l atmosphere	gas amount gas composition particle size particle composition	
Essl et al. ¹⁶⁵	✓	✓	121.5 N ₂	✓	influence of SoC
Liao et al. ¹⁶⁶	✓	✓	24 air	✓	influence of SoC
Somandepalli et al. ¹⁶⁷	✓	✓	n/a Ar	✓	influence of SoC
Koch et al. ¹⁶⁸	✓	✓	n/a air	✓	database containing 51 experiments
Essl et al. ¹²⁴	✓	✓	121.5 N ₂	✓	influence of trigger method
Golubkov et al. ¹⁶⁹	✓	✓	121.5 N ₂	✓	influence of heating method
Zhang et al. ¹⁷⁰	✓	✓	230 N ₂	✓	air heating
Zhang et al. ¹⁷¹	✓	✓	230 n/a	✓	air heating
Wang et al. ¹⁷²	✓	✓	230 N ₂	✓	air heating, oxidation of particles

The effect of SoC on the vented gas amount, gas composition, particle size distribution, and particle composition was investigated by Essl et al. with an autoclave experiment.¹⁶⁵ Liao et al. also studied the effect of SoC, but focused on the composition of vented gas and particles,¹⁶⁶ whilst Somandepalli et al. studied the vented gas amount and the gas composition. Additionally, they characterized the vented gas with respect to their combustion behavior.¹⁶⁷ Koch et al. created a database containing a total of 51 experiments and analyzed the amount of vented gas for various NMC cells.¹⁶⁸ Others investigated the influence of different trigger methods (overheating, overcharge, nail penetration),¹²⁴ or different heating methods (one-sided and two-sided heating of the battery cell with film heaters, or air heating of the full autoclave) on the vented gas amount.¹⁶⁹ Zhang et al. performed an analysis of both ejected gas and particles by analyzing amount and composition,^{170,171} whilst Wang et al. focused on the oxidation characteristics of ejected particles and therefore analyzed their amount and composition.¹⁷²

Special methods that also made a valuable contribution to battery safety testing will be summarized in the following. Finegan et al. developed an experimental setup that allows to perform high-speed X-Ray computed tomography and radiography in combination with thermal imaging during a lithium-ion cell TR. Their studies provided insights into the structural and thermal dynamics of the TR process and therefore improved the overall understanding within the scientific community.^{122,126,127,130,173} Whilst the group of Finegan et al. focused on the cell's internal dynamics, there also exist studies focusing on the venting behavior of lithium-ion cells. Zou et al. investigated the jet characteristics of the vented gas during TR with high-speed cameras,¹³³ Ding et al. focused on the influence of different altitude levels on the mass loss during TR and flame height by using a low pressure chamber,¹⁷⁴ and Garcia et al. provided insights into the venting process by Schlieren visualization, Natural Luminosity and OH* radical tracing.¹⁷⁵

In summary, experimental methods on single cell level can be divided into two groups. The first group of experiments is used to better understand the processes that take place inside of the battery cell before and during a TR, e.g. the trigger mechanisms, occurring reactions, or the spread of the reactions within the cell. The attention within this thesis, however, is rather placed on the second group that deals with the consequences of a TR after its initiation. This includes questions like what are the maximum temperatures to expect during a TR, how much heat is transferred to surrounding components, or how much gas and particles are vented out of the cell. Chapter 2 will deal with these questions by experimentally assessing the TR key characteristics as defined in section 1.2.4.

1.4.2 Multiple cell level

Whilst experiments on single cell level are used to estimate the TR key characteristics of lithium-ion cells, they are not suitable to provide reliable predictions of the TP behavior in a battery module or pack. Therefore, experiments with multiple cells are a necessity for the validation of the complete system.⁵⁸ In order to reduce costs and resource consumption, so called cell stack tests are performed besides abuse experiments with modules or full battery packs.

Cell stack tests Cell stack tests are widely used to investigate the TP process of lithium-ion batteries. For prismatic and pouch cells, the cell stack consists of at least two cells that are stacked together. Then, one of the cells is triggered into TR and parameters such as the propagation time (duration until TR occurs in the next cell) are investigated. For cylindrical cells, a conventional stacking is not possible due to their round shape. Therefore, stacks with cylindrical cells show various designs. The objective of the experiments, however, is the same as for prismatic and pouch cells. The minimum setup with two cells can be extended by various additional components, e.g. further cells, thermal barrier materials between the cells, an electrical connection of the cells, a cooling plate, and so on. On the one hand, the cell stack setup aims to simplify the actual module or pack conditions in order to reduce possible sources of statistical variance. On the other hand, a setup being as close as possible to the actual module or pack design is preferable, so that results of the cell stack experiments can be transferred to module or even pack level. Table 1.4 summarizes and compares an excerpt of most relevant experimental studies using cell stacks.

Matsumura et al. conducted one of the few studies using overcharge to trigger the TR of the first cell,¹⁷⁶ whilst other trigger methods, such as nail penetration, are more widely used.^{177–180} Most of the studies use a thermal trigger method to initiate the first TR in one of the cells. For cylindrical cells, a possibility to provide a thermal abuse condition is a heating wire that is wrapped around one of the cells.^{181–184} It is also possible to replace one of the cells within the stack by a heating element with the same dimensions.^{185–187} Other researchers used radiation heaters,^{88,188,189} although it is difficult to ensure that only a single cell is affected by the heat radiation with this method. For prismatic and pouch cell stacks, film heaters are commonly used to trigger the first TR.^{190–194} The advantage of such film heaters is their low thickness and therefore, the dimensions of the experimental setup can be kept small. If available space is not a problem, block heaters are another option as trigger method.^{195–203}

Common varied parameters that are investigated regarding their influence on the TP process are SoC,^{177,181,182,185–187,189,190,192,198} different thermal barrier materials between the cells,^{177,179,191,192,196,201,202} different electrical connections of the cells (series or parallel),^{178,181,182,184,192,199} or the cell-to-cell spacing.^{182–184} Huang et al. analyzed the composition of the vented gases.^{192,193} Others implemented thermocouples inside of battery cells, which gives additional insights into cell internal temperatures.^{180,199,200} Single studies also investigated the influence of ambient temperature,¹⁸¹ SoH of the cells,¹⁸² heater

Table 1.4: Excerpt of most relevant stack test studies with lithium-ion batteries.

Author(s)	cell type	chemistry	stack setup	method*	varied parameter	miscellaneous ^o
	cylindrical prismatic pouch		number of cells	triggered cell	thermal barrier	cell spacing
	cell capacity / Ah	LCO LFP LMO NMC mixtures			electrical connection	
Matsumura et al. ¹⁷⁶	✓	✓	7	mid	OC	
Torres-Castro et al. ¹⁷⁷	✓	✓	5	side	NP	
Lamb et al. ¹⁷⁸	✓	✓	5 & 10	mid	NP	
Becher et al. ¹⁷⁹	✓	✓	2 & 3	both	NP	
Feng et al. ¹⁸⁰	✓	✓	6	side	NP	
Niu et al. ¹⁸¹	✓	✓	6	side	HW	
Wang et al. ¹⁸²	✓	✓	3	side	HW	
Wang et al. ¹⁸³	✓	✓	9	side	HW	
Lopez et al. ¹⁸⁴	✓	✓	9	mid	HW	
Ouyang et al. ¹⁸⁵	✓	✓	4 – 16	both	HC	
Zhong et al. ¹⁸⁶	✓	✓	3 & 8	side	HC	
Liu et al. ¹⁸⁷	✓	✓	5	side	HC	
Chen et al. ¹⁸⁸	✓	✓	4 – 25	all	RH	
Huang et al. ¹⁸⁸	✓	✓	5	side	RH	
Ping et al. ¹⁸⁹	✓	✓	5	side	PH	
Li et al. ¹⁹⁰	✓	✓	5	side	PH	
Li et al. ¹⁹¹	✓	✓	4	side	PH	
Huang et al. ¹⁹²	✓	✓	4	side	PH	
Huang et al. ¹⁹³	✓	✓	4	side	PH	
Gao et al. ¹⁹⁴	✓	✓	4	side	PH	
Weng et al. ¹⁹⁵	✓	✓	5	side	BH	
Yan et al. ¹⁹⁶	✓	✓	4	side	BH	
Archibald et al. ¹⁹⁷	✓	✓	1 – 10	side	BH	
Kennedy et al. ¹⁹⁸	✓	✓	5 & 10	side	BH	
Xu et al. ¹⁹⁹	✓	✓	12	side	BH	
Lai et al. ²⁰⁰	✓	✓	4	side	BH	
Yang et al. ²⁰¹	✓	✓	6	side	BH	
Rui et al. ²⁰²	✓	✓	6	side	BH	
Wang et al. ²⁰³	✓	✓	4	side	BH	

*Abbreviations: OC (overcharge), NP (nail penetration), HW (heating wire), HC (heating cell), RH (radiation heating), FH (film heater), BH (block heater)
^oAbbreviations: TC (thermocouple)

position,¹⁸⁵ heater power,¹⁸⁶ water mist cooling,¹⁸⁷ (low) ambient pressure,¹⁸⁸ ambient oxygen concentration,¹⁹⁵ or Ni content of the positive electrode material on the TP process.²⁰³ There exist only a few studies that aimed to represent the boundaries as present in a module, e.g. by attaching a cooling plate,^{179,201,202} or integrating the stack into a housing.¹⁸³ Archibald et al. and Kennedy et al. performed their experiments within a pressure vessel, which may be equivalent to a battery pack housing at the beginning of the tests.^{197,198}

Module and pack tests Table 1.5 summarizes and compares an excerpt of most relevant experimental studies investigating the TP process within a battery module or a full battery pack. As battery modules and packs are only available when disassembled from an EV and, hence, linked to high expenses, the number of publications is small. Wilke et al. studied the effect of a phase change material on the TP process of a full battery pack consisting of 40 cylindrical lithium-ion cells.²⁰⁴ Premnath et al. compared nail penetration and overcharging of a single cell within modules of two different cell chemistry types. They further focused on the analysis of the ejected particles.²⁰⁵ A comparison of nail penetration, overcharging and fire as trigger method was conducted by Christensen et al. with modules consisting of eight cells.²⁰⁶ Held et al. analyzed the contamination of surroundings caused by a TP. Therefore, they triggered all cells of a battery module simultaneously with a wedge.²⁰⁷ Chen et al. investigated the difference between single cell heating with a heating wire and heating of the whole module within an oven,²⁰⁸ whilst film heaters and block heaters were also used to induce a TR within battery modules or packs.^{209–211}

In summary, the experimental assessment of the TP behavior of a battery pack for EVs poses a major challenge. On the one hand, OEMs have to proof that the complete system achieves a certain level of safety for type approval, e.g. according to the Chinese GB standard by performing a pack level test.¹¹³ On the other hand, such tests are expensive and can only be performed at a late stage of the development process. Cell stack tests are a promising solution for this problem, as they can be conducted with reduced costs and already within an early stage of the development process. As summarized above, such tests are also commonly performed by researchers from academia. A major limitation, however, is that for most studies the setup differs significantly from battery pack conditions. In particular, setups including a module structure and a housing are scarce. Additionally, an insufficient number of tests within the same setup is conducted to draw conclusions about the statistical variance of the TP process. These limitations will be more closely investigated in chapter 3.

Table 1.5: Excerpt of most relevant module and pack test studies with lithium-ion batteries.

Author(s)	cell type	chemistry	test setup	miscellaneous
Wilke et al. ²⁰⁴	✓ cylindrical	✓ LFP	40 full pack	mid NP
Premnath et al. ²⁰⁵	✓ prismatic	✓ NMC	96 & 30 module	mid NP & OC
Christensen et al. ²⁰⁶	✓ pouch	✓ LFP	8 module	mid NP, OC & fire
Held et al. ²⁰⁷	✓ pouch	✓ NMC	12 module	all WP
Chen et al. ²⁰⁸	✓ pouch	✓ NMC	25 module	mid HW, oven
Cheng et al. ²⁰⁹	✓ pouch	✓ NMC	12 module	mid FH
Gao et al. ²¹⁰	✓ pouch	✓ NMC	5 – 86 full pack	mid FH
Gao et al. ²¹¹	✓ pouch	✓ NMC	37 full pack	side BH

* Abbreviations: NP (nail penetration), OC (overcharge), WP (wedge penetration), HW (heating wire), FH (film heater), BH (block heater)

1.5 Numerical methods in the context of battery safety

The results drawn from experiments allow to directly assess the safety level of an investigated design by measurable quantities, such as the propagation time. However, it is difficult to get deeper insights into the exact mechanisms of the TP process, as measurable quantities are limited and after such tests there often are just debris and burned remains. Additionally, experiments require special laboratory environments, instruments, and facilities. Due to statistical variance, it is also possible that a large number of experiments is necessary. Therefore, one objective of EV battery manufacturers is to reduce costs and time consumption by establishing virtual development and validation methods. In this context, computational modeling is used as an efficient and cost-effective tool to get further insights into the TP process and, hence, to improve the design of battery packs with respect to safety.^{49,212} Battery safety models can be divided into three groups according to the different stages of a typical TR or TP process. The first group of models focuses on the evolution and initiation of a single cell TR, the second one aims to model the TR process after its onset, and the third one concentrates on simulating the TP process on multiple cell level. In the following, an excerpt of most relevant numerical studies of the second (TR process on single cell level after initiation) and the third group (TP process on multiple cell level) is briefly given. Further information on models of the first group (TR evolution and initiation) can be found in literature.^{59,212–214}

1.5.1 Single cell level

The pioneer work of Richard and Dahn marked the basis of TR modeling. They were one of the first to investigate the thermal stability of active material of the negative electrode in combination with electrolyte by mathematical modeling of the occurring chemical reactions with Arrhenius-like expressions.²¹⁵ Nowadays, there exist numerous numerical studies that are based on this approach, which differ mainly in the number of chemical reactions that are considered in the model. One of the main limitations of such TR models is that the occurring reactions are not fully understood until today.²¹² Therefore, many models include additional source terms such as an electrical-thermal conversion equation accounting for an ISC in order to match the experimental results.^{216–226} Coupling the thermal model with an electrochemical model is another possibility to consider the ISC as TR trigger mechanism.^{227–229} Electrochemical models are also necessary when simulating TRs caused by electric abuse conditions such as overcharge or an external short circuit.^{225–227,229–231} An excerpt of the most relevant of such models is summarized in Tab. 1.6.

An accurate modeling of the TR process, however, requires to consider additional phenomena such as electrolyte vaporization,^{232–236} gas and particle venting,^{230,232,234,235,237–239} and/or coupling the thermal model with a fluid model to account for environmental conditions.^{240,241} Last but not least, if a TR model is supposed to be applied to TP simulations, approaches with low computational effort are necessary.^{187,242–245} An excerpt of the most relevant TR models accounting for such effects are summarized in Tab. 1.7.

Table 1.6: Excerpt of most relevant numerical studies modeling a single cell TR of a lithium-ion battery by Arrhenius equations without consideration of electrolyte vaporization, venting, or a fluid phase.

Author(s)	cell type	cell capacity / Ah	chemistry	experiment*	number of chem. reactions	ISC	electro-chemical	dimensions of thermal model	solver ^a
					modeling approach for heat release			simulation setup	
Hatchard et al. ²¹⁶	✓	1.7	LCO	OT	3	✓	✓	0D	LEM
Lee et al. ²¹⁶	✓	2.4 – 3.4	LCO/NCA	OT/ARC	3	✓	✓	n/a	n/a
Kim et al. ²⁴⁷	✓	n/a	LCO	OT	4			0D/3D	LEM/FVM
Santhanagopalan et al. ²¹⁷	✓	0.8	LCO	ISC	4	✓	✓	2D	FEM
Lopez et al. ²⁴⁸	✓	2.8 – 5.3	LCO	OT	4			3D	FVM
Peng and Jiang ²⁴⁹	✓	n/a	several	OT	4			3D	FVM
Parhizi et al. ²⁵⁰	✓	n/a	n/a	OT/ARC	4			3D	FEM
Melcher et al. ²²⁷	✓	n/a	LCO	ARC	4		✓	3D	FEM
Lai et al. ²⁵¹	✓	10	NMC	ARC	4			3D	n/a
Zhang et al. ²¹⁸	✓	86	LFP	FH	4	✓		3D	FEM
Zhang et al. ²²⁸	✓	n/a	LCO	OT	4		✓	3D	FVM
Macedonald et al. ²⁵²	✓	8	LFP	ISC	4			2D	FEM
Chiu et al. ²¹⁹	✓	5.3	LMO	NP	4	✓	✓	3D	n/a
Liang et al. ²²⁰	✓	10	NMC	NP	4	✓	✓	3D	n/a
Yamanaka et al. ²²¹	✓	10.2	NMC	NP	4	✓	✓	3D	FEM
Ye et al. ²²²	✓	20	NMC	NP	4	✓	✓	3D	FEM
Liu et al. ²²³	✓	20	n/a	NP	4	✓	✓	3D	FVM
Kim et al. ²²⁹	✓	20 & 26	LFP/NMC	OT	4	✓	✓	3D	FEM
Kong et al. ²²⁴	✓	3.4	several	FH	5	✓	✓	3D	FVM
Ren et al. ²⁵³	✓	24	NMC	OT/ARC	6			0D	LEM
Ren et al. ²²⁵	✓	40	mixture	ARC	6	✓	✓	0D	LEM
Spotnitz and Franklin ²²⁶	✓	n/a	LMO/NMC	several	7	✓	✓	0D	LEM
Jiang et al. ²⁵⁴	✓	57	NMC	ARC	7			0D	LEM

* Abbreviations: OT (oven test), ARC (accelerating rate calorimetry), FH (film heater), NP (nail penetration), ISC (internal short circuit)
^a Abbreviations: LEM (lumped element method), FVM (finite volume method), FEM (finite element method)

Hatchard et al. were one of the first to model the TR of a full lithium-ion cell by considering three chemical reactions modeled with Arrhenius-like expressions: (1) decomposition of the SEI layer, (2) reaction of the negative electrode with electrolyte, and (3) reaction of the positive electrode with electrolyte.²⁴⁶ This approach was extended in terms of further reactions such as (4) decomposition of the electrolyte,^{217–223,227–229,247–252} or (5) reaction of the binder with active material,^{224,226,253,254} and individually (*) reaction of the active material of both electrodes,^{225,253} (*) decomposition of the electrode’s active material,^{225,226,253,254} reaction of deposited lithium with electrolyte,^{225,226} or (*) separator melting.²⁵⁴ Many researches added an additional electrical-thermal conversion term in their model to account for the Joule heat originating from an ISC.^{216–226} Others coupled their thermal model with an electrochemical model in order to additionally simulate the evolution of an ISC as TR trigger mechanism,^{217,223,228} short circuit currents triggered by nail penetration,^{219–221} electric abuse conditions (e.g. overcharge or external short circuit),^{225,226,229} or the effect of electrochemical parameters such as internal resistance of the cell on the TR behavior.²¹⁶ The validity of such electrochemical models for TR simulation, however, must be questioned in most cases due to the lack of experimental data within the temperature range of a TR that can be used for parameterization of the models.^{59,212} In addition, many studies use literature values instead of characterizing the investigated cells by appropriate experiments.^{217,220,223,225–228} Besides the electrochemical modeling, the modeling of the chemical reactions during TR also has certain limitations. In order to model the Arrhenius equations, so called “kinetic triplets” are required (namely frequency factor, activation energy, and reaction mechanism), which can be determined e.g. by ARC experiments.^{60,137,255–257} In many cases, however, these triplets are obtained from literature even if another cell chemistry is used. In addition, Hildebrand et al. showed, on the one hand, that it is possible to accurately model ARC test results of two-component measurements by using such kinetic triplets.¹³⁷ But on the other hand, the simulated results on full cell level did not fully match with the ARC measurements, in particular for the phase after TR initiation.¹³⁷

In addition to considering all relevant chemical reactions or electrochemical mechanisms, many researches extend their models by phenomena such as heat dissipation due to gas and particle venting,^{230,232,234,235,237,238} or heat absorption due to phase change processes such as electrolyte vaporization or melting of solid components.^{232,234–236} Others aimed to predict forces acting on a cell’s pouch bag by a gas evolution model,²³³ or to consider environmental conditions by additional mechanical,²³¹ or fluid dynamics models.^{240,241} In order to investigate further electrochemical aspects, researchers additionally implemented aging models,^{258,259} accounted for a loss of active material,²³⁹ or added a solubility model for certain gaseous species.²³⁶ Last but not least, there is a small number of publications aiming to reduce the computational effort as much as possible by empirical modeling approaches for the heat release during TR, for example by using only one or two empirical Arrhenius terms that represent the combination of all chemical reactions,^{242,243,260} or empirical functions based on ARC data.^{244,245}

Table 1.7: Excerpt of most relevant numerical studies modeling a single cell TR of a lithium-ion battery with consideration of venting, electrolyte vaporization, or other effects, and simplified approaches.

Author(s)	cell type	modeling approach for heat release	additional effects	simulation setup	solver [◊]		
	cylindrical prismatic pouch	chemistry	experiment*	number of chem. reactions	ISC electro-chemical venting phase change other	dimensions of thermal model	
	cell capacity / Ah						
Coman et al. ²³²	✓	n/a	LCO OT	3 (Arrhenius)	✓	0D	LEM
Cai et al. ²³³	✓	4.5	NMC ISC	3 (Arrhenius)	✓	0D	LEM
Coman et al. ²³⁷	✓	2.4	NCA LH	4 (Arrhenius)	✓	0D/3D	LEM/FEM
Xu and Hendricks ²³¹	✓	n/a	OT/OC	4 (Arrhenius)	✓	2D	FEM
Abada et al. ²⁵⁸	✓	2.3	LFP OT	4 (Arrhenius)	✓	3D	n/a
Kwak et al. ²⁵⁹	✓	2.3	LFP OT/ARC	4 (Arrhenius)	✓	3D	FEM
Shelkea et al. ²⁴⁰	✓	4.8	NMC ARC/HW	4 (Arrhenius)	✓	3D	FVM
Wang et al. ²³⁴	✓	5	LFP ARC	5 (Arrhenius)	✓	3D	FEM
Wu et al. ²³⁸	✓	130 – 150	NMC OT/FH	5 (Arrhenius)	✓	3D	n/a
Ping et al. ²⁴¹	✓	n/a	NMC ARC	5 (Arrhenius)	✓	3D	FVM
Xu and Hendricks ²³⁰	✓	n/a	OC	6 (Arrhenius)	✓	3D	FEM
Ostaneck et al. ²³⁵	✓	n/a	NMC ARC	7 (Arrhenius)	✓	0D	LEM
Feng et al. ²³⁹	✓	25	NMC ARC	7 (Arrhenius)	✓	0D	LEM
Baakes et al. ²³⁶	✓	0.6	LCO ARC	9 (Arrhenius)	✓	0D	LEM
Lalinde et al. ²⁴²	✓	n/a	several OT	1 empirical (Arrhenius)	✓	0D	LEM
Chen et al. ²⁴³	✓	5	NMC ARC/FH/HW	2 empirical (Arrhenius)	✓	0D/2D/3D	LEM/FEM
Lin et al. ²⁶⁰	✓	57	NMC ARC	2 empirical (Arrhenius)	✓	3D	FEM
Jim et al. ²⁴⁴	✓	50	NMC FH	1 empirical (based on ARC)	✓	3D	FEM
Zhang et al. ²⁴⁵	✓	50	NMC NP	1 empirical (based on ARC)	✓	3D	FEM

* Abbreviations: OT (oven test), ISC (internal short circuit), LH (local heating), OC (overcharge), ARC (accelerating rate calorimetry), HW (heating wire), FH (film heater), NP (nail penetration)
 ◊ Abbreviations: LEM (lumped element method), FEM (finite element method), FVM (finite volume method)

The majority of the models summarized in Tab. 1.6 and Tab. 1.7 do not consider gas and particle venting. In addition, the few studies accounting for gas and/or particle venting within the mass and/or energy balance, do not model a gas and/or particle phase.^{230,232,234,235,238} Therefore, numerical studies investigating the venting behavior of a lithium-ion battery cell TR are briefly summarized in the following.

Coman et al. built a mathematical model to predict the temperature-pressure behavior and gas generation inside of a cylindrical cell (18650 format). The purpose of the model was to predict the onset of venting during an overheating experiment.²⁶¹ Kim et al. developed a computational fluid dynamics (CFD) model to study the gas-phase dynamics of 18650 cylindrical cells undergoing thermal runaway. Their model considered a first venting event as soon as the internal pressure exceeds the burst pressure of the safety valve, and a second venting event as soon as TR occurs.²⁶² The model of Srinivasan et al. only considered a first venting event before TR and aimed to predict the distribution of vented gases that cool down and condense on the surroundings, as this condensate can potentially be ignited during a second venting event.²⁶³ Li et al. developed a high resolution CFD model in order to investigate the steady-state flow through different vent geometries for 18650 cylindrical cells.²⁶⁴ Wang et al. were one of the first to also consider solid particles within their CFD model. Based on experimental results, they built a multi-phase model simulating the fluid flow and particle motion outside of the cell, capturing the jet, spread, and final deposition of the particles.²⁶⁵

As already shown for the experimental methods on single cell level, it can be summarized that within the field of numerical studies much research focuses on the question what is happening inside of the battery cell during a TR. This is done by considering as much chemical reactions as possible within numerical models and additionally accounting for electrical and/or electrochemical effects. The focus of this thesis, however, is to develop a rather simple and efficient model that is capable of replicating the “outer” behavior of a battery cell during TR, i.e. releasing the correct amount of heat to the surroundings within the correct amount of time. For this purpose, empirical approaches are considered promising. Unfortunately, studies proposing such empirical approaches are scarce. Therefore, chapter 2 deals with such approaches in more detail.

1.5.2 Multiple cell level

The transfer of single cell TR models to multiple cell level is crucial in order to establish virtual development methods as an efficient and cost-effective tool for battery pack design. From a numerical point of view, however, the TP process is a complex multi-physics problem that has to be solved in several domains. It is not only important to model the solid body heat conduction, but also the fluid phase of the venting gases, as well as the liquid and solid particles within this fluid phase. As coupled models combining solid and fluid phases need high computational resources, the focus for TP simulation is to develop efficient methods within each domain. In particular for battery pack simulation, the geometrical dimensions pose an additional challenge. Table 1.8 summarizes and compares

an excerpt of most relevant numerical studies modeling a TP process within multiple lithium-ion cells.

As on single cell level, there exist various numerical studies that use three,^{266–268} four,^{269–279} or six chemical reactions to model the heat release during TR.^{280,281} Empirical modeling approaches, however, are represented in larger numbers on multiple cell level compared to single cell level, which is explained by the fact that the geometrical dimensions of TP experiments, and hence the computational models, are usually larger compared to TR experiments.^{282–290} On multiple cell level, the modeling approach for heat release during TR can be also extended by either an electrical-thermal conversion term for the ISC,^{266,269,275,277,280,283} or by a coupling of the thermal model with an electrochemical model.^{267,268,276–279,282} Although the venting process during a TR is assumed to have a significant influence on the TP process, the number of publications considering venting either by coupling a thermal model with a fluid model,^{271,285,287} or considering the mass loss within the solid body of the thermal model is small.^{282,289} Researchers rather couple their thermal model with a fluid model to account for natural convection,^{271,273,274} or to study the effect of fluid flow within cooling plates on the TP process.^{218,279}

In summary, the given overview of TP models confirms that there is a need for simplified and efficient methods to model the TR of lithium-ion batteries and, in particular, the TP process within battery packs. Several empirical approaches haven been proposed in recent studies. However, there are no publications comparing different approaches in order to assess their suitability for TR and TP simulation.

In addition, studies focusing not only on modeling solid body heat conduction, but also the vented gas and particles, are scarce. Especially vented particles are neglected in current TP models, probably due to the high computational resource consumption and a lack of experimental data that can be used for model validation. This poses a risk, given that a significant amount of mass, and hence particles, is vented out of the cell during TR that can cause severe consequences. Therefore, coupling a thermal model with a gas-particle-flow model is one of the main objectives of this thesis.

Table 1.8: Excerpt of most relevant numerical studies modeling a TP process within several lithium-ion batteries.

Author(s)	cell type			modeling approach for heat release			additional source terms			simulation setup			
	prismatic	cell capacity / Ah	chemistry	experiment*	number of cells	triggered cell	number and type of chemical source terms ⁺	ISC	electro-chemical	venting (gas)	venting (solid)	other	dimensions of thermal model
Jia and Xu ²⁶⁶	✓	3.4	NCA	NP	2	side	3 chem. reactions (Arrhenius)	✓	✓	✓	✓	3D	FEM
Coman et al. ²⁶⁷	✓	2.4	NCA	ISC	65	side	3 chem. reactions (Arrhenius)		✓			2D/3D	FEM
Kurzawski et al. ²⁶⁸		3	LCO	NP	5	side	3 chem. reactions (Arrhenius)		✓			quasi-1D	FEM
Yuan et al. ²⁶⁹	✓	3.5	NCA	HW	11	mid	4 chem. reactions (Arrhenius)	✓				3D	FVM
Bugryniec et al. ²⁷⁰	✓	1.5	LFP	none	9	side	4 chem. reactions (Arrhenius)					2D	FEM
Mishra et al. ²⁷¹	✓	n/a	LCO	none	25	side	4 chem. reactions (Arrhenius)		✓			3D	FVM
Mishra et al. ²⁷²	✓	n/a	LCO	none	25	mid	4 chem. reactions (Arrhenius)			✓		3D	FVM
Mishra and Jain ²⁷³	✓	n/a	n/a	none	25	both	4 chem. reactions (Arrhenius)			✓		3D	FVM
Li et al. ²⁷⁴	✓	3	NMC	none	192	both	4 chem. reactions (Arrhenius)			✓		3D	FEM+FVM
Shen et al. ²⁷⁵		203	NMC	NP	6	side	4 chem. reactions (Arrhenius)	✓				0D	LEM
Vyroubal et al. ²⁷⁶	✓	2.9	NMC	HW	pack	both	4 chem. reactions (Arrhenius)		✓			3D	FVM
Jia et al. ²⁷⁷	✓	3.4	NCA	NP	2 – 400	side	4 chem. reactions (Arrhenius)	✓	✓			0D	LEM
Zhang et al. ²⁷⁸		25	NMC	none	2	side	4 chem. reactions (Arrhenius)		✓		✓	3D	FEM
Jindal et al. ²⁷⁹	✓	2.8	LCO	none	10	mid	4 chem. reactions (Arrhenius)		✓		✓	3D	FVM
Feng et al. ²⁸⁰		25	NMC	NP	6	side	6 chem. reactions (Arrhenius)	✓				0D	LEM
Chen et al. ²⁸¹		24	NMC	OT	2	both	6 chem. reactions (Arrhenius)					0D	LEM
Liu et al. ²⁸²	✓	2.6	LCO	FH	6	side	1 empirical Arrhenius source term		✓		✓	3D	FEM
Feng et al. ²⁸³		27	n/a	NP	6	side	1 empirical Arrhenius source term	✓				3D	FEM
Xu et al. ²⁸⁴	✓	156	n/a	FH	4 – 54	side	1 empirical Arrhenius source term					0D	ROM
Grimmeisen et al. ²⁸⁵	✓	n/a	NCA	none	7	side	constant HRR			✓		3D	FVM
Qin et al. ²⁸⁶	✓	n/a	n/a	none	9	side	temp. dependent HRR					3D	FVM
Citarella et al. ²⁸⁷		n/a	n/a	none	pack	side	temp. dependent HRR (ARC data)		✓			3D	FVM
Yeow et al. ²⁸⁸		70	NMC	none	3	mid	temp. dependent HRR (ARC data)					3D	FEM
Coman et al. ²⁸⁹	✓	3.5	NCA	ISC	pack	both	time dependent function for HRR					3D	FEM
Bilyaz et al. ²⁹⁰		5 & 10	LCO	FH	5 – 10	side	LPFPT (single reaction)			✓		2D	FEM
												0D	FDM

* Abbreviations: NP (nail penetration), ISC (internal short circuit), HW (heating wire), OT (oven test), ARC (accelerating rate calorimetry), FH (film heater)

⁺ Abbreviations: HRR (heat release rate), LPFPT (laminar premixed flame propagation theory)

^o Abbreviations: FEM (finite element method), FVM (finite volume method), LEM (lumped element method), ROM (reduced order model), FDM (finite difference method)

1.6 Thesis outline

As shown in sections 1.2 and 1.3, potential hazards of lithium-ion batteries, in particular the TR phenomenon and a potential subsequent TP, can lead to catastrophic consequences. Considering the further increase of the specific energy and energy density of future battery packs (see section 1.1), efficient experimental and numerical methods are necessary within the design and validation process of lithium-ion batteries in order to ensure the safety of BEVs.

As pointed out in section 1.4, there exist various experimental setups to characterize a single cell TR or to assess the TP behavior of systems containing multiple cells. Whilst the experimental determination of TR key characteristics can be done by several standardized methods such as ARC, calorimetric and/or autoclave experiments, there exist no such standardized experiments for the evaluation of the TP process. Cell stack experiments are a promising alternative to high-cost abuse testing on module or pack level. However, there is a variety of different setups and varied parameters that need to be designed in a representative fashion. In addition, studies investigating all aspects of the TP process, in particular the effect of vented gas and particles, are rare. There is also a lack of numerical methods that do not only consider heat conduction within solid bodies, but also the heat transfer mechanisms induced by the vented gas and particles (see section 1.5). Especially models that include a domain for the vented particles are scarce.

Therefore, the objective of this work is to develop a multi-stage approach consisting of both experimental and numerical methods, that allows to efficiently assess the TP behavior in cell stacks of prismatic lithium-ion batteries. To account for the relevant heat transfer mechanisms dominating the TP process, all of the three domains solid body, vented gas, and vented particles shall be considered. The development process is divided into the **TR behavior of single lithium-ion battery cells** (see chapter 2) and the **TP behavior of lithium-ion battery cell stacks** (see chapter 3). In chapter 4, the resulting **multi-stage approach** is presented. In this context, a coupled numerical TP model that combines a solid body simulation with a gas-particle-flow simulation is proposed, which is based on efficient empirical approaches and, hence, neglects computationally intensive effects such as electrochemical processes or combustion of gases. Figure 1.8 schematically shows the outline of this thesis highlighting the contributions to either experimental or numerical methods.

The initial step of the development process is an experimental assessment of TR key characteristics. In this context, the focus is laid on the consequences of a TR after its initiation, more precisely which amount of heat is released during the process, how much mass is vented out of the cell, and how is this mass loss distributed into vented gas and vented particles. Therefore, the results of in total 25 different types of prismatic lithium-ion battery cells examined in an autoclave calorimetry experiment are analyzed in section 2.1. The analysis provides several TR key characteristics as defined in section 1.2.4 and consequently serves as an excellent basis for the development of a TR model, which is presented in section 2.2. The main objective here is to identify a simple

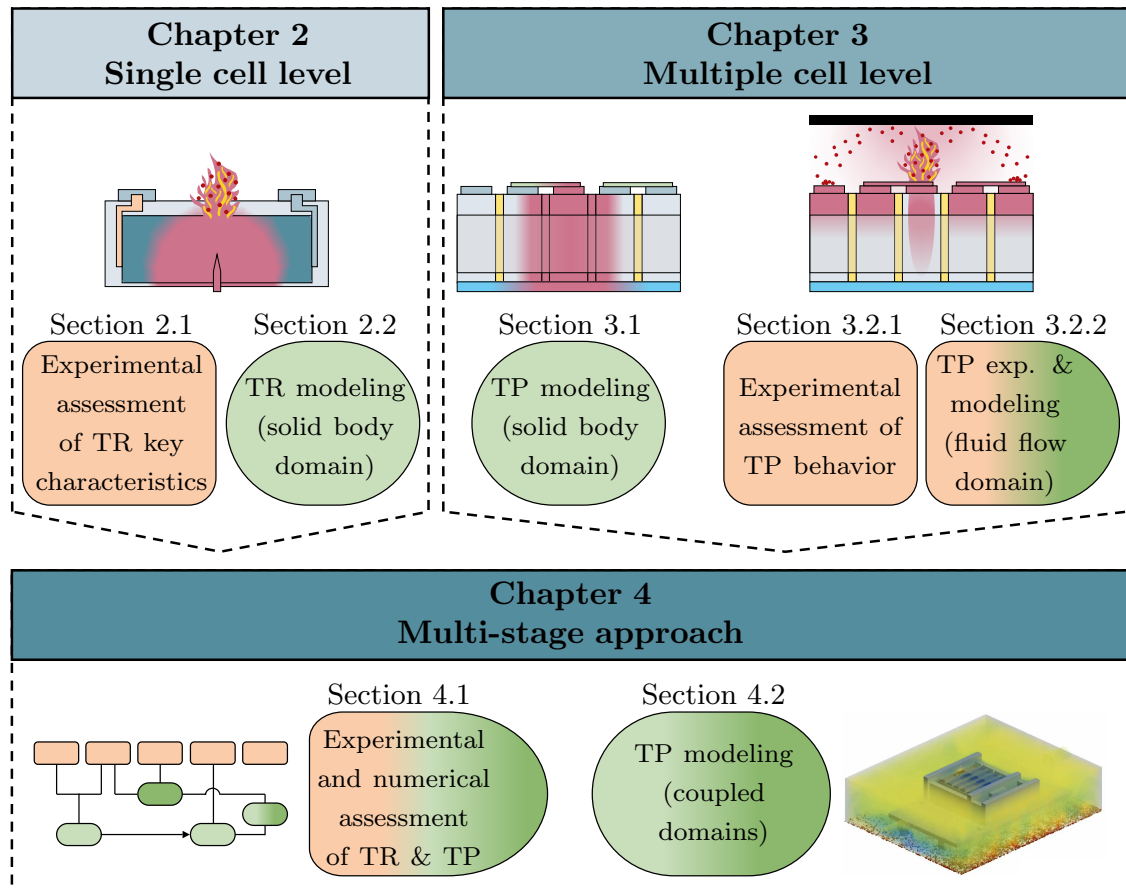


Figure 1.8: Graphical outline of this thesis highlighting the contributions to either experimental methods (orange) or numerical methods (green).

and efficient modeling approach that is capable of replicating the behavior of a battery cell during TR as previously characterized by the autoclave calorimetry experiments with as little complexity as possible, i.e. without modeling each reaction individually and/or electrochemical effects. This is done by simulating the solid body domain of the autoclave calorimetry experiment and comparing three different modeling approaches for the heat release during TR: (1) an empirical time-dependent function based on ARC data, (2) an empirical temperature-dependent function based on ARC data, and (3) a single empirical Arrhenius equation spatially resolving the TR reaction front.

In order to establish a coupled TP model including both solid body and gas-particle-flow simulation, it is crucial to reduce the computational resource consumption. Therefore, the compared modeling approaches are applied to a cell stack experiment consisting of five prismatic lithium-ion cells and analyzed with respect to their suitability for TP simulation in section 3.1. Like on single cell level, only solid body heat conduction is considered within this first step. Results of cell stack experiments conducted without a housing are used for validation, as vented gas and particles have a minor influence on the TP process in this case. As discussed in section 1.4, however, the experimental setup of such cell stack tests has to be as close as possible to battery pack conditions to be able to make reliable predictions of the TP process. In addition, multiple tests have to be performed in order

to evaluate the statistical variances. Therefore, the influence of the module structure and the integration of cell stacks into a housing is investigated by cell stack experiments in section 3.2.1. As especially experiments focusing on vented particles are scarce, the gas-particle-flow occurring during a TR is subsequently investigated in section 3.2.2. In a first step, the deposition of particles vented during a TR in a battery module environment is determined by an experimental study. This is essential, as there is no such experimental data available in literature so far (see sections 1.4 and 1.5). In a second step, the experimental results are used as a basis for the development and validation of a gas-particle-flow model based on the Euler-Lagrangian approach. Such models have practically not been investigated in the past (see section 1.5).

In section 4.1, the multi-stage approach resulting from this work is presented. The most promising modeling approach for TP simulation (section 3.1) is coupled with the gas-particle-flow simulation from section 3.2.2. In addition, all experimental and numerical methods that are necessary to build the coupled TP model are summarized once again. Finally, the cell stack experiments performed with housing, as presented in section 3.2.1, are used to compare experimental results with results of the coupled model in section 4.2. This allows for the first time to answer the question of how vented gas and particles influence the TP process of battery stacks with prismatic lithium-ion cells.

Some of the sections mentioned above have already been published as papers. Section 2.1 includes the article “Analysis on Thermal Runaway Behavior of Prismatic Lithium-Ion Batteries with Autoclave Calorimetry” by S. Hoelle, S. Scharner, S. Asanin, and O. Hinrichsen, *Journal of The Electrochemical Society* 168, No. 120515, 2021. Section 2.2 includes the article “3D Thermal Simulation of Lithium-Ion Battery Thermal Runaway in Autoclave Calorimetry - Development and Comparison of Modeling Approaches” by S. Hoelle, F. Dengler, S. Zimmermann, and O. Hinrichsen, *Journal of The Electrochemical Society* 170, No. 010509, 2023. Section 3.1 includes the article “3D Thermal Simulation of Thermal Runaway Propagation in Lithium-Ion Battery Cell Stack - Review and Comparison of Modeling Approaches” by S. Hoelle, S. Zimmermann, and O. Hinrichsen, *Journal of The Electrochemical Society* 170, No. 060516, 2023. Section 3.2.1 includes the article “Experimental Investigation on Thermal Runaway Propagation in Lithium-Ion Battery Cell Stack” by S. Hoelle, S. Haberl, A. Rheinfeld, P. Osswald, S. Zimmermann, and O. Hinrichsen, *2022 IEEE Transportation Electrification Conference & Expo (ITEC)*, pp. 1174–1179, 2022. Section 3.2.2 includes the article “Lithium-Ion Battery Thermal Runaway: Experimental Analysis of Particle Deposition in Battery Module Environment” by S. Hoelle, H. Kim, S. Zimmermann, and O. Hinrichsen, *Batteries* 10(6), No. 173, 2024.

In summary, the presented multi-stage approach is not only capable of efficiently assessing the TP behavior in cell stacks of prismatic lithium-ion batteries by combining both experimental and numerical methods, but also has the potential to be universally applicable to other cell formats or higher integration levels, such as modules or packs. Such an approach is crucial in order to satisfy both range and safety requirements of current and future battery packs for EVs.

2 Thermal Runaway Behavior of Lithium-Ion Battery Cells

Characterizing the TR behavior of a lithium-ion battery cell is crucial in order to estimate the abuse tolerance of a battery pack comprising several of such cells. As described in section 1.4, experimental methods such as ARC or autoclave tests are readily available and widely applied to assess the TR key characteristics. The findings of such experiments can subsequently be used to derive input parameters for modeling and simulation. In turn, numerical methods give additional insight into the TR process and allow to investigate the impact of parameters that cannot be varied in experiments.

In this chapter, the experimental assessment of TR key characteristics by an autoclave calorimetry experiment is presented (section 2.1). Afterwards, the results of the experimental study are used to parameterize, validate, and compare three different modeling approaches for the heat release during TR: (1) an empirical time-dependent function based on ARC data, (2) an empirical temperature-dependent function based on ARC data, and (3) a single empirical Arrhenius equation spatially resolving the TR reaction front (section 2.2).

2.1 Experimental assessment of thermal runaway key characteristics

The article titled “*Analysis on Thermal Runaway Behavior of Prismatic Lithium-Ion Batteries with Autoclave Calorimetry*” is presented within this section. It was submitted to the peer-reviewed *Journal of The Electrochemical Society* in September 2021 and published online in December 2021.

The objective of this work was to quantify certain TR key characteristics such as mass loss during TR Δm_{TR} , amount of vented gas m_{gas} , and heat remaining in the cell body after TR Q_{remains} . As described in section 1.4, autoclave experiments are suitable for the determination of m_{gas} , whereas calorimetric approaches are necessary in order to quantify Q_{remains} . Therefore, both methods are combined within the autoclave calorimetry experiment, where the investigated cell is integrated into a copper block (similar to the CSBC by Liu et al.)^{160,161} and the resulting assembly is installed within an autoclave. Then, the cell is triggered into TR by nail penetration. Thermally insulating the copper block against the autoclave environment results in two separated domains: on the one hand, the heat released during TR that is not vented out of the cell body is transferred to the copper block, which allows to determine Q_{remains} by measuring the copper block’s temperature increase. On the other hand, the vented gas leads to a pressure rise within

2 Thermal Runaway Behavior of Lithium-Ion Battery Cells

the autoclave, that can be used to evaluate m_{gas} . The mass loss during TR Δm_{TR} is quantified by weighing the cell before and after the test. Further processing of the results allows to additionally estimate the mass of vented particles $m_{\text{particles}}$ and the fraction of released heat during TR that is vented out of the cell Q_{venting} .

In total, 25 different types of prismatic lithium-ion cells with a capacity between 8 and 145 Ah were examined in the described autoclave calorimetry experiment. Due to the wide capacity range, the analysis of the results allowed to derive empirical correlations for the investigated TR key characteristics. On average, the tested cells lost 7.05 g Ah^{-1} of their mass during TR. This mass loss was distributed into 2.05 g Ah^{-1} of gas and 5.00 g Ah^{-1} of particles and liquid droplets, which resulted in 29.1 % of Δm_{TR} being gaseous and 70.9 % being liquid or solid. The heat released during TR Q_{TR} was on average 19.45 kJ Ah^{-1} , of which 10.76 kJ Ah^{-1} or 55.3 % were allocated to Q_{remains} and consequently 8.69 kJ Ah^{-1} or 44.7 % to Q_{venting} . The ratio of Q_{TR} divided by the electrical energy stored within the cell was found to be on average 1.41, i.e. the heat released during a TR was 41 % higher than the energy that was electrically stored within the lithium-ion cell.

The results of the autoclave calorimetry experiment provide input parameters and form the basis for a validation of modeling approaches for the heat release during TR. In addition, it is possible to determine certain input parameters for the gas-particle-flow model. The derived correlations further help to predict the TR behavior of lithium-ion cells within the property range of those tested. Therefore, the study contributes to the design of a safer battery pack.

Analysis on Thermal Runaway Behavior of Prismatic Lithium-Ion Batteries with Autoclave Calorimetry

S. Hoelle, S. Scharner, S. Asanin, and O. Hinrichsen

Journal of The Electrochemical Society 168, No. 120515, 2021

Permanent weblink:

<https://doi.org/10.1149/1945-7111/ac3c27>

Reproduced under the terms of the Creative Commons Attribution 4.0 License (CC BY, <https://creativecommons.org/licenses/by/4.0/>), which permits unrestricted reuse of the work in any medium, provided the original work is properly cited.

Author contributions:

S. Scharner initiated and developed the design of the autoclave calorimetry setup with support of the Fraunhofer Institute for Chemical Technology (ICT), Pfinztal, Germany. S. Hoelle initiated and built the database that was used for data analysis. Therefore, S. Hoelle further developed the evaluation methodology originally proposed by S. Scharner. The data was analyzed by S. Hoelle. The manuscript was written by S. Hoelle and was edited by S. Scharner, S. Asanin, and O. Hinrichsen. All authors discussed the data and commented on the results.



Analysis on Thermal Runaway Behavior of Prismatic Lithium-Ion Batteries with Autoclave Calorimetry

S. Hoelle,^{1,2,z} S. Scharner,¹ S. Asanin,¹ and O. Hinrichsen^{2,3}

¹BMW Group, Munich, Germany

²Technical University of Munich, Department of Chemistry, 85748 Garching near Munich, Germany

³Technical University of Munich, Catalysis Research Center, 85748 Garching near Munich, Germany

A total number of 25 different types of prismatic lithium-ion cells with a capacity between 8 and 145 Ah are examined in an autoclave calorimetry experiment in order to analyze their behavior during thermal runaway (TR). The safety relevant parameters such as mass loss, venting gas production and heat generation during TR are determined in two experiments per cell type and the results are compared to literature. An approximately linear dependency of the three parameters on the cell capacity is observed and hence correlations are derived. Due to the wide range in cell properties the correlations can be used as input for simulations as well as to predict the behavior of future battery cells within the property range of those tested and therefore contribute to the design of a safer battery pack.

© 2021 The Author(s). Published on behalf of The Electrochemical Society by IOP Publishing Limited. This is an open access article distributed under the terms of the Creative Commons Attribution 4.0 License (CC BY, <http://creativecommons.org/licenses/by/4.0/>), which permits unrestricted reuse of the work in any medium, provided the original work is properly cited. [DOI: 10.1149/1945-7111/ac3c27]



Manuscript submitted September 17, 2021; revised manuscript received November 11, 2021. Published December 6, 2021.

One of the top barriers to purchasing an electric vehicle (EV) is the fear of customers to run out of power.¹ This reinforces the manufacturers of EVs to continuously enhance the range of their products: by now several EVs with a range of more than 300 miles have been announced.^{2–5} This is achieved by the usage of battery cells with high energy density. The major safety issue of high energy batteries is the thermal runaway (TR) that can occur e. g. as a result of a traffic accident or a failure during the charging process.⁶ Therefore, many researchers investigate the behavior of battery cells under certain abuse conditions with experimental and numerical methods.

On pack level the work focuses on the thermal propagation (TP) behavior and possible mitigation strategies.^{7–10} On single cell level one objective is to get a better understanding of the TR process for example via X-ray imaging and tracking internal temperatures.¹¹ Other publications aim to determine safety relevant parameters such as mass loss,^{12–16} onset temperature,^{12,13,17–20} energy release,^{15,16,21–26} venting gas composition and generated gas amount during TR.^{12,13,19,20,27,28} It turned out that these parameters depend, among other things, on cell chemistry,^{16,20,22,23,25,29} cell format,^{19,27} trigger method^{12,19} and state-of-charge.^{13,15,29,30} The experimental results are widely used as input parameters or validation data for simulation models.^{17,18,26,28} The latter support engineers to gain further insight into the TR and TP process and consequently are an important tool in the development and design process of safe battery packs.

This publication focuses on the TR behavior of prismatic lithium-ion batteries over a wide capacity range (8 Ah to 145 Ah). The objective is to derive empirical correlations of important parameters such as mass loss, amount of vented gas and generated heat during TR. The correlations can be used to determine crucial input parameters for simulation models as well as to predict the behavior of battery cells within the property range of those tested. To the author's knowledge, comparative analyses of a large number of state of the art automotive lithium-ion batteries have not been the subject of any scientific publication, especially over a wide capacity range and with capacities up to 145 Ah. Therefore, the results of this study contribute to the design of a safer battery pack.

Experimental

A total number of 50 prismatic lithium-ion cells (25 different types —2 tests each) is triggered into TR by nail penetration in order to investigate the TR behavior and identify dependencies of important

parameters. The cells are integrated into an insulated copper block that itself is inside an autoclave as presented by Scharner in Ref. 21. Therefore, it is possible to quantify not only the mass loss and the amount of generated venting gas but also the generated heat. After one of the 50 tests a sample of the generated venting gas is analyzed via gas chromatography to identify the gas composition. This gas composition is assumed to be representative for all tests.

Autoclave calorimetry setup.—Figure 1 shows the autoclave calorimetry setup. The tested battery cell (blue) is wrapped in a silicate fiber fabric (purple—thermal control) and integrated into a copper block (orange). The purpose of the thermal control is to prevent high heat fluxes between cell and copper block that could alleviate the TR reaction. The thickness of the fabric (ThermTextil® TT1200) is 2.3 mm, whereas the dimensions of the cavity inside the copper block are 1.75 mm bigger as the nominal cell dimension in each direction. This results in a compression of the silicate fiber fabric and therefore a tight fit of the cell in the copper block. The copper block itself is also insulated (yellow—PROMALIGHT®-1000X) to ensure a minimal heat transfer from the copper block to the autoclave environment. The thermal insulation has an opening above the vent of the battery cell to provide a flow path into the autoclave's void volume for the generated venting gas and particles. The cell is triggered into TR via nail penetration through another opening in the thermal insulation as well as in the copper block. Therefore, a steel nail with 3.2 mm diameter and 60° nail tip angle is used. The depth of the penetration is 15 mm in the center of the large side with a penetration speed of 80 mm/s. All tests are conducted under inert atmosphere (argon).

Measured parameters and evaluation methodology.—Table I summarizes all measured parameters before, during and after the autoclave calorimetry test. Before each test a preconditioning cycle is performed with each cell to ensure an adequate stabilization of the battery performance and to measure the cell capacity C_{cell} . During this process the following steps are repeated three times at room temperature:

- charging of the cell with the constant current constant voltage (CCCV) charging method,
- pause for 30 minutes,
- discharging of the cell with a constant current of $C_{\text{cell,nominal}}/3$, where $C_{\text{cell,nominal}}$ is the cell's nominal capacity specified by the manufacturer,
- pause for 30 minutes.

^zE-mail: sebastian.hoelle@bmw.de

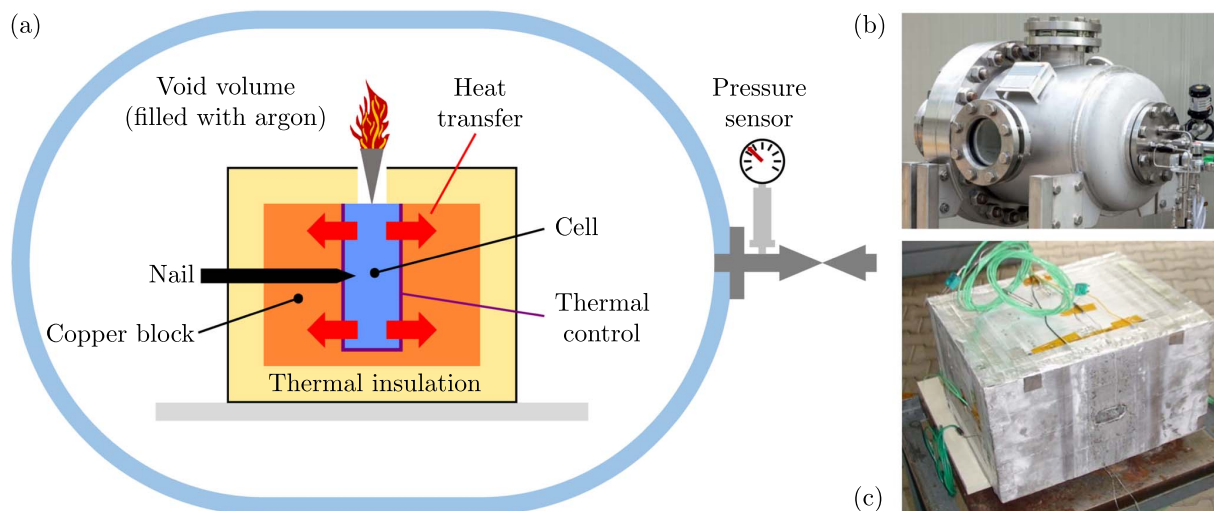


Figure 1. (a) Scheme of the autoclave calorimetry setup. (b) Full view of the autoclave.²¹ (c) Insulated copper block with implemented cell.²¹

Table I. Measured parameters before, during and after the autoclave calorimetry test.

Parameter	Symbol	Unit	Frequency	Comment
Autoclave pressure	p_{gas}	Pa	100 Hz	1 position
Cell can temperature	$T_{i,\text{cell}}$	°C	1 Hz	5 positions
Copper block temperature	$T_{i,\text{Cu}}$	°C	1 Hz	5 positions
Gas temperature	T_{gas}	°C	1 Hz	1 position
Capacity	C_{cell}	Ah	mean value	preconditioning
Copper block mass	m_{Cu}	kg	single value	before test
Pre cell mass	m_{cell}	kg	single value	before test
Post cell mass	$m_{\text{cell,TR}}$	kg	single value	after test

Afterwards, the cell capacity C_{cell} is determined by the mean value of the three discharging cycles. Prior to the test the cell is charged to a state of charge of $SoC = 100\%$ with the CCCV charging method and a CV phase of 12 h. In addition, the weight of the copper block m_{Cu} and the cell m_{cell} is measured before the test as well as the weight of the cell $m_{\text{cell,TR}}$ after the test. The mass loss during TR Δm_{cell} is then calculated by

$$\Delta m_{\text{cell}} = m_{\text{cell}} - m_{\text{cell,TR}} \quad [1]$$

During the test the gas pressure p_{gas} and temperature T_{gas} are measured. The generated venting gas n_{gas} can then be calculated by applying the ideal gas law:

$$n_{\text{gas}}(t) = \frac{p_{\text{gas}}(t) V_{\text{void}}}{RT_{\text{gas}}(t)} - n_{\text{init}} \quad [2]$$

where V_{void} is the void volume inside the autoclave, R is the gas constant and n_{init} is the initial amount of gas at the start of the experiment. The void volume is determined by

$$V_{\text{void}} = V_{\text{autoclave}} - V_{\text{specimen}} \quad [3]$$

where $V_{\text{autoclave}} = 157.65 \text{ l}$ is the inner volume of the autoclave and V_{specimen} is the volume of the investigated cell, the copper block and its thermal insulation.

The ideal gas law (Eq. 2) only applies if the measured T_{gas} is the average gas temperature inside the autoclave. Due to the high local and temporal gradients inside the autoclave during the TR (and thus

the venting process) this is not the case until the gas reaches a thermodynamic equilibrium state. As a consequence the gas amount calculated by Eq. 2 $n_{\text{gas,calc}}$ shows high deviations from the actual amount of gas present inside the autoclave n_{gas} . In this study it is assumed that this deviation is acceptable as soon as the following criteria are fulfilled:

$$0 \frac{\text{K}}{\text{min}} \geq \frac{dT_{\text{gas}}}{dt} \geq -2 \frac{\text{K}}{\text{min}} \quad [4]$$

$$\frac{d^2T_{\text{gas}}}{dt^2} > 0 \quad [5]$$

$$\frac{dn_{\text{gas,calc}}}{dt} \leq 0. \quad [6]$$

Figure 2 visualizes this definition. During the venting process the curve of $n_{\text{gas,calc}}$ shows a nonphysical behavior due to the measurement errors of T_{gas} . After the venting event the gradients decrease due to the approach of the gas to a thermodynamic equilibrium. In this study the temperature inside the autoclave is considered homogeneous when Eqs. 4 and 5 are fulfilled. In addition $n_{\text{gas,calc}}$ has to be either at a (local) maximum or in a decreasing state. This is verified by Eq. 6.

With the calculated vented gas amount at the defined equilibrium state $n_{\text{gas,eq}}$ the vented gas mass m_{gas} and the vented gas volume V_{gas} are determined by

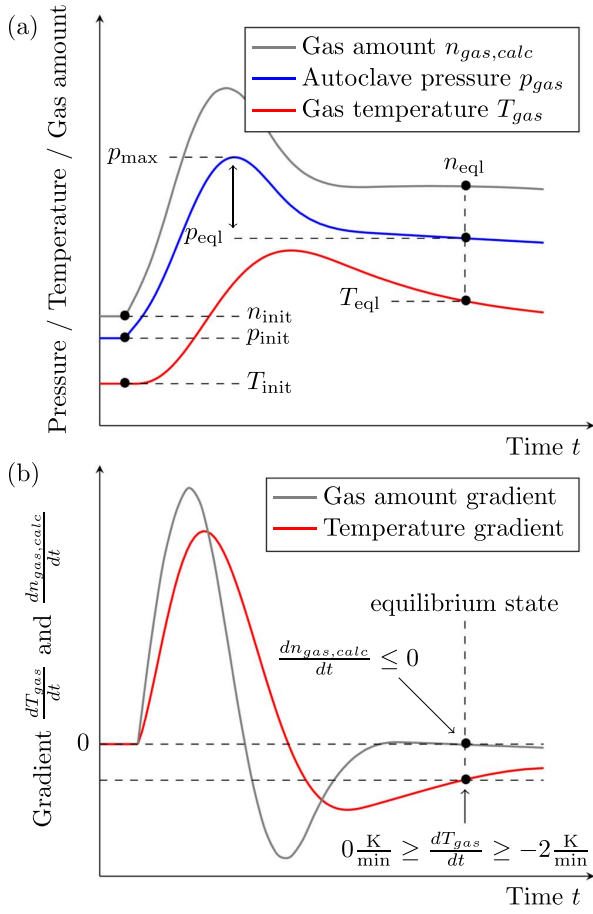


Figure 2. Evaluation methodology: (a) Sample curves of autoclave pressure p_{gas} , gas temperature T_{gas} and the calculated gas amount $n_{\text{gas,calc}}$. (b) Sample curves of gas temperature gradient dT_{gas}/dt and gas amount gradient $dn_{\text{gas,calc}}/dt$ with the criteria for the defined equilibrium state inside the autoclave.

$$m_{\text{gas}} = n_{\text{gas,eq}} M_{\text{gas}} \quad [7]$$

$$V_{\text{gas}} = n_{\text{gas,eq}} V_{\text{m,gas}} \quad [8]$$

with $M_{\text{gas}} = 23.38 \text{ g mol}^{-1}$ being the (assumed) average molar mass of the vented gas mixture and $V_{\text{m,gas}} = 24.465 \text{ l mol}^{-1}$ being the molar volume of an ideal gas at $25 \text{ }^\circ\text{C}$ and 1 atm (SATP conditions). In this study the molar mass M_{gas} is determined in one of the test via gas chromatography (as shown below) and assumed to be constant for all cell types. With the total mass loss Δm_{cell} and the vented gas mass m_{gas} the vented particle mass is calculated by

$$m_{\text{particles}} = \Delta m_{\text{cell}} - m_{\text{gas}} \quad [9]$$

With this definition ‘‘particles’’ also include liquid venting products or gaseous venting products that already condensed at the point of the defined equilibrium state.

The cell can temperature $T_{i,\text{cell}}$ and copper block temperature $T_{i,\text{Cu}}$ are monitored at several positions during the test as shown in Fig. 3. One sensor is placed in the center of each cell can side (circles). The sensor on the penetrated cell side is shifted in order to prevent a damage due to the nail (blue). Equivalent sensors are placed inside of the copper block (triangles). These are positioned at half of the block thickness in each dimension. As suggested by

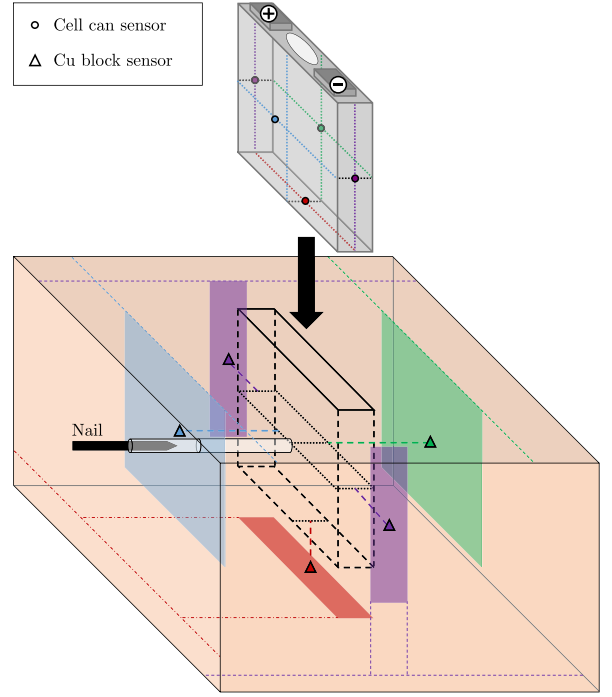


Figure 3. Temperature sensor positions on cell can surface and inside the copper block.

Scharner it is assumed that the total generated heat during TR Q_{tot} is divided into two parts: heat that remains in the cell Q_1 and heat that is transported by vented gas and particles Q_2 .²¹ The remaining heat Q_1 is calculated on the basis of a suggested formula in Ref. 21 as follows:

$$Q_1 = c_{p,\text{Cu}} m_{\text{Cu}} (\bar{T}_{\text{Cu,max}} - \bar{T}_{\text{Cu,init}}) + c_{p,\text{cell}} m_{\text{cell,TR}} (\bar{T}_{\text{cell}@Cu,max} - \bar{T}_{\text{cell,init}}) \quad [10]$$

where $c_{p,\text{Cu}}$ and $c_{p,\text{cell}}$ are the specific heat capacities of the copper block and the cell, respectively, $\bar{T}_{\text{Cu,max}}$ is the maximum value (over time) of the mean over all temperature sensors in the copper block, $\bar{T}_{\text{cell}@Cu,max}$ is the mean over all cell can temperature sensors at the point in time of $\bar{T}_{\text{Cu,max}}$ and $\bar{T}_{\text{Cu,init}}$ as well as $\bar{T}_{\text{cell,init}}$ are the initial values of the mean over all temperature sensors in the copper block and on the cell can, respectively. The heat that is transported by vented gas and particles Q_2 cannot be directly measured with the autoclave calorimetry setup. Therefore, it is assumed that the generated heat per cell weight is constant and consequently Q_1 correlates with the remaining mass in the cell $m_{\text{cell,TR}}$, whereas Q_2 correlates with the mass loss Δm_{cell} .²¹ This results in

$$Q_2 = \frac{\Delta m_{\text{cell}}}{m_{\text{cell,TR}}} Q_1 \quad \text{and} \quad [11]$$

$$Q_{\text{tot}} = Q_1 + Q_2. \quad [12]$$

Investigated cells.—In total 25 different types of prismatic lithium-ion cells are tested in the autoclave setup described above. In order to cover a wide range in cell properties the investigated cells have different geometrical dimensions, exist of either $\text{LiNi}_x\text{Co}_y\text{Al}_z\text{O}_2$ (NCA) or $\text{LiNi}_x\text{Mn}_y\text{Co}_z\text{O}_2$ (NMC) cathodes and contain an electrolyte consisting of lithium hexafluorophosphate (LiPF_6) conducting salt with varying solvent concentrations of ethylene carbonate (EC), ethyl

Table II. Properties of the tested battery cells.

Parameter	Symbol & Range	Unit
Capacity	$8 \leq C_{\text{cell}} \leq 145$	Ah
Energy	$29 \leq E_{\text{cell}} \leq 535$	Wh
Weight	$246 \leq m_{\text{cell}} \leq 2241$	g
Volume	$109 \leq V_{\text{cell}} \leq 973$	cm ³
Gravimetric energy density	$110 \leq \rho_{\text{grav}} \leq 275$	Wh kg ⁻¹
Volumetric energy density	$239 \leq \rho_{\text{vol}} \leq 662$	Wh l ⁻¹
State of charge (SoC)	100%	—
Aging state	fresh, unused	—

methyl carbonate (EMC), diethyl carbonate (DEC) and dimethyl carbonate (DMC). Table II gives an overview over the bandwidth of properties.

After one of the 50 tests a sample of the generated venting gas is analyzed with the gas chromatograph 8610C multigas analyzer of SRI Instruments (TCD and FID, second separation path with FPD/FID for e.g. analysis of organic carbonates) to identify the gas composition. This gas composition is assumed to be representative for all tests. For this analysis the vented gas products of a cell with a nominal capacity of 53 Ah, graphite anode, NMC111 cathode and electrolyte consisting of lithium hexafluorophosphate (LiPF₆) conducting salt with ethylene carbonate (EC), dimethyl carbonate (DMC) and ethyl methyl carbonate (EMC) solvents in 1:1:1 composition is analyzed.

Results and Discussion

Two experiments were conducted in the autoclave calorimetry setup with every of the 25 types of prismatic lithium-ion battery cells. Each of the 50 cells was triggered into TR reproducibly by nail penetration. As observed in previous studies all cells showed the main effects of thermal runaway like cell voltage drop, self-heating of the cell, production of gas and particle ejection.^{12–16,19–21,27,31} Safety relevant parameters such as mass loss, vented gas volume and generated heat during TR are analyzed depending on the capacity of the cells.

In the following plots the symbols (triangles and circles) represent the mean values of the two tests conducted with each cell type. The results of the two individual cell tests are visualized via error bars. Consequently, the greater the deviation of the error bars from the mean value, the greater the variance of the shown results of the two tests conducted with each cell type. If applicable, fits that follow the form of a linear equation $y = m \cdot x$ are used to show a linear dependency of the plotted parameters. In this case, the shaded area represents the 95% confidence interval of this linear fit.

Mass loss during TR.—Figure 4 displays the mass loss during TR Δm_{cell} (Fig. 4a) and the distribution of this mass loss (Fig. 4b) in vented gas mass m_{gas} (red circles) and vented particle mass $m_{\text{particles}}$ (gray triangles) over the cell capacity C_{cell} . The dashed or dashdotted lines represent linear fits of the data.

Figure 4a shows a linear trend between Δm_{cell} and C_{cell} . More precisely, Δm_{cell} is on average 7.05 g Ah^{-1} ($R^2 = 0.88$). The deviations between test results and linear fit tend to increase with C_{cell} . The origin of these deviations can be explained by separating Δm_{cell} into vented particle mass $m_{\text{particles}}$ and vented gas mass m_{gas} as shown in Fig. 4b: On average Δm_{cell} is distributed into 5.00 g Ah^{-1} particles (and liquid components) and 2.05 g Ah^{-1} venting gas. The determination coefficient of the linear fit R^2 for $m_{\text{particles}}$ is smaller ($R^2 = 0.80$) as for m_{gas} ($R^2 = 0.94$), i. e. the variance of the vented particle mass is higher than the variance of the gas mass. In addition, the difference between two tests of the same cell type show a similar behavior. Therefore, it is hypothesized that

the amount of vented gas is mainly dependent on C_{cell} and mostly independent from parameters as the (inner) cell design, whereas the amount of vented particles and consequently the mass loss during TR can be actively influenced up to a certain extent, e.g. by the vent size.

A comparison of the measured mass loss in this study with values from literature is given in Tab. III. Golubkov et al. investigated 11 prismatic 50 Ah cells within a sealed reactor in inert atmosphere using different thermal trigger methods.¹² The cells showed a mass loss from 10.3 to 12.4 g Ah^{-1} and therefore lost more mass than the cells in this study. Essl et al. used the same reactor setup and examined a 41 Ah pouch cell.¹³ With a mass loss of 9.2 g Ah^{-1} the result is at the upper end of this study's range. A possible reason for this observation are the different trigger methods. In previous publications it is stated that nail penetrated cells show a lower mass loss in comparison to overheated cells.^{19,31} Essl et al. explained this behavior with the "nail inside the cell [that] may have prevented further particle emission."¹⁹ Diaz et al. observed a boiling of the (remaining) electrolyte solvents when opening the batteries after the nail-penetration test.³¹ Both explanations are reasonable since during nail-penetration the nail gets stuck and hence prevents the inner cell parts from moving. With thermal triggering of the TR there are two sequences of gas venting: one minor venting before the TR due to the rising temperature inside the cell and one major venting when the TR occurs.¹² During nail-penetration tests there is no minor venting and therefore the vented gas amount may be lower.

On the other hand, there are also experiments with a thermal trigger that show a similar mass loss as this study: Larsson et al. conducted oven tests with 6.6 Ah prismatic cells that showed a mass loss of 4.8 g Ah^{-1} which consequently are at the lower end of this study's results.¹⁴ Liu et al. investigated a 2.2 Ah cylindrical cell (18650 format) in an open environment test setup and found the cell to lose 7.3 g Ah^{-1} of their mass due to a thermal trigger.¹⁵ However, there are significant differences in the experimental setup (lower capacity of the cell and only one single test). Walker et al. examined 18 650 cells in an open environment test setup triggered by over-temperature with a capacity between 2.4 and 3.5 Ah.¹⁶ Their results showed a mass loss up to 12.9 g Ah^{-1} and therefore the highest in the comparison.

In summary, the presented results are generally within the range of previous publications. However, due to differences in the number and type of examined cells as well as experimental methods (e. g. cell format, cathode material, setup, trigger) there are individual deviations from literature values.

Figure 5 illustrates the distribution between vented gas mass m_{gas} (red circles) and vented particle mass $m_{\text{particles}}$ (gray triangles) in relation to the total mass loss during TR Δm_{cell} over the cell capacity C_{cell} (Fig. 5a) and over the gravimetric cell energy density ρ_{grav} (Fig. 5b). The dashed or dashdotted lines represent the mean value of all data points.

Figure 5a shows that m_{gas} makes up 29.1% and $m_{\text{particles}}$ makes up 70.9% of Δm_{cell} on average over all tested cells. This is higher for m_{gas} and hence lower for $m_{\text{particles}}$ in comparison to literature as summarized in Table IV. Furthermore, the vented gas mass m_{gas} normalized with the cell capacity C_{cell} is in good agreement with comparable publications, whereas the vented particle mass $m_{\text{particles}}$ normalized with the cell capacity C_{cell} is lower.^{12,13} This underlines the hypothesis that the generated gas is mainly dependent from the cell capacity, whereas the vented particle mass is influenced by several parameters and therefore individual for each cell (type).

In addition, the data shows that there is a dependency between the gas-particle-distribution and ρ_{grav} as plotted in Fig. 5b. For cells with high ρ_{grav} the fraction of vented gas in total mass loss increases, whereas the fraction of vented particles decreases. A possible reason for this behavior is a higher amount of liquid electrolyte that evaporates during TR due to higher temperatures. Unfortunately, an experimental evidence for this hypothesis cannot

2.1 Experimental assessment of thermal runaway key characteristics

Journal of The Electrochemical Society, 2021 168 120515

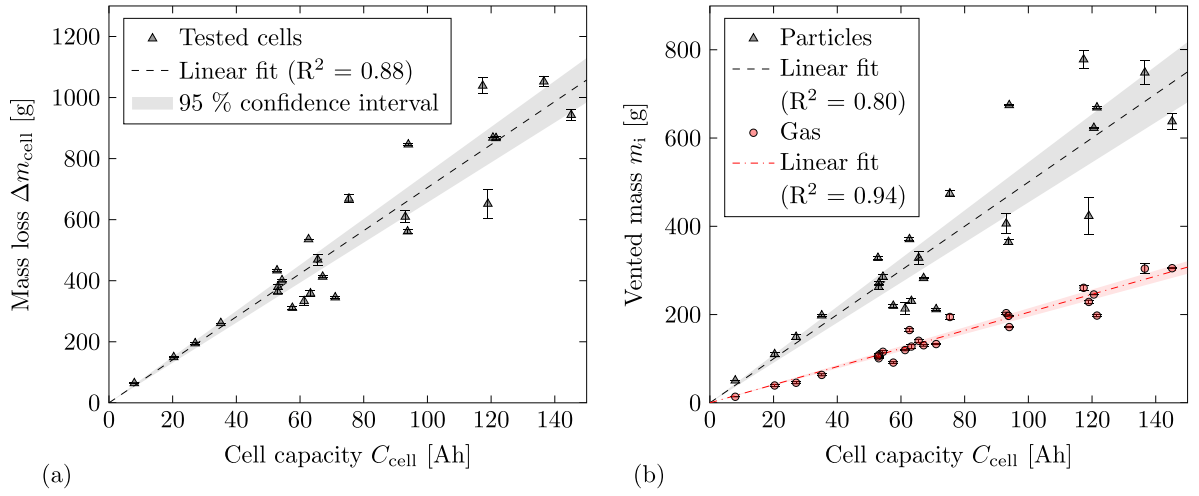


Figure 4. (a) Mass loss during TR Δm_{cell} over cell capacity C_{cell} . The dashed line represents a linear fit with a slope of 7.05 g Ah^{-1} . (b) Vented particle mass $m_{\text{particles}}$ and vented gas mass m_{gas} over cell capacity C_{cell} . The dashed lines represent linear fits with slopes of 5.00 g Ah^{-1} for $m_{\text{particles}}$ and 2.05 g Ah^{-1} for m_{gas} . The shaded areas show the 95% confidence intervals of the fits.

Table III. Comparison of the mass loss during TR for different test setups.

Reference	Investigated cells	Cathode material	Setup	Trigger	C_{cell} [Ah]	Δm_{cell} [%]	$\frac{\Delta m_{\text{cell}}}{C_{\text{cell}}}$ [g Ah^{-1}]
This study	50 (prismatic)	NMC & NCA	autoclave	nail-pen.	8-145	22%–67%	4.8–9.1
Golubkov et al. ¹²	11 (prismatic)	LMO	sealed reactor	over-temp.	50	30%–37%	10.3–12.4
Essl et al. ¹³	1 (pouch)	NMC/LMO	sealed reactor	over-temp.	41	43%	9.2
Larsson et al. ¹⁴	4 (prismatic)	NCA & unknown	oven	over-temp.	6.6	22%–23%	4.8
Liu et al. ¹⁵	1 (18650)	NMC	open	over-temp.	2.2	38%	7.3
Walker et al. ¹⁶	7 (18650)	NCA & unknown	open	over-temp.	2.4–3.5	27%–79%	5.4–12.9
Essl et al. ¹⁹	2 (pouch)	NMC622	sealed reactor	over-temp.	60	56%	8.1
Essl et al. ¹⁹	2 (pouch)	NMC622	sealed reactor	overcharge	60	81%	11.7
Essl et al. ¹⁹	2 (pouch)	NMC622	sealed reactor	nail-pen.	60	47%	6.8
Essl et al. ¹⁹	2 (prismatic)	NMC622	sealed reactor	over-temp.	60	47%	7.5
Essl et al. ¹⁹	2 (prismatic)	NMC622	sealed reactor	overcharge	60	67%	10.7
Essl et al. ¹⁹	2 (prismatic)	NMC622	sealed reactor	nail-pen.	60	33%	5.3

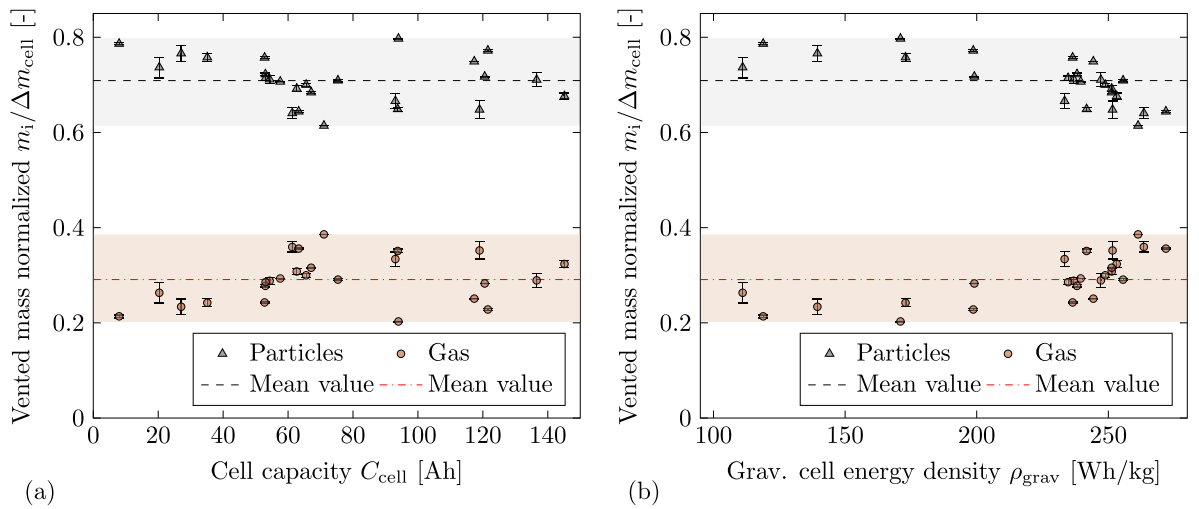


Figure 5. (a) Vented particle mass $m_{\text{particles}}$ and vented gas mass m_{gas} normalized with mass loss Δm_{cell} over cell capacity C_{cell} . The dashed lines represent the mean value with 0.709 for $m_{\text{particles}}$ and 0.291 for m_{gas} . (b) Vented particle mass $m_{\text{particles}}$ and vented gas mass m_{gas} normalized with mass loss Δm_{cell} over the gravimetric cell energy density ρ_{grav} . The dashed lines represent the mean value with 0.709 for $m_{\text{particles}}$ and 0.291 for m_{gas} .

Table IV. Comparison of the mass loss distribution during TR.

Reference	C_{cell} [Ah]	$\frac{m_{\text{gas}}}{\Delta m_{\text{cell}}}$ [%]	$\frac{m_{\text{gas}}}{C_{\text{cell}}}$ [g Ah ⁻¹]	$\frac{m_{\text{particles}}}{\Delta m_{\text{cell}}}$ [%]	$\frac{m_{\text{particles}}}{C_{\text{cell}}}$ [g Ah ⁻¹]
This study	8–145	20%–39%	1.6–2.7	61%–80%	2.9–7.2
Golubkov et al. ¹²	50	12%–25%	1.4–2.9	75%–88%	8.5–11.0
Essl et al. ¹³	41	18%	1.7	82%	7.5

be given as the internal temperature of the cell was not measured. However, the highest mean cell can temperature $T_{\text{cell,max}}$ was measured for the cells with $\rho_{\text{grav}} \geq 250$ Wh/kg.

Another possible explanation is an increasing amount of active cathodic oxygen per unit volume in cells with higher energy density, whereas the amount of electrolyte in the electrode pores is mostly constant. As a consequence, we assume the chemical reaction during the thermal runaway process of a cell with higher energy density results in a higher COCO₂/CO-ratio. Therefore, the average molar mass of the vented gas mixture shall be higher. Anyhow, this hypothesis needs to be further validated by analyzing the COCO₂/CO-ratio for several cells with different energy density.

At this point it has to be mentioned that the distribution of Δm_{cell} into $m_{\text{particles}}$ and m_{gas} as shown in Fig. 4b and 5 depends on the assumed molar mass of the vented gas. As described above, in this study the venting gas composition of a 53 Ah cell with NMC111 cathode was analyzed via gas chromatography. The main detected components were H₂, CO and CO₂ with a concentration of $c_{\text{H}_2} = 32.66$ Vol.-%, $c_{\text{CO}} = 31.34$ Vol.-% and $c_{\text{CO}_2} = 27.34$ Vol.-%, respectively. Additional detected components were C₂H₄ with a concentration of $c_{\text{C}_2\text{H}_4} = 4.33$ Vol.-% and CH₄ with a concentration of $c_{\text{CH}_4} = 4.32$ Vol.-%. These detected components are in accordance with literature.^{12,13,19,20,27} Fig. 6 shows a comparison of each substance's concentration with selected publications.

Koch et al. analyzed 51 cells in total (41 pouch and 10 prismatic—NMC cathode) with a capacity between 20 Ah and 81 Ah inside an autoclave in oxygen atmosphere triggered by heat.²⁷ The bars

show the average substance concentration with the corresponding variance over all tests as error bars. Golubkov et al. analyzed a 1.5 Ah cell (cylindrical - N_{0.45} M_{0.45} C_{0.10} cathode) inside a sealed reactor in inert atmosphere also triggered by heat,²⁰ whereas Essl et al. analyzed two 60 Ah cells (prismatic—NMC622 cathode) in the same reactor in inert atmosphere with nail penetration.¹⁹

This study's results are within the variance of the measurements by Koch et al. except for CO₂. This can be explained by a lack of oxygen due to the inert atmosphere. The analysis of Essl et al. shows a comparable concentration of CO₂.¹⁹ For cells with a low capacity as tested by Golubkov et al. the ratio between CO and CO₂ is also different from measurements done with high capacity cells.²⁰

The main parameter derived from the gas composition is the molar mass as compared in Tab. V for the different gas compositions. The molar mass used in this study is in accordance with the comparable data from literature that examined the cell(s) in inert atmosphere.^{19,20} In addition, the difference of the molar mass for different cells and therefore cathode materials is small even with deviations in the assumed gas composition. Consequently, the error of the evaluation methodology in this study due to the same molar mass for all examined cells is assumed to be negligible.

Table V also compares the COCO₂/CO-ratio resulting from the gas analyses mentioned above. The cell with NMC111 cathode from this study shows the smallest ratio, followed by the cell with NMC622 cathode examined by Essl et al.¹⁹ and the cells examined by Koch et al. with NMC cathodes of different compositions.²⁷ The cell with N_{0.45} M_{0.45} C_{0.10} cathode examined by Golubkov et al.²⁰

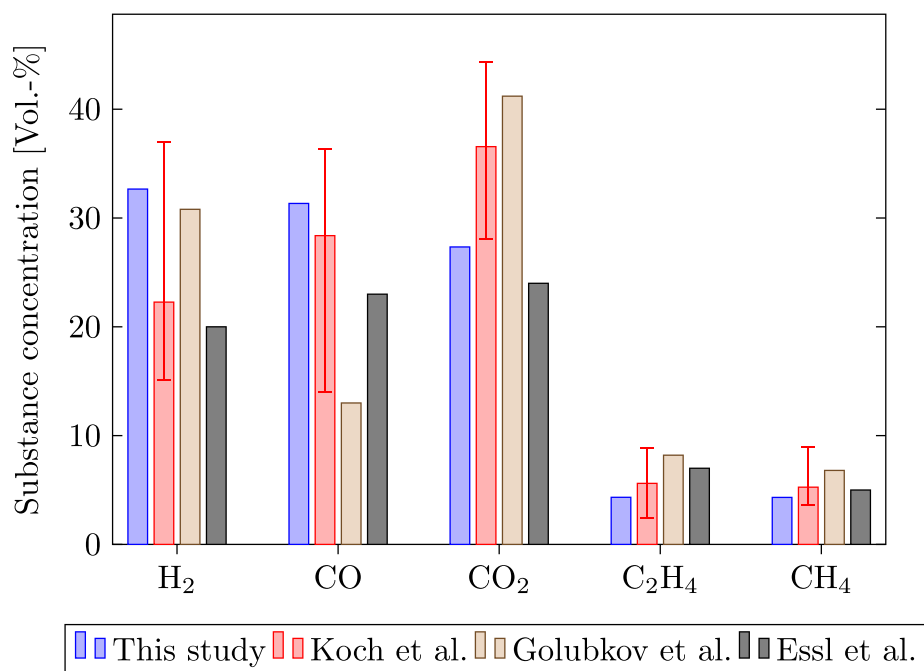


Figure 6. Comparison of the gas composition measured in this study with values from literature.^{19,20,27} As Koch et al. in Ref. 27 analyzed 51 cells in total the error bars of these measurements are also shown.

Table V. Comparison of the molar mass derived from gas composition measurements.

Parameter	This study	Koch et al. ²⁷	Golubkov et al. ²⁰	Essl et al. ¹⁹
Investigated cells	1	51	1	2
Cell format(s)	prismatic	prismatic and pouch	cylindrical	prismatic
Atmosphere	inert	oxygen	inert	inert
Capacity C_{cell}	53 Ah	20–81 Ah	1.5 Ah	60 Ah
Cathode material	NMC111	NMCxxx	$\text{N}_{0.45}\text{M}_{0.45}\text{C}_{0.10}$	NMC622
Molar mass M_{gas}	23.38 g mol ⁻¹	27.42 g mol ⁻¹	23.19 g mol ⁻¹	23.10 g mol ⁻¹
CO ₂ /CO-ratio	0.87	1.29	3.17	1.04

shows the highest ratio. However, the capacity of this cell is significantly smaller. As stated before, this observation could result from the different energy densities of the cathode material, but needs to be further validated.

Vented gas volume.—Figure 7 shows the vented gas volume V_{gas} at 25 °C and 1 atm (SATP conditions) over the cell capacity C_{cell} for the results of this study (gray triangles), of Koch et al. from Ref. 27 (red circles) and of Golubkov et al. from Ref. 12 (blue diamonds). The lines represent linear fits of the data from this study (dashed) and the study of Koch et al. (dashdotted).

As plotted in Fig. 7a the data of this study results in a mean generated gas volume of 2.14 l Ah⁻¹. This is higher than the results of Koch et al. for 41 pouch and 10 prismatic cells triggered by over-temperature (1.96 l Ah⁻¹).²⁷ Measurements of Golubkov et al. with 11 prismatic cells and different trigger mechanisms are within the variance.¹²

A possible reason for deviations is the definition of an equilibrium state via the gas temperature gradient dT_{gas}/dt . The temperature inside the autoclave at this equilibrium state T_{eq} varies between 20 °C and 45 °C and consequently some volatile venting products are present as a liquid and as a gas phase at the same time. Therefore, the partial pressure of those substances has to be taken in consideration. To identify the impact of this phenomena Fig. 7b shows the vented gas volume V_{gas} (SATP conditions) evaluated at $T_{\text{gas}} = 30$ °C and therefore on the same isotherm in the phase diagram for all tests. The slope of the linear fit changes from 2.14 l Ah⁻¹ to 2.06 l Ah⁻¹ and R^2 from 0.94 to 0.96. Hence the influence on the mean value is little but there are single tests for that the chosen equilibrium state criteria has a significant impact on the

result. To gain further insight into the exact distribution between gas, solid and liquid ejecta it would be necessary to collect all of the solid particles after the test. With a measured value of $m_{\text{particles}}$ the liquid “remains” could then be estimated.

Deviations may also result from the cell format, the cathode material and the trigger method as shown in Tab. VI. Diaz et al. and Essl et al. reported a dependency of the vented gas volume from the trigger method.^{19,31} Nevertheless, the results of this study are within the range of previous publications.^{12,13,19,20,27}

Generated heat during TR.—Figure 8 shows the total generated heat Q_{tot} (gray triangles) and the fraction of heat remaining in the cell or being transferred to the copper block Q_1 (red circles) over the cell capacity C_{cell} . The dashed or dashdotted lines represent linear fits of the data that follow the form $y = mx$. The experimental results show an approximately linear increase of Q_1 and therefore of Q_{tot} with C_{cell} , more precisely Q_{tot} is on average 19.45 kJ Ah⁻¹ ($R^2 = 0.96$) and Q_1 is on average 10.76 kJ Ah⁻¹ ($R^2 = 0.84$). The deviations of Q_1 from its linear fit are higher than for Q_{tot} . This is due to the dependency between Q_1 and the mass loss during TR: with increasing mass remaining in the cell $m_{\text{cell,TR}}$ more heat remains in the cell as well and therefore Q_1 is higher. This dependency is illustrated in Fig. 9 that plots Q_1 normalized with the cell capacity C_{cell} over the (relative) remaining cell mass $m_{\text{cell,TR}}$. The dashed line represents a linear fit of the data.

Figure 8 and 9 show that it is possible to actively affect the distribution between Q_1 and Q_2 by influencing the mass loss of the cell. With respect to battery pack design it is conceivable to ensure a high mass loss in combination with a robust way to guide the vented products out of the battery pack. The high mass loss leads to a small

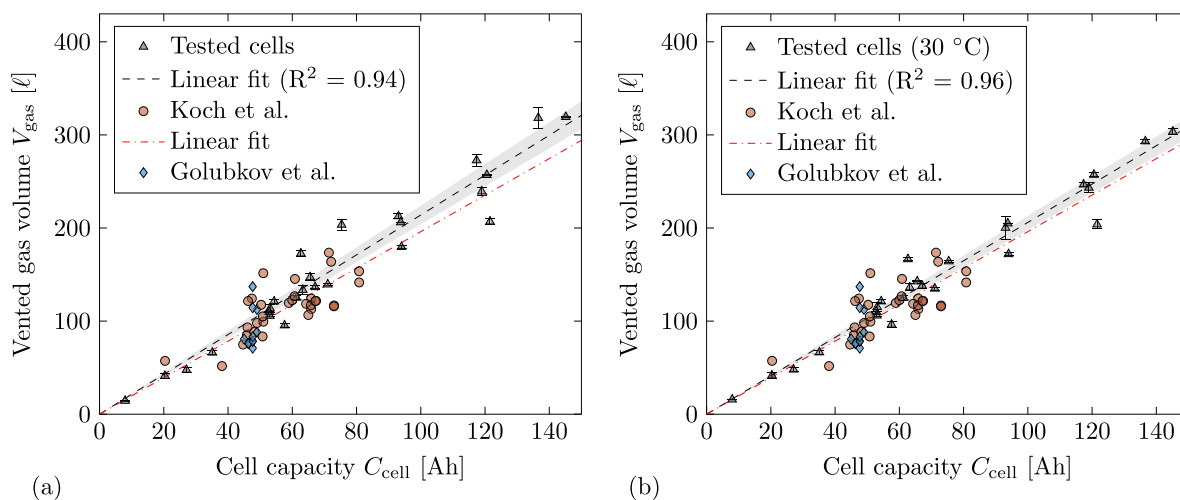


Figure 7. (a) Vented gas volume V_{gas} estimated with equilibrium state criteria over cell capacity C_{cell} . The dashed lines represent linear fits with slopes of 2.14 l Ah⁻¹ for cells tested in this study and 1.96 l Ah⁻¹ for the cells tested by Koch et al.²⁷ (b) Vented gas volume V_{gas} estimated at $T_{\text{gas}} = 30$ °C over cell capacity C_{cell} . The slope of the linear fit for cells tested in this study is 2.06 l Ah⁻¹. The shaded areas show the 95% confidence intervals of the fits of this study's results.

Table VI. Comparison of the generated gas volume during TR.

Reference	Investigated cells	Cathode material	Trigger	C_{cell} [Ah]	V_{gas} [l] @ SATP	$\frac{V_{\text{gas}}}{C_{\text{cell}}}$ [l Ah ⁻¹]
This study	50 (prismatic)	NMC & NCA	nail-pen.	8-145	14.0-329.9	1.6-2.8
Koch et al. ²⁷	51 (pouch & prismatic)	NMC	over-temp.	20-81	51.7-173.5	1.4-3.0
Golubkov et al. ¹²	11 (prismatic)	LMO	over-temp.	50	70.9-114.3	1.4-2.9
Golubkov et al. ²⁰	≥ 3 (18650)	N _{0.45} M _{0.45} C _{0.10}	over-temp.	1.5	3.6	2.4
Golubkov et al. ²⁰	≥ 3 (18650)	NMC + LCO	over-temp.	2.6	6.5	2.5
Essl et al. ¹³	1 (pouch)	NMC + LMO	over-temp.	41	56.5	1.4
Essl et al. ¹⁹	2 (pouch)	NMC622	over-temp.	60	93.0	1.5
Essl et al. ¹⁹	2 (pouch)	NMC622	overcharge	60	168.8	2.8
Essl et al. ¹⁹	2 (pouch)	NMC622	nail-pen.	60	102.8	1.7
Essl et al. ¹⁹	2 (prismatic)	NMC622	over-temp.	60	93.0	1.5
Essl et al. ¹⁹	2 (prismatic)	NMC622	overcharge	60	159	2.7
Essl et al. ¹⁹	2 (prismatic)	NMC622	nail-pen.	60	105.2	1.8

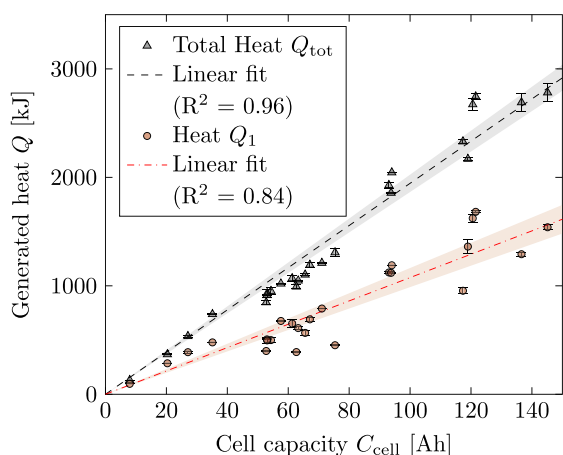


Figure 8. Total generated heat Q_{tot} and fraction of heat remaining in the cell or being transferred to the copper block Q_1 over cell capacity C_{cell} . The dashed lines represent linear fits with slopes of 19.45 kJ Ah^{-1} for Q_{tot} and 10.76 kJ Ah^{-1} for Q_1 . The shaded areas show the 95% confidence intervals of the fits.

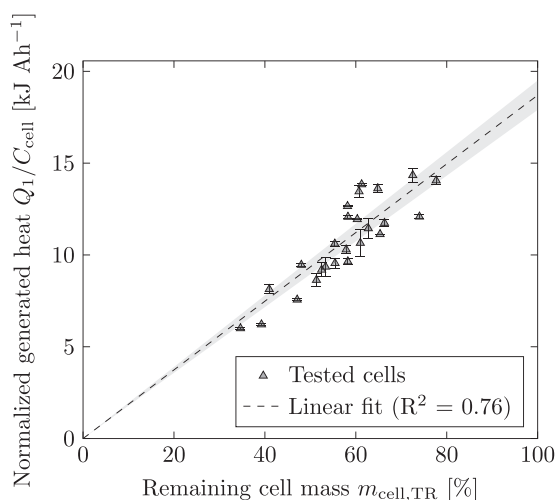


Figure 9. Fraction of heat remaining in cell or being transferred to the copper block Q_1 normalized with cell capacity C_{cell} over (relative) remaining cell mass after TR $m_{\text{cell,TR}}$. The dashed line represents a linear fit with a slope of $0.19 \text{ kJ Ah}^{-1}\%$. The shaded area shows the 95% confidence interval of the fit.

Q_1 and therefore inhibits the thermal propagation triggered by conductive transferred heat. It then has to be secured that the vented products have no direct contact with endangered components to also prevent a thermal propagation triggered by convective transferred heat. A possible approach for this is a venting channel that is separated from the rest of the battery pack.

Figure 10 shows the total generated heat Q_{tot} (gray triangles) and the fraction of heat remaining in the cell or being transferred to the copper block Q_1 (red circles) normalized with the nominal (electrical) cell energy E_{cell} (in Wh—capacity of the cell C_{cell} multiplied by the nominal voltage of the cell U_{nominal}) over the cell capacity C_{cell} and the gravimetric cell energy density ρ_{grav} . The dotted and dashdotted lines represent the mean values.

Figure 10a illustrates that Q_{tot} is on average 1.41 times higher than E_{cell} . There are single test results with a factor of up to 1.72. Consequently, the heat generated by chemical reactions inside the cell is significant and has to be considered in the development process of battery packs with regard to thermal safety. Q_1 is on average 81% of E_{cell} with a minimum factor of 0.48 and a maximum of up to 1.12.

Figure 10b shows that Q_{tot} as well as Q_1 in relation to E_{cell} tend to decrease with increasing ρ_{grav} . A possible reason for this behavior is that the high amount of energy leads to overall higher temperatures of the cell and consequently of the copper block. As a result more heat is transferred from the thermal insulation to the gas inside the autoclave. In this case the measurement error of Q_1 would increase with a higher amount of heat transferred to the copper block.

A comparison of the measured values with data from literature is given in Tab. VII. In general, the results of this study are in accordance with previous reported values,^{15,16,22–25} but it has to be mentioned that the cells examined in this study have a significant higher capacity. Therefore, it is possible that measurement errors of the autoclave calorimetry setup are not noticed at this point. The thermal insulation of the copper block is one source of errors due to the impossibility of creating a perfectly adiabatic system. Consequently, it is assumed that the total generated heat during TR can be slightly higher as 141% of E_{cell} on average. This assumption will be verified in future publications with an improved experimental setup.

Conclusions

The presented results show the TR behavior of prismatic lithium-ion cells in the autoclave calorimetry experiment. The examined cells are covering a wide capacity range (8 Ah to 145 Ah) and therefore correlations for safety relevant parameters are derived. More specifically the dependency of the mass loss, the vented gas volume and the generated heat during TR on the cell capacity are presented in this paper.

Mass loss during TR.—

Table VII. Comparison of the generated heat during TR.

Reference	Investigated cells	Cathode material	Atmosphere	C_{cell} [Ah]	$\frac{Q_{\text{L}}}{C_{\text{cell}}}$ [kJ Ah ⁻¹]	$\frac{Q_{\text{L}}}{E_{\text{cell}}}$ [-]	$\frac{Q_{\text{tot}}}{C_{\text{cell}}}$ [kJ Ah ⁻¹]	$\frac{Q_{\text{tot}}}{E_{\text{cell}}}$ [-]
This study	50 (prismatic)	NMC & NCA	inert	8-145	6.0-14.7	0.5-1.1	15.6-22.8	1.2-1.7
Walker et al. ¹⁶	7 (18650)	NCA & unknown	limited oxygen	2.4-3.5	3.6-7.3	0.3-0.5	15.2-21.5	1.1-1.6
Yayathi et al. ²²	18 (prismatic & 18 650)	NMC & NMC + LCO	limited oxygen	2.4-5.3	9.6-12.0	0.7-0.9	18.1-18.6	1-1.6
Liu et al. ²³	3 (18650)	NMC & LCO & LFP	open	1.5-2.6	9.1-15.1	0.9-1.3	n/a	n/a
Liu et al. ¹⁵	1 (18650)	NMC	open	2.2	15.4	1.2	n/a	n/a
Ye et al. ²⁴	13 (prismatic)	NMC	limited oxygen	1	n/a	n/a	6.6-9.3	0.5-0.7
Walters et al. ²⁵	4 (unknown)	LMO & LCO & NCA	inert	1.0-3.1	n/a	n/a	n/a	1.7

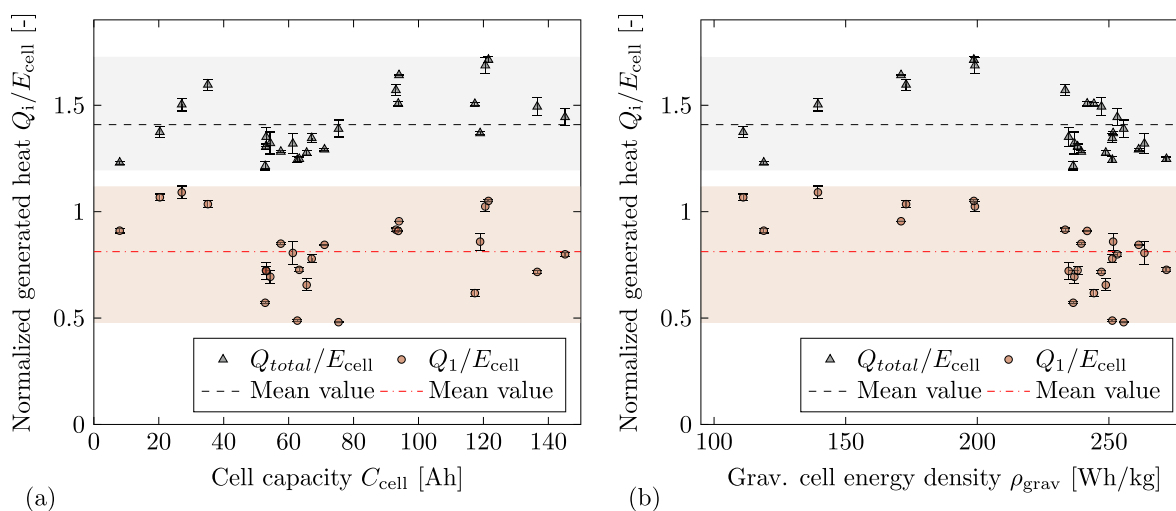


Figure 10. (a) Total generated heat Q_{tot} and heat remaining in cell Q_1 normalized with cell energy E_{cell} over cell capacity C_{cell} . The dashed lines represent the mean value with 1.41 for Q_{tot} and 0.81 for Q_1 . (b) Total generated heat Q_{tot} and heat remaining in cell Q_1 normalized with cell energy E_{cell} over cell energy density ρ_{grav} . The dashed lines represent the mean value with 1.41 for Q_{tot} and 0.81 for Q_1 .

- The tested cells lost on average 7.05 g Ah^{-1} of their mass during TR ($R^2 = 0.88$). This mass loss is distributed into 5.00 g Ah^{-1} particles and liquid components ($R^2 = 0.80$) and 2.05 g Ah^{-1} venting gas ($R^2 = 0.94$). Consequently, the gas makes up 29.1% gas and particles and liquid components make up 70.9% of the total mass loss.

- The vented gas is subject to a smaller variance ($1.6\text{--}2.7 \text{ g Ah}^{-1}$) than the vented particles ($2.9\text{--}7.2 \text{ g Ah}^{-1}$). Therefore, it is concluded that the amount of vented gas is mainly dependent on the cell capacity and cannot be actively influenced by e.g. the cell design. In contrast, the vented particle mass is individual for each cell (type) and depends on several parameters.

- Cells with a high grav. energy density tend to show a higher fraction of gas in their mass loss compared to cells with a low gravimetric energy density.

Vented gas volume.—

- The tested cells generated on average 2.14 l Ah^{-1} of gas during TR (SATP conditions). This is in accordance to reported values in literature.

- The generated gas volume was found to be between 1.6 l Ah^{-1} and 2.8 l Ah^{-1} .

Generated heat.—

- The tested cells generated on average 10.76 kJ Ah^{-1} of heat that remained in the cell during TR ($R^2 = 0.84$). By estimating the fraction of heat that is transported by the venting products the total generated heat during TR was found to be on average 19.45 kJ Ah^{-1} ($R^2 = 0.96$).

- The distribution of the total generated heat into the fraction of heat remaining in the cell (Q_1) and the fraction of heat that is transported by the venting products (Q_2) depends on the mass loss during TR.

- By influencing the vented particle mass the distribution between Q_1 and Q_2 can be actively manipulated.

- The ratio between total generated heat and electrical energy stored in the cell was found to be on average 1.41. The maximum value was 1.72.

In general, the results allow to estimate safety relevant parameters for different battery cells in a wide capacity range. These parameters are crucial for the design process of battery packs, e. g. as input parameters for simulations. Furthermore, the correlations can be used to predict the behavior of other battery cells within the property range of those tested and therefore contribute to the design of a safer battery pack.

Acknowledgments

The authors would like to gratefully acknowledge the support of the Fraunhofer Institute for Chemical Technology (ICT), Pfünz, Germany for the development and execution of the autoclave calorimetry measurements. In addition, S. Hoelle acknowledges the support of the TUM Graduate School.

ORCID

S. Hoelle <https://orcid.org/0000-0002-6381-8104>

O. Hinrichsen <https://orcid.org/0000-0002-3796-6920>

References

1. The Harris Poll on behalf of Volvo, "The State of Electric Vehicles in America." Volvo Reports, Report No. 249123, 2018. Accessed 07 July 2021 <https://www.media.volvocars.com/us/en-us/media/documentfile/249123/volvo-reports-the-state-of-electric-vehicles-in-america>.
2. Daimler AG: Mercedes Benz EQS - Product page. Accessed 07 July 2021, <https://www.mercedes-benz.com/en/vehicles/passenger-cars/eqs/eqs/>.
3. Tesla: Model S - Product page. Accessed 07 July 2021, <https://www.tesla.com/models>.
4. Lucid: Lucid Air - Product page. Accessed 07 July 2021, <https://www.lucidmotors.com/air>.
5. BMW AG: BMW iX - Product page. Accessed 07 July 2021, <https://www.bmwusa.com/future-vehicles/ix.html>.
6. P. Jindal and J. Bhattacharya, "Review—Understanding the Thermal Runaway Behavior of Li-Ion Batteries through Experimental Techniques." *Journal of the Electrochemical Society*, **166**, A2165 (2019).
7. L. Torres-Castro, A. Kurzawski, J. Hewson, and J. Lamb, "Passive Mitigation of Cascading Propagation in Multi-Cell Lithium Ion Batteries." *Journal of the Electrochemical Society*, **167**, 090515 (2020).

2.1 Experimental assessment of thermal runaway key characteristics

Journal of The Electrochemical Society, 2021 **168** 120515

8. S. Gao, L. Lu, M. Ouyang, Y. Duan, X. Zhu, C. Xu, B. Ng, N. Kamyab, R. E. White, and P. T. Coman, "Experimental Study on Module-to-Module Thermal Runaway-Propagation in a Battery Pack." *Journal of the Electrochemical Society*, **166**, A2065 (2019).
9. G. Zhong, H. Li, C. Wang, K. Xu, and Q. Wang, "Experimental Analysis of Thermal Runaway Propagation Risk within 18 650 Lithium-Ion Battery Modules." *Journal of the Electrochemical Society*, **165**, A1925 (2018).
10. D. Ouyang, J. Liu, M. Chen, J. Weng, and J. Wang, "An Experimental Study on the Thermal Failure Propagation in Lithium-Ion Battery Pack." *Journal of the Electrochemical Society*, **165**, A2184 (2018).
11. D. P. Finegan, B. Tjaden, T. M. M. Heenan, R. Jervis, M. Di Michiel, A. Rack., G. Hinds, D. J. L. Brett, and P. R. Shearing, "Tracking Internal Temperature and Structural Dynamics during Nail Penetration of Lithium-Ion Cells." *Journal of the Electrochemical Society*, **164**, A3285 (2017).
12. A. W. Golubkov, R. Planteu, P. Krohn, B. Rasch, B. Brunstein, A. Thaler, and V. Hacker, "Thermal runaway of large automotive Li-ion batteries." *RSC Advances*, **8**, 40172 (2018).
13. C. Essl, A. W. Golubkov, E. Gasser, M. Nachtebel, A. Zankel, E. Ewert, and A. Fuchs, "Comprehensive Hazard Analysis of Failing Automotive Lithium-Ion Batteries in Overtemperature Experiments." *Batteries*, **8**, 30 (2020).
14. F. Larsson, S. Bertilsson, M. Furlani, I. Albinsson, and B.-E. Mellander, "Gas explosions and thermal runaways during external heating abuse of commercial lithium-ion graphite-LiCoO₂ cells at different levels of ageing." *Journal of Power Sources*, **373**, 220 (2018).
15. X. Liu, S. I. Stolarov, M. Denlinger, A. Masias, and K. Snyder, "Comprehensive calorimetry of the thermally-induced failure of a lithium ion battery." *Journal of Power Sources*, **280**, 516 (2015).
16. W. Q. Walker, J. J. Darst, D. P. Finegan, G. A. Bayles, K. L. Johnson, E. C. Darcy, and S. L. Rickman, "Decoupling of heat generated from ejected and non-ejected contents of 18 650-format lithium-ion cells using statistical methods." *Journal of Power Sources*, **415**, 207 (2019).
17. X. Feng, X. He, M. Ouyang, L. Wang, L. Lu, D. Ren, and S. Santhanagopalan, "A Coupled Electrochemical-Thermal Failure Model for Predicting the Thermal Runaway Behavior of Lithium-Ion Batteries." *Journal of the Electrochemical Society*, **165**, A3748 (2018).
18. S. Hildebrand, A. Rheinfeld, A. Friesen, J. Haetge, F. M. Schappacher, A. Jossen, and M. Winter, "Thermal Analysis of LiNi_{0.4}Co_{0.2}Mn_{0.4}O₂/Mesocarbon Microbeads Cells and Electrodes: State-of-Charge and State-of-Health Influences on Reaction Kinetics." *Journal of the Electrochemical Society*, **165**, A104 (2018).
19. C. Essl, A. W. Golubkov, and A. Fuchs, "Comparing Different Thermal Runaway Triggers for Two Automotive Lithium-Ion Battery Cell Types." *Journal of the Electrochemical Society*, **167**, 130542 (2020).
20. A. W. Golubkov, D. Fuchs, J. Wagner, H. Wiltse, C. Stangl, G. Fauler, G. Voitic, A. Thaler, and V. Hacker, "Thermal-runaway experiments on consumer Li-ion batteries with metal-oxide and olivin-type cathodes." *RSC Advances*, **4**, 3633 (2014).
21. S. Scharner, "Quantitative Safety Characterization of Li-Ion Cells." *JRC Exploratory Research Workshop* (2018), <https://ec.europa.eu/jrc/sites/jrcsh/files/quantitative-safety-characterization-of-li-ion-cells.pdf>.
22. S. Yayathi, W. Walker, D. Doughty, and H. Ardebili, "Energy distributions exhibited during thermal runaway of commercial lithium ion batteries used for human spaceflight applications." *Journal of Power Sources*, **329**, 197 (2016).
23. X. Liu, Z. Wu, S. I. Stolarov, M. Denlinger, A. Masias, and K. Snyder, "Heat release during thermally-induced failure of a lithium ion battery: Impact of cathode composition." *Fire Safety Journal*, **85**, 10 (2016).
24. J. Ye, H. Chen, Q. Wang, P. Huang, J. Sun, and S. Lo, "Thermal behavior and failure mechanism of lithium ion cells during overcharge under adiabatic conditions." *Applied Energy*, **182**, 464 (2016).
25. R. N. Walters and R. E. Lyon, "Measuring Energy Release of Lithium-ion Battery Failure Using a Bomb Calorimeter." *U.S. Department of Transportation: Federal Aviation Administration Report No. DOT/FAA/TC-15/40* (2016), <https://www.fire.tc.faa.gov/pdf/TC-15-40.pdf>.
26. X. Liu, Z. Wu, S. I. Stolarov, M. Denlinger, A. Masias, and K. Snyder, "A Thermo-Kinetic Model of Thermally-Induced Failure of a Lithium Ion Battery: Development Validation and Application." *Journal of the Electrochemical Society*, **165**, A2909 (2018).
27. S. Koch, A. Fill, and K. P. Birke, "Comprehensive gas analysis on large scale automotive lithium-ion cells in thermal runaway." *Journal of Power Sources*, **398**, 106 (2018).
28. R. Srinivasan, M. E. Thomas, M. B. Airola, B. G. Carkhuff, L. J. Frizzell-Makowski, H. Alkandry, J. G. Reuster, H. N. Oguz, P. W. Green, J. La Favors, L. J. Currano, and P. A. Demirev, "Preventing Cell-to-Cell Propagation of Thermal Runaway in Lithium-Ion Batteries." *Journal of the Electrochemical Society*, **167**, 020559 (2020).
29. A. R. Baird, E. J. Archibald, K. C. Marr, and O. A. Ezekoye, "Explosion hazards from lithium-ion battery vent gas." *Journal of Power Sources*, **446**, 227257 (2020).
30. Z. Liao, S. Zhang, M. Zhao, Z. Qiu, D. Han, G. Zhang, and T. G. Habetler, "Hazard analysis of thermally abused lithium-ion batteries at different state of charges." *Journal of Energy Storage*, **27**, 101065 (2020).
31. F. Diaz, Y. Wang, R. Wehse, and B. Friedrich, "Gas generation measurement and evaluation during mechanical processing and thermal treatment of spent Li-ion batteries." *Waste Management*, **84**, 102 (2019).

2.2 Modeling approaches for heat release during TR

The article titled “3D Thermal Simulation of Lithium-Ion Battery Thermal Runaway in Autoclave Calorimetry - Development and Comparison of Modeling Approaches” is presented within this section. It was submitted to the peer-reviewed *Journal of The Electrochemical Society* in October 2022 and published online in January 2023.

The objective of this work was to develop a simulation methodology that is able to reproduce the solid body domain of a lithium-ion cell TR, more precisely the heat release during TR and the subsequent heat dissipation to contacting bodies. Therefore, the autoclave experiment as presented in section 2.1 conducted with a prismatic lithium-ion cell (> 60 Ah) with graphite/NMC electrodes was simulated and different modeling approaches for the heat release during TR were applied. In addition, the influence of the jelly roll density ρ_{JR} , specific heat capacity $c_{p,\text{JR}}$, and thermal conductivity λ_{JR} on the simulation results was investigated. As the model is intended to be one part of a coupled model, that combines solid body and gas-particle-flow simulation, the three-dimensional (3D)-CFD framework of *Simcenter STAR-CCM+*[®] was used for this study.

As pointed out in section 1.5, there exist various approaches to model the heat release during TR. The focus in this study was to identify approaches with low computational effort instead of modeling the physics as accurate as possible, e.g. by several Arrhenius-like expressions. Therefore, three empirical methods were considered: a time-dependent function for heat release following the approach of Coman et al.,²⁸⁹ a temperature-dependent heat release rate based on ARC data as used by Citarella et al. and Yeow et al.,^{287,288} and an empirical Arrhenius source term as proposed by Feng et al. that allows to spatially resolve the TR reaction.²⁸³

The comparison showed that the modeling approach for heat release during TR has a major influence on the simulation results for the time range of the TR ($t < t_{\text{TR}}$), whilst the effect for large time scales ($t \gg t_{\text{TR}}$) is negligible. The lowest consumption of computational resources was found for the time-dependent function for heat release. The variation of the jelly roll density ρ_{JR} had a major influence on the simulation results and underlined, that a TR model has to account for Δm_{TR} in order to reproduce the TR phenomenon with acceptable quality. Naturally, a variation of the jelly roll’s specific heat capacity $c_{p,\text{JR}}$ has the same effect on the results of a thermal solid body simulation as a variation of ρ_{JR} . Consequently, correct values for $c_{p,\text{JR}}$ are as important as a consideration of Δm_{TR} . However, experimental measurements of $c_{p,\text{JR}}$ in the temperature range of a TR are rare and consequently, further research is needed in this context. This is also the case for the jelly roll’s thermal conductivity λ_{JR} , as it considerably influences the simulation results and yet there is a lack of experimental measurements in the temperature range of a TR.

The results of the autoclave simulation study are the basis for the selection process of a suitable simulation methodology of the coupled model’s solid body domain. The findings showed, that all of the three investigated modeling approaches are capable to reproduce the experimental results. However, the computational resource consumption differs significantly, which may pose challenges for TP simulation and hence the coupled model.

3D Thermal Simulation of Lithium-Ion Battery Thermal Runaway in Autoclave Calorimetry - Development and Comparison of Modeling Approaches

S. Hoelle, F. Dengler, S. Zimmermann, and O. Hinrichsen

Journal of The Electrochemical Society 170, No. 010509, 2023

Permanent weblink:

<https://doi.org/10.1149/1945-7111/acac06>

Reproduced under the terms of the Creative Commons Attribution 4.0 License (CC BY, <https://creativecommons.org/licenses/by/4.0/>), which permits unrestricted reuse of the work in any medium, provided the original work is properly cited.

Author contributions:

S. Hoelle initiated the idea of comparing different modeling approaches with the focus on suitability for thermal runaway simulation and coordinated the experiments used as simulation input and for validation. S. Hoelle developed the simulation model, implemented the existing modeling approaches, developed the time dependent heat release approach, and carried out the model parameter sensitivity study. F. Dengler supported the model development, the model parameter sensitivity study, and helped to optimize model parameters. The data was analyzed and interpreted by S. Hoelle, F. Dengler, and S. Zimmermann. The manuscript was written by S. Hoelle and was edited by F. Dengler, S. Zimmermann, and O. Hinrichsen. All authors discussed the data and commented on the results.



3D Thermal Simulation of Lithium-Ion Battery Thermal Runaway in Autoclave Calorimetry: Development and Comparison of Modeling Approaches

S. Hoelle,^{1,2,z} F. Dengler,¹ S. Zimmermann,¹ and O. Hinrichsen^{1,2,3}¹BMW Group, Munich, Germany²Technical University of Munich, TUM School of Natural Sciences, 85748 Garching near Munich, Germany³Technical University of Munich, Catalysis Research Center, 85748 Garching near Munich, Germany

In this paper, three different empirical modeling approaches for the heat release during a battery cell thermal runaway (TR) are analyzed and compared with regard to their suitability for TR and TR propagation simulation. Therefore, the so called autoclave calorimetry experiment conducted with a prismatic lithium-ion battery (>60 Ah) is modeled within the 3D-CFD framework of *Simcenter Star-CCM+*[®] and the simulation results are compared to the experiments. In addition, the influence of critical parameters such as mass loss during TR, the jelly roll's specific heat capacity and thermal conductivity is analyzed. All of the three modeling approaches are able to reproduce the experimental results with high accuracy, but there are significant differences regarding computational effort. Furthermore, it is crucial to consider that the mass loss during TR and both specific heat capacity as well as thermal conductivity of the jelly roll have a significant influence on the simulation results. The advantages and disadvantages of each modeling approach pointed out in this study and the identification of crucial modeling parameters contribute to the improvement of both TR as well as TR propagation simulation and help researchers or engineers to choose a suitable model to design a safer battery pack.

© 2023 The Author(s). Published on behalf of The Electrochemical Society by IOP Publishing Limited. This is an open access article distributed under the terms of the Creative Commons Attribution 4.0 License (<http://creativecommons.org/licenses/by/4.0/>), which permits unrestricted reuse of the work in any medium, provided the original work is properly cited. [DOI: 10.1149/1945-7111/acac06]



Manuscript submitted October 11, 2022; revised manuscript received November 21, 2022. Published January 11, 2023.

List of Symbols

Abbreviations

ID	one-dimensional
3D	three-dimensional
ARC	accelerating rate calorimetry
CFD	computational fluid dynamics
MAPE	mean absolute percentage error
NMC	lithium nickel manganese cobalt oxide
RMSPE	root mean square percentage error
SoC	state of charge
TR	thermal runaway
Symbols	
a	polynomial constant, $\text{W m}^{-1} \text{K}^{-4}$
A	pre-exponential factor, K s^{-1}
b	polynomial constant, $\text{W m}^{-1} \text{K}^{-3}$
B	reaction index, —
c	polynomial constant, $\text{W m}^{-1} \text{K}^{-2}$
c_e	normalized concentration of energy, —
c_p	specific heat capacity, $\text{J kg}^{-1} \text{K}^{-1}$
C	reaction rate, s^{-1}
d	polynomial constant, $\text{W m}^{-1} \text{K}^{-1}$
E_j	mean value of both experiments at data point j , —
i	inner iteration, —
m	mass, kg
Δm_{cell}	mass loss of the battery cell during TR, kg
n	number of data points j , —
p_{eq}	pressure at thermodynamic equilibrium, Pa
p_{EoV}	pressure at end of venting, Pa
\dot{q}	volumetric heat source, J m^{-3}
\dot{q}_{onset}	volumetric heat source due to exothermal chemical reactions, J m^{-3}
\dot{q}_{ele}	volumetric heat source due to electrical short circuit, J m^{-3}
Q	heat, J

Q_1	released heat during TR that is dissipated via conduction, J
Q_2	released heat during TR that is transported by gases and particles, J
Q_{control}	(numerically) released heat in simulation, J
\dot{Q}	heat release, W
\dot{Q}_{ARC}	heat release in ARC experiment, W
R_{th}	thermal resistance, $\text{m}^2 \text{K W}^{-1}$
Ra_{Cu}	roughness depth of copper block parts, m
S_j	simulation result of data point j , —
t	time, s
t_{begin}	point in time when a specific sensor shows $T > 50^\circ \text{C}$, s
t_{heating}	duration of (measured) temperature increase, s
t_{max}	point in time when a specific sensor shows its maximum value, s
t_{total}	total physical time being simulated, s
t_{venting}	duration of venting, s
Δt_{sim}	computation time of the simulation, s
Δt_{step}	time step of simulation, s
T	temperature, $^\circ \text{C}$
$T_{\text{cell,mean}}$	mean cell can temperature, $^\circ \text{C}$
$T_{\text{cell,mean,max}}$	maximum value of mean cell can temperature, $^\circ \text{C}$
$T_{\text{Cu,mean}}$	mean copper block temperature, $^\circ \text{C}$
$T_{\text{Cu,mean,500s}}$	mean copper block temperature 500 s after nail penetration, $^\circ \text{C}$
T_{onset}	onset temperature of continuous self-heating, $^\circ \text{C}$
T_{ref}	reference temperature, $^\circ \text{C}$
T_{TR}	thermal runaway trigger temperature, $^\circ \text{C}$
$T_{x,\text{avg}}$	volume averaged temperature in the cell component x , $^\circ \text{C}$
$T_{x,\text{max}}$	maximum temperature in the cell component x , $^\circ \text{C}$
V	Volume, m^3
α_x	(volume) fraction, —
β	normalization factor, —
ϵ	energy residual of simulation, —
e_Q	numerical error, —
λ	thermal conductivity, $\text{W m}^{-1} \text{K}^{-1}$
λ_{air}	thermal conductivity of air, $\text{W m}^{-1} \text{K}^{-1}$

^zE-mail: sebastian.hoelle@bmw.de

ρ	density, kg m ⁻³
σ^2	variance, —
Indices	
avg	index representing a volume averaged value
cell	index representing the battery cell
cell,TR	index representing the battery cell after TR
Cu	index representing the copper block
fabric	index representing the fiber fabric
init	index representing the initial condition
j	index representing a data point of experimental measurements
k	index representing a specific sensor position as shown in Fig. 1c
insulation	index representing the thermal insulation
JR	index representing the jelly roll
JR1mid	index representing the domain of the middle part of jelly roll 1
JR1sides	index representing the domain of the side parts of jelly roll 1
JR2mid	index representing the domain of the middle part of jelly roll 2
JR2sides	index representing the domain of the side parts of jelly roll 2
max	index representing a maximum value
mean	index representing the mean value of several sensors
M1	index representing method 1
M2	index representing method 2
M3	index representing method 3
nail	index representing the nail
x	index representing a battery cell components as shown in Fig. 1b

After the introduction of the lithium-ion battery by Sony in 1991,¹ it did not take long until the first studies regarding thermal hazards were published: Chen and Evans were one of the first to share concerns about the thermal runaway (TR) of such batteries in 1996.² The following years, the scientific attention on this topic increased rapidly with a total cumulative number of 892 articles being published until the end of 2019.³ While many researchers use experimental methods to investigate the TR behavior,^{4–6} there are also numerous publications about the modeling of the TR process. For example, Richard and Dahn were one of the first to investigate the thermal stability of lithium intercalated graphite in electrolyte by mathematical modeling of occurring reactions with Arrhenius-like expressions.⁷ In 2001, Hatchard et al. developed a one-dimensional (1D) model for the simulation of the TR of a full battery cell following a similar modeling approach.⁸ Later, these models were extended by either including more reactions or an expansion to 3D.^{9,10} Until today, there are numerous publications proposing models using reaction kinetics for predicting the TR of lithium-ion batteries.^{9–13}

Modeling the physics as accurate as possible can unveil unknown dependencies and therefore improve the overall understanding of the TR process as shown for example by Baakes et al. in Ref. 12. However, these models are usually complex and many parameters have to be determined in expensive and time-consuming experiments.^{9–13} Therefore, they are unsuitable for supporting engineers in designing safer battery packs, since simple models with low computational effort and acceptable accuracy are required for this purpose. Many researchers address this issue and propose models that are easy to implement and need a reduced number of input parameters. For example, Chen et al. proposed a “simplified mathematical model for heating-induced thermal runaway” with 12 input parameters.¹⁴ Yeow et al. were one of the first to propose an empirical approach for the heat release during TR.¹⁵ They simply approximated the data from accelerating rate calorimetry (ARC) measurements by a Gaussian distribution and implemented a uniform heating inside of the cell depending on its average temperature. Others adopted this approach and approximated ARC data by empirical curves.¹⁶ Another modeling method for the heat release

during TR is to define an empirical function for the heat release depending on the time.¹⁷ However, a spatial resolution of the TR reaction inside of the battery cell is not possible with both methods. Therefore, Feng et al. developed a simple model that is also fitted to experimental data from ARC measurements, but the heat release is depending on the local temperature within the battery.¹⁸ By doing so, a spatial resolution of the heat release is possible. This approach was adopted by other researchers^{19–21} and further simplified to a single equation model.^{22–24}

This publication focuses on thermal modeling of a prismatic state-of-the-art prototype lithium-ion battery during TR and subsequent heat dissipation. The objective is to develop a simulation methodology within the 3D-CFD framework of *Simcenter STAR-CCM+*[®] that is able to reproduce the TR behavior, especially heat release and subsequent heat dissipation. Therefore, the autoclave calorimetry experiment published by Schamer²⁵ and Hoelle et al.²⁶ is simulated and different modeling approaches for the heat release during TR are implemented. In addition, the influence of critical parameters such as mass loss during TR, specific heat capacity of the jelly roll or thermal conductivity of the jelly roll on the simulation results is investigated. The purpose of this study is to identify suitable modeling approaches for the application in TR propagation simulations of battery packs. Consequently, the focus lies on identifying an approach with low computational effort but high accuracy. To the authors’ knowledge, a comparative analysis of different modeling approaches for the TR heat release has not been the subject of any scientific publication. Both, the comparison and the identification of crucial modeling parameters contribute to the improvement of TR as well as TR propagation simulation and therefore help researchers or engineers to choose a suitable model to design a safer battery pack.

Experimental

In this study, the autoclave calorimetry experiment published by Schamer²⁵ and Hoelle et al.²⁶ is modeled and simulated. Therefore, the experimental data of two tests conducted with a prismatic lithium-ion battery cell (>60 Ah) is investigated. The results of the experiments provide input parameters for the simulation model such as mass loss or released heat during TR. Furthermore, the temperature sensor data is used to validate the simulation methodology. Additionally required model parameters, such as the trigger temperature of TR and the specific heat capacity of the cell, are derived from accelerating rate calorimetry experiments and specific heat capacity measurements conducted with the same cell. The following Section covers the geometry of the autoclave calorimetry experiment, further information about the investigated cell and the experimental results used to derive model parameters.

Geometry.—Figure 1 shows the setup of the autoclave calorimetry experiment. The main components are a battery cell (dimensions 180 mm × 32 mm × 72.5 mm) wrapped in a silicate fiber fabric (thickness 1.75 mm) as well as a copper block (dimensions 280 mm × 135.5 mm × 120 mm) that is enclosing the wrapped battery cell. The copper block itself is insulated (thickness 25 mm on each side) against the autoclave environment and consists of several smaller blocks as well as a retainer made out of steel (dimensions 64.75 mm × 40 mm × 32 mm, thickness 2 mm). The lid of the copper block insulation has an opening above the cell vent (dimensions 45.5 mm × 45.5 mm) to allow the venting gases and particles to escape into the autoclave’s void volume. Further details are provided in a previous publication.²⁶

Investigated cell.—In this study, a prismatic state-of-the-art prototype lithium-ion battery cell with a nominal capacity between 60 Ah and 70 Ah, LiNi_{0.8}Mn_{0.1}Co_{0.1}O₂ (NMC811) cathode, and graphite anode is investigated. The electrolyte consists of lithium hexafluorophosphate (LiPF₆) conducting salt with ethylene carbonate (EC), ethyl methyl carbonate (EMC), diethyl carbonate (DEC), and dimethyl carbonate (DMC) solvents. Two nail penetration

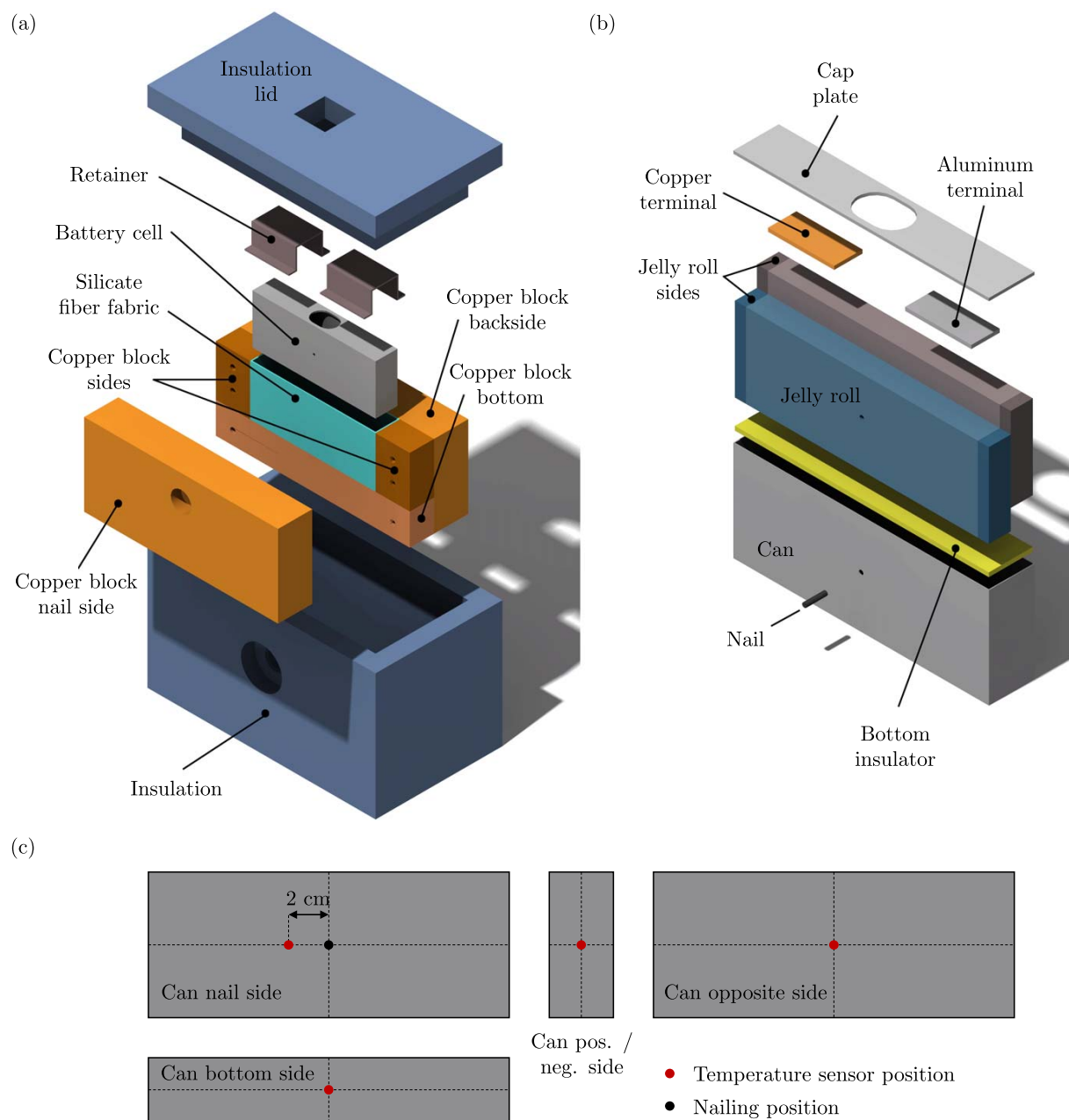


Figure 1. (a) Modeled components of the autoclave calorimetry experiment. (b) Components of the battery cell model. (c) Temperature sensor positions on the cell can.

experiments are conducted following the test procedure described in Ref. 26. The state of charge for both tests is $SoC = 100\%$ and the cells' aging state is fresh/unused. Table 1 summarizes the properties of the investigated cells measured before each test.

Experimental results.—In order to derive required model parameters, the results of three different experimental setups are used in this study:

(i) Autoclave calorimetry is used to determine

- Δm_{cell} being the mass loss during TR,

- Q_1 being the released heat during TR that is dissipated via conduction,
- t_{venting} being the duration of venting, and
- t_{heating} being the duration of (measured) temperature increase.

(ii) Accelerating rate calorimetry (ARC) is used to determine

- T_{onset} being the onset temperature of continuous self-heating and
- T_{TR} being the TR trigger temperature.

(iii) Specific heat capacity measurements are used to determine

Table I. Properties of the battery cells tested in the autoclave calorimetry experiment.

Parameter	Cell 1	Cell 2	Mean	Unit
Measured capacity during preconditioning	67.4	66.8	67.1	Ah
Measured energy during preconditioning	247.6	245.1	246.4	Wh
Measured weight m_{cell}	981.6	979.0	980.3	g
Gravimetric energy density	252.2	250.4	251.3	Wh kg ⁻¹

- $c_{p,\text{JR}}$ being the specific heat capacity of jelly roll.

Autoclave calorimetry.—The mass loss during TR Δm_{cell} is calculated by

$$\Delta m_{\text{cell}} = m_{\text{cell}} - m_{\text{cell,TR}} \quad [1]$$

where m_{cell} is the cell weight before and $m_{\text{cell,TR}}$ is the cell weight after the test. The total heat released during TR can be separated in two parts: heat remaining in the cell Q_1 and heat being transported by venting gases and particles Q_2 .^{25,26} As the autoclave calorimetry experiment is built to separate these effects, only heat conduction from the cell to the copper block is considered in this study and consequently Q_2 will be neglected. Q_1 is estimated as follows:

$$Q_1 = \max(Q_1(t)) \quad \text{with} \quad [2]$$

$$Q_1(t) = [mc_p \Delta T(t)]_{\text{Cu}} + [mc_p \Delta T(t)]_{\text{cell,TR}} + [mc_p \Delta T(t)]_{\text{insulation}}, \quad [3]$$

where t is the time since nail penetration, m is the mass of the components copper block (index: Cu), cell after TR (index: cell,TR), and thermal insulation (index: insulation), respectively, c_p is the specific heat capacity of the respective components, and ΔT is the temperature increase compared to the test's initial condition T_{init} of the respective components. As there is no temperature sensor information for the thermal insulation, its temperature increase is estimated by a simulation. For $t = 2000$ s after nail penetration, this results in a volume averaged temperature of approximately

$$\Delta T_{\text{insulation}} = \frac{1}{3} \Delta T_{\text{Cu}}. \quad [4]$$

The initial temperature T_{init} is defined by the initial mean value of all temperature sensors at the cell can and the copper block, that means in the center of each cell side (except the top side) and in the center of each corresponding copper block area (compare Fig. 1c).

The duration of venting t_{venting} is estimated as suggested by Schamer in Ref. 25. In the autoclave calorimetry experiment, the pressure curve shows a peak followed by an asymptotic approach to an equilibrium state. Schamer²⁵ assumed, that the venting stops at the point in time when the pressure is

$$p_{\text{EoV}} = p_{\text{eql}} + \frac{1}{2}(p_{\text{max}} - p_{\text{eql}}), \quad [5]$$

where p_{EoV} is the pressure at end of venting (index: EoV), p_{eql} is the pressure measured at temperature equilibrium inside the autoclave (index: eql), and p_{max} is the maximum pressure. Consequently, the duration of venting is

$$t_{\text{venting}} = t(p = p_{\text{EoV}}) - t_{\text{init}} \quad [6]$$

where t_{init} is the point in time of nail penetration. Another parameter estimated during the experiment is the duration of measured temperature increase of the cell t_{heating} . It is set to the point in

Table II. Experimental results used as model parameters.

Parameter	Cell 1	Cell 2	Mean	Unit
Δm_{cell}	409.4	416.4	412.9	g
T_{init}	20.9	22.4	21.7	°C
Q_1	748.8	709.7	729.3	kJ
t_{venting}	17.2	18.2	17.7	s
t_{heating}	33.1	46.7	39.9	s
T_{onset}	—	—	75.2 ^a	°C
T_{TR}	—	—	137.5 ^a	°C
$c_{p,\text{JR}}$	—	—	see Fig. 3	J kg ⁻¹ K ⁻¹

a Mean value of three cells tested in ARC experiments.

time when the cell reaches its maximum mean temperature $T_{\text{cell,mean,max}}$ (average value of all sensors on the cell can surface):

$$t_{\text{heating}} = t(T = T_{\text{cell,mean,max}}) - t_{\text{init}}. \quad [7]$$

Accelerating rate calorimetry (ARC).—The onset temperature of continuous self-heating T_{onset} and the TR trigger temperature T_{TR} are estimated by ARC experiments. The parameters are estimated by three standard heat-wait-see tests conducted with the same type of battery cell as used in the autoclave calorimetry experiment. The EV + ARC manufactured by *THT*[®] (Thermal Hazard Technology) is used to perform the experiments. The following criteria are used:

- 0.02 K min⁻¹ is detected as onset of self-heating and
- 30 K min⁻¹ is detected as onset of TR.

Specific heat capacity measurements.—Specific heat capacity measurements on full cell level are performed in order to estimate the specific heat capacity of the jelly roll $c_{p,\text{JR}}$. Therefore, two cells are stacked together with a heating pad in-between and the heating power needed for a temperature increase from 25 °C to 60 °C is analyzed. Unfortunately, temperatures higher than 60 °C could not be tested due to the safety limits defined by the cell manufacturer. With the resulting specific heat capacity of the full cell $c_{p,\text{cell}}$ the specific heat capacity of the jelly roll is then calculated by

$$c_{p,\text{JR}} = \frac{m_{\text{cell}} c_{p,\text{cell}} - \sum_x m_x c_{p,x}}{m_{\text{JR}}}, \quad [8]$$

with m_{cell} being the mass of the full cell, m_x being the mass, and $c_{p,x}$ being the specific heat capacity of each component x of the full cell (except jelly roll), respectively, and m_{JR} being the mass of the jelly roll. Table II summarizes all experimental results used as model parameters.

Model Structure and Simulation Methodology

A three-dimensional thermal model is built in the commercial (CFD) software *Simcenter STAR-CCM+*[®], which is based on the finite volume approximation approach. In this study, only heat

Table III. Material properties of the model components used for the reference simulation.

Component as shown in Fig. 1	Density ρ [kg m ⁻³]	Specific heat capacity c_p [J kg ⁻¹ K ⁻¹]	Thermal conductivity λ [W m ⁻¹ K ⁻¹]
Can / cap plate	2730.0	893.0	159.0
Jelly Roll (in-plane)	2620.6	1000.0	23.1
Jelly Roll (through-plane)	2620.6	1000.0	1.034
Bottom insulator	619.0	1807.0	0.254
Copper terminal	8960.0	385.0	402.0
Aluminum terminal	2960.0	905.0	237.0
Nail	8055.0	480.0	15.1
Silicate fiber fabric	734.0	720.0	$\lambda_{\text{fabric}}(T)$ (see Eq. 10)
Copper block	8960.0	385.0	402.0
Retainer	8055.0	480.0	15.1
Thermal insulation	280.0	860.0	0.023

conduction within solids is considered. The governing equation for energy transport within a solid is given as follows:

$$\rho c_p \frac{\partial T}{\partial t} = \nabla \cdot \lambda \nabla T + \dot{q} \quad [9]$$

with ρ , c_p , and λ being the thermophysical properties of the solid (density, specific heat capacity, and thermal conductivity, respectively), T being the temperature of the solid, and \dot{q} being the sum of all heat sources within the solid.

In order to compare different modeling approaches for the heat release during TR, it is necessary to implement material properties that are capable of reproducing the experimental behavior. Therefore, a sequential sensitivity study of the following parameters is carried out first:

- ρ_{JR} being the density of the jelly roll,
- $c_{p,\text{JR}}$ being the specific heat capacity of the jelly roll, and
- λ_{JR} being the through-plane thermal conductivity of the jelly roll.

In this context, the term “sequential” means that for each parameter variation the parameter set with the best fit to the experimental data is considered as baseline. Consequently, the baseline parameter set is not necessarily the same for each varied parameter. On the one hand, the results of this sensitivity study help to analyze the influence of each parameter on the simulation results and point out the importance of a correct application in TR simulations. On the other hand, the results help to define a final parameter set for the comparison of modeling approaches for heat release during TR, that is done in a second step. The following Section deals with the model geometry and numerical setup, used boundary conditions as well as the sensitivity study and the modeling approaches for heat release during TR.

Model geometry and mesh.—The battery cell components are modeled as shown in Fig. 1b. Each of the two jelly rolls is represented by three rectangular cuboids: a large middle cuboid and two smaller side cuboids. This allows to assign different material properties in each of the three regions and accounts for the orthotropic thermal conductivity of the jelly roll depending on the winding structure. The terminals are also simplified as cuboids (dimensions 46.56 mm × 20 mm × 2.5 mm) with a density and specific heat capacity assigned to match the actual current collectors and terminals of the cell. Moreover, there is a bottom insulator underneath the jelly rolls (thickness 2.9 mm). The cell can is modeled as hollow body with the safety vent being open and air or gas flow inside of the cell can is neglected.

As shown in Fig. 1a, the battery cell is enclosed by a silicate fiber fabric. The thermal conductivity of this fabric λ_{fabric} is assumed to be

temperature dependent according to the manufacturers information. The following fitting curve is used:

$$\lambda_{\text{fabric}}(T) = \begin{cases} \text{const.} = 0.0858 \text{ W m}^{-1} \text{ K}^{-1} & \text{for } T < 0 \text{ }^\circ\text{C} \\ a \cdot T^3 + b \cdot T^2 + c \cdot T + d & \text{for } 20 \text{ }^\circ\text{C} < T < 1200 \text{ }^\circ\text{C} \\ \text{const.} = 1.0894 \text{ W m}^{-1} \text{ K}^{-1} & \text{for } T > 1200 \text{ }^\circ\text{C} \end{cases} \quad [10]$$

with $a = 5.83\text{e-}10 \text{ W m}^{-1} \text{ K}^{-4}$, $b = -3.71\text{e-}7 \text{ W m}^{-1} \text{ K}^{-3}$, $c = 4.42\text{e-}4 \text{ W m}^{-1} \text{ K}^{-2}$, and $d = 8.58\text{e-}2 \text{ W m}^{-1} \text{ K}^{-1}$ being the polynomial constants for the (fabric) temperature T in $^\circ\text{C}$. The material properties of all (other) components are summarized in Table III.

The mesh used is the result of a mesh sensitivity study. It is ensured that all parts, in particular thin parts, are resolved by a minimum number of three cell layers in each direction. Figure 2 shows two plane Sections of the mesh. Table IV summarizes the element count of volume cells for each component.

Boundary conditions and numerical setup.—The experiment is modeled as a transient solid-body simulation with a total physical time of $t_{\text{total}} = 2000 \text{ s}$. For the first 50 s, the time step is set small enough to ensure that numerical errors due to the heat release can be neglected. For the simulations of the model parameter sensitivity study, the time step is set to

$$\Delta t_{\text{step}} = 0.05 \text{ s} \quad \text{for } t < 50 \text{ s.} \quad [11]$$

Afterwards, Δt_{step} is increased step-wise over six seconds to $\Delta t_{\text{step}} = 2 \text{ s}$. The energy residual ϵ is used as stopping criteria for inner iterations i . As soon as a minimum number of 15 inner iterations is calculated, the following criteria needs to be fulfilled to end the solving process of the current time step:

$$\frac{\max(\epsilon(i - 14; i)) - \min(\epsilon(i - 14; i))}{\text{mean}(\epsilon(i - 14; i))} \leq 0.1. \quad [12]$$

The maximum number of inner iterations is set to 125. The initial temperature T_{init} for all solids is set to the mean value of both conducted autoclave calorimetry experiments with

$$T_{\text{init}} = 21.7 \text{ }^\circ\text{C}. \quad [13]$$

An ideal interface is set between all solid contacts except the contact faces between the single copper block parts. For the latter, a thermal resistance $R_{\text{th,Cu}}$ is applied to the solid-to-solid contact, as the single blocks are screwed together and therefore, an air layer with a thickness of the doubled roughness depth of the blocks $R_{\text{a,Cu}}$ is set as thermal resistance:

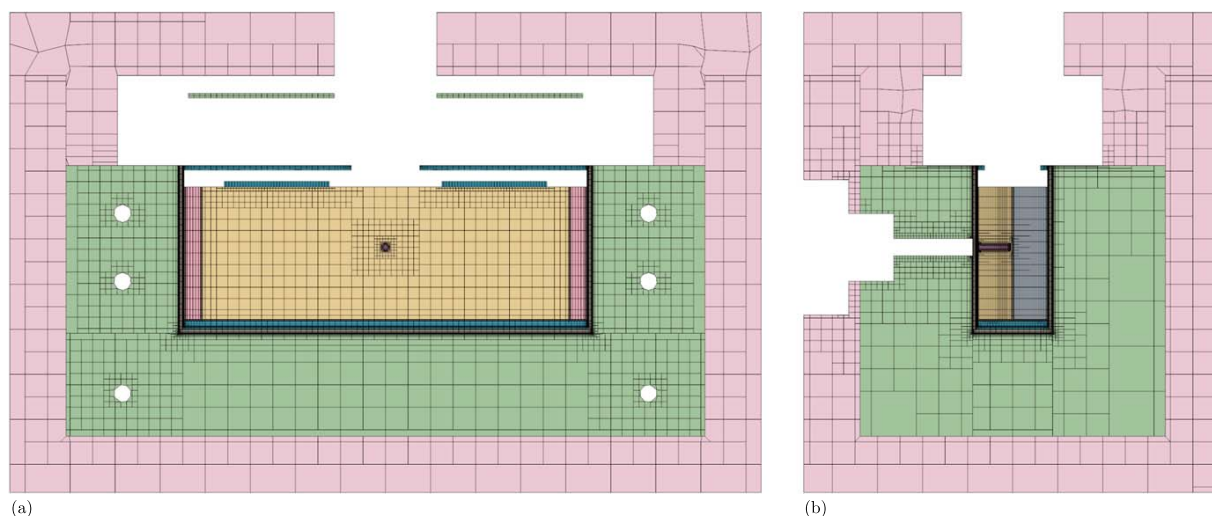


Figure 2. (a) Plane Section of the mesh perpendicular to the nailing direction. (b) Plane Section of the mesh in nailing direction.

Table IV. Summary of the element count of volume cells for each component.

Component	Cell count
Can	53731
Jelly Roll	62191
Bottom insulator	19572
Terminal Cu	2432
Terminal Al	2432
Nail	1944
Silicate fiber fabric	79342
Copper block	58539
Retainer	9072
Thermal insulation	18896
Total	308151

$$\begin{aligned}
 R_{\text{th,Cu}} &= \frac{2 \cdot Ra_{\text{Cu}}}{\lambda_{\text{air}}} \\
 &= \frac{2 \cdot 6 \mu\text{m}}{0.026 \text{ W m}^{-1} \text{ K}^{-1}} \\
 &= 2.31 \text{e} - 4 \text{ m}^2 \text{ K W}^{-1}, \quad [14]
 \end{aligned}$$

with λ_{air} being the thermal conductivity of air. All faces without contacts are set as adiabatic. Since there are no high temperature differences between contacting bodies expected, heat radiation is not considered in this study.

Model parameter sensitivity study.—In order to analyze the influence of model parameters such as mass loss during TR, specific heat capacity of the jelly roll, and (through-plane) thermal conductivity of the jelly roll, a sensitivity study is performed. Therefore, the thermophysical properties of the jelly roll material are varied. Table V shows an overview over the variations of jelly roll density ρ_{JR} , specific heat capacity $c_{p,\text{JR}}$, and thermal conductivity λ_{JR} . It should be pointed out that the first modeling approach for heat release during TR (method 1) is used for the model parameter sensitivity study. A detailed description of the different methods is provided below.

Mass loss during TR.—As shown in previous work, a lithium-ion battery cell loses a significant amount of its mass during the autoclave calorimetry experiment.²⁶ According to

$$Q = mc_p \Delta T = \rho V c_p \Delta T, \quad [15]$$

this mass loss will influence the temperature increase ΔT of a battery cell during TR. Most of the previous studies do not account for this effect and assume the cell to maintain its full mass.^{12–16,18–22,27–35}

Coman et al. were one of the first to consider a loss of mass in their model by adapting the jelly roll density ρ_{JR} depending on the amount of vented electrolyte.³⁶ The outcome was, that the consideration of venting and hence mass loss improves the simulation results compared to experiments. Other publications confirmed this observation.^{23,37} Unfortunately, all these models include a gas phase based on flow equations and therefore are not directly applicable to solid body simulations. However, Liu et al. and Coman et al. published models of solid body simulations, that adapt ρ_{JR} when TR occurs.^{17,24}

As shown in Table II, the mean mass loss of the autoclave calorimetry experiments is $\Delta m_{\text{cell}} = 412.9 \text{ g}$. To show the influence of this phenomenon, it is assumed that this mass loss originates from the jelly roll only and consequently, the mass loss is modeled by adapting the jelly roll density ρ_{JR} . In this study, three different (constant) jelly roll masses will be modeled (Table V, No. 1–3):

- “Full mass” assumes no mass loss and therefore, the standard jelly roll density of $\rho_{\text{JR}} = 2620.6 \text{ kg m}^{-3}$ is applied.
- “End mass” assumes that the mass loss already occurred before the heat release of TR and hence the jelly roll density is set to match the jelly roll mass after TR.
- “Half mass” is the mean value of the “Full mass” and “End mass” case.

Specific heat capacity of the jelly roll.—As shown in Eq. 15, the specific heat capacity c_p is supposed to have the same influence on the temperature increase ΔT as the mass m . However, the mass (loss) during TR is time dependent, whereas a material’s specific heat capacity is usually depending on temperature. Previous studies do not account for a temperature dependent specific heat capacity of the jelly roll.^{13,14,17–21,23,24,27–32,34–38} Although there are some measurements of temperature dependent values as summarized in Ref. 39, a major issue with these is the limited temperature range (usually $T < 60 \text{ }^\circ\text{C}$). Due to the onset of TR at higher temperatures, there is a lack of experimental investigations and consequently an analysis of the specific heat capacity’s influence on TR in simulation is necessary.

Table V. Variation of jelly roll (JR) material properties for the model parameter sensitivity study.

No.	JR mass	ρ_{JR} [kg m ⁻³]	JR specific heat capacity		JR thermal conductivity	
			$c_{p,JR}$ [J kg ⁻¹ K ⁻¹]		λ_{JR} [W m ⁻¹ K ⁻¹]	
1	Full mass	2620.6	const.	1000	const.	1.034
2	Half mass	1990.3	const.	1000	const.	1.034
3	End mass	1360.1	const.	1000	const.	1.034
4	End mass	1360.1	$c_p(T)$	$c_{p,JR,max} = 1200$	const.	1.034
5	End mass	1360.1	$c_p(T)$	$c_{p,JR,max} = 1400$	const.	1.034
6	End mass	1360.1	$c_p(T)$	$c_{p,JR,max} = 1600$	const.	1.034
7	End mass	1360.1	$c_p(T)$	$c_{p,JR,max} = 1400$	const.	0.517
8	End mass	1360.1	$c_p(T)$	$c_{p,JR,max} = 1400$	const.	2.068

In order to analyze the influence of an increasing specific heat capacity of the jelly roll $c_{p,JR}$ with rising temperature, three different dependencies according to Fig. 3 are implemented in this study. The black crosses show the results of specific heat capacity measurements on full cell level that are converted to values for the jelly roll by Eq. 8. The temperature dependency of $c_{p,JR}$ is chosen to match these measurements. Outside of the measurement's temperature range, an asymptotic value of $c_{p,JR,max} = 1100 \text{ J kg}^{-1} \text{ K}^{-1}$ could be suggested. However, it is expected that a maximum value of $c_{p,JR,max} = 1100 \text{ J kg}^{-1} \text{ K}^{-1}$ would not lead to a significant change of the simulation results in comparison to the standard case of $c_{p,JR} = \text{const.} = 1000 \text{ J kg}^{-1} \text{ K}^{-1}$. Therefore, $c_{p,JR}$ is set constant to three different (purely empirical) maximum values of $c_{p,JR,max} = 1200 \text{ J kg}^{-1} \text{ K}^{-1}$, $1400 \text{ J kg}^{-1} \text{ K}^{-1}$, and $1600 \text{ J kg}^{-1} \text{ K}^{-1}$ (Table V, No. 4–6). It should be pointed out that for the sensitivity analysis of the mass loss during TR the specific heat capacity is set to $c_{p,JR} = \text{const.} = 1000 \text{ J kg}^{-1} \text{ K}^{-1}$.

Thermal conductivity of the jelly roll.—The third varied material property is the through-plane thermal conductivity of the jelly roll λ_{JR} . For prismatic cells with NMC cathode, values between $0.82 \text{ W m}^{-1} \text{ K}^{-1} < \lambda_{JR} < 1.1 \text{ W m}^{-1} \text{ K}^{-1}$ are reported.^{40,41} However, these values are estimated under normal operating conditions with temperatures of $T < 60 \text{ }^\circ\text{C}$ and therefore not necessarily applicable to TR simulations. Comparing the experimentally measured values to assumptions made in previous publications for TR modeling shows a greater range. For example, Parhizi et al. and Mishra et al. used a value of $\lambda_{JR} = 0.2 \text{ W m}^{-1} \text{ K}^{-1}$ ^{27–30} whereas others use values up to $\lambda_{JR} = 3.4 \text{ W m}^{-1} \text{ K}^{-1}$.^{17,31–33,36,38}

In this study, the median value of $\lambda_{JR} = 1.034 \text{ W m}^{-1} \text{ K}^{-1}$ as reported by Steinhardt et al. will be used as a baseline.³⁹ This is also in accordance with other publications.^{13,14,21,24,34,35} In order to evaluate the influence of lower and higher values, this baseline value will be halved and doubled (Table V, No. 7–8).

Modeling approaches for heat release during TR.—In this study, three different modeling approaches for the heat release during TR will be investigated. As the focus lies on approaches with low computational effort, only empirical heat sources are considered. The heat release is implemented in the jelly roll only and is subsequently spreading to the other cell components as well as the experimental setup.

- Method 1: Time dependent and spatially uniform heat release (reference - used for model parameter sensitivity study)
- Method 2: Temperature dependent and spatially uniform heat release
- Method 3: Temperature dependent and spatially resolved heat release

It should be pointed out that for the comparison of heat release approaches during TR the parameters according to simulation “No. 5” are used (see Table V).

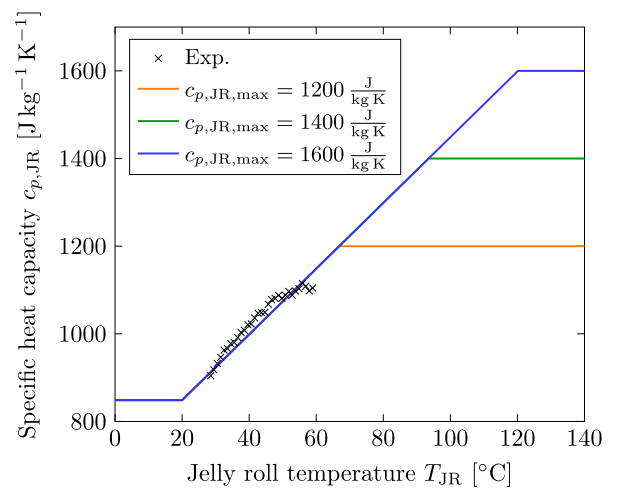


Figure 3. Specific heat capacity of jelly roll $c_{p,JR}$ over jelly roll temperature T_{JR} estimated from measurements on full cell level (black crosses) and implemented dependencies for sensitivity study (colored curves).

Method 1: Time dependent and spatially uniform heat release.—The first approach is based on an empirical time dependent heat release function that is derived from experimental data of ARC tests. A comparable approach was also used by Coman et al. in Ref. 17. Figure 4 shows the heat release \dot{Q}_{ARC} over time t since TR initiation for three ARC experiments (colored dots) and the assumed heat release function for the simulation model (black curve). In the ARC experiments, the heat release is reaching a maximum directly after TR initiation for several seconds followed by a decrease to lower values. Comparing the venting duration of the autoclave calorimetry experiments of $t_{venting} = 17.7 \text{ s}$ to the ARC data shows that there is still a heat release detected for $t > t_{venting}$.

This observed behavior is approximated by a superposition of a Gaussian distribution ($\dot{Q}_{1,1}$) and a linear function ($\dot{Q}_{1,2}$):

$$\dot{Q}_{ARC}(t) = \begin{cases} \frac{1}{\beta} \dot{Q}_{1,1}(t) & \text{for } t < t_{venting} \\ \frac{1}{\beta} \dot{Q}_{1,2}(t) & \text{for } t_{venting} \leq t \leq t_{heating} \end{cases} \quad [16]$$

with the normalization factor β :

$$\beta = \int_0^{t_{venting}} \dot{Q}_{1,1}(t) dt + \int_{t_{venting}}^{t_{heating}} \dot{Q}_{1,2}(t) dt. \quad [17]$$

The result of this superposition is the black curve shown in Fig. 4: as soon as the TR is triggered, heat is released in form of a Gaussian distribution (Eq. 18) with a subsequent linear decrease (Eq. 20) for

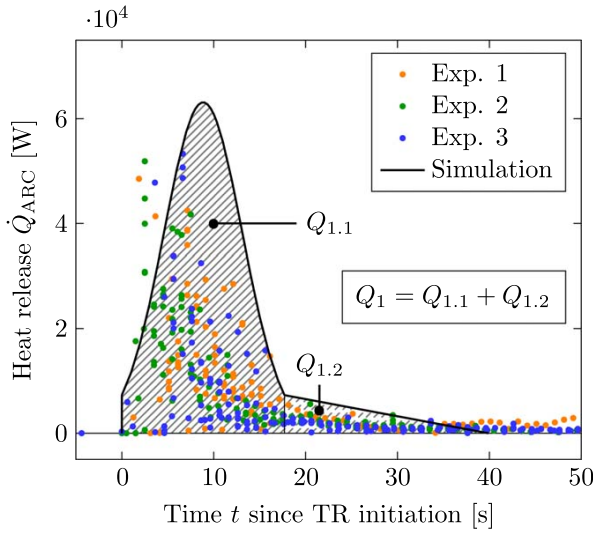


Figure 4. Method 1: heat release during TR \dot{Q}_{ARC} over time t since TR initiation estimated from ARC measurements (colored dots) and implemented function for the simulation model (black curve).

the duration of (measured) temperature increase t_{heating} (see Table II):

$$\dot{Q}_{1,1}(t) = \frac{1}{\sqrt{2\pi\sigma^2}} \exp\left(-\frac{1}{2\sigma^2}\left(t - \frac{t_{\text{venting}}}{2}\right)^2\right) \quad \text{with} \quad [18]$$

$$\sigma^2 = \frac{1}{4}(0.175 t_{\text{venting}} + 1)t_{\text{venting}} \quad [19]$$

and

$$\dot{Q}_{1,2}(t) = \dot{Q}_{1,1}(t_{\text{venting}}) - \frac{\dot{Q}_{1,1}(t_{\text{venting}})}{t_{\text{heating}} - t_{\text{venting}}}(t - t_{\text{venting}}). \quad [20]$$

Due to the normalization, it is possible to implement \dot{Q}_{ARC} on several parts of a model and assign certain fractions of the total heat released. In this study, the heat release of method 1 $\dot{Q}_{M1,x}$ is therefore modeled for each jelly roll part x as follows:

$$\dot{Q}_{M1,JR1\text{mid}} = \dot{Q}_{ARC}(t)\alpha_{JR1\text{mid}}(Q_1 - Q_{\text{nail}}) \quad \text{for} \quad T_{JR1\text{mid,max}} > T_{TR}, \quad [21]$$

$$\dot{Q}_{M1,JR1\text{sides}} = \dot{Q}_{ARC}(t)\alpha_{JR1\text{sides}}(Q_1 - Q_{\text{nail}}) \quad \text{for} \quad T_{JR1\text{sides,max}} > T_{TR}, \quad [22]$$

$$\dot{Q}_{M1,JR2\text{mid}} = \dot{Q}_{ARC}(t)\alpha_{JR2\text{mid}} Q_1 \quad \text{for} \quad T_{JR2\text{mid,max}} > T_{TR} \quad \text{and} \quad [23]$$

$$\dot{Q}_{M1,JR2\text{sides}} = \dot{Q}_{ARC}(t)\alpha_{JR2\text{sides}} Q_1 \quad \text{for} \quad T_{JR2\text{sides,max}} > T_{TR}. \quad [24]$$

with α_x being the volume fraction of the jelly roll part x related to the total volume of the jelly roll (that means both middle parts and all 4 sides - compare Fig. 1b), Q_1 being the heat remaining in the cell as measured in the autoclave calorimetry experiments, Q_{nail} being the heat released in the nail for triggering the TR and $T_{x,\text{max}}$ being the maximum temperature in the jelly roll part x .

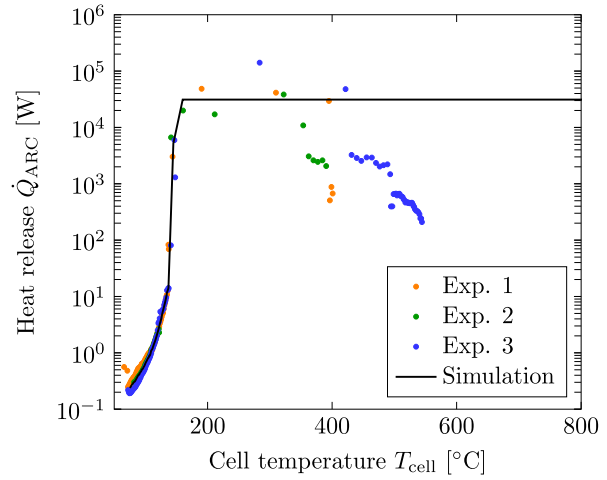


Figure 5. Method 2: heat release \dot{Q}_{ARC} over average cell temperature T_{cell} .

As stated in Eqs. 21–24, the heat release in each jelly roll part is initiated by exceeding the TR trigger temperature T_{TR} . In the autoclave calorimetry experiments, this is caused by the electrical short circuit due to the nail, that penetrates the jelly roll. To model the heat release of this short circuit, the approach of Feng et al.¹⁸ is adopted:

$$\dot{Q}_{\text{nail}} = Q_{\text{nail}} f(t) = \alpha_{\text{nail}} Q_1 f(t) \quad [25]$$

with $f(t)$ being the short circuit release rate in the nail as defined by Feng et al.¹⁸ and $\alpha_{\text{nail}} = 0.01$ being the fraction of heat that is released in the nail.

Method 2: Temperature dependent and spatially uniform heat release.—The second approach is based on a model proposed by Yeow et al.¹⁵ in 2013. The heat source is modeled as a function depending on the volume averaged jelly roll temperature $T_{JR,\text{avg}}$. Yeow et al.¹⁵ used a Gaussian distribution to approximate the self-heating rate of the cell vs. the cell temperature measured in ARC experiments. This approach is applied to the experimental data of this study: Fig. 5 shows the heat release $\dot{Q}_{ARC}(T)$ over (measured) cell temperature T_{cell} of the three ARC tests (colored dots) and the assumed heat release function (black curve). The measured heat release is approximated by the mean value of the three tests and is directly implemented in the simulation model as table data set. The simulation software then linearly interpolates between these table values. After reaching T_{TR} in the ARC experiments, the number of measured data points is low. Therefore, the heat release rate is set to $\dot{Q}_{M2,x,\text{max}} = \text{const.} = 31177 \text{ W}$ which is equivalent to a temperature rate of 3000 K min^{-1} as conventionally measured during ARC experiments.

As the heat release depends on the volume averaged temperature of the jelly roll, the electrical short circuit in the nail is not releasing enough heat to trigger the TR. Therefore, the initial temperature of the middle part of the nailed jelly roll is set to $T_{JR1\text{mid,init}} = 150 \text{ °C}$. The heat release of method 2 $\dot{Q}_{M2,x}$ is then modeled as a separate heat source for the middle and both side parts of each jelly roll:

$$\dot{Q}_{M2,JR1\text{mid}} = \dot{Q}_{ARC}(T_{JR1\text{mid,avg}}(t)) \quad \text{for} \quad \int \dot{Q}_{M2,JR1\text{mid}} dt \leq \alpha_{JR1\text{mid}}(Q_1 - Q_{\text{init}}), \quad [26]$$

$$\dot{Q}_{M2,JR1\text{sides}} = \dot{Q}_{ARC}(T_{JR1\text{sides,avg}}(t)) \quad \text{for} \quad \int \dot{Q}_{M2,JR1\text{sides}} dt \leq \alpha_{JR1\text{sides}} Q_1, \quad [27]$$

$$\begin{aligned} \dot{Q}_{M2, JR2mid} &= \dot{Q}_{ARC}(T_{JR2mid, avg}(t)) \\ \text{for } \int \dot{Q}_{M2, JR2mid} dt &\leq \alpha_{JR2mid} Q_1, \end{aligned} \quad [28]$$

$$\begin{aligned} \dot{Q}_{M2, JR2sides} &= \dot{Q}_{ARC}(T_{JR2sides, avg}(t)) \\ \text{for } \int \dot{Q}_{M2, JR2sides} dt &\leq \alpha_{JR2sides} Q_1 \end{aligned} \quad [29]$$

where $\dot{Q}_{ARC}(T_{x, avg})$ is the heat release interpolated from the curve shown in Fig. 5 depending on the volume averaged temperature $T_{x, avg}$ of the jelly roll part x and Q_{init} is the amount of cumulated heat that is assumed to be already released due to the initial condition. It should be pointed out that there is no more heat release in the nail itself, as the initial condition triggers the TR in the middle part of the nailed jelly roll. The heat release in each part x stops as soon as the equivalent amount of Q_1 is released. This is achieved by the integration of $\dot{Q}_{M2, x}$ over time t and monitoring the amount of released heat.

Method 3: Temperature dependent and spatially resolved heat release.—The third approach is based on a model proposed by Feng et al.¹⁸ in 2016. The main difference to method 2 is that the heat release is depending on the local temperature in each volume element of the jelly roll mesh and therefore, the heat release is spatially resolved. Feng et al.¹⁸ splitted the volumetric heat source \dot{q} into three parts:

$$\dot{q} = \dot{q}_{nail} + \dot{q}_{onset} + \dot{q}_{ele} \quad [30]$$

with \dot{q}_{nail} being caused by the electric short circuit in the nail, \dot{q}_{onset} being caused by exothermal chemical reactions at elevated temperatures, and \dot{q}_{ele} being caused by the electrical energy release after separator collapse followed by an internal short circuit in the cell. While \dot{q}_{nail} is released in the nail only, \dot{q}_{onset} and \dot{q}_{ele} are released in the whole jelly roll material (compare Fig. 1b). In contrast to the original publication, the heat released during TR Q_1 is known from the autoclave calorimetry experiments. Therefore, \dot{q}_{onset} and \dot{q}_{ele} are simplified and put together into a single source term for the JR \dot{q}_{JR} . Adopting \dot{q}_{nail} from the original publication leads to:¹⁸

$$\dot{q}_{nail} = \frac{1}{V_{nail}} \alpha_{nail} Q_1 f(t) \quad \text{and} \quad [31]$$

$$\dot{q}_{JR} = \dot{q}_{onset} + \dot{q}_{ele} = \frac{1}{V_{JR}} (1 - \alpha_{nail}) Q_1 \frac{dc_e}{dt}, \quad [32]$$

with V_{nail} and V_{JR} being the volume of the nail and the jelly roll(s), respectively, $\alpha_{nail} = 0.01$ being the fraction of heat released in the nail, $f(t)$ being the short circuit release rate in the nail as defined by Feng et al. in Ref. 18, and c_e being the normalized concentration of energy in each volume element of the mesh. The reaction rate dc_e/dt is then defined as follows:

$$\frac{dc_e}{dt} = \begin{cases} \frac{m_{JR} c_p, JR}{(1 - \alpha_{nail}) Q_1} A \left(\frac{T}{T_{ref}} \right)^B & \text{for } 0 \leq c_e \leq 1 \text{ and } T_{onset} < T \leq T_{TR} \\ C & \text{for } 0 \leq c_e \leq 1 \text{ and } T > T_{TR} \\ 0 & \text{otherwise} \end{cases} \quad [33]$$

with m_{JR} being the mass of the jelly roll(s), $A = 0.0185 \text{ K s}^{-1}$ being a pre-exponential factor, $B = 24.94$ being the reaction index, $T_{ref} = 410.65 \text{ K}$ ($137.5 \text{ }^\circ\text{C}$) = T_{TR} being used to normalize the temperature T , $C = 1 \text{ s}^{-1} = \text{const.}$ being the reaction rate during TR, and $T_{onset} = 75.2 \text{ }^\circ\text{C}$ being the onset temperature of continuous self-heating in the ARC experiments. It should be pointed out that A , B ,

C , T_{onset} , and T_{TR} are adapted to fit the experimental results of this study and consequently differ from the values used by Feng et al. in Ref. 18.

Evaluation methodology.—In order to compare the individual simulations with each other, as well as with the experiments, the following quantities/parameters are defined:

- **Temperature curves.** The simulation results are compared to the experimental data by analyzing the temperature curves of the available temperature sensors. In the two autoclave calorimetry experiments investigated in this study, there are temperature sensors placed in the center of each side of the cell can surface (except the top side, compare Fig. 1c). The sensor on the nail penetrated side is shifted by 1 cm to prevent a damage by the nail. Equivalent sensors are placed on the copper block surface directed to the cell. That means, each pair of sensors is only separated by the silicate fiber fabric. These ten temperature sensor positions are also monitored in all simulations. The comparison between simulation and experimental results is then made either for each sensor on its own or for the mean cell can temperature $T_{cell, mean}$ and the mean copper block temperature $T_{Cu, mean}$.

(i) **Mean temperature curves.** In order to compare the mean temperatures curves of cell can and copper block, the following characteristics are analyzed:

— $T_{cell, mean, max}$ is the maximum value of the mean cell can temperature.

— $\Delta T_{Cu, mean, 500s}$ is the difference between the mean copper block temperature of simulation and experiments at $t = 500 \text{ s}$.

—To quantify the overall deviation between simulation and experiment the mean absolute percentage error (MAPE) as well as the root mean square percentage error (RMSPE) is calculated for the time span $0 \text{ s} \leq t \leq 2000 \text{ s}$ according to

$$\text{MAPE} = 100 \% \cdot \frac{1}{n} \cdot \sum_{j=1}^n \left| \frac{E_j - S_j}{E_j} \right| \quad \text{and} \quad [34]$$

$$\text{RMSPE} = 100 \% \cdot \sqrt{\frac{1}{n} \cdot \sum_{j=1}^n \left(\frac{E_j - S_j}{E_j} \right)^2} \quad [35]$$

with n being the number of data points j within the given time span, E_j being the (mean) experimental value of data point j , and S_j being the simulation results of data point j .

(ii) **Single sensor temperature curves.** In order to compare the different temperature curves for each sensor position the following three characteristics are analyzed:

—Time t_{begin} at $T > 50 \text{ }^\circ\text{C}$ is the point in time when the specific sensor shows temperatures of $T > 50 \text{ }^\circ\text{C}$ for the first time since nail penetration. This value is supposed to represent the begin of temperature increase at each sensor position. The value of $50 \text{ }^\circ\text{C}$ is chosen because the simulation case “method 2” shows a temperature on the nailed side of $T_{cell, nail} \approx 50 \text{ }^\circ\text{C}$ after the initial time step.

— T_{max} is the maximum temperature at each position on the cell can and on the copper block respectively.

—Mean $\Delta T/\Delta t$ is defined by the maximum temperature increase $\Delta T = T_{max} - T_{init}$ divided by $\Delta t = t_{max} - t_{begin}$ with the time t_{max} needed to reach this maximum temperature at each sensor position. This value is supposed to represent the temperature gradient at each sensor position.

- **Accuracy.** As the simulation is modeled with adiabatic boundaries, the numerical error ϵ_Q between specified released heat Q_1 and actually in the simulation released heat $Q_{control}$ can be calculated by

$$c_Q = \frac{Q_{\text{control}} - Q_1}{Q_1} \quad \text{with} \quad [36]$$

$$Q_{\text{control}} = \sum m_x c_{p,x} (T_{x,\text{avg}} - T_{\text{init}}), \quad [37]$$

where m_x is the mass, $c_{p,x}$ is the specific heat capacity, and $T_{x,\text{avg}}$ is the volume averaged temperature of each component x respectively.

• Computation time. All simulations are performed on the same hardware with the same amount of computational resources (six Intel® Xeon® Gold 6254 CPUs and 32 GB RAM). Therefore, the computation time Δt_{sim} can be compared.

Results and Discussion

A total of 11 simulations of the TR behavior in the autoclave calorimetry experiment was performed. In a first step, the model parameter sensitivity study is analyzed. The results show the influence of the parameters mass loss during TR, specific heat capacity of the jelly roll, and through-plane thermal conductivity of the jelly roll. In addition, the parameter set with the smallest deviations from the experimental results is identified. In a second step, the three different modeling approaches for heat release during TR (simulated with this identified “best” set of parameters) are compared with the experimental results as well as with each other.

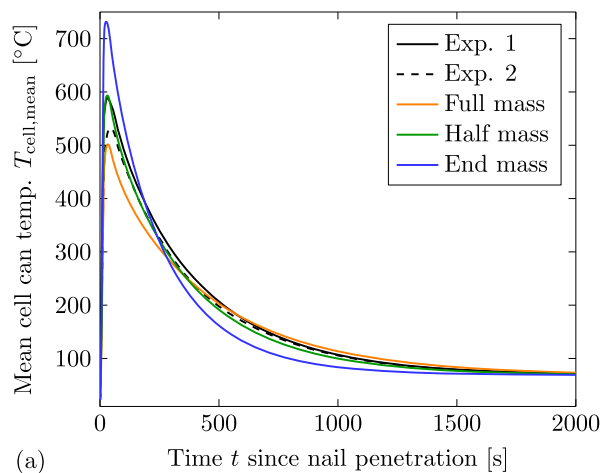
Model parameter sensitivity study.—Mass loss during TR.—

Figure 6 shows the mean cell can temperature $T_{\text{cell,mean}}$ (Fig. 6a) as well as the mean copper temperature $T_{\text{Cu,mean}}$ (Fig. 6b) over time t since nail penetration for both experiments (black and black dashed) and the three simulations with different densities ρ_{JR} (colored). A variation of ρ_{JR} is equivalent to a variation of the jelly roll mass and consequently shows the influence of the mass loss during TR Δm_{cell} on the simulation results (orange for “Full mass”, green for “Half mass” and blue for “End mass”).

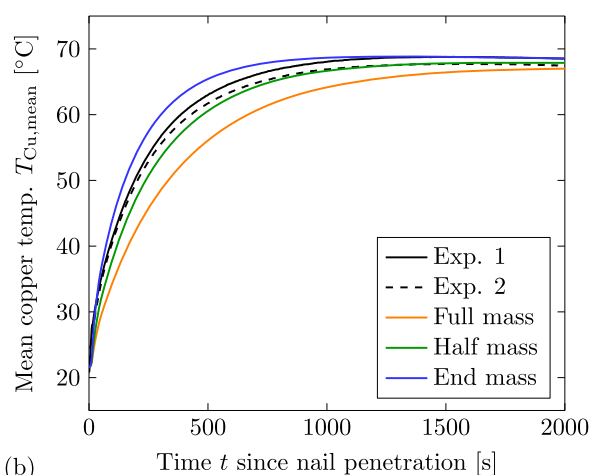
Figure 6a illustrates that the mass of the jelly roll has an influence on both $T_{\text{cell,mean,max}}$ and the heat dissipation behavior of the cell after TR, which is indicated by the course of the temperature curve after reaching $T_{\text{cell,mean,max}}$. The “Full mass” simulation shows the lowest maximum temperature with $T_{\text{cell,mean,max}} = 501.8$ °C, followed by the “Half mass” case with $T_{\text{cell,mean,max}} = 593.4$ °C. Assuming the jelly roll lost the vented mass before TR (“End mass”) results in $T_{\text{cell,mean,max}} = 731.8$ °C. Comparing these values to the mean of both experiments $T_{\text{cell,mean,max}} = 561.0$ °C shows that $T_{\text{cell,mean,max}}$ is lower compared to the experiments for the “Full mass” case and higher for the “Half mass” as well as the “End mass” case. This observed behavior can be explained by Eq. 15: with a given Q and c_p , less mass m leads to a higher ΔT .

Another possible cause for the deviations is the assumption of constant values for ρ_{JR} . There are previous studies which considered the mass loss during TR by implementing a time dependency.^{17,23,24,36,37} However, in the experiments, the investigated cells lose the vented mass over a time span of $t_{\text{venting}} = 17.7$ s (mean value). If it is considered that $t_{\text{venting}} \ll t_{\text{total}} = 2000$ s, the “End mass” case is replicating the reality for approximately the entire amount of t_{total} . Therefore, it is hypothesized that the influence of the time dependent character of Δm_{cell} is negligible. Nevertheless, the heat dissipation behavior for this case is not matching the experimental data. A possible reason is the assumption of the specific heat capacity of the jelly roll $c_{p,\text{JR}}$ being constant. Considering, in particular, that $c_{p,\text{JR}}$ increases with rising temperatures,³⁹ both the “Half mass” and “End mass” case show potential to be in better agreement with the experiments. A modeling of the full jelly roll mass is not reasonable as ΔT would be even lower.

Figure 6b shows the temperature increase over time t for the copper block. For the “Full mass” and the “Half mass” case, this increase in temperature is slower compared to the experiments,



(a)



(b)

Figure 6. (a) Mean cell can temperature $T_{\text{cell,mean}}$ over time t since nail penetration for both experiments (black and black dashed) and the three simulations with different densities ρ_{JR} (colored). (b) Mean copper temperature $T_{\text{Cu,mean}}$ over time t since nail penetration for both experiments (black and black dashed) and the three simulations with different densities ρ_{JR} (colored).

whereas the temperature increase of the “End mass” case is faster. Quantifying the deviation at $t = 500$ s results in

$$\Delta T_{\text{Cu,mean,500 s}} = \begin{cases} -6.3 \text{ K} & \text{for the “Full mass” case,} \\ -1.8 \text{ K} & \text{for the “Half mass” case, and} \\ 3.1 \text{ K} & \text{for the “End mass” case.} \end{cases}$$

Consequently, the “Half mass” case shows the smallest deviation from the experiments. This is confirmed by analyzing the MAPE and RMSPE (see Table VI). However, if it is taken into account that $c_{p,\text{JR}}$ is assumed constant instead of temperature dependent, it is not reasonable to model the “Full mass” or the “Half mass” case. This would result in the copper temperatures being lower and consequently in an underestimation of the heat transfer to adjacent components. This is a problem, in particular, for TR propagation simulations as the predicted propagation time would be higher compared to reality and hence would give a distorted impression of safety. Therefore, the “End mass” case is used as a baseline for further sensitivity analysis.

Table VI. Mean absolute percentage error (MAPE) and root mean square percentage error (RMSPE) between mean cell can temperature and mean copper temperature of the simulations and the mean experimental data.

No.	Name	MAPE $T_{\text{cell,mean}}$ [%]	MAPE $T_{\text{Cu,mean}}$ [%]	RMSPE $T_{\text{cell,mean}}$ [%]	RMSPE $T_{\text{Cu,mean}}$ [%]
1	Full mass	5.9	6.6	7.0	8.1
2	Half mass	4.2	2.1	4.9	3.1
3	End mass	14.2	2.9	16.2	3.9
4	$c_{p,\text{JR,max}} = 1200$	9.3	1.2	10.6	1.7
5	$c_{p,\text{JR,max}} = 1400$	4.8	1.1	5.6	2.1
6	$c_{p,\text{JR,max}} = 1600$	1.4	2.4	2.5	3.8
7	$\lambda_{\text{JR}} = 0.517$	2.7	3.3	4.0	4.9
8	$\lambda_{\text{JR}} = 2.068$	9.7	1.4	11.0	1.8

In conclusion, the mass loss during TR has to be considered in the simulation model to reproduce the experimental results. The “End mass” case shows the highest potential, although both the cell and copper block temperatures are higher than the experimental results. However, when accounting for a specific heat capacity of the jelly roll that increases with rising temperatures, the temperatures are lowered.

Specific heat capacity of the jelly roll.—Figure 7 shows the mean cell can temperature $T_{\text{cell,mean}}$ (Fig. 7a) as well as the mean copper temperature $T_{\text{Cu,mean}}$ (Fig. 7b) over time t since nail penetration for both experiments (black and black dashed) and the four simulations with different specific heat capacities of the jelly roll $c_{p,\text{JR}}$. It should be pointed out that all shown simulations are calculated with $\rho_{\text{JR}} = 1360.1 \text{ kg m}^{-3}$ and therefore assume the cell to have the mass after a TR (“End mass” case).

As shown in Fig. 7a, $c_{p,\text{JR}}$ has a similar influence on the investigated temperatures as ρ_{JR} , although $c_{p,\text{JR}}$ is depending on temperature instead of being constant as ρ_{JR} . The maximum mean cell can temperature $T_{\text{cell,mean,max}}$ is reduced by adding a temperature dependency for $c_{p,\text{JR}}$:

$$T_{\text{cell,mean,max}} = \begin{cases} 731.8 \text{ }^\circ\text{C} & \text{for } c_{p,\text{JR}} = \text{const.} = 1000 \text{ J kg}^{-1} \text{ K}^{-1}, \\ 666.5 \text{ }^\circ\text{C} & \text{for } c_{p,\text{JR,max}} = 1200 \text{ J kg}^{-1} \text{ K}^{-1}, \\ 614.6 \text{ }^\circ\text{C} & \text{for } c_{p,\text{JR,max}} = 1400 \text{ J kg}^{-1} \text{ K}^{-1}, \text{ and} \\ 572.9 \text{ }^\circ\text{C} & \text{for } c_{p,\text{JR,max}} = 1600 \text{ J kg}^{-1} \text{ K}^{-1}. \end{cases}$$

Comparing these values to the experimental data results in the temperature of the $c_{p,\text{JR,max}} = 1600 \text{ J kg}^{-1} \text{ K}^{-1}$ case to be in-between both experiments. For the other cases, $T_{\text{cell,mean,max}}$ is higher than both experiments. Interestingly, comparing the constant $c_{p,\text{JR}}$ (orange) to the temperature dependent $c_{p,\text{JR}}$ (green, blue and red) shows no significant difference in the course of the mean temperature curve of the cell can. This can be explained as follows: the temperature dependent curves of $c_{p,\text{JR}}$ differ in a temperature range of approximately $40 \text{ }^\circ\text{C} < T < 120 \text{ }^\circ\text{C}$ (compare Fig. 3). The experimental data shows that the mean temperature is outside of this range at $t \approx 4 \text{ s}$. Consequently, the $c_{p,\text{JR}}$ -curves are in the constant regime for a large amount of the simulation time and therefore, the temperature dependency has only a minor effect. Nevertheless, $T_{\text{cell,mean,max}}$ can be lowered by increasing $c_{p,\text{JR,max}}$. At the same time, the heat dissipation and therefore, the temperature decrease of the cell slows down. This behavior was also observed in a previous study.²⁷

Figure 7b shows the effect of $c_{p,\text{JR}}$ on $T_{\text{Cu,mean}}$. An increasing $c_{p,\text{JR,max}}$ leads to a slower increase of $T_{\text{Cu,mean}}$ as the cell temperatures are lower and therefore, the driving force of the heat transfer, which is the temperature difference between cell surface and copper

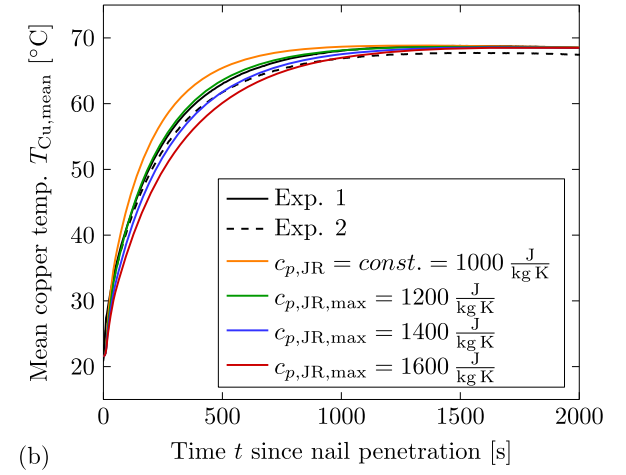
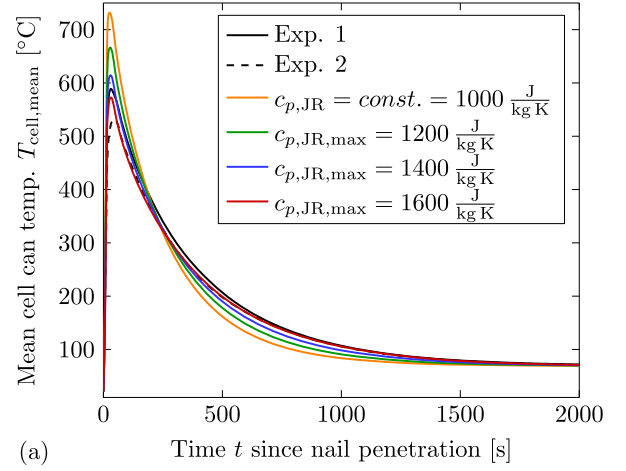


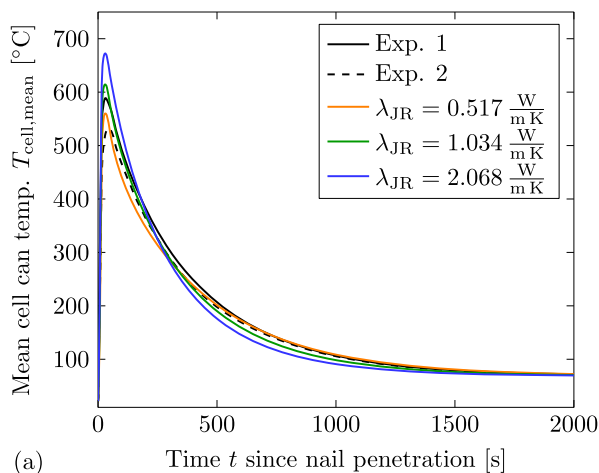
Figure 7. (a) Mean cell can temperature $T_{\text{cell,mean}}$ over time t since nail penetration for both experiments (black and black dashed) and the 4 simulations with different specific heat capacity of the jelly roll $c_{p,\text{JR}}$ (colored). (b) Mean copper temperature $T_{\text{Cu,mean}}$ over time t since nail penetration for both experiments (black and black dashed) and the 4 simulations with different specific heat capacity of the jelly roll $c_{p,\text{JR}}$ (colored).

block, is smaller. Quantifying the deviation at $t = 500 \text{ s}$ results in

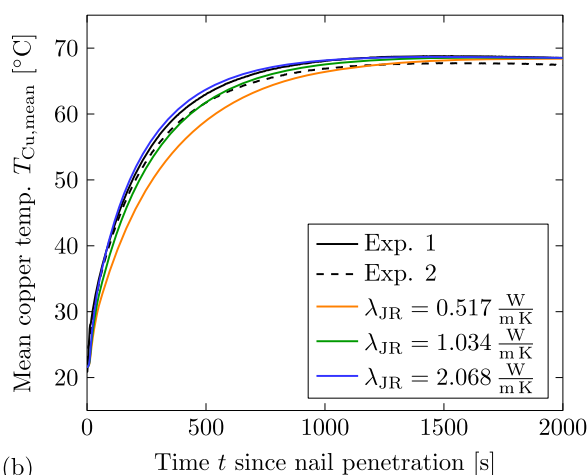
$$\Delta T_{\text{Cu,mean,500 s}} = \begin{cases} 3.1 \text{ K} & \text{for } c_{p,\text{JR}} = \text{const.} = 1000 \text{ J kg}^{-1} \text{ K}^{-1}, \\ 1.3 \text{ K} & \text{for the } c_{p,\text{JR,max}} = 1200 \text{ J kg}^{-1} \text{ K}^{-1} \text{ case,} \\ -0.6 \text{ K} & \text{for the } c_{p,\text{JR,max}} = 1400 \text{ J kg}^{-1} \text{ K}^{-1} \text{ case, and} \\ -2.3 \text{ K} & \text{for the } c_{p,\text{JR,max}} = 1600 \text{ J kg}^{-1} \text{ K}^{-1}. \end{cases}$$

Consequently, the case with $c_{p,\text{JR,max}} = 1400 \text{ J kg}^{-1} \text{ K}^{-1}$ shows the smallest deviation. Taking into account the MAPE and RMSPE values confirms this result for $T_{\text{Cu,mean}}$, whereas for $T_{\text{cell,mean}}$ the case with $c_{p,\text{JR,max}} = 1600 \text{ J kg}^{-1} \text{ K}^{-1}$ shows the smallest deviation from the experimental data (compare Table VI).

In conclusion, the specific heat capacity of the jelly roll is found to have a strong impact on the temperatures during TR. The curve with $c_{p,\text{JR,max}} = 1400 \text{ J kg}^{-1} \text{ K}^{-1}$ is assumed to be the best fit to the test results. Although the mean cell temperature is not matching as good as for the $c_{p,\text{JR,max}} = 1600 \text{ J kg}^{-1} \text{ K}^{-1}$ case, the mean copper block temperature is in better agreement. Therefore,



(a)



(b)

Figure 8. (a) Mean cell can temperature $T_{\text{cell,mean}}$ over time t since nail penetration for both experiments (black and black dashed) and the three simulations with different through-plane thermal conductivity of the jelly roll λ_{JR} (colored). (b) Mean copper temperature $T_{\text{Cu,mean}}$ over time t since nail penetration for both experiments (black and black dashed) and the three simulations with different through-plane thermal conductivity of the jelly roll λ_{JR} (colored).

$c_{p,\text{JR,max}} = 1400 \text{ J kg}^{-1} \text{ K}^{-1}$ is set as baseline for the further parameter study.

Thermal conductivity of the jelly roll.—Figure 8 shows the mean cell can temperature $T_{\text{cell,mean}}$ (Fig. 8a) as well as the mean copper temperature $T_{\text{Cu,mean}}$ (Fig. 8b) over time t since nail penetration for both experiments (black and black dashed) and the three simulations with different through-plane thermal conductivity of the jelly roll λ_{JR} (colored). It should be pointed out that all shown simulations are calculated with $\rho_{\text{JR}} = 1360.1 \text{ kg m}^{-3}$ and $c_{p,\text{JR}}(T)$ with $c_{p,\text{JR,max}} = 1400 \text{ J kg}^{-1} \text{ K}^{-1}$.

As shown in Fig. 8a, a variation of λ_{JR} (through-plane) has the same effect on the simulation results as a variation of ρ_{JR} or $c_{p,\text{JR}}$. The baseline case with $\lambda_{\text{JR}} = 1.034 \text{ W m}^{-1} \text{ K}^{-1}$ results in $T_{\text{cell,mean,max}} = 614.6 \text{ °C}$. Reducing the thermal conductivity to $\lambda_{\text{JR}} = 0.517 \text{ W m}^{-1} \text{ K}^{-1}$ shows a reduction of the maximum mean cell can temperature to $T_{\text{cell,mean,max}} = 560.2 \text{ °C}$, whereas an increase to $\lambda_{\text{JR}} = 2.068 \text{ W m}^{-1} \text{ K}^{-1}$ leads to $T_{\text{cell,mean,max}} = 672.5 \text{ °C}$. Consequently, increasing λ_{JR} leads to higher temperatures at the

cell can. At the same time, this results in lower core temperatures as shown in previous studies.^{27,42} This behavior can be explained by a higher heat conduction from the center of the jelly roll to the cell can. In contrast, reducing λ_{JR} slows down the internal jelly roll heat conduction and therefore, the heat is dissipated slower. In comparison to the experiments, the low thermal conductivity is in best agreement for $T_{\text{cell,mean}}$ (compare Table VI).

Figure 8b shows the effect of λ_{JR} on $T_{\text{Cu,mean}}$. A reduction of λ_{JR} leads to a slower increase of $T_{\text{Cu,mean}}$, as the heat released in the jelly roll is transferred slower to the cell can and eventually to the copper block. High values of λ_{JR} consequently lead to a faster increase of $T_{\text{Cu,mean}}$. Quantifying the deviation $t = 500 \text{ s}$ results in

$$\Delta T_{\text{Cu,mean},500 \text{ s}} = \begin{cases} -3.4 \text{ K} & \text{for } \lambda_{\text{JR}} = 0.517 \text{ W m}^{-1} \text{ K}^{-1}, \\ -0.6 \text{ K} & \text{for } \lambda_{\text{JR}} = 1.034 \text{ W m}^{-1} \text{ K}^{-1}, \text{ and} \\ 1.4 \text{ K} & \text{for } \lambda_{\text{JR}} = 2.068 \text{ W m}^{-1} \text{ K}^{-1}. \end{cases}$$

The case with $\lambda_{\text{JR}} = 1.034 \text{ W m}^{-1} \text{ K}^{-1}$ shows the smallest deviation between simulation and test results. Taking into account the MAPE and RMSPE values does confirm this observation for $T_{\text{Cu,mean}}$, whereas for $T_{\text{cell,mean}}$ the case with $\lambda_{\text{JR}} = 0.517 \text{ W m}^{-1} \text{ K}^{-1}$ shows the smallest deviation from the experimental data (compare Table VI).

In conclusion, the through-plane thermal conductivity is found to have a significant influence on the temperatures during TR. For the investigated case, a lower λ_{JR} leads to better results for $T_{\text{cell,mean}}$, but the temperature increase of the copper block is too slow. Therefore, a thermal conductivity of $\lambda_{\text{JR}} = 1.034 \text{ W m}^{-1} \text{ K}^{-1}$ is used for the subsequent comparison of modeling approaches for the heat release during TR.

In summary, all of the three investigated parameters show a similar influence on the simulation results. Consequently, there are various possibilities to fit the simulation results to experimental data. However, the authors recommend to choose the investigated parameters within a physically reasonable range and want to stress that further experimental studies on temperature dependent material parameters of the jelly roll in the temperature range of a TR are crucial for the improvement of TR simulation accuracy.

Modeling approaches for heat release during TR.—For the following comparison of different modeling approaches for heat release during TR the following parameter set is used:

- $\rho_{\text{JR}} = 1360.1 \text{ kg m}^{-3}$ (“End mass” case),
- $c_{p,\text{JR}}(T)$ with $c_{p,\text{JR,max}} = 1400 \text{ J kg}^{-1} \text{ K}^{-1}$, and
- $\lambda_{\text{JR}} = 1.034 \text{ W m}^{-1} \text{ K}^{-1}$.

Mean temperature curves.—Figure 9 shows the mean cell temperature $T_{\text{cell,mean}}$ (Fig. 9a) as well as the mean copper temperature $T_{\text{Cu,mean}}$ (Fig. 9b) over time t since nail penetration for both experiments (black and black dashed) and the three simulations with different modeling approaches for heat release during TR \dot{Q} (colored). It should be pointed out that all shown simulations are calculated with $\rho_{\text{JR}} = 1360.1 \text{ kg m}^{-3}$, $c_{p,\text{JR}}(T)$ with $c_{p,\text{JR,max}} = 1400 \text{ J kg}^{-1} \text{ K}^{-1}$ (see Fig. 3), and $\lambda_{\text{JR}} = 1.034 \text{ W m}^{-1} \text{ K}^{-1}$.

As shown in Fig. 9a, the modeling approach of heat release during TR has a minor influence on the temperature curves for $t \gg 0$. This is explained by the short duration of heat release compared to the heat dissipation process. However, there is an influence on the maximum mean cell temperatures: method 1 shows the lowest temperatures with $T_{\text{cell,mean,max}} = 614.6 \text{ °C}$, followed by method 2 with $T_{\text{cell,mean,max}} = 620.8 \text{ °C}$, and method 3 with $T_{\text{cell,mean,max}} = 691.8 \text{ °C}$.

Figure 9b shows the temperature increase over time t for the copper block. As also observed for $T_{\text{cell,mean}}$, the modeling approach of heat release during TR has a minor influence on $T_{\text{Cu,mean}}$ for $t \gg 0$. Comparing the MAPE and RMSPE values confirms this observation (compare Table VII), as the difference between the

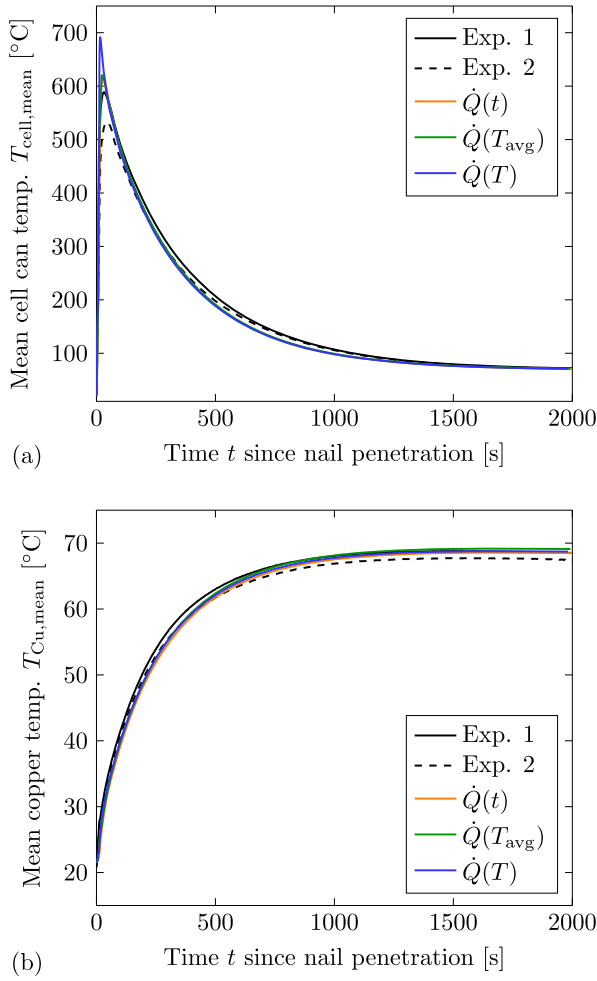


Figure 9. (a) Mean cell can temperature $T_{\text{cell,mean}}$ over time t since nail penetration for both experiments (black and black dashed) and the three simulations with different modeling approaches for heat release during TR (colored). (b) Mean copper temperature $T_{\text{Cu,mean}}$ over time t since nail penetration for both experiments (black and black dashed) and the three simulations with different modeling approaches for heat release during TR (colored).

Table VII. Mean absolute percentage error (MAPE) and root mean square percentage error (RMSPE) between mean cell can temperature and mean copper temperature of the simulations and the mean experimental data.

No.	Name	MAPE $T_{\text{cell,mean}}$ [%]	MAPE $T_{\text{Cu,mean}}$ [%]	RMSPE $T_{\text{cell,mean}}$ [%]	RMSPE $T_{\text{Cu,mean}}$ [%]
Method 1	$\dot{Q}(t)$	4.8	1.1	5.6	2.1
Method 2	$\dot{Q}(T_{\text{avg}})$	4.4	1.4	6.2	1.7
Method 3	$\dot{Q}(T)$	5.3	0.9	7.6	1.3

three methods is $\Delta\text{MAPE}_{\text{cell,mean}} = 0.9\%$ for the cell and $\Delta\text{MAPE}_{\text{Cu,mean}} = 0.5\%$ for the copper block. The difference for the RMSPE is slightly higher with $\Delta\text{RMSPE}_{\text{cell,mean}} = 2.0\%$ for the cell and $\Delta\text{MAPE}_{\text{Cu,mean}} = 0.8\%$ for the copper block. Therefore, it is concluded that for processes with focus on the heat dissipation after a TR ($t \gg 0$) it is more critical to ensure a correct

implementation of boundary parameters such as mass loss during TR or material parameters of the jelly roll than to precisely model the time dependent character of heat release. However, if the focus is on the single cell and its TR process, the modeling approach of heat release can be of significant importance.

Single sensor temperature curves.—Figure 10 shows the cell can temperatures $T_{\text{cell},k}$ at the positions k (Figs. 10a–10e) as well as the copper temperatures $T_{\text{Cu},k}$ at the equivalent positions k (Figs. 10f–10j) over time t since nail penetration for both experiments (black and black dashed) and the three simulations with different modeling approaches for the heat release during TR \dot{Q} (colored). It should be pointed out that all shown simulations are calculated with $\rho_{\text{JR}} = 1360.1 \text{ kg m}^{-3}$, $c_{p,\text{JR}}(T)$ with $c_{p,\text{JR,max}} = 1400 \text{ J kg}^{-1} \text{ K}^{-1}$ (see Fig. 3), and $\lambda_{\text{JR}} = 1.034 \text{ W m}^{-1} \text{ K}^{-1}$. In addition, Table VIII summarizes the three characteristics for sensor curve comparison as described above.

Figure 10a presents the cell can temperature on the nailed side with a focus on the time span of the TR and the early heat dissipation. There is a high deviation between both experiments for this certain position. The data of experiment 1 shows temperatures that are approximately 200 °C higher compared to experiment 2. A possible reason for this behavior is that gas vented through the nail penetration hole and influenced the temperature measurement. Therefore, only experiment 2 is considered to show plausible results for this particular position.

In contrast to the long term behavior, the focus on the first seconds after nail penetration reveals clear differences between the single modeling approaches. The temperature increase on the nail side starts earlier compared to the experiment for all three modeling approaches (compare Fig. 10a and Table VIII). Method 2 stands out in particular: as the initial temperature of one jelly roll has to be set high enough to trigger the heat source, the temperature at $t = 0 \text{ s}$ is already at an elevated level. With respect to the maximum temperature T_{max} , method 1 only shows a small deviation, whereas method 2 and 3 result in higher values. Analyzing the mean temperature gradient $\Delta T/\Delta t$ leads to method 3 being in best agreement with the experiment, while the temperature increase of method 2 and, in particular, method 1 is too low for the sensor on the nailed side.

This observed behavior can be explained by the different modeling approaches. The more heat is released in less time, the higher the maximum temperature becomes due to less time for heat dissipation. For method 1, the total “heating power” of the jelly roll is directly set by the modeling approach with a maximum of $\dot{Q}_{\text{M1,max}} \approx 63 \text{ kW}$ at $t = \frac{1}{2}t_{\text{venting}}$ (see Fig. 4). For method 2, the maximum power is defined as $\dot{Q}_{\text{M2,x,max}} = 31177 \text{ W}$, but it can occur in each of the four jelly roll parts independently. For the specific case presented in this paper, only two jelly roll parts release heat at the same time, which leads to $\dot{Q}_{\text{M2,max}} = 2 \dot{Q}_{\text{M2,x,max}} \approx 62 \text{ kW}$. This maximum value is already reached at $t \approx 6 \text{ s}$ and therefore, the gradient is higher compared to method 1. In addition, the duration of heat release for method 2 is $\Delta t_{\text{M2,heating}} \approx 21 \text{ s}$, while the total time of heat release for method 1 is set to $\Delta t_{\text{M1,heating}} = 39.9 \text{ s}$. The duration of heat release for method 3 is $\Delta t_{\text{M3,heating}} \approx 12 \text{ s}$, which leads to a maximum “heating power” of $\dot{Q}_{\text{M3,max}} \approx 110 \text{ kW}$ and hence the highest temperature gradient as well as maximum temperature.

Focusing on the other positions on the cell can and comparing the begin of temperature increase reveal a disadvantage of method 1: Due to the time dependent heat release in the whole jelly roll material, the temperature increase starts to early, especially on the short sides and the opposite side of nailing (compare Figs. 10a–10e and Table VIII). For method 2, the begin of temperature increase fits to the experimental data. Although both method 1 and 2 release the heat homogeneously, method 2 triggers the second jelly roll not as

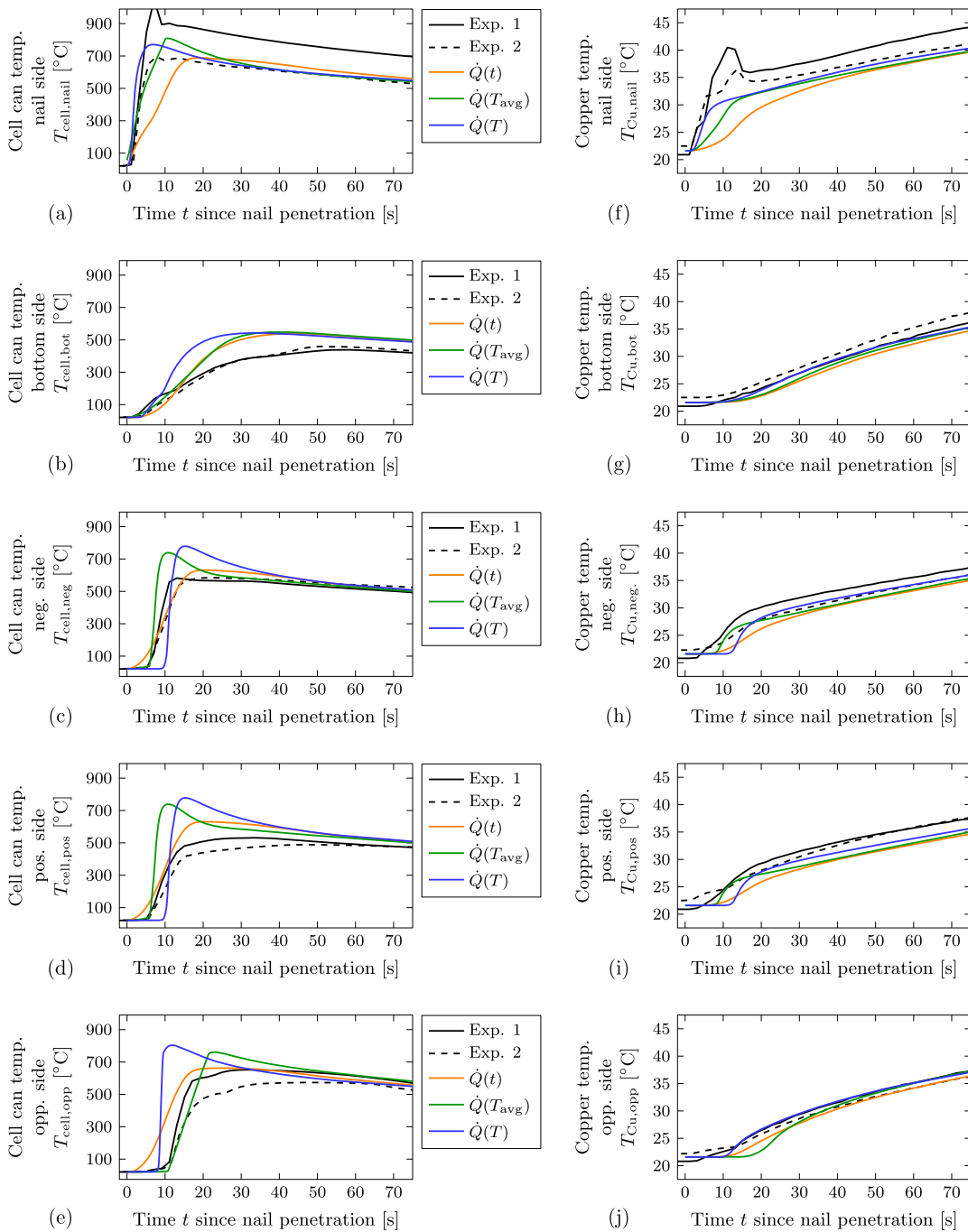


Figure 10. (a)–(e) Cell can temperature $T_{cell,k}$ at positions k over time t since nail penetration for both experiments (black and black dashed) and the three simulations with different modeling approaches for heat release during TR \dot{Q} (colored). (f)–(j) Copper block temperature $T_{Cu,k}$ at positions k over time t since nail penetration for both experiments (black and black dashed) and the three simulations with different modeling approaches for heat release during TR \dot{Q} (colored).

fast as method 1. This is due to the different trigger mechanisms. For method 1, the maximum temperature is decisive for the begin of heat release, while method 2 uses the volume averaged temperature of the jelly roll as trigger criterion. Therefore, the second jelly roll is triggered at a later point in time and consequently the temperature on the opposite side of nailing increases later. The heat release of method 3 is spatially resolved and therefore, the TR reaction is

propagating through the jelly roll in form of a reaction front. The velocity of this front is mainly depending on the reaction rate C .²⁰ On the one hand, decreasing the reaction rate C would help to match the simulation results with the sensor on the opposite side of nailing, but on the other hand it would also shift the short sides to a later point in time. That is why it is hypothesized, that the reaction rate is actually direction dependent, that means that the through-plane

Table VIII. Comparison of temperature curve characteristics of each sensor on the cell can for both experiments and the three different modeling approaches for heat release during TR.

Cell can temperature on nail side $T_{\text{cell,nail}}$				
No.	Name	Time t_{begin} at $T > 50$ °C	T_{max}	Mean $\Delta T/\Delta t$
Exp. 1	—	$t = 1.3$ s	faulty	faulty
Exp. 2	—	$t = 1.7$ s	696 °C	135 K s ⁻¹
Method 1	$\dot{Q}(t)$	$t = 0.7$ s	688 °C	37 K s ⁻¹
Method 2	$\dot{Q}(T_{\text{avg}})$	$t = 0.0$ s	809 °C	71 K s ⁻¹
Method 3	$\dot{Q}(T)$	$t = 0.7$ s	771 °C	122 K s ⁻¹
Cell can temperature on bottom side $T_{\text{cell,bot}}$				
Exp. 1	—	$t = 3.4$ s	439 °C	8 K s ⁻¹
Exp. 2	—	$t = 5.3$ s	460 °C	10 K s ⁻¹
Method 1	$\dot{Q}(t)$	$t = 6.9$ s	538 °C	14 K s ⁻¹
Method 2	$\dot{Q}(T_{\text{avg}})$	$t = 4.3$ s	548 °C	15 K s ⁻¹
Method 3	$\dot{Q}(T)$	$t = 4.8$ s	543 °C	18 K s ⁻¹
Cell can temperature on side of negative terminal $T_{\text{cell,neg}}$				
Exp. 1	—	$t = 6.3$ s	582 °C	94 K s ⁻¹
Exp. 2	—	$t = 5.9$ s	585 °C	37 K s ⁻¹
Method 1	$\dot{Q}(t)$	$t = 3.0$ s	631 °C	35 K s ⁻¹
Method 2	$\dot{Q}(T_{\text{avg}})$	$t = 6.0$ s	740 °C	148 K s ⁻¹
Method 3	$\dot{Q}(T)$	$t = 9.9$ s	779 °C	141 K s ⁻¹
Cell can temperature on side of positive terminal $T_{\text{cell,pos}}$				
Exp. 1	—	$t = 6.2$ s	531 °C	20 K s ⁻¹
Exp. 2	—	$t = 6.4$ s	489 °C	12 K s ⁻¹
Method 1	$\dot{Q}(t)$	$t = 3.0$ s	631 °C	34 K s ⁻¹
Method 2	$\dot{Q}(T_{\text{avg}})$	$t = 6.0$ s	740 °C	147 K s ⁻¹
Method 3	$\dot{Q}(T)$	$t = 9.9$ s	779 °C	141 K s ⁻¹
Cell can temperature on opposite side of nailing $T_{\text{cell,opp}}$				
Exp. 1	—	$t = 10.1$ s	652 °C	32 K s ⁻¹
Exp. 2	—	$t = 10.5$ s	573 °C	15 K s ⁻¹
Method 1	$\dot{Q}(t)$	$t = 3.4$ s	662 °C	30 K s ⁻¹
Method 2	$\dot{Q}(T_{\text{avg}})$	$t = 11.2$ s	761 °C	63 K s ⁻¹
Method 3	$\dot{Q}(T)$	$t = 8.3$ s	804 °C	214 K s ⁻¹

direction is too fast in this case, but the in-plane direction is too slow. Another possible reason is a wrong assumption for the in-plane thermal conductivity of the jelly roll, as the latter also has an influence on the velocity of the reaction front.²⁰

Comparing the maximum temperatures of simulations and experiments shows that method 2 and method 3 overestimate T_{max} for all sensor positions on the cell can. However, this overestimation is occurring as a temperature peak and therefore, the deviation exists only over a short amount of time. Method 1 better estimates the maximum temperatures.

The mean temperature gradient $\Delta T/\Delta t$ of method 1 shows in general the smallest deviations, but there is still room for improvement, such as the nail side sensor (compare Figs. 10b–10e and Table VIII). Method 2 results in higher gradients compared to the experiments except for the sensor on the nailed side, which is directly depending on $\dot{Q}_{M2,x,\text{max}} = 31177$ W. Consequently, this value is assumed to be too high. Method 3 shows the highest mean $\Delta T/\Delta t$ except for the short sides. Therefore, the reaction rate during TR $C = 1$ s⁻¹ is also assumed to be too high.

Figures 10f–10j shows the copper block temperatures at the given positions with a focus on the time span of TR and the early temperature increase. The observations on the cell side also match to the behavior on the copper block side. A fast temperature increase on the cell side leads to a fast temperature increase on the copper block side. Except for the nailed side, all three simulation methods are in good agreement with the experimental results. As stated before, on the nailed side, there may be some deviations due to the venting gases flowing out of the nail penetration hole.

There are further observations that have an influence on the results of all three methods:

- Melting of the aluminum can is not considered in the model. Especially on the nailed side the temperature sensors show temperatures higher than the melting point of aluminum and therefore, the phase change of the can absorbs additional heat.
- The assumptions for the material parameters of the bottom insulator may be inaccurate, for example there is no temperature dependency implemented in the simulation model. A rising specific heat capacity of the bottom insulator with increasing temperature would result in lower temperatures.
- Internal venting gas flow is not considered. This could either cause an additional convective heat transfer to the cell can or transport energy out of the cell through the vent.
- A possible reason for the difference of positive and negative side in the experiments is the different material of the current collectors. It is safe to conclude, that for the negative side (copper current collector) the heat transfer into the side of the can is higher, as the thermal conductivity is higher compared to aluminum. In addition, the specific heat capacity of copper is lower compared to aluminum. A third possible reason is the melting of the aluminum current collector which results in a heat dissipation due to the phase change. As the simulation model is symmetrical (except from the material of the simplified terminals) there is no significant difference between the simulation results on the short cell sides and hence, this behavior cannot be replicated.
- The gas and particle flow out of the vent is not considered in the simulation model. Both could result in an additional heat transfer

Table IX. Comparison of the modeling approaches for heat release during TR.

Criteria	Method 1 $\dot{Q}(t)$	Method 2 $\dot{Q}(T_{\text{avg}})$	Method 3 $\dot{Q}(T)$
Accuracy ϵ_Q	0.60%	1.91%	1.06%
Time step Δt_{step}	0.05 s	0.02 s	0.005 s
Computational time Δt_{sim}	9954 s	36091 s	149555 s
Needed input parameters	• Q_1 • T_{TR}	• Q_1 • $\dot{Q}_{\text{ARC}}(T)$	• Q_1 • $\dot{Q}_{\text{ARC}}(T)$ • T_{TR} • T_{onset} • C
(Optional) fitting parameters	• t_{venting} • t_{heating} • α_{nail}	• T_{onset} • T_{TR} • $\dot{Q}_{\text{M2},x,\text{max}}$	• α_{nail}
Miscellaneous	Lowest computational effort	Easy to implement and parameterize, but high initial temperature necessary	Spatial resolution of TR reaction, but small time step necessary

to the copper block, for example (hot) particles rebounding from the retainer and sticking to the copper block or convective heat transfer from gas to the retainer and subsequent heat conduction into the copper block.

In conclusion, all modeling approaches are able to replicate the TR behavior in the autoclave calorimetry experiment. However, all methods show potential for further improvement, which can be achieved by adapting the heat source parameters. Another opportunity for improvement of the simulation results are temperature dependent material parameters for all components or the consideration of melting.

Comparison of the modeling approaches.—Table IX compares the modeling approaches for heat generation during TR regarding the accuracy ϵ_Q according to Eq. 36, the needed time step Δt_{step} to reach this accuracy, and the total computational time Δt_{sim} needed for the simulation. In addition, the input as well as the fitting parameters and further advantages or disadvantages are summarized.

Method 1 shows the best accuracy ϵ_Q with the biggest time step Δt_{step} and therefore, the lowest computational time. To maintain $\epsilon_Q < 2\%$ for method 2 and 3, the time step has to be reduced and subsequently the computational time is longer. The number of needed input parameters is higher for method 3 in comparison to method 1 and 2. However, all input parameters can be estimated by a calorimetric measurement of Q_1 and an ARC test with the heat-wait-see method. The main advantage of method 1 is the low computational effort and therefore, it is suitable for simulations of large models such as battery packs. On the other hand, unlike the other methods, method 1 is not able to reproduce the self-heating of the battery cell that occurs for $T_{\text{onset}} < T < T_{\text{TR}}$. Whether this is crucial for TR propagation simulation needs to be investigated in further work. Method 2 is easy to implement and parameterization requires a minor effort, as all fitting parameters can be estimated by ARC tests. However, the necessity of a high initial temperature can cause deviations. Method 3 is the only method that is able to model a spatial resolution of the TR reaction, but requires a higher computational time.

Conclusions

The presented study compares three different modeling approaches for the heat release during TR of a prismatic lithium-ion battery (>60 Ah) tested in the autoclave calorimetry experiment. More specifically, the deviations of the simulated temperature curves from experimental results are investigated and the accuracy as well as the computational effort of the modeling approaches are compared. In addition, the influence of the parameters mass loss during TR, specific heat capacity of the jelly roll, and (through-plane)

thermal conductivity of the jelly roll on the simulation results is presented.

Mass loss during TR.—

- The mass loss during TR Δm_{cell} has a major influence on the simulation results and consequently has to be considered in TR simulations of a lithium-ion battery. One possibility to do so is an adaption of the jelly roll's density to match the mass after TR.
- For the particular case investigated in this study, the time dependency of this mass loss can be neglected. However, a time dependent adaption of the mass during TR could further improve the simulation results and should be investigated in the future.

Specific heat capacity of the jelly roll.—

- The specific heat capacity of the jelly roll has a similar effect on the simulation results as the mass loss during TR.
- The temperature dependent character is useful to fit simulation results to experimental data.
- However, there are no experimental measurements in the temperature range of a TR. Further investigation is needed to improve the results of TR simulations.

Thermal conductivity of the jelly roll.—

- The through-plane thermal conductivity of the jelly roll shows the same influence on simulation results as the mass loss during TR and the specific heat capacity of the jelly roll.
- There is also a lack of experimental measurements in the temperature range of a TR. Therefore, a need of further studies is identified in order to facilitate more accurate TR simulations.

Modeling approaches for heat release during TR.—

- The effect of different modeling approaches for heat release during TR is only significant during the time range of the TR ($t < t_{\text{heating}}$). If the focus of the simulation is on large time scales ($t \gg t_{\text{heating}}$), such as TR propagation simulation, the deviations between the single methods are negligible.
- Further investigation and parameter adaption is necessary for all three methods to better match the experimental results within the time range of the TR.
- A time dependent and uniform heat release (method 1) is recommended for TR propagation simulations with expected large time spans between the single TRs, as the computational effort is

significantly lower compared to the other temperature dependent methods.

• Further investigations will focus on the confirmation of this hypothesis by applying all three approaches to TR propagation simulations.

In conclusion, choosing a suitable modeling approach for the heat release during TR depends on the specific application and the objective of the simulation. The results of this study point out the advantages and disadvantages of the investigated modeling approaches and crucial modeling parameters are identified. Furthermore, the authors want to stress the necessity of additional experimental investigations regarding material parameters in the TR temperature range. The results contribute to the improvement of both TR as well as TR propagation simulations and therefore help researchers and engineers to choose a suitable model for designing safer battery packs.

Acknowledgments

The authors would like to gratefully acknowledge the support of the Fraunhofer Institute for Chemical Technology (ICT), Pfinztal, Germany for the development and execution of the autoclave calorimetry measurements as well as the support of the Institute for Applied Materials - Applied Materials Physics of the Karlsruhe Institute of Technology, Eggenstein-Leopoldshafen, Germany for the execution of the accelerating rate calorimetry and heat capacity measurements. In addition, S. Hoelle acknowledges the support of the TUM Graduate School.

ORCID

S. Hoelle  <https://orcid.org/0000-0002-6381-8104>
 S. Zimmermann  <https://orcid.org/0000-0002-1399-9242>
 O. Hinrichsen  <https://orcid.org/0000-0002-3796-6920>

References

1. T. Nagaura, "Development of rechargeable lithium batteries. II. Lithium ion rechargeable batteries." *Progress in Batteries & Battery Materials*, **10**, 218 (1991).
2. Y. Chen and J. W. Evans, "Thermal analysis of lithium-ion batteries." *J. Electrochem. Soc.*, **143**, 2708 (1996).
3. J. Liu, J. Li, and J. Wang, "In-depth analysis on thermal hazards related research trends about lithium-ion batteries: a bibliometric study." *J. Energy Storage*, **35**, 102253 (2021).
4. X. Feng, M. Fang, X. He, M. Ouyang, L. Lu, H. Wang, and M. Zhang, "Thermal runaway features of large format prismatic lithium ion battery using extended volume accelerating rate calorimetry." *J. Power Sources*, **255**, 294 (2014).
5. A. W. Golubkov, D. Fuchs, J. Wagner, H. Wilsche, C. Stangl, G. Fauler, G. Voitic, A. Thaler, and V. Hacker, "Thermal-runaway experiments on consumer Li-ion batteries with metal-oxide and olivin-type cathodes." *RSC Adv.*, **4**, 3633 (2014).
6. D. P. Finegan et al., "In-operando high-speed tomography of lithium-ion batteries during thermal runaway." *Nat. Commun.*, **6**, 6924 (2015).
7. M. N. Richard and J. R. Dahn, "Accelerating rate calorimetry study on the thermal stability of lithium intercalated graphite in electrolyte. II. Modeling the results and predicting differential scanning calorimeter curves." *J. Electrochem. Soc.*, **146**, 2078 (1999).
8. T. D. Hatchard, D. D. MacNeil, A. Basu, and J. R. Dahn, "Thermal model of cylindrical and prismatic lithium-ion cells." *J. Electrochem. Soc.*, **148**, A755 (2001).
9. R. Spotnitz and J. Franklin, "Abuse behavior of high-power, lithium-ion cells." *J. Power Sources*, **113**, 81 (2003).
10. G.-H. Kim, A. Pesarani, and R. Spotnitz, "A three-dimensional thermal abuse model for lithium-ion cells." *J. Power Sources*, **170**, 476 (2007).
11. B. Liu, Y. Jia, C. Yuan, L. Wang, X. Gao, S. Yin, and J. Xu, "Safety issues and mechanisms of lithium-ion battery cell upon mechanical abusive loading: a review." *Energy Storage Materials*, **24**, 85 (2020).
12. F. Baakes, M. Lütke, M. Gerasimov, V. Laue, F. Röder, P. B. Balbuena, and U. Kreuer, "Unveiling the interactions of reactions and phase transition during thermal runaway abuse of Li-ion batteries." *J. Power Sources*, **522**, 230881 (2022).
13. C. Liu, H. Li, X. Kong, and J. Zhao, "Modeling analysis of the effect of battery design on internal short circuit hazard in LiNi_{0.8}Co_{0.1}Mn_{0.1}O₂/SiO_x-graphite lithium ion batteries." *Int. J. Heat and Mass Transfer*, **153**, 119590 (2020).
14. H. Chen, J. E. H. Bustin, J. Gill, D. Howard, R. C. E. Williams, E. Read, A. Abaza, B. Cooper, and J. X. Wen, "A simplified mathematical model for heating-induced thermal runaway of lithium-ion batteries." *J. Electrochem. Soc.*, **168**, 010502 (2021).
15. K. F. Yeow and H. Teng, "Characterizing thermal runaway of lithium-ion cells in a battery system using finite element analysis approach." *SAE Int. J. Alt Power*, **2**, 179 (2013).
16. M. Citarella, D. Suzzi, B. Brunstner, P. Schiffbänker, G. Maier, and J. Schneider, "Computational modelling of thermal runaway propagation in lithium-ion battery systems." *2019 IEEE Transportation Electrification Conference (ITEC-India)* (2019).
17. P. T. Coman, E. C. Darcy, and R. E. White, "Simplified thermal runaway model for assisting the design of a novel safe li-ion battery pack." *J. Electrochem. Soc.*, **169**, 040516 (2022).
18. X. Feng, L. Lu, M. Ouyang, J. Li, and X. He, "A 3D thermal runaway propagation model for a large format lithium ion battery module." *Energy*, **115**, 194 (2016).
19. C. Jin et al., "Model and experiments to investigate thermal runaway characterization of lithium-ion batteries induced by external heating method." *J. Power Sources*, **504**, 230065 (2021).
20. F. Zhang, X. Feng, C. Xu, F. Jiang, and M. Ouyang, "Thermal runaway front in failure propagation of long-shape lithium-ion battery." *Int. J. Heat and Mass Transfer*, **182**, 121928 (2022).
21. C. Yuan, Q. Wang, Y. Wang, and Y. Zhao, "Inhibition effect of different interstitial materials on thermal runaway propagation in the cylindrical lithium-ion battery module." *Appl. Thermal Eng.*, **153**, 39 (2019).
22. I. Lalinde, A. Berrueta, P. Sanchis, and A. Ursúa, "Applied method to model the thermal runaway of lithium-ion batteries." *2021 IEEE International Conference on Environment and Electrical Engineering and 2021 IEEE Industrial and Commercial Power Systems Europe (EEEIC/IC&CPS Europe)* (2021).
23. J. Kim, A. Mallarapu, D. P. Finegan, and S. Santhanagopalan, "Modeling cell venting and gas-phase reactions in 18650 lithium-ion batteries during thermal runaway." *J. Power Sources*, **489**, 229496 (2021).
24. X. Liu, Z. Wu, S. I. Stolarov, M. Denlinger, A. Masias, and K. Snyder, "A thermo-kinetic model of thermally-induced failure of a lithium ion battery: development, validation and application." *J. Electrochem. Soc.*, **165**, A2909 (2018).
25. S. Scharner, "Quantitative safety characterization of Li-ion cells." *JRC Exploratory Research Workshop 2018* accessed Dec 2021 <https://ec.europa.eu/jrc/sites/jrcsh/files/quantitative-safety-characterization-of-li-ion-cells.pdf>.
26. S. Hoelle, S. Scharner, S. Asanin, and O. Hinrichsen, "Analysis on thermal runaway behavior of prismatic Lithium-ion batteries with autoclave calorimetry." *J. Electrochem. Soc.*, **168**, 120515 (2021).
27. M. Parhizi, M. B. Ahmed, and A. Jain, "Determination of the core temperature of a Li-ion cell during thermal runaway." *J. Power Sources*, **370**, 27 (2017).
28. D. Mishra, K. Shah, and A. Jain, "Investigation of the impact of flow of vented gas on propagation of thermal runaway in a Li-ion battery pack." *J. Electrochem. Soc.*, **168**, 060555 (2021).
29. D. Mishra, K. Shah, and A. Jain, "Investigation of the impact of radiative shielding by internal partition walls on propagation of thermal runaway in a matrix of cylindrical Li-ion cells." *J. Electrochem. Soc.*, **168**, 120507 (2021).
30. D. Mishra and A. Jain, "Multi-mode heat transfer simulations of the onset and propagation of thermal runaway in a pack of cylindrical Li-ion cells." *J. Electrochem. Soc.*, **168**, 020504 (2021).
31. P. T. Coman, E. C. Darcy, C. T. Veje, and R. E. White, "Numerical analysis of heat propagation in a battery pack using a novel technology for triggering thermal runaway." *Appl. Energy*, **203**, 189 (2017).
32. J. Qin, S. Zhao, X. Liu, and Y. Liu, "Simulation study on thermal runaway suppression of 18650 lithium battery." *Energy Sources, Part A: Recovery, Utilization, and Environmental Effects*, **1** (2020).
33. D. Kong, G. Wang, P. Ping, and J. Wen, "Numerical investigation of thermal runaway behavior of lithium-ion batteries with different battery materials, and heating conditions." *Appl. Thermal Eng.*, **189**, 116661 (2021).
34. T. Yamanaka, Y. Takagishi, Y. Tozuka, and T. Yamaue, "Modeling lithium ion battery nail penetration tests and quantitative evaluation of the degree of combustion risk." *J. Power Sources*, **416**, 132 (2019).
35. M. P. Macdonald, S. Chandrasekaran, S. Garimella, and T. F. Fuller, "Thermal runaway in a prismatic lithium ion cell triggered by a short circuit." *J. Energy Storage*, **40**, 102737 (2021).
36. P. T. Coman, S. Rayman, and R. E. White, "A lumped model of venting during thermal runaway in a cylindrical Lithium Cobalt Oxide lithium-ion cell." *J. Power Sources*, **307**, 56 (2016).
37. J. K. Ostanek, W. Li, P. P. Mukherjee, K. R. Crompton, and C. Hacker, "Simulating onset and evolution of thermal runaway in Li-ion cells using a coupled thermal and venting model." *Appl. Energy*, **268**, 114972 (2020).
38. P. T. Coman, E. C. Darcy, C. T. Veje, and R. E. White, "Modelling Li-ion cell thermal runaway triggered by an internal short circuit device using an efficiency factor and arrhenius formulations." *J. Electrochem. Soc.*, **164**, A587 (2017).
39. M. Steinhart, J. V. Barreras, H. Ruan, B. Wu, G. J. Offer, and A. Jossen, "Meta-analysis of experimental results for heat capacity and thermal conductivity in lithium-ion batteries: a critical review." *J. Power Sources*, **522**, 230829 (2022).
40. M. Akbarzadeh, T. Kalogiannis, J. Jaguemont, J. He, L. Jin, M. Berecibar, and J. V. Mierlo, "Thermal modeling of a high-energy prismatic lithium-ion battery cell and module based on a new thermal characterization methodology." *J. Energy Storage*, **32**, 101707 (2020).
41. M. Steinhart, E. I. Gillich, M. Stiegler, and A. Jossen, "Thermal conductivity inside prismatic lithium-ion cells with dependencies on temperature and external compression pressure." *J. Energy Storage*, **32**, 101680 (2020).
42. Y. Li, Z. Zhou, and W.-T. Wu, "Three-dimensional thermal modeling of internal shorting process in a 20 Ah Lithium-ion polymer battery." *Energies*, **13**, 1013 (2020).

3 Thermal Propagation Behavior of Lithium-Ion Battery Cell Stacks

If a cell failure occurs within a lithium-ion battery pack, the heat released during a single cell TR potentially triggers further TRs in neighboring cells and hence a TP emerges. As described in section 1.3, the TP process can be divided into two pathways: Whilst Q_{venting} is transferred by all the three heat transfer mechanisms heat conduction, heat convection, and heat radiation, Q_{remains} is transferred only via heat conduction from the failed cell to its surroundings. In order to provide a fundamental understanding of both pathways, it is desirable to investigate each one individually. As pointed out in section 1.4, a common approach to investigate the Q_{remains} pathway is performing experiments in “open setups” without any housing, as the influence of vented gas and particles may be neglected in this case. Minimizing the influence of Q_{venting} also simplifies modeling and simulation, as it is possible to consider the solid body domain only.

Consequently, the first part of this chapter, section 3.1, deals with the transfer of the single cell TR model presented in section 2.2 to multiple cell level. Therefore, the modeling approaches for heat release during TR are applied to a cell stack experiment in an open setup. The result is a validated TP model for the solid body domain of the coupled model developed in this thesis. Subsequently, the Q_{venting} pathway is investigated in section 3.2 in order to develop a model for the fluid flow domain. First, a study comparing the experimental results of the cell stack experiment performed with and without housing is presented in section 3.2.1, which allows to evaluate the influence of Q_{venting} on the TP process. In a second step, the deposition of vented particles in a battery module environment is experimentally investigated and, based on these experimental results, a gas-particle-flow model is set up in section 3.2.2.

3.1 Thermal propagation in open systems without housing

The article titled “*3D Thermal Simulation of Thermal Runaway Propagation in Lithium-Ion Battery Cell Stack - Review and Comparison of Modeling Approaches*” is presented within this section. It was submitted to the peer-reviewed *Journal of The Electrochemical Society* in April 2023 and published online in June 2023.

The objective of this work was to identify a suitable modeling approach for TP simulation, which can be used as first part of the coupled model developed in this thesis, that combines solid body and gas-particle-flow simulation. Therefore, the three modeling approaches for heat release during TR investigated in section 2.2 were applied to a cell stack experiment and evaluated with respect to their influence on the TP process and

computational resource consumption. The cell stack consisted of five prismatic lithium-ion batteries (> 60 Ah) with a cell-to-cell insulation material in between. In addition, aluminum plates were attached to the bottom and the sides of the cell stack in order to represent the effect of a cooling and side plates. The resulting stack assembly was tested in an open setup without housing, which allowed to neglect the influence of vented gas and particles. As in the previous study on single cell level, the 3D-CFD framework of *Simcenter Star-CCM+*[®] was used for this study.

During the experiments, a bulging of the cells 2 to 5 was observed during the heating phase, which was attributed to electrolyte vaporization and the release of gaseous products by chemical reactions that occur before TR, such as SEI decomposition. A bulging of the cell results in a gas layer between jelly roll and cell can, that consequently influences the heat transfer to the jelly roll. In contrast to previous studies (see section 1.5), the model therefore considered the formation of such a gas layer between jelly roll and cell can in form of a thermal resistance. In addition, the model accounted for the mass loss during TR by an adaption of the jelly roll density ρ_{JR} . The consideration of both these phenomena was necessary to reproduce the experimental results.

The different modeling approaches for heat release during TR showed a significant effect on the simulation results. Whilst the temperature-dependent heat release rate based on ARC data was found to be not suitable for the investigated simulation case, both the time-dependent function for heat release and the empirical Arrhenius source term spatially resolving the TR reaction are capable of modeling the TP process. As on single cell level, however, the time-dependent approach showed the lowest computational resource consumption and is therefore identified as best option for the coupled model developed in this thesis.

3D Thermal Simulation of Thermal Runaway Propagation in Lithium-Ion Battery Cell Stack - Review and Comparison of Modeling Approaches

S. Hoelle, S. Zimmermann, and O. Hinrichsen

Journal of The Electrochemical Society 170, No. 060516, 2023

Permanent weblink:

<https://doi.org/10.1149/1945-7111/acd966>

Reproduced under the terms of the Creative Commons Attribution 4.0 License (CC BY, <https://creativecommons.org/licenses/by/4.0/>), which permits unrestricted reuse of the work in any medium, provided the original work is properly cited.

Author contributions:

S. Hoelle initiated the work and coordinated the experiments used as simulation input and for validation. S. Hoelle developed the simulation model and optimized the model parameters. The data was analyzed and interpreted by S. Hoelle and S. Zimmermann. The manuscript was written by S. Hoelle and was edited by S. Zimmermann and O. Hinrichsen. All authors discussed the data and commented on the results.



3D Thermal Simulation of Thermal Runaway Propagation in Lithium-Ion Battery Cell Stack: Review and Comparison of Modeling Approaches

S. Hoelle,^{1,2,z} S. Zimmermann,¹ and O. Hinrichsen^{2,3}¹BMW Group, Munich, Germany²Technical University of Munich, TUM School of Natural Sciences, Lichtenbergstraße 4, 85748 Garching near Munich, Germany³Technical University of Munich, Catalysis Research Center, Ernst-Otto-Fischer-Straße 1, 85748 Garching near Munich, Germany

Three empirical modeling approaches for the heat release during a lithium-ion battery cell thermal runaway (TR) are analyzed and compared with regard to their suitability for TR propagation simulation. Therefore, the experimental results of a battery cell stack experiment consisting of five prismatic lithium-ion batteries (>60 Ah) are compared to simulation results of a model that is built within the 3D-CFD framework of *Simcenter Star-CCM+*[®]. In contrast to previous studies, the proposed model takes into account detailed phenomena such as the formation of a gas layer between jelly roll and cell can due to electrolyte vaporization, which is crucial to reproduce experimental results. Only two of the three modeling approaches are suitable for TR propagation simulation of the cell stack experiment investigated in this study. These approaches either use time-dependent or spatially resolved temperature-dependent heat release rates. The proposed consideration of gas layer formation as well as the comparative analysis of the modeling approaches contribute to the improvement of TR propagation simulations and support engineers as well as researchers to design a safer battery pack.

© 2023 The Author(s). Published on behalf of The Electrochemical Society by IOP Publishing Limited. This is an open access article distributed under the terms of the Creative Commons Attribution 4.0 License (CC BY, <http://creativecommons.org/licenses/by/4.0/>), which permits unrestricted reuse of the work in any medium, provided the original work is properly cited. [DOI: 10.1149/1945-7111/acd966]



Manuscript submitted April 26, 2023; revised manuscript received May 23, 2023. Published June 7, 2023.

Nomenclature

Abbreviations

1D	one-dimensional
2D	two-dimensional
3D	three-dimensional
ARC	accelerating rate calorimetry
CFD	computational fluid dynamics
DEC	diethyl carbonate
DMC	dimethyl carbonate
EC	ethylene carbonate
EMC	ethyl methyl carbonate
EV	electric vehicle
FDM	finite difference method
FEM	finite element method
FVM	finite volume method
HRR	heat release rate
ISC	internal short circuit
LEM	lumped element method
LiPF ₆	lithium hexafluorophosphate
NMC	lithium nickel manganese cobalt oxide
ROM	reduced order model
SoC	state of charge
TR	thermal runaway

Symbols

a	pre-exponential factor, K s^{-1}
A	area, m^2
B	reaction index, —
c_e	normalized concentration of energy, —
c_p	specific heat capacity, $\text{J kg}^{-1} \text{K}^{-1}$
C	reaction rate, s^{-1}
d	thickness/distance, m
E	energy, J
f	function, —
h	heat transfer coefficient, $\text{W m}^{-2} \text{K}^{-1}$

i	iteration, —
m	mass, kg
\dot{q}	volumetric heat release rate, W m^{-3}
Q	heat release rate, W
Q	heat, J
R_{th}	thermal resistance, $\text{m}^2 \text{K W}^{-1}$
t	time, s
T	temperature, $^{\circ}\text{C}$
V	volume, m^3
x, y, z	coordinates, —
α	(volume) fraction, —
β	normalization factor, —
ϵ	energy residual of simulation, —
δ	relative mass loss, %
Δ	difference, —
λ	thermal conductivity, $\text{W m}^{-1} \text{K}^{-1}$
ρ	density, kg m^{-3}
σ^2	variance, —

Indices

AC	index representing the autoclave experiment
adhesive	index representing the adhesive
avg	index representing an average value
can	index representing the cell can
cell	index representing the cell
C1	index representing cell 1
C2	index representing cell 2
C3	index representing cell 3
C4	index representing cell 4
C5	index representing cell 5
DEC	index representing diethyl carbonate
DMC	index representing dimethyl carbonate
vap	index representing parameters related to vaporization
EC	index representing ethylene carbonate
EMC	index representing ethyl methyl carbonate
Fourier	index representing Fourier's law
gaslayer	index representing the gas layer between jelly roll and cell can

^zE-mail: sebastian.hoelle@bmw.de

heating	index representing the temperature increase during TR
HS	index representing parameters related to the heat-shields
HS1	index representing heatshield 1
HS2	index representing heatshield 2
HS3	index representing heatshield 3
HS4	index representing heatshield 4
init	index representing the initial state
IF	index representing an interface
JR	index representing parameters related to the jelly roll
JR2	index representing the jelly roll of cell 2
JRmid	index representing the middle part of the jelly roll
JRsides	index representing the side parts of the jelly roll
loss	index representing the mass loss during TR
max	index representing a maximum value
mod	index representing a modified method
M1	index representing method 1
M2	index representing method 2
M3	index representing method 3
nail	index representing the nail
onset	index representing the onset of detectable self-heating
postTR	index representing the state after TR
ref	index representing a reference value
remains	index representing the cell remains
sides	index representing the small side(s) of the cell
sink	index representing a (heat) sink
stack	index representing the cell stack experiment
step	index representing the time step
total	index representing the total time of the simulation
TR	index representing the TR process
venting	index representing the venting process during TR
x	index representing a battery cell components as shown in Fig. 1b

The design of battery packs for electric vehicles (EV) can be time-consuming and expensive. Especially when it comes to the validation of the thermal safety concept, large numbers of experiments are necessary. These experiments usually require special laboratories, instruments, and facilities. In addition, the battery packs can no longer be used for other purposes afterwards. Therefore, the manufacturers of EV battery packs aim to reduce the amount of experiments by establishing virtual development and validation methods.^{1,2}

In this context, the modeling of thermal runaway (TR) and TR propagation processes has received much attention during the last years. A lot of effort is put into this topic, not only in industry, but also in the scientific community as shown in the number of publications in recent years.³ There exist a large number of modeling approaches to predict the TR behavior in single battery cells. Many of these models aim to improve the overall understanding of the TR process by an accurate modeling of the physics as shown for example by Baakes et al. in Ref. 4. Others focus on more simplified and empirical approaches that can be applied to large simulation models with multiple battery cells.

Table I summarizes the state of the art in TR propagation simulation. A common approach to model the heat release during TR is to implement the occurring decomposition reactions with Arrhenius-type equations. Most models include four reactions as introduced in the pioneer work by Hatchard et al. in Ref. 5. Some researchers additionally included electrochemical heat source terms,^{6–11} joule heating due to the internal short circuit (ISC),^{6,9,12,13} or additional chemical reactions.^{12,14} However, these detailed modeling approaches usually require much computational power and consequently are not suitable for large

simulation models of full battery packs. In order to reduce computational time, the number of chemical reactions in the model can either be reduced,^{6–9} or all source terms can be represented by a single equation.^{15–17} A further simplification is achieved by implementing empirical heat source terms, which can be time-dependent,¹⁸ temperature-dependent,^{19–21} or constant.²² In conclusion, there are many different modeling approaches for the heat release during TR that are applicable to TR propagation simulation. However, there is no assessment on the influence of different approaches on the simulation results so far.

This publication focuses on thermal modeling of the TR propagation process in a battery cell stack consisting of five prismatic state-of-the-art prototype lithium-ion batteries. The objective is to analyze the influence of different modeling approaches for the heat release during TR on the TR propagation process. Therefore, the battery cell stack experiment published in previous work is simulated within the 3D-CFD framework of *Simcenter STAR-CCM+*[®] and three modeling approaches investigated on single cell level in a previous study are implemented.^{23,24} In addition, the influence of the modeling approach on computational time is evaluated. This allows to identify suitable approaches for TR propagation simulation on multiple cell level. To the authors' knowledge, a comparative analysis of different modeling approaches for TR propagation simulation has not been the subject of any scientific publication. The results help engineers as well as researchers to choose a suitable model for TR propagation simulation and therefore contribute to the improvement of battery pack design.

Experimental Setup

In this study, the cell stack experiment introduced in a previous publication is modeled and simulated.²³ The investigated setup consists of five prismatic lithium-ion battery cells with an insulation material in between (also referred to as "heatshield") and aluminum plates attached to the bottom and the sides of the stack. The first cell of the cell stack is triggered into TR by nail penetration from the bottom side. In the course of the experiment, further TRs then propagate from cell to cell. The temperature sensor data monitored at various positions is used for comparison with the simulation results. Data of other experimental setups that is required for the simulation model is adopted from a previous publication (Ref. 24).

Geometry.—Figure 1a shows the setup of the cell stack experiment that is modeled in this study. The main components are five battery cells (dimensions 180 mm × 32 mm × 72.5 mm) that are stacked together with a heatshield in between (thickness 1.1 mm). In addition, there are aluminum plates attached to the bottom (thickness 1.2 mm) and the sides (thickness 1.8 mm) of the cell stack. The resulting assembly is integrated into a steel frame (thickness 20 mm) that is attached to a base plate (thickness 15 mm). The steel frame provides compression of the cell stack and ensures that there is no direct contact to the base plate. In order to minimize the heat transfer between cell stack and steel frame, a thermal insulation material is used (thickness 10 mm). The temperature sensor naming and positions used for comparison of experimental and simulation results are shown in Fig. 1b. The sensors are placed in the center of each cell can's largest sides. Further information of the experimental setup is provided in a previous publication.²³

Investigated cells.—The battery cells investigated in this study are the same as described in Ref. 24. The cells are lithium-ion battery cells of prismatic format with a capacity between 60 Ah and 70 Ah. The prototype cells use LiNi_{0.8}Mn_{0.1}Co_{0.1}O₂ (NMC811) cathodes, graphite anodes, and an electrolyte consisting of lithium hexafluorophosphate (LiPF₆) conducting salt with ethylene carbonate (EC), ethyl methyl carbonate (EMC), diethyl carbonate (DEC), and dimethyl carbonate (DMC) solvents. The test procedure is according to Ref. 23: the tested cells are charged to a state of charge

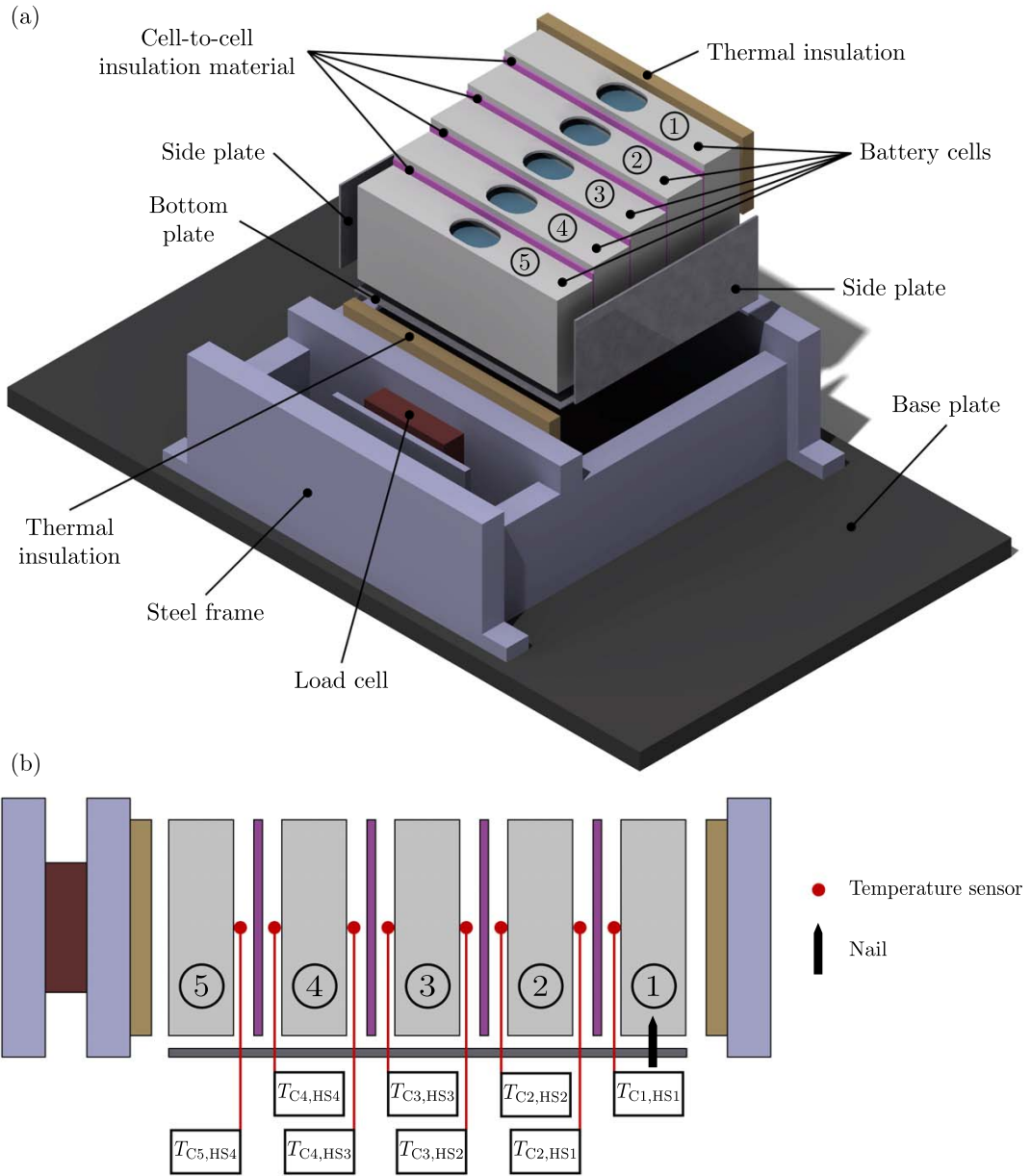


Figure 1. (a) Modeled components of the cell stack experiment. (b) Temperature sensor naming and positions on the cell cans (center of the large side).

of SoC = 100 % before the tests and the cell stack is compressed with a force of 1 kN at test begin. All cells are in a fresh/unused aging state.

Experimental results.—In order to model the cell stack experiment, it is necessary to derive several model parameters. Table II summarizes all parameters that are required to model a TR according to Ref. 24 as well as the experiments that are used to determine these parameters in this study.

Cell stack test.—Two nail penetration tests are performed in the cell stack setup. Therefore, cell 1 is triggered into TR by penetrating its bottom side with a nail of 3 mm in diameter, a penetration depth of 17.5 mm, and a penetration speed of 7 mm s^{-1} . The mass loss during TR propagation of the whole cell stack can be estimated by

$$\Delta m_{\text{loss,stack}} = m_{\text{stack}} - m_{\text{stack,postTR}} \quad [1]$$

with m_{stack} being the mass of the cell stack before the test and $m_{\text{stack,postTR}}$ being the mass of the cell stack after the test. In this context, the “cell stack” includes five battery cells, four heatshields, the bottom and the sides plates, as well as attached temperature sensors. It is then assumed, that the relative mass loss of each single cell $\delta_{\text{loss,TR}}$ is equivalent to the relative mass loss of the complete cell stack, i.e. each cell loses the same amount of mass during the TR propagation process:

$$\delta_{\text{loss,TR}} = \frac{\Delta m_{\text{loss,stack}}}{m_{\text{stack}}} \quad [2]$$

Table I. Overview of modeling approaches for the heat release during TR in thermal propagation simulations.

Author(s)	Modeling approach for heat release				Setup			
	Type	No. of source terms			Dimensions	Solver	No. of cells	Format
		Chemical	Electrochemical	Joule heat (ISC)				
Jia et al. ⁶	Arrhenius	4	1	1	1D	LEM	2 & 9	Cylindrical
Shen et al. ²⁷	Arrhenius	4	—	—	1D	LEM	6	Prismatic
Feng et al. ¹²	Arrhenius	6	—	1	1D	LEM	6	Prismatic
Chen et al. ¹⁴	Arrhenius	6	—	—	1D	LEM	2	Pouch
Kurzawski et al. ⁷	Arrhenius	3	1	—	quasi 1D	FEM	5	Pouch
Bugryniec et al. ²⁸	Arrhenius	4	—	—	2D	FEM	9	Cylindrical
Coman et al. ⁸	Arrhenius	3	1	—	2D & 3D	FEM	65	Cylindrical
Yikai et al. ⁹	Arrhenius	3	—	1	3D	FEM	2	Cylindrical
Zhang et al. ¹⁰	Arrhenius	4	1	—	3D	FEM	2	Pouch
Li et al. ²⁹	Arrhenius	4	—	—	3D	FEM+FVM	192	Cylindrical
Jindal et al. ¹¹	Arrhenius	4	Full model	—	3D	FVM	10	Cylindrical
Mishra et al. ³⁰	Arrhenius	4	—	—	3D	FVM	25	Cylindrical
Mishra et al. ³¹	Arrhenius	4	—	—	3D	FVM	25	Cylindrical
Mishra et al. ³²	Arrhenius	4	—	—	3D	FVM	25	Cylindrical
Vyroubal et al. ³³	Arrhenius	4	—	—	3D	FVM	4 × 10	Cylindrical
Yuan et al. ¹³	Arrhenius	4	—	1	3D	FVM	11	Cylindrical
Xu et al. ¹⁵	Arrhenius	Single equation fitted to ARC data			1D	ROM	4, 18 & 3 × 18	Prismatic
Liu et al. ¹⁶	Arrhenius	Single equation fitted to experimental data			3D	FEM	6	Cylindrical
Feng et al. ¹⁷	Arrhenius	Single equation fitted to ARC data + Joule heat (ISC)			3D	FEM	6	Prismatic
Coman et al. ¹⁸	Empirical	Time dependent function for HRR			2D	FEM	48	Cylindrical
Yeow et al. ¹⁹	Empirical	Temperature dependent function for HRR fitted to ARC data			3D	FEM	3	Pouch
Citarella et al. ²⁰	Empirical	Temperature dependent function for HRR fitted to ARC data			3D	FVM	2 × 12	Prismatic
Qin et al. ²¹	Empirical	Temperature dependent heat release rate (ARC data)			3D	FVM	9	Cylindrical
Grimmeisen et al. ²²	Empirical	Constant heat release rate			3D	FVM	7	Cylindrical
Bilyaz et al. ³⁴	Other	Laminar Premixed Flame Propagation Theory with single reaction			1D	FDM	5 & 10	Pouch

*Abbreviations: ISC (internal short circuit), ARC (accelerating rate calorimetry), HRR (heat release rate), (1D/2D/3D) one-/two-/three-dimensional, LEM (lumped element method), FEM (finite element method), FVM (finite volume method), ROM (reduced order model), FDM (finite difference method).

Table II. Required model parameters for the simulation of a TR according to Ref. 24.

Required parameters	Symbol	Experiment used for determination
Relative mass loss during TR	$\delta_{\text{loss,TR}}$	Cell stack
Released heat during TR	Q_{TR}	Autoclave calorimetry
TR trigger temperature	T_{TR}	Accelerating rate calorimetry
Optional parameters		
Duration of venting	t_{venting}	Autoclave calorimetry
Duration of temperature increase	t_{heating}	Autoclave calorimetry
Onset temperature of self-heating	T_{onset}	Accelerating rate calorimetry

Table III. Experimental results used as model parameters.

Parameter	Value	Unit	Source
$\delta_{\text{loss,TR}}$	46.5	%	Cell stack experiments (see Eq. 2)
Q_{TR}	1260.0	kJ	Autoclave calorimetry
$Q_{\text{remains,stack}}$	674.5	kJ	Eqs. 3 and 4
t_{venting}	17.7	s	Ref. 24
t_{heating}	39.9	s	Ref. 24
T_{onset}	75.2	°C	Ref. 24
T_{TR}	137.5	°C	Ref. 24

Autoclave calorimetry.—The results of two autoclave calorimetry tests from a previous publication are used in this study.²⁴ The released heat during TR (Q_{TR}) can be separated in a first part that remains in the cell (Q_{remains}) and a second part that is transported out of the cell by the vented gas and particles (Q_{venting}).^{25,26} In the autoclave calorimetry experiment (index: AC), the investigated cell showed a value of $Q_{\text{remains,AC}} = 729.3$ kJ.²⁴ According to Scharner,²⁵ Q_{TR} can then be estimated by

$$Q_{\text{TR}} = (Q_{\text{remains}} + Q_{\text{venting}})_{\text{AC}} = Q_{\text{remains,AC}} \left(1 + \frac{m_{\text{cell}} - m_{\text{cell,postTR}}}{m_{\text{cell,postTR}}} \right) \quad [3]$$

where m_{cell} is the mass of the cell before the autoclave calorimetry test and $m_{\text{cell,postTR}}$ is the mass of the cell after the autoclave calorimetry test. Due to a different mass loss in the cell stack experiment compared to the autoclave calorimetry test, the heat of the cell remains in the cell stack experiment $Q_{\text{remains,stack}}$ is calculated as follows:

$$Q_{\text{remains,stack}} = Q_{\text{TR}} (1 - \delta_{\text{loss,TR}}). \quad [4]$$

Additionally, the duration of venting t_{venting} and the duration of measurable temperature increase t_{heating} are adopted from Ref. 24.

Accelerating rate calorimetry (ARC).—ARC experiments are widely used to determine the onset temperature of continuous self-heating T_{onset} and the TR trigger temperature T_{TR} . For the investigated cell, the values are already published and therefore adopted from Ref. 24. The following criteria have been used:

- 0.02 K min⁻¹ is detected as onset of self-heating and
- 30 K min⁻¹ is detected as onset of TR.

Table III summarizes all experimental results used in this study for model parameterization.

Model Structure and Simulation Methodology

The commercial computational fluid dynamics (CFD) software *Simcenter STAR-CCM+*[®] is used to build a three-dimensional (3D)

thermal model that is based on the finite volume approximation approach. As all cell stack experiments were conducted in an open setup without any cover or housing, the gases and particles vented during the TR propagation process spread to the environment. Therefore, it is assumed that a convective heat transfer can be neglected and consequently, only heat conduction within solids is considered in this study. The governing equation for energy transport within solids is given as follows:

$$\rho c_p \frac{\partial T}{\partial t} = \nabla \cdot \lambda \nabla T + \dot{q} \quad [5]$$

where ρ , c_p , and λ are the thermophysical properties of the solid (density, specific heat capacity, and thermal conductivity, respectively), T is the temperature of the solid, and \dot{q} is the sum of all heat sources (and sinks) within the solid.

Model geometry and mesh.—Figure 2 shows the components of the battery cell model, which is for the most part adopted from Ref. 24. In its original state, the battery cell consists of two separate jelly rolls, that were simplified to three rectangular cuboids in a previous study: a large middle cuboid and two small side cuboids.²⁴ The latter allow to assign different material properties and hence to account for the orthotropic thermal conductivity of the jelly roll in dependence of the winding structure. In this study, the six cuboids as used in Ref. 24 are further simplified to a single jelly roll represented by three cuboids. The side cuboids are in direct contact with the cell can, which is not representing the gap between jelly roll and cell can at the sides due to the winding structure. Therefore, a thermal resistance is added between side cuboids and cell can. The value is set to

$$R_{\text{th,sides}} = \frac{d_{\text{sides}}}{\lambda_{R_{\text{th,sides}}}} = 0.04885 \text{ m}^2 \text{ K W}^{-1}, \quad [6]$$

which accounts for an average gap between jelly roll and can of $d_{\text{sides}} = 1.27$ mm with a thermal conductivity of $\lambda_{R_{\text{th,sides}}} = 0.026 \text{ W m}^{-1} \text{ K}^{-1}$.

As shown in Fig. 1, aluminum plates are attached to the bottom and the sides of the cell stack. For this purpose, an adhesive is used that is not considered as a solid in the model. Instead, a thermal resistance is applied to the interfaces between stack and aluminum plates. The adhesive's thermal conductivity is $\lambda_{\text{adhesive}} = 1.0 \text{ W m}^{-1} \text{ K}^{-1}$ and its thickness is $d_{\text{adhesive}} = 0.6$ mm, which results in a thermal resistance of

$$R_{\text{th,adhesive}} = \frac{d_{\text{adhesive}}}{\lambda_{\text{adhesive}}} = 0.0006 \text{ m}^2 \text{ K W}^{-1}. \quad [7]$$

All other components are modeled as homogeneous solids with material properties as specified in Table IV.

The mesh used in this study (see Fig. 3) is the results of a mesh convergence study. It is ensured that all parts, in particular thin parts, are resolved by a minimum number of three cell layers in each direction. The total number of volume elements is 1390175.

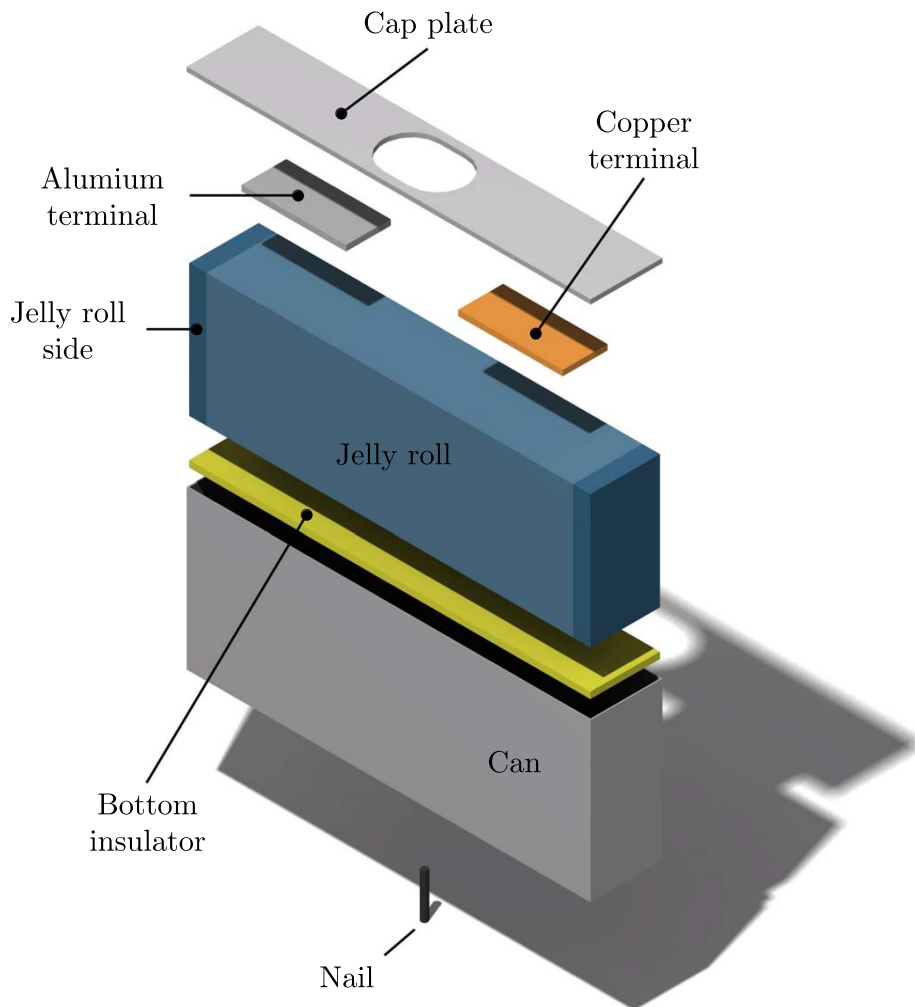


Figure 2. Components of the battery cell model.

Table IV. Material properties of the model components used for the baseline simulation. Values according to Ref., 24 if not indicated otherwise.

Component as shown in Figs. 1 and 2	Density ρ [kg m ⁻³]	Specific heat capacity c_p [J kg ⁻¹ K ⁻¹]	Thermal conductivity λ [W m ⁻¹ K ⁻¹]
Can/cap plate	2730.0	893.0	159.0
Jelly Roll (in-plane)	2612.7 ^a	1380.0 ^b	23.1
Jelly Roll (through-plane)	2612.7 ^a	1380.0 ^b	1.034 ³⁵
Bottom insulator	619.0	1807.0	0.254
Copper terminal	8960.0	385.0	402.0
Aluminum terminal	2960.0	905.0	237.0
Nail ^c	8055.0	480.0	15.1
Heatshield ^d	8.13	1130.0	0.06
Bottom plate/side plates ^c	2702.0	903.0	237.0
Thermal insulation ^d	1000.0	1100.0	0.32
Steel frame/load cell/base plate ^c	8055.0	480.0	15.1

a chosen to match the mass of the cell stack before test m_{stack} . b constant value leading to the same temperature increase as the temperature-dependent c_p proposed in Ref. 24. c Simcenter Star-CCM+[®] standard values for aluminum or steel, respectively. d as specified by manufacturer.

Boundary conditions and numerical setup.—The solid-body simulations are calculated with the implicit unsteady solver for a total physical time of $t_{\text{total}} = 800$ s. An adaptive time step is used in order to reduce the total simulation time. During each TR, a small time step is set to ensure that numerical errors can be neglected. This

small time step is depending on the modeling approach for the heat release during TR and is chosen according to the results of Ref. 24. In between the single TRs, the time step is increased step-wise to $\Delta t_{\text{step}} = 2$ s as the temperature gradients decrease. As stopping criteria for the inner iterations i the energy residual ϵ is used. A

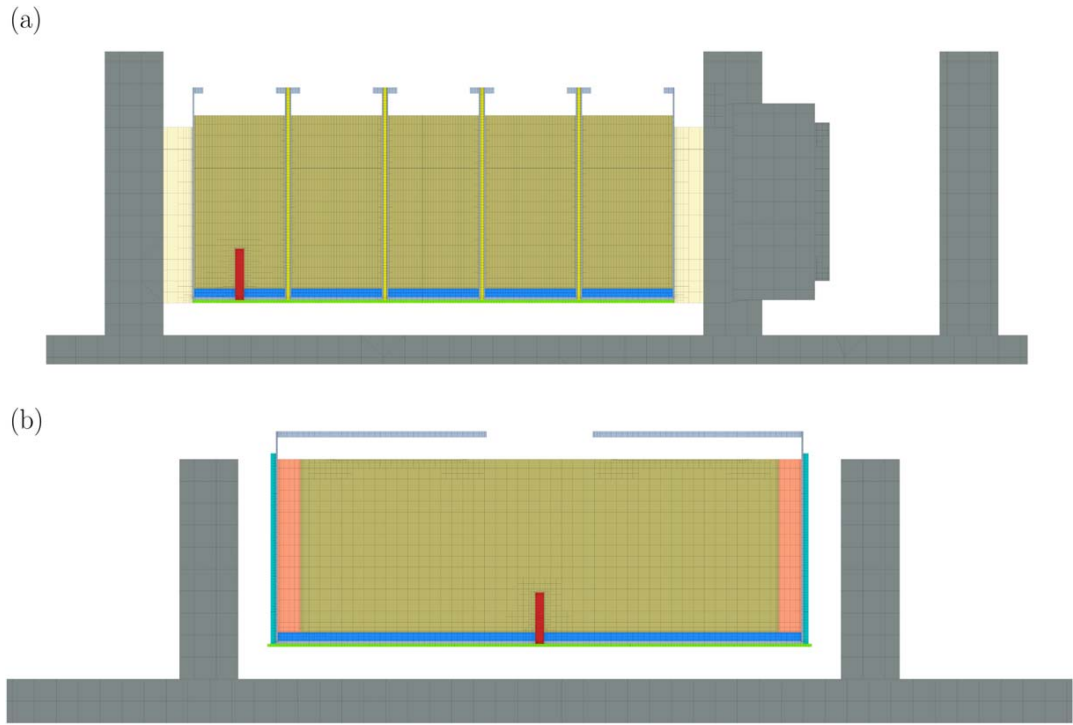


Figure 3. (a) Plane Section of the mesh in propagation direction. (b) Plane Section of the mesh through cell 1 (nail penetrated cell).

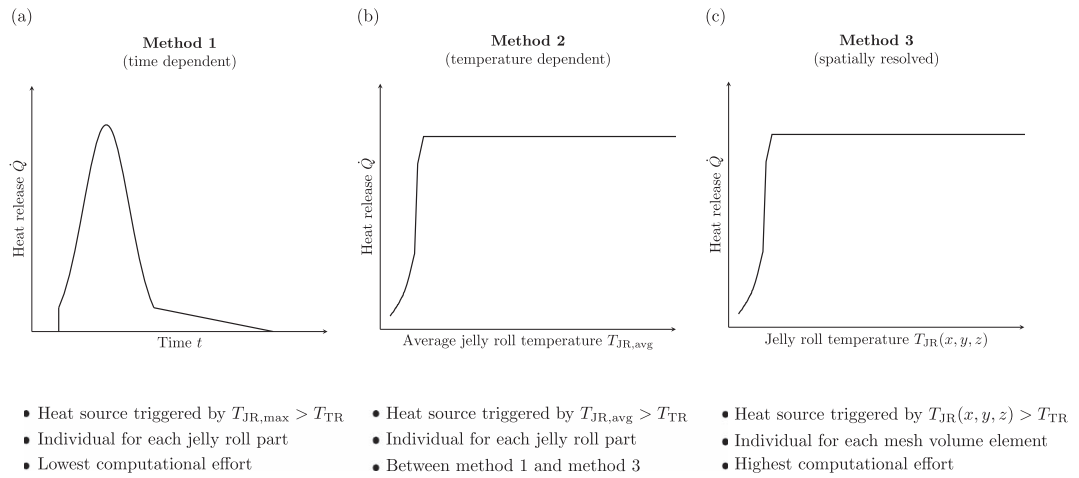


Figure 4. Comparison of investigated modeling approaches for the heat release during TR according to Ref. 24. (a) Method 1: time dependent heat release rate (spatially uniform). (b) Method 2: temperature dependent heat release rate (spatially uniform). (c) Method 3: spatially resolved heat release.

minimum number of 15 inner iterations is ensured, while the maximum number of inner iterations is set to 125. The solving process of each time step ends as soon as ϵ shows an asymptotic behavior defined by the following criteria:

$$\frac{\max(\epsilon(i-14:i)) - \min(\epsilon(i-14:i))}{\text{mean}(\epsilon(i-14:i))} \leq 0.1$$

for $\epsilon > 14$. [8]

All solids are initialized with the mean value of both experiment's initial temperature $T_{init} = 27.6$ °C. Ideal interfaces are set between all solid contacts for the baseline simulation, except for the contact faces between cell cans and aluminum plates

(compare Fig. 1) as well as the faces between the side cuboids of the jelly rolls and the cell cans. As described above, a thermal resistance representing the adhesive and the gap, respectively, is applied to the solid-to-solid contact (see Eqs. 6 and 7). As high temperatures are expected for the outer faces of the cell stack, a convective boundary condition is used for all faces that are in contact with the surrounding air during the experiments. The ambient temperature is set equal to T_{init} in combination with a heat transfer coefficient of $h = 20 \text{ W m}^{-2} \text{ K}^{-1}$ as proposed by Coman et al. in Ref. 18. For all faces inside of the cell cans (inner can walls, current collectors and top jelly roll faces), an adiabatic boundary condition is used. There are two reasons for this assumption: first, the actual geometry of the inner cell components

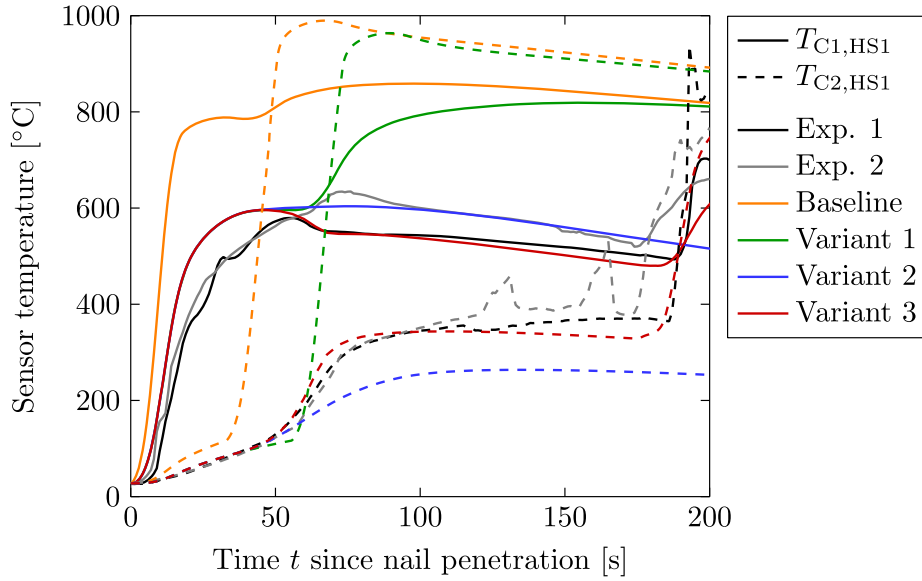


Figure 5. Sensor temperature on both sides of the first heatshield (between cell 1 and 2) over time t since nail penetration of cell 1 for both experiments (black and gray) and four simulations with different parameter sets (colored). The numeric results show the influence of a thermal resistance between can and jelly roll as well as the insulation material's thermal conductivity.

after a TR is hard to predict, as a large fraction of the components is ejected out of the cell during venting. Second, the gas temperature inside of the cell can be expected to be approximately as high as the solid temperature and therefore the heat transfer would be negligibly small. Heat radiation is not considered within this study.

Modeling approaches for heat release during TR.—Three different modeling approaches for the heat release during a TR were investigated in a previous study:²⁴

- Method 1: time-dependent function for the heat release rate (spatially uniform)
- Method 2: temperature-dependent heat release rate (spatially uniform)
- Method 3: spatially resolved heat release

They concluded that the effect of the different modeling approaches is only significant during the TR process itself and can be neglected during larger time scales such as a thermal propagation process.²⁴ This hypothesis is investigated in this study.

Method 1: time-dependent function for the heat release rate (spatially uniform).—Method 1 is characterized by an empirical time-dependent function for the heat release rate, which is fitted to experimental data of ARC tests. Figure 4a shows the heat release rate $\dot{Q}_{M1}(t)$ over time t since TR initiation, resulting from the function $f_{M1}(t)$ as used in the previous publication.²⁴ The function is divided into two parts:

$$f_{M1}(t) = \begin{cases} \frac{1}{\beta} f_{M1.1}(t) & \text{for } t < t_{\text{venting}} \\ \frac{1}{\beta} f_{M1.2}(t) & \text{for } t_{\text{venting}} \leq t \leq t_{\text{heating}} \end{cases} \quad [9]$$

where $f_{M1.1}(t)$ is representing high heat release rates directly after TR initiation ($t < t_{\text{venting}}$), and $f_{M1.2}(t)$ is representing lower heat release rates until $t = t_{\text{heating}}$. Both parts of the function are normalized by

the factor β :

$$\beta = \int_0^{t_{\text{venting}}} f_{M1.1}(t) dt + \int_{t_{\text{venting}}}^{t_{\text{heating}}} f_{M1.2}(t) dt. \quad [10]$$

The two different phases of heat release are modeled as a superposition of a Gaussian distribution and a subsequent linear decrease:

$$f_{M1.1}(t) = \frac{1}{\sqrt{2\pi\sigma^2}} \exp\left(-\frac{1}{2\sigma^2}\left(t - \frac{t_{\text{venting}}}{2}\right)^2\right) \quad \text{with} \quad [11]$$

$$\sigma^2 = \frac{1}{4}(0.175 t_{\text{venting}} + 1)t_{\text{venting}} \quad [12]$$

and

$$f_{M1.2}(t) = f_{M1.1}(t_{\text{venting}}) - \frac{f_{M1.1}(t_{\text{venting}})}{t_{\text{heating}} - t_{\text{venting}}}(t - t_{\text{venting}}). \quad [13]$$

The heat release rate is then defined in each jelly roll part x as follows:

$$\dot{Q}_{M1,JRmid} = f_{M1}(t) \alpha_{JRmid} (Q_{\text{remains}} - Q_{M1,nail}) \quad \text{for } T_{JRmid,max} > T_{TR}, \quad [14]$$

$$\dot{Q}_{M1,JRsides} = f_{M1}(t) \alpha_{JRsides} (Q_{\text{remains}} - Q_{M1,nail}) \quad \text{for } T_{JRsides,max} > T_{TR}, \quad [15]$$

where α_x is the volume fraction of the jelly roll part x related to the total volume of the jelly roll (that means the middle part and both sides - compare Fig. 2), Q_{remains} is the heat dissipated by heat conduction as measured in the autoclave calorimetry experiments, $Q_{M1,nail}$ is the heat released in the nail for triggering the TR, and $T_{x,max}$ is the maximum temperature in the jelly roll part x .

Consequently, the heat release is initiated as soon as the temperature in the jelly roll part(s) exceeds the TR trigger

temperature T_{TR} . In the cell stack experiments, the cause for this condition within the first cell is the nail penetration with subsequent electrical short circuit. Feng et al. proposed an approach to model the heat release of such a short circuit, which is adopted for this study:¹⁷

$$\dot{Q}_{M1,nail} = Q_{nail} f_{nail}(t) = \alpha_{nail} Q_1 f_{nail}(t) \quad [16]$$

where $f_{nail}(t)$ is the short circuit release rate in the nail as defined by Feng et al.¹⁷ and $\alpha_{nail} = 0.01$ is the fraction of heat that is released in the nail. For the other cells, the TR trigger temperature T_{TR} is exceeded by the heat transfer from adjacent cells that underwent TR in advance. In contrast to the two following methods, there is no heat release before exceeding T_{TR} for method 1. That means, that the exothermic side reactions that are typical for the temperature range of $T_{onset} < T < T_{TR}$ are neglected.

Method 2: temperature dependent heat release rate (spatially uniform).—Method 2 is characterized by temperature dependent heat release rate values, that are obtained from experimental data of ARC tests. Figure 4b shows the heat release rate $\dot{Q}_{M2}(T)$ over the volume averaged jelly roll temperature $T_{JR,avg}$. In 2013, Yeow et al. proposed to approximate the self-heating rate of Li-ion batteries during TR with a Gaussian distribution depending on the cell temperature as measured in ARC experiments.¹⁹ This approach is adopted for this study similar to Ref. 24, as the experimental data of three ARC tests is available. The heat release rate is specified as the mean value of these three ARC tests and provided to the simulation model as table data set. Subsequently, the software interpolates linearly between the table values depending on the current volume averaged jelly roll temperature $T_{JR,avg}$. For temperatures above T_{TR} , the number of measured data points during the ARC experiments is low. Therefore, a constant heat release rate of $\dot{Q}_{M2,max} = \text{const.} = 31177 \text{ W}$ is used for $T > T_{TR}$. This is equivalent to a temperature rate of 3000 K min^{-1} as conventionally measured during ARC experiments. Due to the dependency of the heat release rate on the volume averaged jelly roll temperature, a modeling of the electrical short circuit in the nail is not suitable as trigger condition for the nail penetrated cell. Therefore, the middle part of the jelly roll in cell 1 is initialized with a temperature of $T_{M2,JRmid,init} = 150 \text{ }^\circ\text{C}$. It is assumed, that a fraction of $Q_{remains}$ is already released (Q_{init}), which has to be considered within the heat source terms (for the middle part of the jelly roll in cell 1 only).²⁴

$$\begin{aligned} \dot{Q}_{M2,JR1mid} &= \dot{Q}_{M2}(T_{JRmid,avg}(t)) \\ \text{for } \int \dot{Q}_{M2,JRmid} dt &\leq \alpha_{JRmid} Q_{remains} - Q_{init}, \end{aligned} \quad [17]$$

$$\begin{aligned} \dot{Q}_{M2,JR2mid-JR5mid} &= \dot{Q}_{M2}(T_{JRmid,avg}(t)) \\ \text{for } \int \dot{Q}_{M2,JRmid} dt &\leq \alpha_{JRmid} Q_{remains}, \end{aligned} \quad [18]$$

$$\begin{aligned} \dot{Q}_{M2,JRsidest} &= \dot{Q}_{M2}(T_{JRsidest,avg}(t)) \\ \text{for } \int \dot{Q}_{M2,JRsidest} dt &\leq \alpha_{JRsidest} Q_{remains}, \end{aligned} \quad [19]$$

with $\dot{Q}_{M2}(T)$ being the heat release rate interpolated from the curve shown in Fig. 4b. In order to stop the heat release in each part x as soon as the equivalent of $Q_{remains}$ is released, $\dot{Q}_{M2,x}$ is integrated over time t and monitored.

Method 3: spatially resolved heat release.—Method 3 is similar to method 2 characterized by temperature dependent heat release rate values, that are obtained from experimental data of ARC tests. The main difference is, that the (volumetric) heat release rate \dot{q}_{M3} is depending on the local temperature in the jelly roll $T_{JR}(x, y, z)$ and not on the volume averaged jelly roll temperature (compare Fig. 4c). Therefore, the heat release is spatially resolved. This approach was proposed by Feng et al.¹⁷ in 2016 and simplified in a previous

publication.²⁴ The heat source is divided into two parts: $\dot{q}_{M3,nail}$ being caused by the electric short circuit in the nail and $\dot{q}_{M3,JR}$ being caused by exothermic chemical reactions at elevated temperatures.²⁴

$$\dot{q}_{M3,nail} = \frac{1}{V_{nail}} \alpha_{nail} Q_{remains} f_{nail}(t) \quad \text{and} \quad [20]$$

$$\dot{q}_{M3,JR} = \frac{1}{V_{JR}} (1 - \alpha_{nail}) Q_{remains} \frac{dc_e}{dt}, \quad [21]$$

where V_{nail} and V_{JR} are the volume of the nail and the jelly roll, respectively, $\alpha_{nail} = 0.01$ is the fraction of heat released in the nail, $f_{nail}(t)$ is the short circuit release rate in the nail as defined by Feng et al. in Ref. 17, and c_e is the normalized concentration of energy in each volume element of the mesh. The reaction rate dc_e/dt is then defined as follows:

$$\frac{dc_e}{dt} = \begin{cases} \left(\frac{V \rho c_p JR}{(1 - \alpha_{nail}) Q_{remains}} a \left(\frac{T}{T_{ref}} \right)^B \right) & \text{for } 0 \leq c_e \leq 1 \text{ and } T_{onset} < T \leq T_{TR} \\ C & \text{for } 0 \leq c_e \leq 1 \text{ and } T > T_{TR} \\ 0 & \text{otherwise} \end{cases} \quad [22]$$

where m_{JR} is the mass of the jelly roll, $a = 0.0185 \text{ K s}^{-1}$ is a pre-exponential factor, $B = 24.94$ is the reaction index, $T_{ref} = 410.65 \text{ K}$ ($137.5 \text{ }^\circ\text{C}$) = T_{TR} is used to normalize the temperature T , $C = 0.2 \text{ s}^{-1} = \text{const.}$ is the reaction rate during TR, and $T_{onset} = 75.2 \text{ }^\circ\text{C}$ is the onset temperature of continuous self-heating in the ARC experiments. Please note that A , B , C , T_{onset} , and T_{TR} are taken from Ref. 24 and partly adapted. Therefore, the values differ from the original values used by Feng et al. in Ref. 17.

Adaptions made to the approaches.—In order to apply the different heat source methods to a TR propagation simulation instead of a single TR simulation, further adaptions are necessary. As concluded by Hoelle et al. in Ref. 24, the mass loss during TR δ_{cell} has a major influence on the simulation results and hence has to be considered. For a single TR simulation, this can be achieved by an adaption of the jelly roll's density to match the mass after TR.²⁴ Consequently, the jelly roll density of cell 1 is set constant as $\rho_{JR,C1} = \rho_{JR,postTR} = 1216.3 \text{ kg m}^{-3}$. However, this assumption cannot be made for the whole duration of the cell stack test, as cells 2–5 maintain their full mass over a large phase of the experiment. Therefore, the jelly roll's density of cell 2–5 $\rho_{JR,C2-5}$ is adapted during TR, in order to model the the mass loss:

$$\begin{aligned} \rho_{JR,C2-5}(t) &= \rho_{JR,init} - \frac{\rho_{JR,init} - \rho_{JR,postTR}}{t_{venting}} t \\ \text{for } t &\leq t_{venting} \text{ and } T > T_{TR}, \end{aligned} \quad [23]$$

with $\rho_{JR,init} = 2612.7 \text{ kg m}^{-3}$ being the initial density as defined in Table IV and $\rho_{JR,postTR}$ being the density to match the cell mass after a TR (compare mass loss δ_{cell} in Table III). Due to the constant volume of the jelly roll V_{JR} within the simulation model and the conservation of the system's energy E , an adaption of the density results in a temperature increase:

$$\begin{aligned} E &= V \rho c_p T = \text{const.} \\ \rightarrow 0 &= (\rho T)_{JR,init} = (\rho T)_{JR,postTR} \\ \text{with } V_{JR} &= \text{const.}, c_{p,JR} = \text{const.} \\ \rightarrow T_{JR,postTR} &= T_{JR,init} \frac{\rho_{JR,init}}{\rho_{JR,postTR}} \end{aligned} \quad [24]$$

By coupling the reduction of the jelly roll's density with a (constant) heat sink \dot{Q}_{sink} within the jelly roll material, the energy conservation within the system is fulfilled and consequently, there is no

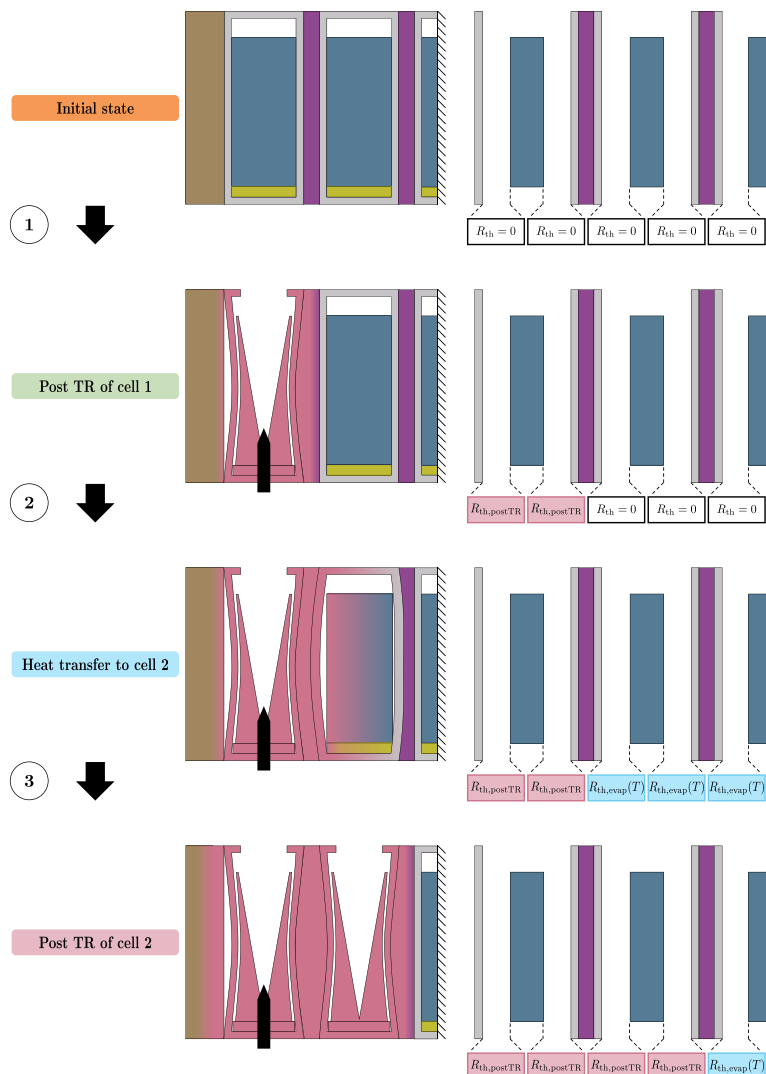


Figure 6. Schematic representation of the propagation process during the modeled experiment.

Table V. Boiling points of electrolyte solvents according to Ref. 39.

Solvent	Boiling point/°C
DMC	91
EMC	110
DEC	126
EC	248

temperature increase due to the density change:

$$\dot{Q}_{\text{sink}} = V_{\text{JR}}(\rho c_p)_{\text{JR,TR}} \frac{T_{\text{JR,init}} - T_{\text{JR,postTR}}}{t_{\text{venting}}} \quad \text{for } t \leq t_{\text{venting}} \text{ and } T > T_{\text{TR}}, \quad [25]$$

Additional influencing factors during cell stack TR propagation.—In order to compare the different modeling approaches for the heat release during TR, a common parameter set has to be defined. For this purpose, method 1 is applied as heat release approach to the simulation model and a numerical solution of the propagation

process of the cell stack experiment is calculated. Although method 3 models the physics more accurately due to the spatial resolving of heat release, method 1 is chosen to find a common parameter set, as the computational effort is lower compared to the other two methods.²⁴ First, the material parameters as defined above are used as a baseline version. Subsequently, additional effects of the cell stack TR propagation are added to the simulation model in order to reduce the deviations between experimental and simulation results.

Figure 5 displays the temperature sensor values on both sides of the first heatshield (between cell 1 and 2) over time t since nail penetration of cell 1 for both experiments (black and gray) and four simulations with different parameter sets (colored). The experimental values of $T_{\text{C1,HS1}}$ (solid lines) show noticeable differences for $t > 55$ s, which, however, can be related to the statistical variance of TR experiments. In addition, there exist two peaks in the curve of $T_{\text{C2,HS1}}$ for experiment 2 at $t \approx 130$ s and $t > 165$ s. Such irregularities can occur since the insulation of sensor cables may start to burn after the TR of the first cell.

The usage of the baseline parameters (orange curves in Fig. 5) results in a faster propagation than observed in the experiments (black and gray). The solid orange curve shows that the temperature increase of the first cell ($T_{\text{C1,HS1}}$) is higher compared to the experimental results (black and gray). This results in the TR in

cell 2 being triggered at approximately 30 s in comparison to the experimental mean value of approximately 181 s. The temperature sensor $T_{C2,HS1}$ also shows a higher gradient for the baseline parameter set compared to the experimental results.

The observed behavior of the baseline parameter set (orange curves in Fig. 5) can be explained as follows: in its initial state, the simulation model uses ideal interfaces between jelly roll and can (except for the side cuboids). Consequently, the heat transfer from the (hot) jelly roll of cell 1 after the first TR to the (cold) jelly roll of the second cell is dominated by heat conduction through the can of cell 1 (thickness $d_{can} = 0.5$ mm), the heatshield (thickness $d_{HS} = 1.1$ mm) and the can of cell 2 (thickness $d_{can} = 0.5$ mm). That means that the distance between both jelly rolls in the initial state is only 2.1 mm. Assuming that the jelly roll temperature after TR of cell 1 is $T_{JR,postTR} = 1000$ °C and the jelly roll temperature of cell 2 is still in its initial state $T_{init} = 27.6$ °C leads according to Fourier's law to a (1D) heat flux of

$$\dot{Q}_{\text{Fourier}} = \frac{A(T_{\text{JR}} - T_{\text{init}})}{2 \frac{d_{\text{can}}}{\lambda_{\text{can}}} + \frac{d_{\text{HS}}}{\lambda_{\text{HS}}} + \frac{d_{\text{JR}}}{\lambda_{\text{JR}}}} \approx 263 \text{ W}. \quad [26]$$

If such a heat flux is absorbed by the cell can of cell 2 (assumed mass $m_{can} = 58$ g), it takes approximately 22 s until the cell can is heated to the TR trigger temperature of $T_{\text{TR}} = 137.5$ °C. A large amount of the transferred heat is obviously absorbed by the temperature increase of the jelly roll of cell 2. However, this rough estimation shows that the simulation model in its baseline state is not representing the reality correctly.

Variant 1.—In order to achieve a better matching between simulation and experimental results, the model is extended by further aspects of the thermal propagation process as illustrated in Fig. 6 (indicated as step 1). The first extension of the model is the introduction of a thermal resistance between jelly roll and can after a TR, that can be explained by the mass loss of the jelly roll. As shown in previous publications, the jelly roll structure after a TR cannot be treated as “full” solid anymore.^{36–38} This means, that the assumption of an ideal contact between jelly roll and can cannot be made. In addition, the thermal conductivity of the jelly roll could significantly change during a TR. To account for both these effects, a thermal resistance of

$$R_{\text{th,postTR}} = \frac{d_{\text{gaslayer}}}{\lambda_{\text{gaslayer}}} = 0.00577 \text{ m}^2 \text{ K W}^{-1} \quad \text{for } t > t_{\text{venting}} \quad [27]$$

is applied to the interfaces between jelly roll and can after a TR, which is equivalent to a gas layer with a thickness of $d_{\text{gaslayer}} = 0.15$ mm and a thermal conductivity of $\lambda_{\text{gaslayer}} = 0.026 \text{ W m}^{-1} \text{ K}^{-1}$. The effect of this gas layer between jelly roll and can after a TR is shown in Fig. 5 (variant 1 - green curves). On the one hand, the temperature increase of the first cell is lower compared to the baseline parameter set and therefore, the deviation to the experimental results is reduced. In addition, the temperature curve of $T_{C2,HS1}$ shows a slower increase in temperature and consequently a better matching between experiment and simulation. On the other hand, the point in time of TR initiation in cell 2 (approximately at 55 s) is still observed too early compared to the experiment as shown in Fig. 5 (variant 1 - green curves).

Variant 2.—A second effect observed during the cell stack experiments is a bulging of the cells at elevated temperatures, that can be explained by the vaporization of the electrolyte solvents (see Table V).^{14,15,39} As illustrated in Fig. 6 (indicated as step 2), the bulging of the cell leads to a gas layer between can and jelly roll and therefore influences the heat transfer. This is particularly relevant for cells 2 to 5, where the TR is heat-initiated. Besides electrolyte vaporization, the formation of this gas layer is enhanced by chemical

reactions occurring before TR that release gaseous products, such as the decomposition of the solid electrolyte interphase (SEI). Depending on the heating rate, the pressure buildup within the cell and hence the gas layer formation can last for several minutes.⁴⁰ For cell 1, however, vent opening was observed within the first seconds after nail penetration, potentially caused by high gas release rates of the TR reactions. Therefore, the gas layer formation is assumed to be irrelevant for nail-penetrated cells. To account for this effect, a temperature dependent thermal resistance is applied to the interfaces between can and jelly roll on the large face sides of cell 2 to 5:

$$R_{\text{th,vap}}(T_{\text{IF}}) = \begin{cases} 0 & \text{for } T_{\text{IF}} < T_{\text{vap,DMC}}, \\ \frac{R_{\text{th,vap,max}}}{(\Delta T_{\text{vap}})^2} (T_{\text{IF}} - T_{\text{vap,DMC}})^2 & \text{for } T_{\text{vap,DMC}} \leq T_{\text{IF}} \leq T_{\text{vap,EC}}, \\ R_{\text{th,vap,max}} & \text{for } T_{\text{IF}} > T_{\text{vap,EC}}, \end{cases} \quad [28]$$

with

$$\Delta T_{\text{vap}} = T_{\text{vap,EC}} - T_{\text{vap,DMC}}, \quad [29]$$

where T_{IF} is the (local) temperature of the interface between can and jelly roll, $R_{\text{th,vap,max}} = 0.03077 \text{ m}^2 \text{ K W}^{-1}$ is the maximum value used for the thermal resistance which is equivalent to a gas layer thickness of $d_{\text{vap,max}} = 0.8$ mm, $T_{\text{vap,DMC}}$ is the boiling point of DMC (minimum value of Table V), and $T_{\text{vap,EC}}$ is the boiling point of EC (maximum value of Table V).

Figure 5 shows the influence of this gas layer during the heating phase (variant 2 - blue curves). There is no noticeable difference between the temperature curve of $T_{C1,HS1}$ for variant 1 and variant 2 until approximately 55 s when cell 2 goes into TR for variant 1. However, cell 2 is not going into TR for variant 2 within the first 200 s, as the heat transfer into the jelly roll of cell 2 is decreased compared to variant 1. The lower temperatures of $T_{C2,HS1}$ compared to the experiments show, that the heat transfer over the heatshield is too small.

Variant 3.—As shown in Fig. 6 between step 2 and 3 (indicated as “heat transfer to cell 2”), the bulging of the cells due to gas layer formation leads to a compression of the heatshield. As the heatshield material is compressible up to a certain limit, the decrease of the heatshield thickness is considered as third effect. Since the geometrical dimensions of the heatshield solid within the simulation cannot be changed during the calculation, the compression of the heatshield is realized by adapting the thermal conductivity with the similar temperature dependency as $R_{\text{th,vap}}$:

$$\lambda_{\text{HS}}(T_{\text{IF,avg}}) = \begin{cases} \lambda_{\text{HS,init}} & \text{for } T_{\text{IF,avg}} < T_{\text{vap,DMC}}, \\ \frac{\lambda_{\text{HS,max}}}{(\Delta T_{\text{vap}})^2} (T_{\text{IF,avg}} - T_{\text{vap,DMC}})^2 & \text{for } T_{\text{vap,DMC}} \leq T_{\text{IF,avg}} \leq T_{\text{vap,EC}}, \\ \lambda_{\text{HS,max}} & \text{for } T_{\text{IF,avg}} > T_{\text{vap,EC}}, \end{cases} \quad [30]$$

where $T_{\text{IF,avg}}$ is the surface average temperature of the interface between can and jelly roll, $\lambda_{\text{HS,init}}$ is the initial thermal conductivity of the heatshield as defined in Table IV, and $\lambda_{\text{HS,max}} = 0.15 \text{ W m}^{-1} \text{ K}^{-1}$ is the maximum value used for the thermal conductivity of the heatshield.

The influence of this heatshield compression is shown in Fig. 5 (variant 3 - red curves). Beginning at approximately 50 s, the $T_{C2,HS1}$ temperature curves of variant 2 and 3 start to diverge due to a faster temperature increase for variant 3. This is the result of the overlapping effect of the gas layer building up and the thermal conductivity of the heatshield increasing. The TR initiation in cell 2 is in between the time range of both experiments for variant 3. Therefore, variant 3 is considered to be able to reproduce the TR propagation process from cell 1 to cell 2.

Variant 4 and 5.—In Fig. 7, the simulation results are compared to the experimental results for the total time of the experiment t_{total} . Figure 7a displays the temperature sensor values on both sides of the

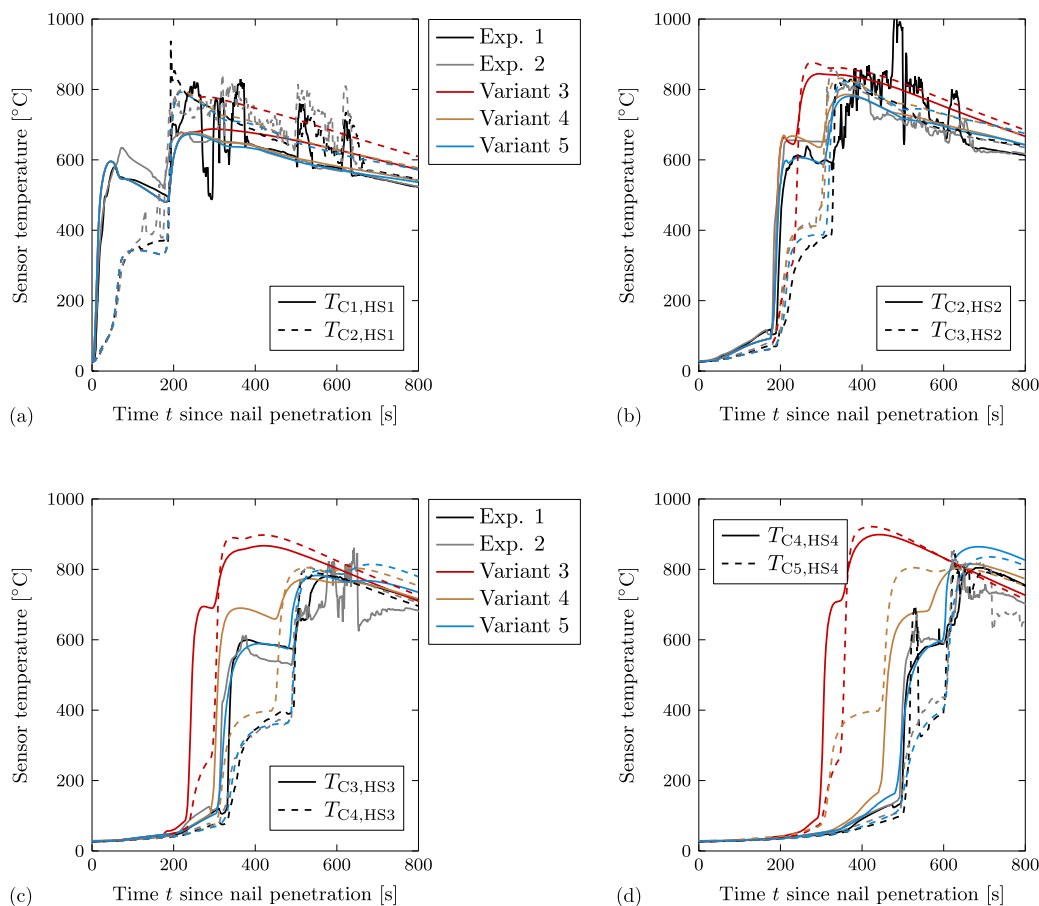


Figure 7. Sensor temperature on both sides of each heatshield over time t since nail penetration of cell 1 for both experiments (black and gray) and two simulations with different parameter sets (colored). (a) Sensor temperature on both sides of heatshield 1 (between cell 1 and 2). (b) Sensor temperature on both sides of heatshield 2 (between cell 2 and 3). (c) Sensor temperature on both sides of heatshield 3 (between cell 3 and 4). (d) Sensor temperature on both sides of heatshield 4 (between cell 4 and 5).

first heatshield (between cell 1 and 2) over time t since nail penetration of cell 1 for both experiments (black and gray) and two simulations with different parameter sets (colored). Figures 7b–7d displays the temperature sensor values on both sides of the second, third, and fourth heatshield, respectively (between cell 2 and 3, cell 3 and 4, and cell 4 and 5, respectively).

The simulation results of variant 3 (red curves) show a faster propagation for cell 3 to 5 compared to the experimental results. This can be explained by the fact that the same values for the maximum gas layer thickness are assumed for all cells (except cell 1). This assumption may be wrong as the cells have more space within the stack with each TR that occurs. Due to the mass loss of each cell during TR and the subsequent decrease of its mechanical stability, the compression force within the cell stack reduces during the course of the experiment. As a result, the resistance against a bulging of the cans is lower and it is assumed, that the maximum thickness of the gas layer increases for higher cell numbers. At the same time, the compression of the heatshields decreases. For variant 4 (brown curves), both the maximum gas layer thickness and the maximum thermal conductivity of the heatshield are adapted for each cell individually. However, there are still deviations between simulation and experimental results. In order to achieve acceptable results, the thermal resistances between jelly roll and can have to be set individually for the heated side (directed toward the cell that

underwent TR) and the “cold” side (in propagation direction). In particular, individual values of $R_{th,vap,max}$ and $R_{th,postTR}$ are defined for both sides of each cell (except cell 1). In addition, $R_{th,postTR}$ on the cold side interface is set after the TR of the adjacent cell instead of after the TR of the cell itself. This results in the curves shown for variant 5 (blue). The adaptations can be explained by the cell can’s bulging not being uniform in both directions. As illustrated in Fig. 6 for the heat transfer from cell 1 to cell 2, the gas layer may have a different thickness on the heated side in comparison to the cold side. Table VI summarizes the values used for the final parameter set (variant 5), that is able to reproduce the experimental results in acceptable quality.

In summary, the following effects of the thermal propagation process of the cell stack experiment are considered in the model:

- The jelly roll density is adapted time dependently in order to account for the mass loss during TR (except for cell 1). For the nail penetrated cell, the mass loss is already considered before the TR, i.e. the jelly roll density is set to the value after TR from the beginning of the simulation as investigated in Ref. 24.
- A thermal resistance between jelly roll and can is applied after the TR of a cell. This is supposed to represent the geometrical change of the jelly roll during TR that leads to the jelly roll being not in direct contact with the can anymore.

Table VI. Parameter values of the final parameter set (variant 5).

	$R_{\text{th,vap,max}}$ $\text{m}^2 \text{K W}^{-1}$	$R_{\text{th,postTR}}$ $\text{m}^2 \text{K W}^{-1}$	$R_{\text{th,vap,max}}$ $\text{m}^2 \text{K W}^{-1}$	$R_{\text{th,postTR}}$ $\text{m}^2 \text{K W}^{-1}$	$\lambda_{\text{HS,max}}$ $\text{W m}^2 \text{K}^{-1}$	Heatshield
	heated side		"cold" side			
Cell 1	—	0.00577	—	0.00577	—	—
Cell 2	0.03077	0.00577	0.00962	0.00462	0.15	Heatshield 1
Cell 3	0.04615	0.00865	0.02163	0.00577	0.12	Heatshield 2
Cell 4	0.06923	0.01442	0.03365	0.01442	0.072	Heatshield 3
Cell 5	0.10769	0.02308	0.05168	0.02308	0.067	Heatshield 4

- A temperature dependent thermal resistance between jelly roll an can is set for the heating phase before a TR (except for cell 1). This accounts for electrolyte vaporization, that results in bulging and gas layer formation between can and jelly roll. The maximum thickness of this gas layer is assumed to be increasing with the number of TRs, as more space is available in the cell stack due to the mass loss during TR and decreasing structural strength as a result of elevated temperatures. In addition, it is set individually for both sides of the cell (heated and "cold" side).

- The thermal conductivity of the cell-to-cell insulation material (or heatshield) is adapted in dependency of the gas layer thickness in order to consider a compression of the heatshield material due to the bulging of the cells. This phenomenon is overlapped by increasing available space within the cell stack and also adapted with an increasing number of TRs.

Results and Discussion

In a first step, three simulations of the TR propagation behavior in the cell stack experiment are performed. The results of the three different modeling approaches for heat release during TR are compared to the experimental results as well as with each other. In order to better understand the influence of the heat release method on the simulation results, further investigations in form of minor adaptations are performed and analyzed in a second step.

Figure 8 displays the temperature sensor values on both sides of the four heatshields (heatshield 1-4 in Figs. 8a–8d, respectively) over time t since nail penetration of cell 1 for both experiments (black and gray) and the three simulations with different modeling approaches for heat release during TR (colored). In Fig. 8a, it is shown that within the time span of the TR of cell 1 ($t < t_{\text{heating}} = 39.9 \text{ s}$) the deviation between the different heat release methods is small. The usage of a spatially resolved heat release ($\dot{q}(T)$ - method 3) results in a slightly higher maximum temperature value as well as a slightly higher temperature gradient for $T_{\text{C1,HS1}}$ compared to the other two methods. This behavior is also observed for $T_{\text{C2,HS1}}$. Even though the differences seem to be small, there is a significant influence of the modeling approach on the point in time when the TR in cell 2 is initiated as shown in Table VII. This behavior observed for the first heatshield between cell 1 and 2 can be also seen for the other heatshields as shown in Figs. 8b–8d. The simulation results of method 1 are within the range of the experimental results, whereas method 2 shows no TR propagation, and the TR propagation process of method 3 is too fast compared to the experimental results.

Overall, the results of method 1 show the best match with the experimental values compared to the other two methods. This is explained by the fact that the parameter fitting was done using this approach. For method 2, there is no TR propagation at all, as the volume averaged temperature of the jelly roll in cell 2 stays below the TR trigger temperature ($T_{\text{JR2,avg}} < T_{\text{TR}}$). Even though there is heat release within the jelly roll of cell 2 for $T_{\text{onset}} \leq T_{\text{JR2,avg}} < T_{\text{TR}}$, the heat generation within this temperature range in combination with the heat transferred from cell 1 does not exceed the heat dissipation from cell 2. As this is not representing the experimental results, it is concluded that method 2 is unsuitable for TR

propagation modeling with high temperature gradients within the jelly roll due to the dependence of the heat release rate on the volume averaged jelly roll temperature $T_{\text{JR,avg}}$. However, method 2 might still be applicable to TR simulations, especially for modeling of experiments with low temperature gradients within the jelly roll such as ARC. For method 3, the TR in cell 2 is triggered at $t \approx 118 \text{ s}$, which is $t \approx 63 \text{ s}$ earlier compared to the experiments. However, the temperature curves until this point in time are practically the same as for the other two methods. A crucial difference between method 1 and method 3, that can cause this deviation, is the consideration of exothermic side reactions that are occurring at temperatures below T_{TR} . For method 3, the onset of (small) heat release rates is at $T_{\text{onset}} = 75.2 \text{ }^\circ\text{C}$, whereas for method 1 this heat release due to side reactions is neglected. Although the heat release rates within the temperature range of $T_{\text{onset}} \leq T_{\text{JR}} < T_{\text{TR}}$ are significantly lower compared to the heat release rates during TR, it is hypothesized that these accelerate the TR propagation process in the simulation model. In order to further analyze this phenomenon, a simulation with a modified version of method 3 ($\dot{q}_{\text{mod}}(T)$) is performed. By setting $T_{\text{onset}} = T_{\text{TR}}$, there is no more modeling of the heat release due to side reactions and consequently, the criteria for the begin of heat release is the same as for method 1.

Figure 9 displays the temperature sensor values on both sides of the four heatshields (heatshield 1–4 in Figs. 9a–9d, respectively) over time t since nail penetration of cell 1 for both experiments (black and gray) and the simulation results of both method 1 and the modified method 3 (colored). If the heat release is neglected within the temperature range of $T_{\text{onset}} \leq T_{\text{JR}} < T_{\text{TR}}$, the results of method 1 and method 3 (modified) show smaller deviations compared to the results in Fig. 8. For both method 1 and method 3 (modified), the time of TR initiation is within the range of the experiments range for cell 2 and cell 3 (see Table VIII). For cell 4 and 5, however, there are still deviations from method 1 and the experiments. A possible reason for this behavior are the chosen parameters for method 3, such as the reaction rate C . Decreasing C leads to a slower TR reaction within each cell and hence to a longer TR duration. As a consequence, the heat release rates during TR are lower. This results in reduced maximum temperatures of the jelly roll and therefore, the time between TRs is prolonged. By further adapting the heat source parameters, it should be possible to achieve matching results for both methods.

Concluding the results shown in Figs. 8 and 9, it remains to be seen whether the assumption of neglecting the heat release due to side reactions is justified. On the one hand, the simulated sensor values are in accordance with the experimental temperature curves. Therefore, it is concluded that the heat transfer paths are modeled correctly. On the other hand, it was proven in many experiments, that there is a heat release within the temperature range of $T_{\text{onset}} \leq T_{\text{JR}} < T_{\text{TR}}$ and consequently, method 3 in its unmodified version models the actual physics more accurate than the other methods. An effect that can resolve this issue is for example the heat of vaporization.⁴¹ It is hypothesized that the heat of vaporization of the electrolyte solvents is approximately in equilibrium with the heat generation due to side reactions. Eventually, this could explain why the simulation results without consideration of side reactions are in better agreement with the experiments than the simulation results with consideration of side reactions.

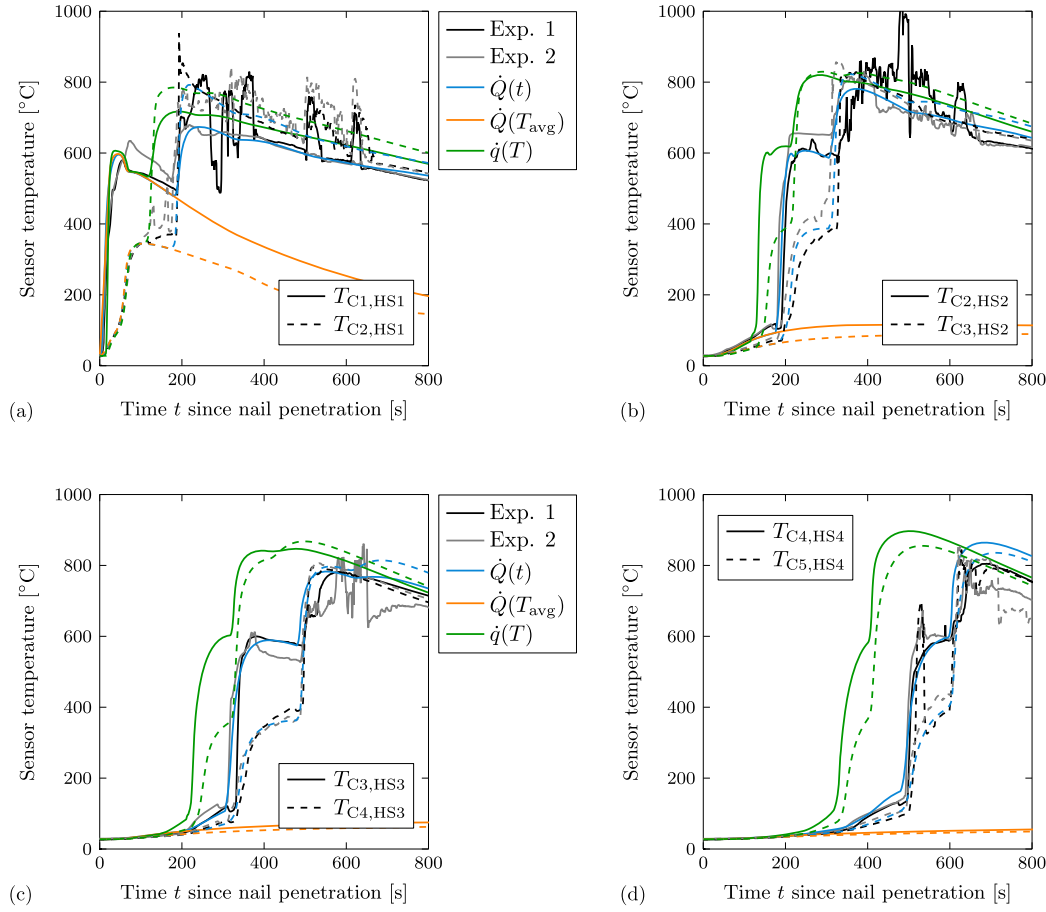


Figure 8. Sensor temperature on both sides of each heatshield over time t since nail penetration of cell 1 for both experiments (black and gray) and the three simulations with different modeling approaches for the heat release during TR (colored). (a) Sensor temperature on both sides of heatshield 1 (between cell 1 and 2). (b) Sensor temperature on both sides of heatshield 2 (between cell 2 and 3). (c) Sensor temperature on both sides of heatshield 3 (between cell 3 and 4). (d) Sensor temperature on both sides of heatshield 4 (between cell 4 and 5).

Table VII. Time of TR initiation in each cell for both experiments and the three simulations.

No.	Cell 2	Cell 3	Cell 4	Cell 5
Exp. 1	187 s	326 s	494 s	599 s
Exp. 2	175 s	306 s	488 s	607 s
Exp. Mean	181 s	316 s	491 s	603 s
Method 1: $\dot{Q}(t)$	182 s	313 s	487 s	604 s
Method 2: $\dot{Q}(T_{\text{avg}})$	no TR	no TR	no TR	no TR
Method 3: $\dot{q}(T)$	118 s	217 s	323 s	407 s

Table IX summarizes the computational time needed to run the simulations. All simulations were performed on the same high performance cluster, but with different numbers of CPU cores. Therefore, the computation time per core is used to compare the different methods. The simulation with method 1 needs the lowest number of iterations and hence the lowest amount of time per core. As there is no propagation for the simulation with method 2, the computational time is not comparable to the other methods. This is due to the adaptive time step, that is significantly lower for the phase of a TR ($\Delta t_{\text{step}} \leq 0.05$ s) compared to the phase between

Table VIII. Time of TR initiation in each cell for both experiments, the reference simulation (method 1), and the modified simulation (method 3).

No.	Cell 2	Cell 3	Cell 4	Cell 5
Exp. 1	187 s	326 s	494 s	599 s
Exp. 2	175 s	306 s	488 s	607 s
Exp. Mean	181 s	316 s	491 s	603 s
Method 1: $\dot{Q}(t)$	182 s	313 s	487 s	604 s
Method 3: $\dot{q}_{\text{mod}}(T)$	185 s	310 s	474 s	563 s

TRs ($\Delta t_{\text{step}} \leq 2$ s). Therefore, the total time of simulation is correlating with the number of occurring TRs and a simulation with less TRs will always be faster. The simulation using method 3 needs approximately 4.6 times more iterations to perform the calculation. This leads to an approximately 2.3 times higher time per core. As the number of TRs is the same for method 1 and method 3, it is assumed that a further parameter fitting for method 3 in order to better match the experimental findings will result in comparable values. In conclusion, method 1 is the most efficient modeling approach for TR propagation simulations investigated in this study.

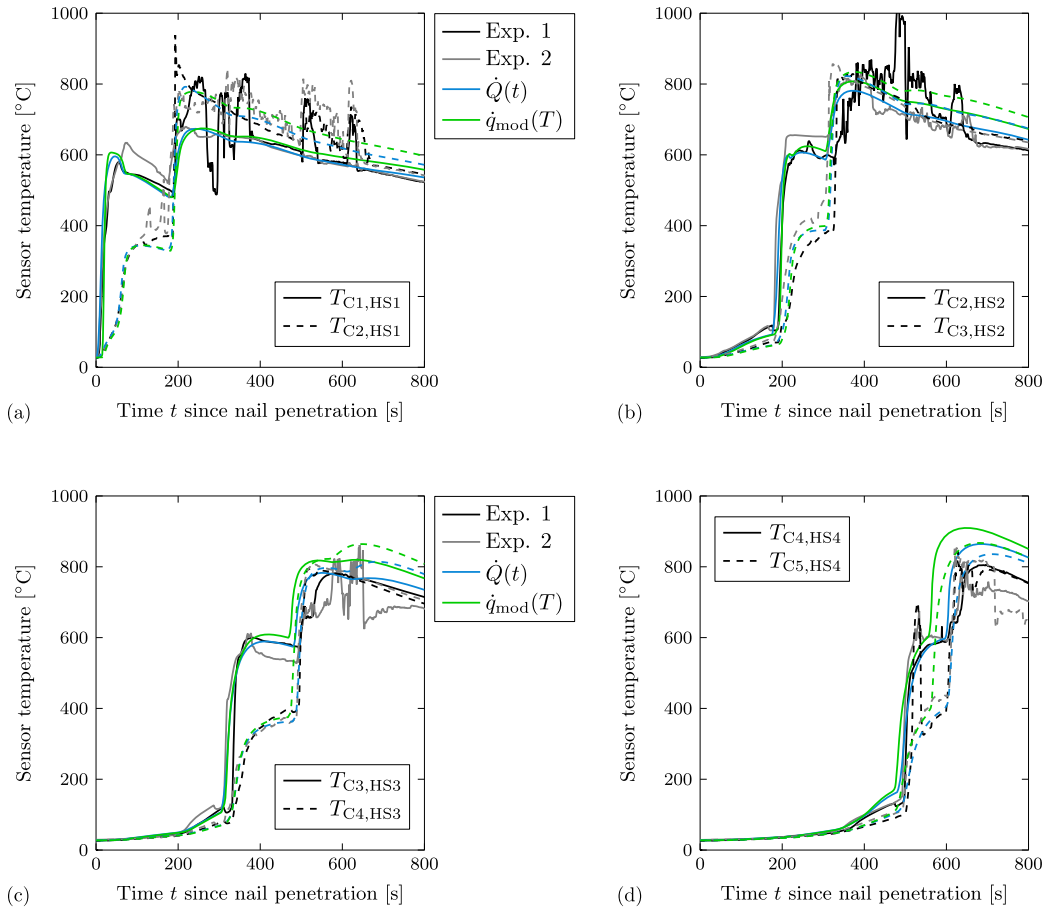


Figure 9. Sensor temperature on both sides of each heatshield over time t since nail penetration of cell 1 for both experiments (black and gray) and the simulations results for method 1 and modified method 3 (colored). (a) Sensor temperature on both sides of heatshield 1 (between cell 1 and 2). (b) Sensor temperature on both sides of heatshield 2 (between cell 2 and 3). (c) Sensor temperature on both sides of heatshield 3 (between cell 3 and 4). (d) Sensor temperature on both sides of heatshield 4 (between cell 4 and 5).

Table IX. Comparison of the modeling approaches regarding computational time.

No.	Number of iterations	Total time	Number of cores	Time per core
Method 1: $\dot{Q}(t)$	139655	35070 s	64	548 s/core
Method 2: $\dot{Q}(T)$	not comparable, as there is no propagation			
Method 3: $\dot{q}_{\text{mod}}(T)$	637000	134651 s	108	1247 s/core

Conclusions

In this study, three empirical modeling approaches for the heat release during a lithium-ion battery TR are analyzed and compared with regard to their suitability for TR propagation simulation. More specifically, a simulation model of a battery cell stack experiment conducted with prismatic lithium-ion batteries (>60 Ah) is set up and the different modeling approaches are applied. In contrast to previous studies, the model takes into account phenomena that were observed in the experiments such as the formation of a gas layer between jelly roll and can due to electrolyte vaporization. The simulation results of the three modeling approaches are analyzed and compared to the experimental results. In addition, the computational effort of the different approaches is investigated.

In order to reproduce the experimental results, two phenomena of the thermal propagation process have to be considered: the mass loss during TR as well as the electrolyte vaporization. To model the mass loss during TR, it is proposed to adapt the jelly roll density by a time dependent function. In addition, a thermal resistance between jelly roll and can is introduced after a TR. This is supposed to represent the geometrical change of the jelly roll during TR due to the mass loss, that leads to the jelly roll being not in direct contact with the can anymore. For the electrolyte vaporization, a temperature dependent thermal resistance between jelly roll and can is proposed. This accounts for the gas layer between jelly roll and can and the subsequent bulging of the cell. The latter also leads to a compression of the cell-to-cell insulation materials. Therefore, the insulation material's thermal conductivity is adjusted with the same dependency. In addition, both the thermal resistance of the gas layer and

the compression of the cell-to-cell insulation material are set individually for each cell. This accounts for more space being available in the cell stack with each cell that is going into TR.

The effect of different modeling approaches for the heat release during TR is significant for TR propagation simulation. Only two of the three compared modeling approaches are suitable for the application to the investigated cell stack experiment. The time dependent approach shows the best agreement with the experiment and the lowest computational time. Consequently, this method is recommended for TR propagation simulations where large time spans are expected. The spatially resolved temperature dependent method also shows promising results, but further parameter adaptations are necessary. Within this study, the experimental results are only reproducible if the side reactions occurring before a TR at elevated temperatures are neglected. Therefore, it is assumed that further effects such as heat of vaporization of the electrolyte should be considered for the spatially resolved heat release method. The temperature dependent method with spatially uniform heat release is unsuitable to model the investigated cell stack experiment. This is due to the heat release rates depending on the volume averaged jelly roll temperature, which is not exceeding the TR trigger temperature for the second cell of the cell stack. Consequently, this method fails to model the TR propagation for the investigated case. However, this method might still be applicable to TR simulations, especially for the modeling of experiments with low temperature gradients within the jelly roll such as ARC.

In conclusion, the modeling of a TR propagation process still remains challenging. On the one hand, this study shows that it is possible to reproduce the experimental results of a battery cell stack experiment with empirical methods and acceptable computational effort. On the other hand, it is crucial to consider physical effects such as the electrolyte vaporization and subsequent cell can bulging in order to achieve these results. The authors therefore want to stress the necessity of additional investigations regarding this phenomenon. Especially the usage of heat release methods that aim to accurately model the TR process require further adaptations as for example taking into account the heat of electrolyte vaporization when side reactions at temperatures lower than the TR trigger temperature are included. The results presented in this study contribute to the improvement of TR propagation simulations and therefore help engineers or researchers to design a safer battery pack.

Acknowledgments

The authors would like to gratefully acknowledge the support of ZSW Ulm, Germany for the execution of the 5 cell stack experiments. In addition, S. Hoelle acknowledges the support of the TUM Graduate School.

ORCID

S. Hoelle  <https://orcid.org/0000-0002-6381-8104>

S. Zimmermann  <https://orcid.org/0000-0002-1399-9242>

O. Hinrichsen  <https://orcid.org/0000-0002-3796-6920>

References

1. K. Brandt and J. Garche, "General overview of Li-secondary battery safety issues. Electrochemical power sources: fundamentals, systems, and applications: Li-battery safety." *Electrochemical Power Sources: Fundamentals, Systems, and Applications*, ed. J. Garche and K. Brandt (Elsevier) p. 127 (2019).
2. J. Deng, C. Bae, A. Denlinger, and T. Miller, "Progress in battery safety modeling." *Progress in Energy*, **4**, 043001 (2022).
3. J. Liu, J. Li, and J. Wang, "In-depth analysis on thermal hazards related research trends about lithium-ion batteries: a bibliometric study." *Journal of Energy Storage*, **35**, 102253 (2021).
4. F. Baakes, M. Lütke, M. Gerasimov, V. Laue, F. Röder, P. B. Balbuena, and U. Kreuer, "Unveiling the interactions of reactions and phase transition during thermal runaway abuse of Li-ion batteries." *Journal of Power Sources*, **522**, 230881 (2022).
5. T. D. Hatchard, D. D. MacNeil, A. Basu, and J. R. Dahn, "Thermal model of cylindrical and prismatic lithium-ion cells." *J. Electrochem. Soc.*, **148**, A755 (2001).
6. Y. Jia, M. Uddin, Y. Li, and J. Xu, "Thermal runaway propagation behavior within 18,650 lithium-ion battery packs: a modeling study." *Journal of Energy Storage*, **31**, 101668 (2020).
7. A. Kurzawski, L. Torres-Castro, R. Shurtz, J. Lamb, and J. C. Hewson, "Predicting cell-to-cell failure propagation and limits of propagation in lithium-ion cell stacks." *Proceedings of the Combustion Institute*, **38**, 4737 (2021).
8. P. T. Coman, E. C. Darcy, C. T. Veje, and R. E. White, "Numerical analysis of heat propagation in a battery pack using a novel technology for triggering thermal runaway." *Applied Energy*, **203**, 189 (2017).
9. J. Yikai and J. Xu, "Modeling of thermal propagation based on two cylindrical lithium-ion cells." *Journal of Electrochemical Energy Conversion and Storage*, **17**, 1 (2019).
10. W. Zhang, Z. Liang, X. Yin, and G. Ling, "Avoiding thermal runaway propagation of lithium-ion battery modules by using hybrid phase change material and liquid cooling." *Applied Thermal Engineering*, **184**, 116380 (2021).
11. P. Jindal, B. S. Kumar, and J. Bhattacharya, "Coupled electrochemical-abuse-heat-transfer model to predict thermal runaway propagation and mitigation strategy for an EV battery module." *Journal of Energy Storage*, **39**, 102619 (2021).
12. X. Feng, X. He, M. Ouyang, L. Lu, P. Wu, C. Kulp, and S. Prasser, "Thermal runaway propagation model for designing a safer battery pack with 25 Ah LiNi_{0.8}Co_{0.1}Mn_{0.1}O₂ large format lithium ion battery." *Applied Energy*, **154**, 74 (2015).
13. C. Yuan, Q. Wang, Y. Wang, and Y. Zhao, "Inhibition effect of different interstitial materials on thermal runaway propagation in the cylindrical lithium-ion battery module." *Applied Thermal Engineering*, **153**, 39 (2019).
14. J. Chen, D. Ren, H. Hsu, L. Wang, X. He, C. Zhang, X. Feng, and M. Ouyang, "Investigating the thermal runaway features of lithium-ion batteries using a thermal resistance network model." *Applied Energy*, **295**, 117038 (2021).
15. C. Xu, H. Wang, F. Jiang, X. Feng, L. Lu, C. Jin, F. Zhang, W. Huang, M. Zhang, and M. Ouyang, "Modelling of thermal runaway propagation in lithium-ion battery pack using reduced-order model." *Energy*, **268**, 126646 (2023).
16. X. Liu, Z. Wu, S. I. Stolarov, M. Denlinger, A. Masias, and K. Snyder, "A Thermo-Kinetic model of thermally-induced failure of a lithium ion battery: development, validation and application." *J. Electrochem. Soc.*, **165**, A2909 (2018).
17. X. Feng, L. Lu, M. Ouyang, J. Li, and X. He, "A 3D thermal runaway propagation model for a large format lithium ion battery module." *Energy*, **115**, 194 (2016).
18. P. T. Coman, E. C. Darcy, and R. E. White, "Simplified thermal runaway model for assisting the design of a novel safe li-ion battery pack." *J. Electrochem. Soc.*, **169**, 040516 (2022).
19. K. F. Yeow and H. Teng, "Characterizing thermal runaway of lithium-ion cells in a battery system using finite element analysis approach." *SAE Int. J. Alt Power*, **2**, 179 (2013).
20. M. Citarella, D. Suzzi, B. Brunsteiner, P. Schiffbänker, G. Maier, and J. Schneider, "Computational modelling of thermal runaway propagation in lithium-ion battery systems." *2019 IEEE Transportation Electrification Conference (ITEC-India)* (2019).
21. J. Qin, S. Zhao, X. Liu, and Y. Liu, "Simulation study on thermal runaway suppression of 18650 lithium battery." *Energy Sources, Part A: Recovery, Utilization, and Environmental Effects*, **1** (2020).
22. D. Grimmisen and M. S. Schneider, "Numerical simulation of cell venting within a simplified 18650 li-ion battery pack." *13th European LS-DYNA Conference 2021* (2021).
23. S. Hoelle, S. Haberl, A. Rheinfeld, P. Osswald, S. Zimmermann, and O. Hinrichsen, "Experimental investigation on thermal runaway propagation in lithium-ion battery cell stack." *2022 IEEE Transportation Electrification Conference & Expo (ITEC)* (2022).
24. S. Hoelle, F. Dengler, S. Zimmermann, and O. Hinrichsen, "3D thermal simulation of lithium-ion battery thermal runaway in autoclave calorimetry—development and comparison of modeling approaches." *J. Electrochem. Soc.*, **170**, 010509 (2023).
25. S. Schamer, "Quantitative safety characterization of Li-ion cells." *JRC Exploratory Research Workshop* (2018).
26. S. Hoelle, S. Schamer, S. Asanin, and O. Hinrichsen, "Analysis on thermal runaway behavior of prismatic lithium-ion batteries with autoclave calorimetry." *J. Electrochem. Soc.*, **168**, 120515 (2021).
27. K. Shen, Y. Mao, Y. Zheng, W. Yang, and B. Wu, "One-dimensional modeling and experimental analysis of nail penetration thermal runaway for large capacity Li-ion power battery." *J. Electrochem. Soc.*, **169**, 040502 (2022).
28. P. J. Bugryniec, J. N. Davidson, and S. F. Brown, "Computational modelling of thermal runaway propagation potential in lithium iron phosphate battery packs." *Energy Reports*, **6**, 189 (2020).
29. Y. Li, G. Liu, and Z. Li, "Numerical modeling of thermal runaway in high-energy lithium-ion battery packs induced by multipoint heating." *Case Studies in Thermal Engineering*, **38**, 102335 (2022).
30. D. Mishra, K. Shah, and A. Jain, "Investigation of the impact of flow of vented gas on propagation of thermal runaway in a Li-ion battery pack." *J. Electrochem. Soc.*, **168**, 060555 (2021).
31. D. Mishra, K. Shah, and A. Jain, "Investigation of the impact of radiative shielding by internal partition walls on propagation of thermal runaway in a matrix of cylindrical Li-ion cells." *J. Electrochem. Soc.*, **168**, 120507 (2021).
32. D. Mishra and A. Jain, "Multi-mode heat transfer simulations of the onset and propagation of thermal runaway in a pack of cylindrical Li-ion cells." *J. Electrochem. Soc.*, **168**, 020504 (2021).
33. P. Vyroubal, T. Kazda, and M. Mačák, "The numerical simulation of thermal abuse and runaway in lithium ion battery pack." *ECS Trans.*, **105**, 549 (2021).
34. S. Bilyaz, K. C. Marr, and O. A. Ezekoye, "Modeling of thermal runaway propagation in a pouch cell stack." *Fire Technology*, **56**, 2441 (2020).
35. M. Steinhardt, J. V. Barreras, H. Ruan, B. Wu, G. J. Offer, and A. Jossen, "Meta-analysis of experimental results for heat capacity and thermal conductivity in lithium-ion batteries: a critical review." *Journal of Power Sources*, **522**, 230829 (2022).

3.1 Thermal propagation in open systems without housing

Journal of The Electrochemical Society, 2023 **170** 060516

36. D. P. Finegan et al., "In-operando high-speed tomography of lithium-ion batteries during thermal runaway." *Nat. Commun.*, **6**, 6924 (2015).
37. D. P. Finegan et al., "Characterising thermal runaway within lithium-ion cells by inducing and monitoring internal short circuits." *Energy & Environmental Science*, **10**, 1377 (2017).
38. M. Sharp et al., "Thermal runaway of Li-ion cells: how internal dynamics, mass ejection, and heat vary with cell geometry and abuse type." *J. Electrochem. Soc.*, **169**, 020526 (2022).
39. K. Xu, "Nonaqueous liquid electrolytes for lithium-based rechargeable batteries." *Chem. Rev.*, **104**, 4303 (2004).
40. P. T. Coman, S. Matefi-Tempfli, C. T. Veje, and R. E. White, "Modeling vaporization, gas generation and venting in Li-ion battery cells with a dimethyl carbonate electrolyte." *J. Electrochem. Soc.*, **164**, A1858 (2017).
41. B. Wang, C. Ji, S. Wang, and S. Pan, "A detailed finite element model of internal short circuit and venting during thermal runaway in a 32650 lithium-ion battery." *Fire Technology*, **56**, 2525 (2020).

3.2 Thermal propagation in closed systems with housing

As shown in section 1.4, studies investigating all aspects of the TP process, in particular the effect of vented gas and particles, are rare. Especially on battery pack level, where a major influence of Q_{venting} on the TP process is expected, the number of publications is small. This can be related to the high expenses that are linked to battery pack testing. Cell stack experiments represent a promising alternative for addressing both the lack of studies considering Q_{venting} and the high expenses of battery pack testing. Therefore, the cell stack has to be integrated into a housing, as done for example by Wang et al. in Ref. [183]. In order to quantify the influence of Q_{venting} on the propagation time, however, it is necessary to compare the same stack setup with and without housing. This was done in the study presented in section 3.2.1. Another aspect that was studied little so far is the behavior of vented particles. Section 3.2.2 therefore presents both an experimental study that aims to determine the deposition of particles vented during a TR in a battery module environment, as well as a gas-particle-flow model simulating this experiment. The results not only provide a better understanding of the gas-particle-flow evolving within battery packs during a TR, but also are the basis for the fluid domain of the coupled simulation model developed in this thesis.

3.2.1 Experimental comparison of open and closed systems

The conference paper titled “*Experimental Investigation on Thermal Runaway Propagation in Lithium-Ion Battery Cell Stack*” is presented within this section. It was submitted to the peer-reviewed *2022 IEEE Transportation Electrification Conference & Expo (ITEC)* in December 2021 and published online in July 2022. The main findings of this work were presented by S. Hoelle at the conference in Anaheim, CA, USA, in June 2022.

The objective of this work was to evaluate the effect of components that are related to the integration of lithium-ion cells into a battery pack, such as cooler, module structure, or housing, on the TP behavior in terms of propagation time and mass loss during TR. Therefore, five different setup variants of a cell stack consisting of five prismatic lithium-ion cells ($> 60 \text{ Ah}$) were examined with three test repetitions each. More precisely, the baseline variant of the cell stack consisted of five cells with a cell-to-cell insulation material in between that were compressed between two pressure plates. For the first variant, an aluminum plate imitating a cooler was attached to the bottom of the cell stack. The second variant additionally contained aluminum plates attached to the sides of the cell stack representing a battery module’s side plates. These three variants were investigated within an open setup without housing. In order to quantify the influence of vented gas and particles, both the baseline setup and the second variant were also tested within a housing.

The attachment of a cooling plate reduced the total propagation time of the cell stack (time span between nail penetration of cell 1 and TR initiation in cell 5) to 52.4% compared to the reference case without cooling plate. Additional side plates resulted in a reduction of the total propagation time to 47.5% compared to the reference case. As the

first comparison was conducted within an open setup, vented gas and particles played a minor role. Consequently, the acceleration of the TP process was explained by additional heat transfer paths via the cooling and/or side plates. Both variations also had an effect on the mass loss: the cell stacks with an attached cooling plate showed a lower mass loss during TR than the cell stacks of the reference case. The additional side plates further reduced the mass loss during TR. This was explained by the different constraints the cells were exposed to. Without cooling and side plates, the integration of the cell stack into a housing reduced the total propagation time to 48.7%. Comparing the setup with cooling and side plates in an open and closed setup resulted in a reduction of the total propagation time to 64.3%.

In conclusion, the results of the study showed, that not only gas and particles, but also the module structure have a major influence on the TP process within a battery cell stack. This has to be considered when performing cell stack tests that aim to replace or reduce the number of experiments conducted on module or battery pack level. In addition, the results of the closed variants provide an excellent basis for the validation of simulation models that consider at least a gas and maybe even a particle phase.

Experimental Investigation on Thermal Runaway Propagation in Lithium-Ion Battery Cell Stack

S. Hoelle, S. Haberl, A. Rheinfeld, P. Osswald, S. Zimmermann, and O. Hinrichsen

2022 IEEE Transportation Electrification Conference & Expo (ITEC), pp. 1174–1179

Permanent weblink:

<https://doi.org/10.1109/ITEC53557.2022.9813813>

© 2022 IEEE.

Reprinted, with permission, from the IEEE, which does not require individuals working on a thesis to obtain a formal reuse license. In reference to IEEE copyrighted material which is used with permission in this thesis, the IEEE does not endorse any of Technical University of Munich's products or services. Internal or personal use of this material is permitted. If interested in reprinting/republishing IEEE copyrighted material for advertising or promotional purposes or for creating new collective works for resale or redistribution, please go to http://www.ieee.org/publications_standards/publications/rights/rights_link.html to learn how to obtain a License from RightsLink.

Author contributions:

S. Hoelle developed the evaluation methodology, carried out the data analysis, and supported in design and development of the experimental setup as well as in test planning and execution. S. Haberl designed and developed the experimental setup and supported in test planning, execution and data analysis. A. Rheinfeld and P. Osswald supported in design and development of the experimental setup as well as in test planning and execution. The manuscript was written by S. Hoelle and was edited by S. Haberl, A. Rheinfeld, P. Osswald, S. Zimmermann, and O. Hinrichsen. All authors discussed the data and commented on the results.

Experimental Investigation on Thermal Runaway Propagation in Lithium-Ion Battery Cell Stack

Sebastian Hoelle^{*†§}, Simon Haberl[†], Alexander Rheinfeld[†],
Patrick Osswald[†], Sascha Zimmermann[†] and Olaf Hinrichsen^{*‡}

^{*}Technical University of Munich, Department of Chemistry, 85748 Garching near Munich, Germany

[†]BMW Group, 80809 Munich, Germany

[‡]Technical University of Munich, Catalysis Research Center, 85748 Garching near Munich, Germany

[§]Email: sebastian.hoelle@bmw.de, ORCID: 0000-0002-6381-8104

Abstract—The propagation behavior of a prismatic state-of-the-art prototype lithium-ion battery (NMC811–graphite) is examined in a 5 cell stack experiment in order to evaluate the influence of components that come along with the integration into a battery pack such as cooler, module structure or housing. A total number of 15 experiments are conducted (5 different setup variants with 3 test repetitions each). Thereby, the propagation time is evaluated and compared. The results show that for example the integration of the cell stack into a housing leads to a total propagation time that is 48.7% of the reference setup’s propagation time without housing. This study helps not only to get a better understanding of the TR propagation process in general, but also to estimate the thermal runaway propagation behavior on module or pack level by conducting tests on a smaller scale with reduced costs.

I. INTRODUCTION

The annual number of publications on thermal hazards of lithium-ion batteries increased in an approximately exponential manner during the last years. One of the current research hotspots within this field are the thermal runaway (TR) propagation mechanisms within large format battery modules or packs [1]. Feng et al. [2] were one of the first to investigate the TR propagation behavior with a cell stack consisting of 6 prismatic cells in 2015. During the following years, researchers performed comparable experiments with prismatic cells of higher capacity and different trigger methods [3]–[10]. These studies mainly focus for example on the influence of

- a cooling plate (filled with liquid coolant) [3], [4],
- different cell-to-cell insulation materials [3]–[5],
- different cathode materials [6], [7],
- different trigger mechanisms [8],
- different states of charge [9]
- or different electrical connections [10].

Others used the cell stack setup to study the TR propagation behavior of pouch cells with a similar focus [11]–[13]. However, the chosen cell stack setups / configurations discussed within the latter publications often do not adequately account for the geometric conditions defined by a certain battery pack application, such as an electric vehicle. Usually, there are additional components which ought to be represented within the test configuration, such as the module structure and / or the module surroundings within the battery pack housing. There is only a small number of publications that take into account

these components [14]–[16]. Possible reasons are the increased costs for the battery module or pack itself as well as a limited access to test facilities that are capable of performing such tests.

This publication focuses on the TR propagation behavior of a prismatic state-of-the-art prototype lithium-ion battery. The objective is to evaluate the influence of components that come along with the integration into a battery pack such as cooler, module structure and battery pack housing. A novel cell stack test setup with the possibility to examine different variations of attached components is proposed. The results help not only to get a better understanding of the TR propagation process in general, but also to estimate the TR propagation behavior on module or pack level by conducting tests on a smaller scale with reduced costs. To the authors’ knowledge, the influence of battery pack components applied to a cell stack have not been the subject of any scientific publication and consequently, the results of this study contribute to the design of safer battery packs.

II. EXPERIMENTAL

In total, 15 cell stacks (5 different setup variants with 3 test repetitions each) consisting of 5 lithium-ion battery cells are triggered into TR by nail penetration in order to investigate the TR propagation behavior. The batteries used in this study are state-of-the-art prototype cells with $\text{LiNi}_{0.8}\text{Mn}_{0.1}\text{Co}_{0.1}\text{O}_2$ (NMC811) / graphite electrodes, prismatic cell format and a nominal capacity of 63.5 Ah. The objective is to analyze the influence of components that are attached to a cell stack due to the integration into a module or battery pack. Therefore, a cooling plate and side plates are successively attached to the investigated cell stack. The resulting variants are then tested in an open setup as well as integrated into a housing.

A. 5 cell stack setup

Fig. 1 shows the 5 cell stack setup with its different components. The tested battery cells (light gray) are stacked together with a compressible cell-to-cell insulation material in between (blue - thickness 1.1 mm). The stack itself is compressed by pressure plates (dark blue), whereby the outer pressure plates are fixed and the intermediate pressure plate is movable. This allows to measure the compression force that

3 Thermal Propagation Behavior of Lithium-Ion Battery Cell Stacks

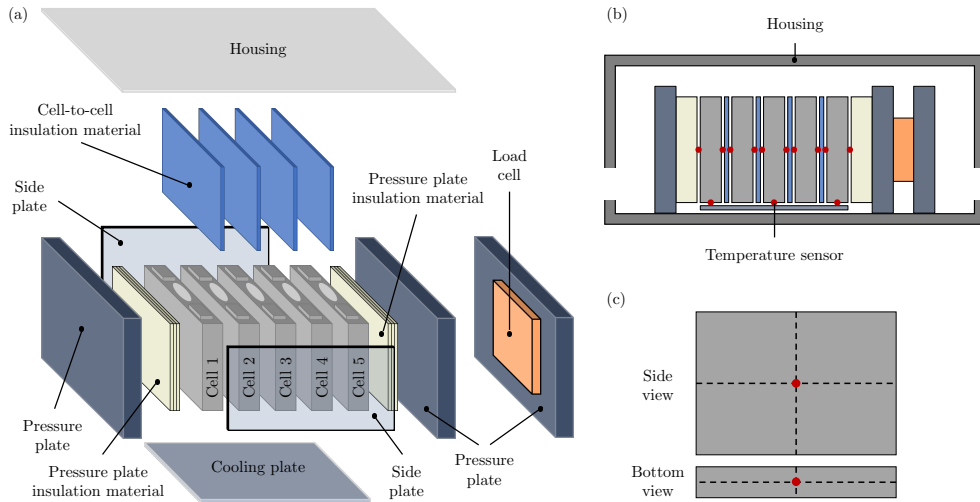


Fig. 1. (a) Experimental test setup with all components. (b) Plane section of the experimental test setup. (c) Positioning of temperature sensors on cell sides.

acts on the cell stack with the integrated load cell (orange). An insulation material (light yellow – fermacell®, 10 mm thickness) is placed between the outer cells (cell 1 and cell 5) and the pressure plates to ensure a minimal heat transfer to the test frame.

This described base setup can be extended by a cooling plate (dark gray – aluminum plate, 1.2 mm thickness) and / or side plates (transparent blue – aluminum plate, 1.8 mm thickness). Both are attached to the cell stack with a structural adhesive (thermal conductivity of 1 W(mK)^{-1} , 0.8 mm thickness). Furthermore, the whole setup can be integrated into a housing as shown in Fig. 1b. It is ensured that there is a gap similar to the battery pack condition between the cooling plate and the test setup surroundings as well as between the cells’ top surface and the housing. Tab. I provides an overview over all variants of the cell stack setup that are examined in this study. For each variant, 3 tests are conducted to evaluate the variance.

TABLE I
SETUP VARIANTS EXAMINED IN THIS STUDY

Variant	Cell-to-cell insulation material	Cooling plate	Side plates	Housing	Number of tests
Reference	yes	no	no	no	3
Variant 1	yes	yes	no	no	3
Variant 2	yes	yes	yes	no	3
Variant 3	yes	no	no	yes	3
Variant 4	yes	yes	yes	yes	3

Cell 1 is triggered into TR by nail penetration for all tests. Therefore, a steel nail with 3 mm diameter and 30° nail tip angle is used. The penetration depth is 17.5 mm in the center of the bottom side with a penetration speed of 7 mm s^{-1} .

B. Measured parameters and test procedure

Tab. II summarizes all measured parameters before, during and after the stack test. The setup is built up at a state of charge of $SoC = 30\%$. Afterwards, the stack is compressed to a force of 3 kN, followed by a charging of the cells to $SoC = 100\%$ with the CCCV charging method. It is ensured that the compression force at start of testing is within a range of $4.3 \pm 0.3 \text{ kN}$. In addition, the weight of the cell stack m_{stack} is measured before as well as after the test ($m_{\text{stack,TR}}$). In this case, the “cell stack” includes the 5 cells, the 4 thermal barriers and the attached sensors. The relative mass loss during TR propagation Δm_{stack} is then calculated by

$$\Delta m_{\text{stack}} = \frac{m_{\text{stack}} - m_{\text{stack,TR}}}{m_{\text{stack}}} . \quad (1)$$

Temperature sensors are placed in the center of the large sides of each cell as shown in Fig. 1b and 1c. Additional sensors are located in the center of the bottom side of cell 1, cell 3 and cell 5. The sensor on the nail-penetrated side is shifted by 1 cm in order to prevent a damage by the nail.

TABLE II
MEASURED PARAMETERS BEFORE, DURING AND AFTER THE CELL STACK TEST

Parameter	Symbol	Unit	Frequency	Comment
Cell can temperature	$T_{j,\text{cell},i}$	°C	10 Hz	2 - 3 positions per cell
Cell voltage	$U_{\text{cell},i}$	V	10 Hz	
Compression force	F_{stack}	N	10 Hz	
Stack mass (before test)	m_{stack}	kg	single value	
Stack mass (after test)	$m_{\text{stack,TR}}$	kg	single value	

III. RESULTS AND DISCUSSION

For each variant of the 5 cell stack setups, 3 experiments were conducted (see Tab. I). The first cell was triggered into TR reproducibly by nail penetration and a thermal propagation through the whole stack was observed in all tests. The resulting propagation time and its dependency on the setup's variant is analyzed. Therefore, the begin of the propagation event at $t = 0$ s is set to the moment when the nail penetrates cell 1. All results given as time t or duration Δt are normalized with the total propagation time, i.e. the time of TR in cell 5, of the reference case t_{ref} :

$$\text{Time of TR : } \frac{t_{\text{TR,cell},i}}{t_{\text{ref}}} \cdot 100 \% \quad (2)$$

$$\text{Time span between TRs : } \frac{\Delta t_{\text{TR,cell},i \rightarrow i+1}}{t_{\text{ref}}} \cdot 100 \% \quad (3)$$

In this context, the criteria for the start of a TR in cell i is

$$\frac{dU_{\text{cell},i}}{dt} < 0 \text{ V s}^{-1} \quad \text{and} \quad (4)$$

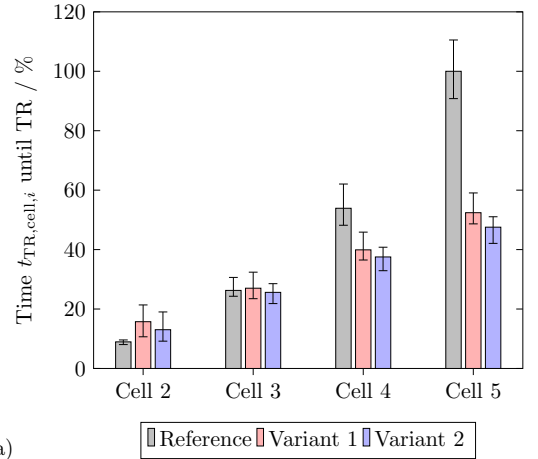
$$\frac{dT_{j,\text{cell},i}}{dt} > 10 \text{ K s}^{-1} \quad (5)$$

with $U_{\text{cell},i}$ being the voltage of cell i and $T_{j,\text{cell},i}$ being any temperature sensor j on the cell can surface of cell i .

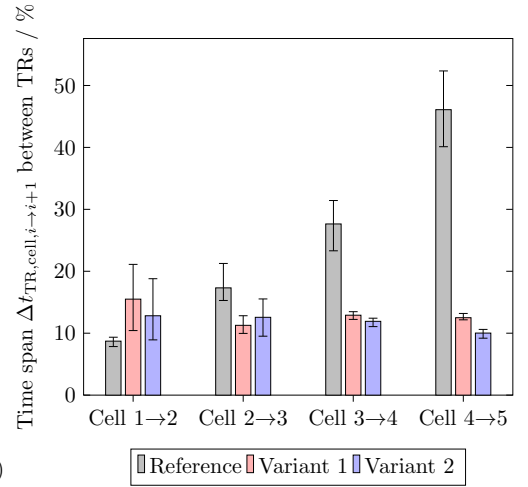
Fig. 2 displays the time $t_{\text{TR,cell},i}$ at which the TR of cell i occurs after nail penetration of cell 1 (Fig. 2a) and the time span $\Delta t_{\text{TR,cell},i \rightarrow i+1}$ between the TRs of two adjacent cells (Fig. 2b) for the test variants without housing. For each variant, the mean value over all 3 tests is presented including error bars that show the variance between the repeated tests within each setup.

As shown in Fig. 2a, the total propagation time of the stack $t_{\text{TR,cell},5}$ is reduced to 52.4% of t_{ref} by attaching a cooling plate (Variant 1 - red). Additional side plates (Variant 2 - blue) reduce the total propagation time to 47.5% of t_{ref} (Reference - gray). Cell 4 shows a similar behavior and is going to TR earlier for variant 1 and 2 in comparison to the reference case. The TR time of cell 3 is comparable for all 3 setups with an open housing, whereas the TR time of cell 2 is higher for variant 1 and 2 in comparison to the reference case.

These phenomena are explained as follows: for the reference case, there is only one heat transfer path from the cell going into TR to the adjacent cell (conductive heat transfer through the cell-to-cell insulation material). For variant 1 and 2, a second and a third path are added (conductive heat transfer through the cooling plate and the side plates, respectively). Considering the state directly after TR of cell 1, all components of the cell stack are at their initial temperature (except from cell 1). For the reference case, the heat is then transferred through the cell-to-cell insulation material to cell 2. This results in an temperature increase of both the cell-to-cell insulation material and the battery cell. For variant 1, the cooling plate on the one hand increases the heat transfer to cell 2. On the other hand, the cooling plate itself



(a)



(b)

Fig. 2. (a) Influence of module structure components on propagation time $t_{\text{TR,cell},i}$. All values are normalized with t_{ref} . (b) Influence of module structure components on time span $\Delta t_{\text{TR,cell},i \rightarrow i+1}$ between TRs. All values are normalized with t_{ref} .

is another component that is heating up. The same applies for the side plates in variant 2. These two effects of an enhanced heat transfer to cell 2 and a certain heat “absorbing” due to the thermal inertia and temperature increase of additional components are counteracting each other. The results show that for cell 2, the heat absorbing effect is predominant and therefore the propagation is slowed down, whereas for cell 3, the effects are in balance. For cell 4 and 5, the additional heat transfer paths become the dominant effect. The latter is also amplified by the fact that for the reference case, the cell going into TR (cell i) will only transfer heat to the next cell (cell $i + 1$), while for variant 1 and 2 the heat generated by TR of cell i can be also transferred to cell $i + x$ with $x \in 2, 3, 4$. This results for example in cell 4 being already at an elevated temperature when cell 3 is going into TR

for variant 1 and 2 in comparison to the reference case and consequently comes with a faster propagation.

As shown in Fig. 2b the time span $\Delta t_{TR,cell,i \rightarrow i+1}$ between the TRs of two adjacent cells increases from cell to cell for the reference case (gray), whereas $\Delta t_{TR,cell,i \rightarrow i+1}$ remains almost constant for variant 1 (red - except from cell 1 \rightarrow 2) and variant 2 (blue). This is explained by a different mechanical integrity of the cell stack due to the attached components. For the reference case, the mechanical integrity of the stack results from both the mechanical integrity of each single cell and the cell-to-cell insulation material. The cell loses a significant amount of its mass during TR and therefore a void volume is formed inside of the cell can. The high temperatures lead to an additional weakening of the aluminum cell can. Therefore, the large cell sides are collapsing to the cell's center plane after a TR and the cell-to-cell spacing increases with each cell going to TR. As a consequence, the cell-to-cell insulation material is less compressed and the heat transfer is reduced. For variant 1, this increase of cell-to-cell spacing is mitigated by the cooling plate that is glued to the cell bottom. However, the cells can still increase their distance at the top side. This is not the case for variant 2, where the additional side plates completely prevent the cells from moving.

Fig. 3 displays the time $t_{TR,cell,i}$ at which the TR of cell i occurs after nail penetration of cell 1 (Fig. 3a) and the time span $\Delta t_{TR,cell,i \rightarrow i+1}$ between the TRs of two adjacent cells (Fig. 3b) for the comparable test variants with and without housing. For each variant, the mean value over all 3 tests is presented including error bars that show the variance between the repeated tests within each setup.

As shown in Fig. 3a, the total propagation time of the stack $t_{TR,cell,5}$ is reduced to 48.7% of t_{ref} by integrating the reference variant (gray) into a housing (variant 3 - gray with pattern). Cell 4 shows a similar behavior and is going to TR earlier for variant 3 in comparison to the reference case. The TR time of cell 3 is comparable for both setups, whereas the TR time of cell 2 is higher for variant 3 in comparison to the reference case.

A possible reason for this behavior is the lack of oxygen for variant 3: for all tests with the reference setup, a flame is observed during and also after the venting process of each cell. Due to the burning of the vented gases, additional heat is released and affects the temperature increase of adjacent cells. For variant 3, the integration of the cell stack into a housing limits the amount of available oxygen and hence the duration of a flame being present as an additional heat source. This effect is compensated by the ambient temperature increase inside the housing. Therefore, the time of TR in cell 3 $t_{TR,cell,3}$ is similar for both the reference case and variant 3. As a consequence, the authors assume that this increase in temperature in combination with a convective heat transfer between cell and vent gas flow significantly accelerates the propagation process as seen in the time of TR in cell 4 and 5.

This acceleration is also observed for the second setup

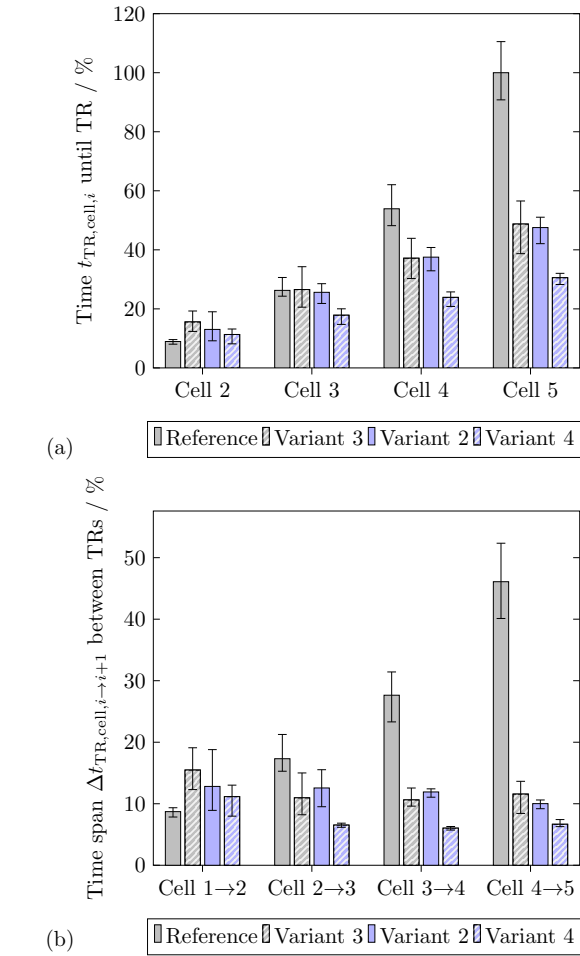


Fig. 3. (a) Influence of a housing on propagation time $t_{TR,cell,i}$. All values are normalized with t_{ref} . (b) Influence of a housing on time span $\Delta t_{TR,cell,i \rightarrow i+1}$ between TRs. All values are normalized with t_{ref} .

variant tested inside of the housing: for variant 4, $t_{TR,cell,5}$ is reduced to 30.6% of t_{ref} . Comparing variant 4 (blue with pattern) with variant 2 (blue), i.e. the influence of the housing with attached cooling and side plates, the total propagation time $t_{TR,cell,5}$ is reduced to 64.3% of t_{ref} . Cell 2, 3 and 4 show a similar behavior and go to TR earlier for variant 4 in comparison to variant 2. The amount of oxygen seems to have a minor role in this case. However, it is important to mention that the TR propagation from cell 1 to cell 2 highly depends on the TR behavior of cell 1. The nail penetration method reliably triggers a TR, but it can also cause deviations in various parameters as for example the mass loss. The mass loss is in turn one major factor for the amount of heat remaining in cell 1 [17] and therefore influences the time of TR in cell 2.

This effect is also shown in Fig. 3b: the time span between

two TRs $\Delta t_{\text{TR,cell},i \rightarrow i+1}$ remains approximately constant from cell 2 to cell 5 for variant 3 (gray with pattern) and variant 4 (blue with pattern), whereas the TR propagation from cell 1 to cell 2 differs from the other cells.

Fig. 4 displays the relative mass loss Δm_{stack} during the propagation process for the different setups. For each variant, the mean value over all 3 tests is presented including error bars that show the variance between the repeated tests within each setup.

It is observed that the nail penetrated stacks of the reference variant (gray) show on average the highest mass loss, followed by the stacks of variant 1 (cooling plate - red). Variant 2 (cooling and side plates - blue) and variant 4 (variant 2 integrated into a housing - blue with pattern) have similar values that are slightly lower compared to variant 1. Variant 3 (reference case integrated into a housing - gray with pattern) lies significantly below the other variants.

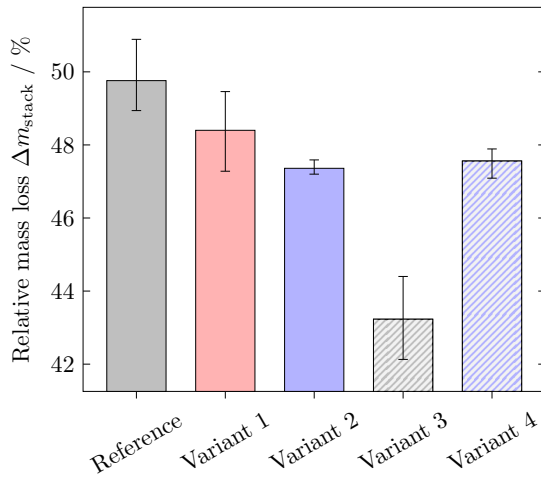


Fig. 4. Relative mass loss of the cell stack Δm_{stack} during the propagation process for each variant.

The shown difference in Δm_{stack} is explained by different constraints the cells were exposed to. During the heating process of the cells, the electrolyte inside of each cell evaporates due to the increasing temperature and therefore the cell is bulging as long as the safety vent is still closed. For the reference case, the cell-to-cell spacing is increasing with each cell that goes into TR as described above. As a consequence, the cells have more available space for bulging compared to variant 1 or variant 2. At the moment of safety vent opening, this increased bulging leads to an increased flow velocity out of the vent as there is more gas present inside of the cell. Unfortunately, there is no experimental evidence for this hypothesis. In addition, the behavior of variant 3 cannot be explained by this theory.

IV. CONCLUSIONS

The presented results show the TR propagation behavior of a prismatic state-of-the-art prototype lithium-ion battery cell in a 5 cell stack setup. The influence of components that come along with the integration into a battery pack such as cooler, module structure or battery pack housing are evaluated by conducting tests with different variants of the cell stack setup.

- The total propagation time of a 5 cell stack is on average reduced to 52.4% of the reference propagation time by attaching a cooling plate.
- The total propagation time of a 5 cell stack is on average reduced to 47.5% of the reference propagation time by attaching a cooling plate and side plates.
- The time span between the TRs of two adjacent cells increases with the test duration for an open setup without any attached components due to an increasing cell gap caused by a decreasing compression force with every TR.
- The time span between the TRs of two adjacent cells remains approximately constant for a setup with attached components (cooling and / or side plates) as the attached components prevent an increase of the cell-to-cell spacing.
- The total propagation time of a 5 cell stack is on average reduced to 48.7% of the reference propagation time by integrating the stack into a housing (setup without cooling or side plates).
- The total propagation time of a 5 cell stack is on average reduced to 64.3% of the reference propagation time by integrating the stack into a housing (setup with cooling and side plates).
- The main effect for the accelerated propagation inside of a battery pack housing is an ambient temperature increase combined with a convective heat transfer between vent gas flow and adjacent cells.
- The mass loss during the TR propagation process is influenced by attaching additional components (cooling and / or side plates).

In general, the results help to get a better understanding of the TR propagation process with regards to the different heat transfer paths and influencing factors. In addition, the presented test setup allows to estimate the TR propagation behavior on module or pack level by conducting tests on a smaller scale with reduced costs. Therefore, the results of this study contribute to the design of a safer battery pack.

ACKNOWLEDGMENT

The authors would like to gratefully acknowledge the support of ZSW Ulm, Germany, for the execution of the 5 cell stack tests. An additional gratitude goes to our BMW Group colleagues from the technology material and process analysis (TWA) for the support in proof-of-concept experiments. In addition, S. Hoelle acknowledges the support of the TUM Graduate School.

REFERENCES

- [1] J. Liu, J. Li and J. Wang, "In-depth analysis on thermal hazards related research trends about lithium-ion batteries: A bibliometric study," *Journal of Energy Storage*, vol. 35, no. 102253, 2021.
- [2] X. Feng, J. Sun, M. Ouyang, F. Wang, X. He, L. Lu and H. Peng, "Characterization of penetration induced thermal runaway propagation process within a large format lithium ion battery module," *Journal of Power Sources*, vol. 275, pp. 261–273, 2015.
- [3] X. Yang, Y. Duan, X. Feng, T. Chen, C. Xu, X. Rui, M. Ouyang, L. Lu, X. Han, D. Ren, Z. Zhang, C. Li and S. Gao, "An Experimental Study on Preventing Thermal Runaway Propagation in Lithium-Ion Battery Module Using Aerogel and Liquid Cooling Plate Together," *Fire Technology*, vol. 56, pp. 2579–2602, 2020.
- [4] X. Rui, X. Feng, H. Wang, H. Yang, Y. Zhang, M. Wan, Y. Wei and M. Ouyang, "Synergistic effect of insulation and liquid cooling on mitigating the thermal runaway propagation in lithium-ion battery module," *Applied Thermal Engineering*, vol. 199, no. 117521, 2021.
- [5] L. Li, C. Xu, R. Chang, C. Yang, C. Jia, L. Wang, J. Song, Z. Li, F. Zhang, B. Fang, X. Wei, H. Wang, Q. Wu, Z. Chen, X. He, X. Feng, H. Wu and M. Ouyang, "Thermal-responsive, super-strong, ultrathin firewalls for quenching thermal runaway in high-energy battery modules," *Energy Storage Materials*, vol. 40, pp. 329–336, 2021.
- [6] H. Wang, Z. Du, X. Rui, S. Wang, C. Jin, L. He, F. Zhang, Q. Wang and X. Feng, "A comparative analysis on thermal runaway behavior of $\text{Li}(\text{Ni}_x\text{Co}_y\text{Mn}_z)\text{O}_2$ battery with different nickel contents at cell and module level," *Journal of Hazardous Materials*, vol. 393, no. 122361, 2020.
- [7] Z. Huang, X. Li, Q. Wang, Q. Duan, Y. Li, L. Li and Q. Wang, "Experimental investigation on thermal runaway propagation of large format lithium ion battery modules with two cathodes," *International Journal of Heat and Mass Transfer*, vol. 172, no. 121077, 2021.
- [8] X. Lai, S. Wang, H. Wang, Y. Zheng, X. Feng, "Investigation of thermal runaway propagation characteristics of lithium-ion battery modules under different trigger modes," *International Journal of Heat and Mass Transfer*, vol. 171, no. 121080, 2021.
- [9] H. Li, Q. Duan, C. Zhao, Z. Huang and Q. Wang, "Experimental investigation on the thermal runaway and its propagation in the large format battery module with $\text{Li}(\text{Ni}_{1/3}\text{Co}_{1/3}\text{Mn}_{1/3})\text{O}_2$ as cathode," *Journal of Hazardous Materials*, vol. 375, pp. 241–254, 2019.
- [10] Z. Huang, C. Zhao, H. Li, W. Peng, Z. Zhang and Q. Wang, "Experimental study on thermal runaway and its propagation in the large format lithium ion battery module with two electrical connection modes," *Energy*, vol. 205, no. 117906, 2020.
- [11] S. Gao, X. Feng, L. Lu, N. Kamyab, J. Du, P. Coman, R. E. White and M. Ouyang, "An experimental and analytical study of thermal runaway propagation in a large format lithium ion battery module with NCM pouch-cells in parallel," *International Journal of Heat and Mass Transfer*, vol. 135, pp. 93–103, 2019.
- [12] H. Matsumura, S. Itoh and K. Ando, "Basic Study on Thermal Runaway Propagation through Lithium Ion Cells," *SAE International Journal of Passenger Cars – Mechanical Systems*, vol. 8 (2), pp. 546–555, 2015.
- [13] C. Xu, F. Zhang, X. Feng, F. Jiang, D. Ren, L. Lu, Y. Yang, G. Liu, X. Han, B. Friess and M. Ouyang, "Experimental Study on Thermal Runaway Propagation of Lithium-Ion Battery Modules with Different Parallel-series Hybrid Connections," *Journal of Cleaner Production*, vol. 284, no. 124749, 2021.
- [14] X. Cheng, T. Li, X. Ruan and Z. Wang, "Thermal Runaway Characteristics of a Large Format Lithium-Ion Battery Module," *Energies*, vol. 12, no. 3099, 2019.
- [15] S. Gao, X. Feng, L. Lu, M. Ouyang and D. Ren, "A Test Approach for Evaluating the Safety Considering Thermal Runaway Propagation within the Battery Pack," *ECS Transactions*, vol. 77 (11), pp. 225–236, 2017.
- [16] S. Gao, L. Lu, M. Ouyang, Y. Duan, X. Zhu, C. Xu, B. Ng, N. Kamyab, R. E. White and P. T. Coman, "Experimental Study on Module-to-Module Thermal Runaway-Propagation in a Battery Pack," *Journal of The Electrochemical Society*, vol. 166 (10), pp. A2065–A2073, 2019.
- [17] S. Hoelle, S. Scharner, S. Asanin and O. Hinrichsen, "Analysis on Thermal Runaway Behavior of Prismatic Lithium-Ion Batteries with Autoclave Calorimetry," *Journal of The Electrochemical Society*, vol. 168, no. 120515, 2021.

3.2.2 Particle deposition during lithium-ion battery thermal runaway

The following section is divided into two parts: first, an experimental analysis of the particle deposition during a lithium-ion cell TR is presented. Subsequently, a gas-particle-flow model is proposed with the objective to reproduce the experimental results.

Experimental analysis The article titled “*Lithium-Ion Battery Thermal Runaway: Experimental Analysis of Particle Deposition in Battery Module Environment*” is presented within this section. It was submitted to the peer-reviewed *Batteries* in April 2024 and published online in May 2024.

The objective of this work was to experimentally determine the particle deposition during the TR of a lithium-ion cell in a battery module. Therefore, an experimental setup was designed that integrates a single prismatic lithium-ion cell into an environment representing battery module conditions with a defined flow path for the vented gas and particles. In total, 86 weighing plates, positioned within this flow path, could be individually removed from the setup in order to determine the spatial mass distribution of the deposited particles. Two nail penetration tests with a prismatic lithium-ion cell (> 60 Ah) were performed with different distances between cell vent and module cover (24 mm and 48 mm). Moreover, the mass loss of the cell during TR and the size distribution of the collected particles were analyzed. In order to provide further input data for simulation models, additional specific heat capacity measurements were performed via differential scanning calorimetry (DSC) for both the vented particles and the jelly roll remains.

The results revealed that the distance between cell vent and module cover has a major influence on the particle deposition. Whilst particle accumulations concentrated at the side walls for 24 mm distance between vent and cover, the particles were randomly distributed over the entire weighing plate area for 48 mm distance. In addition, the total mass depositing on the weighing plates was higher for 48 mm distance, and larger particles were observed on the weighing plates after the test. This was explained by different gas flow velocities that resulted in different gas-particle as well as particle-wall interactions. Besides particle deposition, the mass loss during TR was also found to be different for the two tests: due to a lower distance between cell vent and module cover, the pressure loss within the flow path is higher, which led to a lower Δm_{TR} for the 24 mm distance case. Another finding of the study was an influence of the distance between cell vent and module cover on the particle size distribution, especially for larger particles ($d > 80 \mu\text{m}$). The specific heat capacity measurements delivered comparable results for all investigated particle size ranges of both tests, whilst the results for the jelly roll remains indicated a dependency of c_p on the position within the jelly roll remains. In addition, c_p of the vented particles was found to be slightly lower compared to c_p of the jelly roll remains.

The results gain further insights into the particle ejection process during a lithium-ion cell TR, which is of utmost importance as there is a lack of studies investigating the effect of vented particles on the TP behavior. In addition, the results serve as a basis for the development and validation of gas-particle-flow models.

Lithium-Ion Battery Thermal Runaway: Experimental Analysis of Particle Deposition in Battery Module Environment

S. Hoelle, H. Kim, S. Zimmermann, and O. Hinrichsen

Batteries 10, No. 173, 2024

Permanent weblink:

<https://doi.org/10.3390/batteries10060173>

© 2024 MDPI.

Reproduced under the terms of the Creative Commons Attribution 4.0 License (CC BY, <https://creativecommons.org/licenses/by/4.0/>), which permits unrestricted reuse of the work in any medium, provided the original work is properly cited.

Author contributions:

S. Hoelle initiated the work and developed the proposed experimental setup. S. Hoelle and H. Kim carried out the experiments. The data was analyzed and interpreted by S. Hoelle and H. Kim. The manuscript was written by S. Hoelle and was edited by H. Kim, S. Zimmermann, and O. Hinrichsen. All authors discussed the data and commented on the results.

Article

Lithium-Ion Battery Thermal Runaway: Experimental Analysis of Particle Deposition in Battery Module Environment

 Sebastian Hoelle ^{1,2,*} , Hyojeong Kim ^{2,3} , Sascha Zimmermann ²  and Olaf Hinrichsen ^{1,4} 

¹ Department of Chemistry, TUM School of Natural Sciences, Technical University of Munich, Lichtenbergstraße 4, 85748 Garching near Munich, Germany

² BMW Group, 80937 Munich, Germany

³ Institute for Applied Materials (IAM-AWP), Karlsruhe Institute of Technology, 76344 Eggenstein-Leopoldshafen, Germany

⁴ Catalysis Research Center, Technical University of Munich, Ernst-Otto-Fischer-Straße 1, 85748 Garching near Munich, Germany

* Correspondence: sebastian.hoelle@tum.de

Abstract: In this paper, a novel experimental setup to quantify the particle deposition during a lithium-ion battery thermal runaway (TR) is proposed. The setup integrates a single prismatic battery cell into an environment representing similar conditions as found for battery modules in battery packs of electric vehicles. In total, 86 weighing plates, positioned within the flow path of the vented gas and particles, can be individually removed from the setup in order to determine the spatial mass distribution of the deposited particles. Two proof-of-concept experiments with different distances between cell vent and module cover are performed. The particle deposition on the weighing plates as well as the particle size distribution of the deposited particles are found to be dependent on the distance between cell vent and cover. In addition, the specific heat capacity of the deposited particles as well as the jelly roll remains are analyzed. Its temperature dependency is found to be comparable for both ejected particles and jelly roll remains. The results of this study help researchers and engineers to gain further insights into the particle ejection process during TR. By implementing certain suggested improvements, the proposed experimental setup may be used in the future to provide necessary data for simulation model validation. Therefore, this study contributes to the improvement of battery pack design and safety.

Keywords: Li-ion battery; thermal runaway; cell venting; particle emission; particle size distribution; specific heat capacity



Citation: Hoelle, S.; Kim, H.; Zimmermann, S.; Hinrichsen, O. Lithium-Ion Battery Thermal Runaway: Experimental Analysis of Particle Deposition in Battery Module Environment. *Batteries* **2024**, *10*, 173. <https://doi.org/10.3390/batteries10060173>

Academic Editors: Zhi Wang, Tong Liu and Mingzhi Jiao

Received: 23 April 2024

Revised: 13 May 2024

Accepted: 21 May 2024

Published: 23 May 2024



Copyright: © 2024 by the authors. Licensee MDPI, Basel, Switzerland. This article is an open access article distributed under the terms and conditions of the Creative Commons Attribution (CC BY) license (<https://creativecommons.org/licenses/by/4.0/>).

1. Introduction

The thermal runaway (TR) of lithium-ion batteries attracts increasingly more attention as one of the most critical safety issues related to electric vehicles (EVs). On the one hand, this is caused by the occasionally emerging fire accidents of EVs that attract public attention [1–3]. On the other hand, the phenomenon is extensively studied within the scientific community, as shown in the increasing number of annual publications [4].

The main characteristics of a TR can be summarized as significant heat release caused by self-sustaining exothermic reactions, accompanied by gas and particle ejection. A TR can be triggered by either mechanical, electrical, or thermal abuse and may lead to fire or explosion of the battery cell [3,5]. Within an EV battery pack, the occurrence of a single cell TR results in the risk of so-called TR propagation, which is the process of TRs propagating from one cell to neighboring ones, resulting in catastrophic consequences [6–8]. Feng et al. proposed two different pathways for this failure development: an “expected” and an “unexpected” failure sequence. The expected sequence is primarily driven by heat conduction and consequently the TR first propagates from the triggering cell to its neighbors within the module. Secondly, the TR propagates to adjacent modules. The unexpected

sequence is primarily caused by the gas–particle flow vented out of the trigger cell. The ignition of the venting gases may lead to fire and the particle accumulations can result in short circuits between cells or modules. Such fires and short circuits cause uncertainties and therefore the propagation sequence is difficult to predict for the unexpected pathway [8].

The gas–particle flow during TR as the origin of the unexpected pathway has been investigated by several researchers in recent years [9]. Experimental and numerical studies have been conducted to investigate the behavior of the ejected gas and particles in order to explore potential strategies to prevent or mitigate the unexpected failure sequence. On the experimental side, previous studies focused on different topics such as the characteristics of the jet stream out of the vent [10–13], the elemental composition of the venting gas [14–16], the size distribution of the ejected particles [12,16–20], and the elemental composition of the vented particles [14–17,20–22]. For example, Zou et al. investigated the jet manifestation, temperature and velocity of a prismatic 38 Ah cell triggered by external heating into TR [10]. Garcia et al. focused on optical jet observations by Schlieren visualization and Natural Luminosity of a 2.6 Ah cylindrical cell [11]. Wang et al. used the planar laser scattering technique to observe the jet flow of a prismatic 27 Ah cell and estimate characteristics such as gas and particle velocities [12]. Ding et al. conducted experiments with a cylindrical 5 Ah cell and investigated the influence of a low-pressure/high-altitude environment on the mass loss and flame height during TR [13]. The size distribution of the particles ejected during TR was investigated among others by Zhang et al. in Refs. [16,17]. They triggered a prismatic 50 Ah cell by external heating into TR within a sealed chamber. Wang et al. used the same cell within the same setup and additionally investigated the thermal oxidation characteristics of the ejected particles depending on their size [18]. Wang et al. analyzed the particle size distribution as well as the particle deposition of a prismatic 27 Ah cell within a combustion chamber [12]. Premnath et al. investigated battery modules containing either cylindrical 2.3 Ah cells or prismatic 60 Ah cells. However, their focus was on particles with a diameter smaller than 2.5 μm [19]. Liao et al. investigated the elemental composition of the ejected particles during TR for a cylindrical 2.4 Ah cell. They used an autoclave and focused on the influence of a varying state of charge on the venting behavior [14]. Chen et al. also evaluated the elemental composition of the ejected particles during TR for a cylindrical 2.4 Ah cell. They varied the state of charge, heating temperature, as well as heating power and additionally analyzed the thermal properties of the collected powder by thermogravimetric analysis—differential scanning calorimetry (TGA-DSC) [20]. Essl et al. analyzed the elemental composition of the ejected particles during TR of a 41 Ah pouch cell [15]. Zhang et al. and Wang et al. also determined the elemental composition of the ejected particles within their studies [16,17,22]. Held et al. focused on the contamination after a battery fire. Therefore, they triggered a module containing 12 prismatic cells with 90 Ah each into TR and analyzed the elemental composition of the fire soot depositing on the surroundings [21].

On the numerical side, there is only a small number of publications dealing with the venting behavior of lithium-ion batteries. Coman et al. were one of the first to introduce isentropic flow equations in their TR models to account for the heat dissipation due to gas and particle ejection [23]. They also extended their model from the single-cell level to the battery-pack level in the following years [24]. However, their model did not simulate the gas flow itself but the influence of the venting process on the thermal behavior of the solid body [23,24]. Ostanek et al. performed a similar study investigating the influence of the electrolyte vaporization and gas generation due to decomposition reactions on the cell body modeled as a solid [25]. Li et al. studied the flow through different vent geometries for 18,650 cells by performing CFD simulations. The results provide insights into the jet structure as well as the turbulence levels and can be used to estimate the influence on combustion and heat transfer to the surrounding cells [26]. Kim et al. focused on the internal pressure increase, the resulting venting process and the subsequent gas-phase dynamics of 18,650 cells [27]. However, both models consider a single cell only and consequently are not capable of predicting the thermal impact of the vented gas and particles on the

neighboring cells. Citarella et al. were one of the first to consider the gas flow within their model to investigate the TR propagation behavior of a battery pack [28]. Another study of Mishra et al. focused on the spread of the gas flow within a battery pack by studying parameters such as the cell-to-cell gap, the distance between cell vent and housing, as well as the location of the vent [29].

The models mainly focused on the gas phase of the venting process, although the ejected particles are assumed to have a significant influence on the TR propagation process. To address this issue, Wang et al. built a multiphase model including both fluid flow and particles. They investigated not only the jet behavior and particle ejection, but also the particle deposition after TR [12]. However, there is a lack of experimental data that are needed to validate such simulation models.

This publication focuses on the experimental determination of the particle deposition during a lithium-ion battery TR. The objective is to develop an experimental setup that allows for quantification of the mass distribution of ejected particles in a battery module-like environment. Therefore, a novel experimental setup for prismatic batteries is proposed and two proof-of-concept experiments are performed with different distances between battery cell and cover. In addition, the particle size distribution of depositing particles is analyzed and specific heat capacity measurements are conducted. To the authors' knowledge, an experimental determination of the mass distribution of depositing particles during TR has not been the subject of any scientific publication. In addition, specific heat capacity measurements of ejected particles and jelly roll remains after a TR are not yet available in the literature. The results of this study help engineers or researchers to gain further insights into the particle ejection process during TR. By implementing certain suggested improvements, the proposed experimental setup may be used in the future to provide necessary data for simulation model validation. Therefore, this study contributes to the improvement of battery pack design and safety.

2. Experimental Setup

In this study, a novel experimental setup to quantify the particle deposition during a lithium-ion battery TR is proposed. The setup integrates a single prismatic battery cell into a battery module-like environment as found in EV battery packs. Within the flow path of the vented gas and particles, there are several weighing plates that can be individually removed from the setup in order to determine the spatial mass distribution of the deposited particles. Afterwards, the collected particles as well as the remains of the jelly roll are further analyzed to determine mass loss of the battery cell during TR, size distribution of the vented particles, and specific heat capacity measurements of both vented particles and jelly roll remains.

2.1. Geometry

The experimental setup used in this study is shown in Figure 1. The main component is the investigated battery cell (dimensions 180 mm × 32 mm × 72.5 mm) that is compressed within a steel frame. In order to reduce the heat transfer from the cell to its surroundings, a thermal insulation material is used on both sides of the cell (thickness of 10 mm). In addition, there is a built-in load cell to adjust the compression force to specified values. The steel frame can be attached to a base plate, resulting in the substructure shown in Figure 1a. As shown in Figure 1b, an intermediate sheet metal surrounding the battery cell can be attached to the base plate. Grooves are milled into this sheet metal, so that in total 86 weighing plates (T-shape with an upper surface of 32 mm × 45 mm) can be inserted. Afterwards, two fixation plates are screwed to each side of the intermediate sheet metal as shown in Figure 1c. The result is a flat surface that is on the level of the top of the battery cell. Finally, a cover is attached to the base plate via telescopic legs, allowing for setting different distances between the battery cell's vent and the cover. Figure 1d shows the resulting assembly that can be integrated into a steel box as shown in Figure 1e. Figure 1f schematically shows the nailing process for TR initiation.

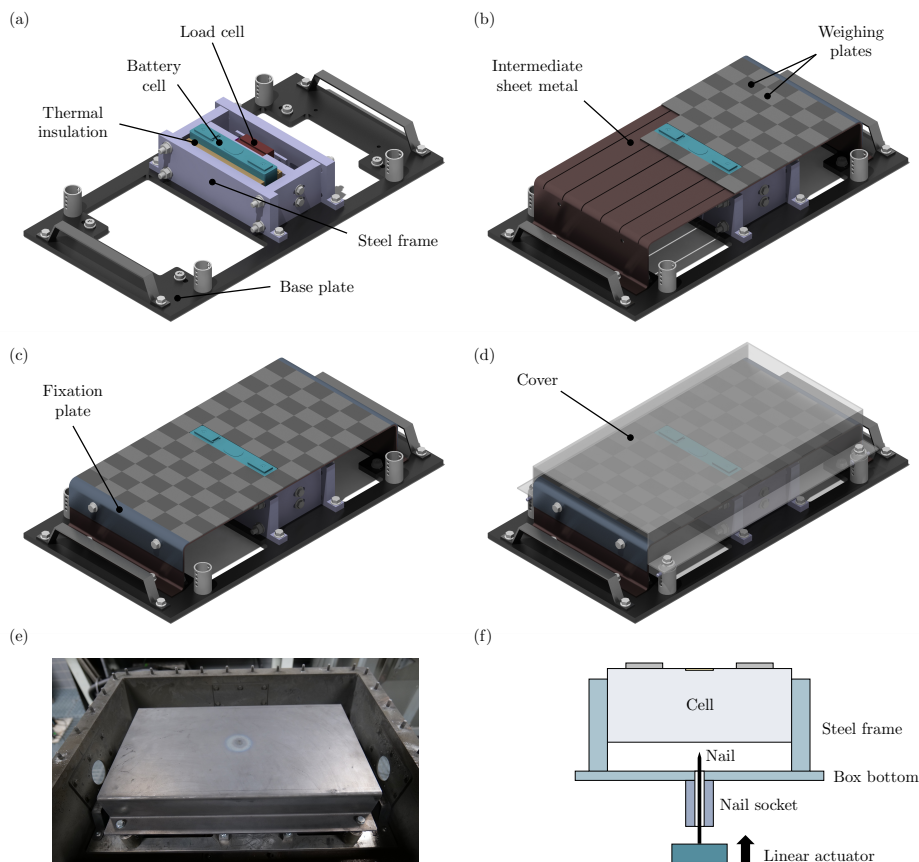


Figure 1. (a) Substructure of the experimental setup including a steel frame to fix the position of the battery cell. (b) Intermediate sheet metal that is used to position the weighing plates. (c) Fully assembled and fixed weighing plates. (d) Full experimental setup with cover. (e) Full view of the setup within a steel box. (f) Schematic representation of linear actuator for nailing process.

2.2. Test Procedure and Evaluation Methodology

Two proof-of-concept experiments with different distances between cell vent and cover are performed. Therefore, the cell is installed into the steel frame and compressed with a force of 3 kN in order to ensure a fixed position during nail penetration and simulate conditions as found in a battery module for EV battery packs. Afterwards, the intermediate sheet metal is screwed to the base plate and the weighing plates are inserted into the grooves. Subsequently, the position of the weighing plates is fixed by mounting the fixation plates to both ends of the intermediate sheet metal. The cell is then charged from a state of charge of SoC = 30% (used during logistics) to SoC = 100% with the constant current constant voltage (CCCV) charging method. In the final step, the cover is attached at two specified heights h :

- Test 1: $h = 24$ mm distance between cell vent and cover, which aims to represent EV battery pack conditions.
- Test 2: $h = 40$ mm distance between cell vent and cover, which aims to show the influence of the distance on particle deposition.

The full setup is attached to the steel box, which comes with a nail actuator that is used to penetrate the bottom side of the battery cell with a steel nail (3.2 mm diameter) as shown in Figure 1f. The penetration depth is 15 mm with a penetration speed of 7 mm s^{-1} . The nail is not retracted from the battery after TR initiation.

The nail penetration triggers a TR and consequently results in gas and particles being ejected out of the cell vent. Since the cover is flushed with the long sides of the intermediate sheet metal, the resulting flow path is directed towards both fixation plates. Vented particles that are carried by the gas flow eventually deposit either on one of the weighing plates or within/outside of the steel box.

In preparation for the disassembly of the test setup and the evaluation of the results, 86 sealable glasses are labeled and weighed in order to collect the particles deposited on each individual weighing plate. As soon as the setup is cooled down, the cover and the fixation plates are dismantled. Next, each weighing plate is individually taken out of the intermediate sheet metal and deposited particles are collected in the prepared glasses. To do so, loose particles on each weighing plate are first poured into the corresponding glass with the aid of a funnel as exemplary shown in Figure 2a. Then, the weighing plates are wiped off with the aid of a brush to collect non-adherent particles. Particles that are sticking to the weighing plates and therefore cannot be collected by pouring or wiping are not collected in this step, but scraped off in the second step. This helps to differentiate the mass of particles that are sticking to the weighing plates from particles that are loose as shown in Figure 2b. After collecting all particles, the intermediate sheet metal is dismantled from the base plate, and the tested cell can be removed from the steel frame for further analysis.

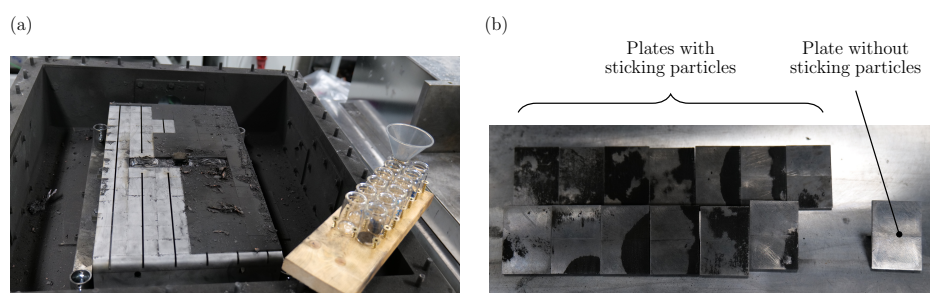


Figure 2. (a) Process of particle collecting with sealable glasses and funnel. (b) Examples of plates with sticking particles and a plate without sticking particles.

2.2.1. Particle Deposition and Particle Size Distribution

After each test, the mass loss during TR of the battery cell Δm_{cell} is calculated by

$$\Delta m_{\text{TR}} = m_{\text{cell}} - m_{\text{cell,postTR}} \quad (1)$$

with m_{cell} being the mass of the cell before the test and $m_{\text{cell,postTR}}$ being the mass of the cell after the test. The mass of deposited particles $m_{\text{particles},i}$ is determined for each weighing plate i by

$$m_{\text{particles},i} = m_{\text{glass},i,\text{postTR}} - m_{\text{glass},i} \quad (2)$$

where $m_{\text{glass},i}$ is the mass of each glass in its empty state and $m_{\text{glass},i,\text{postTR}}$ is the mass of each glass with the collected particles inside. The weighing of the glasses is performed twice: first, the glasses with collected loose particles are weighed. Afterwards, the sticking particles are scraped off the weighing plates and added to the corresponding glass. The second weighing results in the mass of sticking particles $m_{\text{particles},i,\text{stick}}$ for each weighing plate i :

$$m_{\text{particles},i,\text{stick}} = m_{\text{glass},i,\text{scraped}} - m_{\text{glass},i,\text{postTR}} \quad (3)$$

with $m_{\text{glass},i,\text{scraped}}$ being the mass of the glass with added scraped-off particles. The total sum of particles deposited on the weighing plates $m_{\text{particles},\text{total}}$ is the sum of all loose particles $m_{\text{particles},\text{loose}}$ and all sticking particles $m_{\text{particles},\text{stick}}$:

$$\begin{aligned} m_{\text{particles},\text{total}} &= m_{\text{particles},\text{loose}} + m_{\text{particles},\text{stick}} \\ &= \sum_i m_{\text{particles},i} + \sum_i m_{\text{particles},i,\text{stick}} \end{aligned} \quad (4)$$

After the mass distribution on the weighing plates is determined, the particle size distribution is analyzed. Therefore, the particles (diameter d) are separated into four different size ranges by sieving:

1. $d < 80 \mu\text{m}$,
2. $80 \mu\text{m} \leq d < 200 \mu\text{m}$,
3. $200 \mu\text{m} \leq d < 800 \mu\text{m}$,
4. $d \geq 800 \mu\text{m}$.

2.2.2. Specific Heat Capacity Measurements

The specific heat capacity of the four particle size samples is measured via the differential scanning calorimetry (DSC) apparatus 204 F1 Phoenix manufactured by Netzsch®, Selb, Germany. In addition, four samples of the jelly roll remains, i.e., the burnt remains inside the cell after the TR process from four different positions as shown in Figure 3 are analyzed. Therefore, three probes of approximately 10 mg of each sample are loaded in aluminum crucibles under air atmosphere. In order to ensure specimens containing all chemical components, the three particle samples with $d > 80 \mu\text{m}$ as well as all four samples out of the jelly roll remains are ground in a ball mill before loading the crucibles (four times of milling for 2 min with 2500 rpm and a 1 min pause in between). The measurements are performed in a temperature range of 25–500 °C with a temperature rate of 10 K min⁻¹. The blank measurement is performed with an empty crucible and the calibration measurement with a sapphire standard (mass: 24.38 mg, diameter: 5 mm, thickness: 0.5 mm).

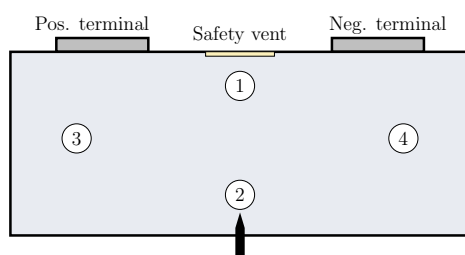


Figure 3. Schematic representation of the battery cell with the four positions of sample extraction out of the jelly roll remains after TR: (1) beneath the safety vent, (2) above the nailing position, (3) middle of the jelly roll beneath the positive terminal, and (4) middle of the jelly roll beneath the negative terminal.

2.3. Investigated Cell

The properties of the investigated battery cell are summarized in Table 1. The cells are prismatic prototype lithium-ion batteries with a nominal capacity between 60 Ah and 70 Ah. The cell consists of a $\text{LiNi}_{0.8}\text{Mn}_{0.1}\text{Co}_{0.1}\text{O}_2$ (NMC811) cathode and a graphite anode. The electrolyte is based on lithium hexafluorophosphate (LiPF_6) conducting salt with ethylene carbonate (EC), ethyl methyl carbonate (EMC), diethyl carbonate (DEC), and dimethyl carbonate (DMC) solvents. The cells are in a fresh/unused aging state.

Table 1. Basic properties of the investigated cell.

Parameter	Value
Capacity	60–70 Ah
Mass	$980.2 \pm 4.2 \text{ g}$
Dimensions	$180 \text{ mm} \times 32 \text{ mm} \times 72.5 \text{ mm}$
Cathode	$\text{LiNi}_{0.8}\text{Mn}_{0.1}\text{Co}_{0.1}\text{O}_2$ (NMC811)
Anode	Graphite
Electrolyte	LiPF_6 with EC, EMC, DEC, and DMC

3. Results and Discussion

Two proof-of-concept experiments with different distances between the battery cell's vent and the experimental setup's cover were performed to investigate the suitability of the setup for quantifying the particle deposition after a lithium-ion battery TR. In both experiments, the cell was triggered into TR by nail penetration and showed an expected venting behavior with gas release and particle ejection (only) through the vent, i.e., post-test analysis did not show any indications of gas or particle venting through the nailing hole. In the following, the particle deposition on the weighing plates as well as the mass loss of the cells during TR, the size distribution of the collected particles, as well as the specific heat capacity of both collected particles and samples out of the jelly roll remains are analyzed and discussed. The authors would like to point out that all results analyzed and discussed in the following are based on just the two proof-of-concept experiments and consequently the reliability of the statements made is limited.

3.1. Particle Deposition

Figure 4 shows the view on the weighing plates after cover removal for Test 1 with a 24 mm distance between cell vent and cover (Figure 4a) and Test 2 with a 40 mm distance between cell vent and cover (Figure 4b). In order to facilitate the result description and interpretation, the weighing plates are assigned to six columns as indicated with the numbered circles.

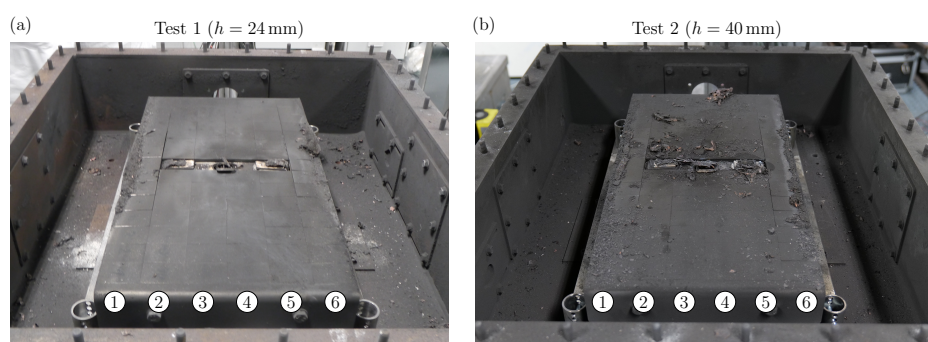


Figure 4. (a) View on the weighing plates of Test 1 after cover removal. (b) View on the weighing plates of Test 2 after cover removal. The numbered circles indicate the weighing plates' column number.

For Test 1 (see Figure 4a), there is no blank surface visible, which means that all weighing plates are fully covered with particles. On the outer Columns 1 and 6, accumulations of particles can be seen. These seem to concentrate towards the center of the intermediate sheet metal (at the position of the battery cell) and decrease towards the fixation plates. On the weighing plates within the middle Columns 2–5, there are no larger clumps of particles visible. In addition, a significant amount of particles deposits within the steel box. This is also the case for Test 2 (compare with Figure 4b). However, the particle deposition on the weighing plates shows significant differences compared to Test 1. The particle accumulations on the outer Columns 1 and 6 are also visible, but not as clearly as for Test 1. Also, there are bigger particles depositing towards the fixation plates over all the weighing plate columns as well as around the battery cell. In general, the particle deposition on the weighing plates appears random for Test 2.

A possible cause of the observed differences in particle deposition is the varying distance between cell vent and cover. As shown in Figure 5, the lower distance of $h = 24$ mm for Test 1 compared to $h = 40$ mm for Test 2 results in the flow path area A being smaller in Test 1. More precisely, the flow path area is $A_1 = 270 \text{ mm} \times 24 \text{ mm} = 6480 \text{ mm}^2$ in Test 1 and $A_2 = 270 \text{ mm} \times 40 \text{ mm} = 10,800 \text{ mm}^2$ in Test 2. Because A_1 is 40% smaller than A_2 , the gas flow velocities are higher in Test 1 assuming that the volume flow rate of venting gas is the same in both tests. As a consequence of higher flow velocities, the forces

acting on particles within the flow, such as drag force or Saffman lift, are higher. Therefore, the flow is capable of carrying larger particles and particles of the same size for a longer distance. Consequently, large particles are carried by the gas flow into the steel box for Test 1, whereas the lower gas velocities in Test 2 lead to the deposition of such large particles on the weighing plates. The accumulations of particles in Columns 1 and 6 are observed for both tests, which is in accordance with the expected flow field. Assuming ideal conditions, three stagnation points form: one above the cell vent at the cover, and two more at each side wall of the intermediate sheet metal (Columns 1 and 6) in the row of the battery cell. Independently of flow path area A , the gas velocity approaches zero towards a stagnation point. Therefore, particles are likely to accumulate next to these positions.

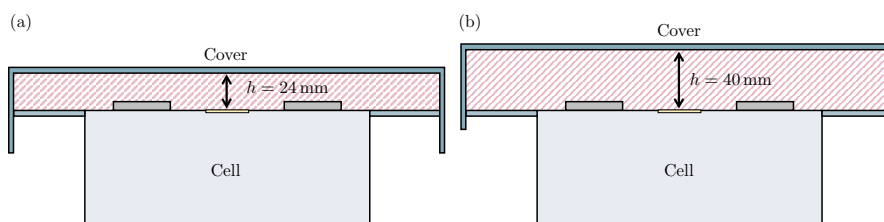


Figure 5. Schematic representation of flow area A during (a) Test 1 with $h = 24$ mm and (b) Test 2 with $h = 40$ mm.

The results of visual observation are in accordance with the measured mass distributions of deposited particles as shown in Figure 6. For each weighing plate, the mass of collected particles according to Equation (4) is shown for Test 1 in Figure 6a and for Test 2 in Figure 6b.

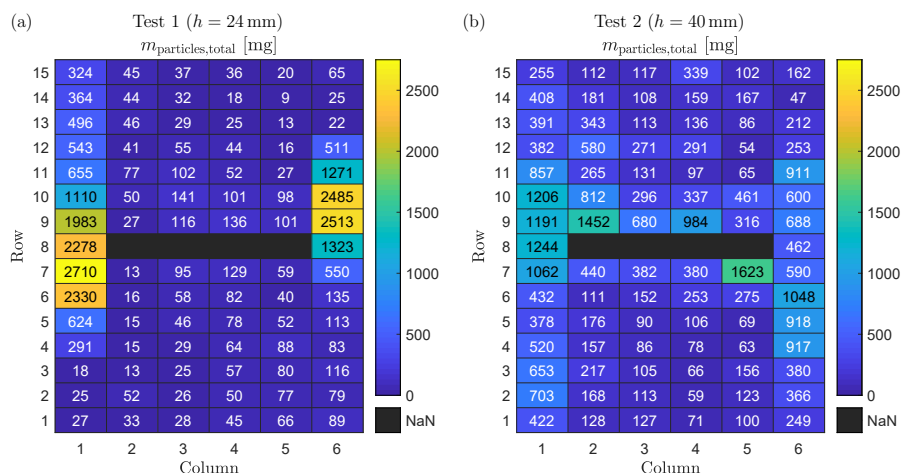


Figure 6. (a) Mass of deposited particles on each weighing plate for Test 1. (b) Mass of deposited particles on each weighing plate for Test 2.

For Test 1 (see Figure 6a), the maximum mass of particles collected from a single weighing plate is 2710 mg (Row 7, Column 1), whereas the minimum mass is 9 mg (Row 14, Column 5). The accumulation of particles in the outer Columns 1 and 6 as seen in the visual observation is confirmed by the measured mass values. Interestingly, the mass of collected particles in Column 6 decreases to values ≤ 135 mg already in Row 6, while for Column 1 this is the case just from Row 3 to 1. For Rows 9 to 15, a similar observation is made: in Column 1, the minimum collected particle mass is 324 mg (Row 15), whereas in Column 6 the minimum values are ≤ 65 mg for Rows 13 to 15. A possible cause is that particles on weighing plates of the outer columns fall down into the steel box when the cover is removed after the test. There is a conflict of objectives in the design of the experimental

setup in this respect. On the one hand, the cover has to be flush with the weighing plates so that no gas or particles escape at the sides of the outer columns. On the other hand, the cover can be under tension due to the high temperatures during the test, which can lead to particles falling from the weighing plates into the steel box when the cover is removed. For the inner Columns 2 to 5, more particle mass seems to deposit next to the battery cell (e.g., Row 9, Columns 3 to 5). However, there exist also outliers such as Rows 7 and 9 in Column 2.

For Test 2 (see Figure 6b), the maximum mass of particles collected from a single weighing plate is 1623 mg (Row 7, Column 5), whereas the minimum mass is 47 mg (Row 14, Column 6). As for Test 1, the particle accumulation in Columns 1 and 6 that has been observed visually is confirmed by the measured mass distribution on the weighing plates. However, a significant higher mass of deposited particles is found in the inner Columns 2 to 5 compared to Test 1. In addition, the two weighing plates with the maximum mass of particles collected are in Columns 2 and 5 and therefore not in the outer columns. As explained above, it is hypothesized that this observed behavior is the result of lower gas flow velocities in Test 2 compared to Test 1 due to the higher distance between cell vent and cover.

The separate evaluation of the measured mass distribution of loose and sticking deposited particles is shown in Figure 7. For each weighing plate, the total mass of loose and sticking particles according to Equations (2) and (3), respectively, is shown for Test 1 in Figure 7a,c, as well as for Test 2 in Figure 7b,d.

For Test 1, the mass distribution of loose particles (Figure 7a) is similar to the mass distribution of all particles (Figure 6a). One exception is the area around the battery cell: the mass of loose particles is increasing from Row 7 or 9 (next to the battery cell) towards Row 1 or 15 (next to the fixation plates). This can be explained by the mass distribution of sticking particles as shown in Figure 7c that accumulate towards the battery cell. The sticking of particles to the weighing plates is caused by high temperature above the melting point of the particle's material composition. Therefore, the high mass of sticking particles is equivalent to the high temperatures of both gas and particles during TR. This is in accordance with the shown results: the further away from the battery cell, the longer the vented gas and particles can cool down, and consequently the less particle mass is sticking to the weighing plates.

As observed in Test 1, the mass distribution of loose particles in Test 2 (Figure 7b) is similar to the mass distribution of all particles in Test 2 (Figure 6b), and sticking particles are only present in the area close to the battery cell (Rows 7 to 11) as shown in Figure 7d. However, the total mass of sticking particles is significantly lower for Test 2 compared to Test 1, which can be related to lower temperatures: as the distance between cell vent and cover is longer for Test 2 compared to Test 1, the pressure loss between the inner battery cell and the environment is lower. Consequently, the total pressure in the area next to the battery cell is also lower, which results in decreased gas temperatures due to a higher expansion of the gas from inside of the cell to outside of the cell.

The sum of collected particle mass on all weighing plates as well as the mass loss during the TR of the cells is summarized in Table 2 for each test. The results are in accordance with the observations made above:

- The battery cell's mass loss during TR Δm_{TR} is lower for the 24 mm distance between cell vent and cover (Test 1) compared to the 40 mm distance between cell vent and cover (Test 2). This behavior can be explained by a higher pressure loss from the inside of the battery cell to the outside of the battery cell for Test 1 due to the smaller flow area, A . However, the difference may also be caused by the statistical variance of nail penetration tests.
- The total mass of particles deposited on the weighing plates, $m_{\text{particles, total}}$, is lower for the 24 mm distance between cell vent and cover (Test 1) compared to the 40 mm distance between cell vent and cover (Test 2). This is explained by higher gas flow velocities in Test 1 compared to Test 2 due to the smaller flow area A .

- The total mass of sticking particles deposited on the weighing plates $m_{particles,stick}$ is higher for the 24 mm distance between cell vent and cover (Test 1) compared to the 40 mm distance between cell vent and cover (Test 2). This is explained by higher gas flow temperatures in Test 1 compared to Test 2.
- Only 7.3% of the total ejected particle mass deposits on the weighing plates for Test 1, assuming that 70.9% of the total mass loss during TR are particles as found in the literature [30]. For Test 2, 8.4% of the total mass of ejected particles deposits on the weighing plates under the same assumption.

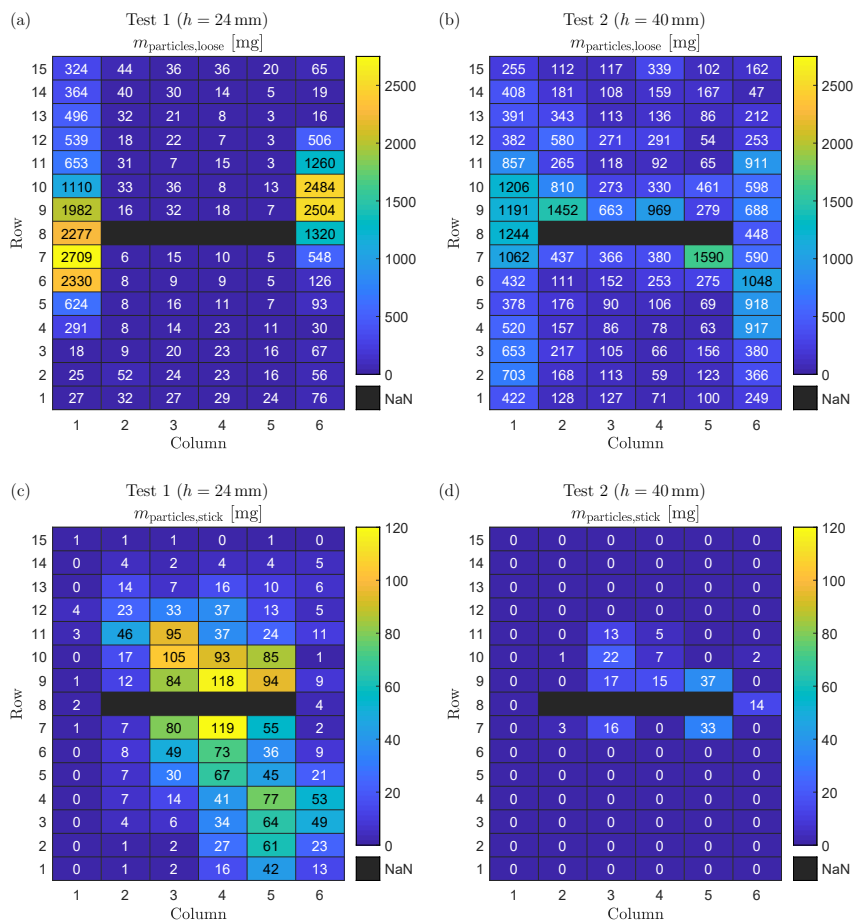


Figure 7. (a) Mass of deposited loose particles on each weighing plate for Test 1. (b) Mass of deposited loose particles on each weighing plate for Test 2. (c) Mass of deposited sticking particles on each weighing plate for Test 1. (d) Mass of deposited sticking particles on each weighing plate for Test 2.

Table 2. Experimental results of the two tests with different distance between cell vent and cover.

Parameter	Test 1 24 mm	Test 2 40 mm
Distance Vent to Cover		
m_{cell}	984.4 g	976.0 g
$m_{cell,postTR}$	477.7 g	426.0 g
Δm_{TR}	507.1 g/51.5%	550.0 g/56.4%
$m_{particles,total}$	26.13 g	32.83 g
$m_{particles,loose}$	23.95 g	32.65 g
$m_{particles,stick}$	2.18 g	0.18 g

3.2. Particle Size Distribution

Figure 8 shows the mass percentage of the four particle size ranges for both tests of this study (black and red bars) and compares these results to values from the literature [12,16–18]. Zhang et al. (blue bars) triggered a prismatic 50 Ah lithium-ion battery with an NMC622 cathode into the TR within a sealed chamber by external heating and analyzed the ejected solid particles regarding particle size distribution. They found particles within the range of $2.9 \mu\text{m} < d < 15 \text{ mm}$. However, particles with a size of $d < 500 \mu\text{m}$ were found to account for 90% of the total ejected particle mass [16]. Within a second study, Zhang et al. (brown bars) also analyzed the ejected particles for the same cell within the same experimental setup. The maximum particle size was found to be $\approx 8 \text{ mm}$ [17]. Wang et al. (green bars) conducted a third study with the setup of Zhang et al. and found particles within the size range of $1 \mu\text{m} < d < 2000 \mu\text{m}$ [18]. Wang et al. (violet bars) investigated the vented particles of a prismatic 27 Ah lithium-ion battery with an LFP cathode within a sealed chamber. They used an electric heater to trigger the TR and collected particles with sizes up to $d > 2 \text{ mm}$ [12]. Note that the mass percentage of Sizes 3 ($200 \mu\text{m} < d < 800 \mu\text{m}$) and 4 ($d > 800 \mu\text{m}$) could not be estimated for the results of Wang et al. published in Ref. [12].

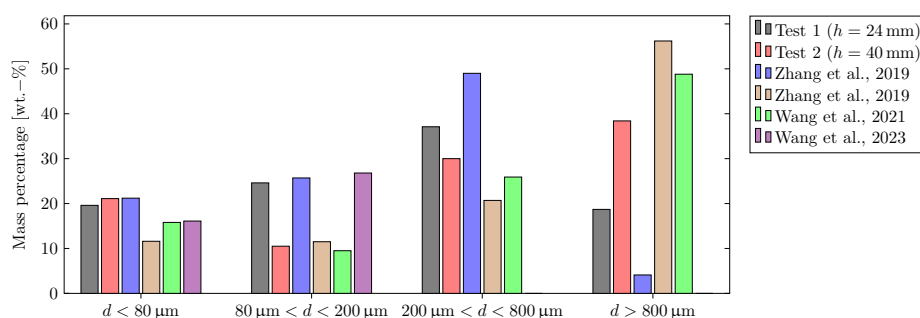


Figure 8. Comparison of the particle size distribution evaluated for both tests in this study with values from the literature [12,16–18]. The mass percentage of Sizes 3 and 4 could not be estimated for the study of Wang et al. (Ref. [12]).

For Test 1 (24 mm distance between cell vent and cover), there is an increase in the mass percentage values from Size range 1 ($d < 80 \mu\text{m}$: 19.6%) over Size range 2 ($80 \mu\text{m} < d < 200 \mu\text{m}$: 24.6%) to Size range 3 ($200 \mu\text{m} < d < 800 \mu\text{m}$: 37.1%). The mass percentage of Size range 4 ($d > 800 \mu\text{m}$: 18.7%) shows the lowest value. An explanation for these results is that a large fraction of Size range 4 particles is not depositing on the weighing plates but within the steel box due to the high gas flow velocities. It is also possible that particles of Size range 4 shatter into smaller pieces when they impinge into the walls. This can additionally explain the high mass percentage values for particle Size range 3. In addition, the shape of larger particles usually deviates more from the shape of an ideal sphere as shown in previous publications [12,17]. This may lead to higher drag coefficients.

The results of Test 2 (a 40 mm distance between cell vent and cover) show that the mass percentage of Size range 1 particles ($d < 80 \mu\text{m}$: 21.1%) is close to the results of Test 1. It is therefore hypothesized that the deposition of Size range 1 particles is nearly independent of the gas flow velocities and therefore the distance between cell vent and cover due to their small diameter. In contrast to Test 1, there is an increase in the mass percentage values from Size range 2 ($80 \mu\text{m} < d < 200 \mu\text{m}$: 10.5%) over Size range 3 ($200 \mu\text{m} < d < 800 \mu\text{m}$: 30.0%) to Size range 4 ($d > 800 \mu\text{m}$: 38.4%) for Test 2. Due to the lower gas velocities during Test 2, the forces of the gas flow acting on Size range 4 particles are not high enough to carry them into the steel box.

The results of this study are comparable to the results found in the literature [12,16–18]. For Size range 1, both tests of this study show comparable values to those of the study of Zhang et al. in Ref. [16]. However, comparison of the results of all three studies conducted

within the sealed reactor introduced by Zhang et al. reveals that there can be deviations in the particle size distributions for experiments conducted with the same cell and test procedure within the same setup [16–18]. These deviations are also observed for particle Size range 2: while the results of Test 1 are comparable to the results of Refs. [12,16], the results of Test 2 are close to the values published in Refs. [17,18]. For Size range 3, the results of this study's tests are within the range of the literature values, which is also the case for Size range 4 [16–18]. At this point, however, it has to be mentioned that for the results of this study, the size distribution of particles depositing on the weighing plates is analyzed, whereas for the studies in the literature all ejected particles are collected and investigated.

3.3. Specific Heat Capacity Measurements

Figure 9 shows the specific heat capacity over temperature for the four particle size ranges measured via DSC for Test 1 (solid line) and Test 2 (dashed line). The shown curves are the mean values of at least two of the three measurements conducted with probes of each particle size range sample. Some measurements had to be neglected due to significant swelling of the crucible and/or high mass loss (>4%) during the measurement.

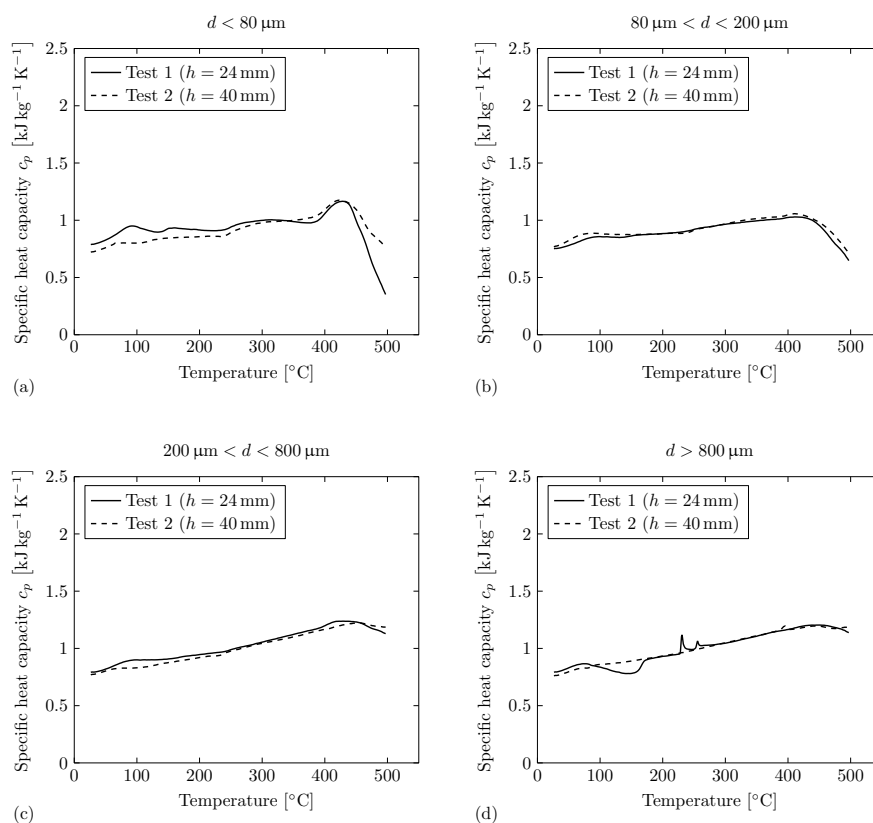


Figure 9. Specific heat capacity of the collected particles depositing on the weighing plates for both tests measured via DSC. The shown curves are the mean values of three probes measured for each size range. (a) Particle size range of $d < 80 \mu\text{m}$. (b) Particle size range of $80 \mu\text{m} < d < 200 \mu\text{m}$. (c) Particle size range of $200 \mu\text{m} < d < 800 \mu\text{m}$. (d) Particle size range of $d > 800 \mu\text{m}$.

For particle Size range 1 ($d < 80 \mu\text{m}$), the specific heat capacity curves over temperature are comparable for both tests. For Test 1, the values of the specific heat capacity are on a slightly elevated level compared to Test 2 for $T < 350 \text{ }^\circ\text{C}$. The curves of both tests show a decreasing trend of the specific heat capacity for $T > 425 \text{ }^\circ\text{C}$, which could be related to an exothermic reaction. For particle Size ranges 2 ($80 \mu\text{m} < d < 200 \mu\text{m}$) and 3

($200\ \mu\text{m} < d < 800\ \mu\text{m}$), the specific heat capacity curves over temperature are also comparable for both tests. There exist no irregularities within the course of the curves, besides the decreasing trend of the specific heat capacity for $T > 425\ ^\circ\text{C}$ for particle Size range 2. For particle Size range 3, the decreasing trend is not as significant as for particle Size ranges 2 or 1. For particle Size range 4 ($d > 800\ \mu\text{m}$), there exist individual irregularities for the specific heat capacity curves over temperature for each test. For Test 1, an exothermic reaction can be observed for $75\ ^\circ\text{C} < T < 170\ ^\circ\text{C}$. Two endothermic peaks appear at $T \approx 230\ ^\circ\text{C}$ and $T \approx 255\ ^\circ\text{C}$. For Test 2, there exists an endothermic peak at $T \approx 395\ ^\circ\text{C}$.

In conclusion, the specific heat capacity measurements deliver comparable values for all four particle size ranges in both tests. This is an important finding that helps to determine correct parameters for, e.g., simulation models of the gas–particle flow during TR. The found differences between the particle size ranges are potentially caused by the different oxidation characteristics due to different surface areas, which was already investigated in previous studies [18,22]. With increasing particle size, however, the decreasing trend at temperatures of $T > 420\ ^\circ\text{C}$ seems to be less significant. Explicit irregularities are only observed for particle Size range 4. This corresponds with the results of the thermal gravimetric analysis of Wang et al. conducted on ejected particles during TR of a 50 Ah prismatic battery with an NMC622 cathode [18]. They observed a moderate mass loss within the temperature range of $250\ ^\circ\text{C} < T < 600\ ^\circ\text{C}$ for particles of all size ranges. In addition, the results of the smallest particles ($10\ \mu\text{m} < d < 100\ \mu\text{m}$) indicated gas that evolved from volatile thermal decomposition or a diffusion of volatiles that were adsorbed in the pores of particles [18].

Figure 10 shows the specific heat capacity over temperature of the four samples out of the jelly roll remains (compare to Figure 3) measured via DSC for Test 1 (solid line) and Test 2 (dashed line). The shown curves are the mean values of at least two of the three measurements conducted with probes of each sample out of the jelly roll remains. Some measurements had to be neglected due to significant swelling of the crucible and/or high mass loss (>4%) during the measurement.

For Position 1 (underneath vent, compare to Figure 3), the specific heat capacity curves over temperature are comparable for both tests. For Test 2, the specific heat is on a slightly elevated level compared to Test 1. In addition, an endothermic reaction can be observed for $60\ ^\circ\text{C} < T < 165\ ^\circ\text{C}$ for Test 2. For Test 1, the curve shows a decreasing trend of the specific heat capacity for $T > 400\ ^\circ\text{C}$. For Position 2 (close to the nail, compare to Figure 3), the specific heat capacity curves over temperature show a comparable behavior for both tests besides individual irregularities. For Test 1, there exists an endothermic reaction for $45\ ^\circ\text{C} < T < 160\ ^\circ\text{C}$. For higher temperatures, the course of the curve is on a lower level compared to Test 2. For Test 2, a small exothermic peak is observed at $T \approx 85\ ^\circ\text{C}$, followed by an endothermic reaction within the temperature range of $90\ ^\circ\text{C} < T < 160\ ^\circ\text{C}$. For Position 3 (positive terminal side, compare to Figure 3), the specific heat capacity curves over temperature show significant irregularities for both tests. An exothermic peak can be observed for $T \approx 90\ ^\circ\text{C}$ for Test 1 and $T \approx 100\ ^\circ\text{C}$ for Test 2. In addition, there exist strong endothermic peaks at $T \approx 395\ ^\circ\text{C}$ for both tests. Further exothermic peaks are observed at $T \approx 425\ ^\circ\text{C}$ and $T \approx 450\ ^\circ\text{C}$. For Position 4 (negative terminal side, compare to Figure 3), the specific heat capacity curves over temperature also show significant irregularities for both tests. For both tests, endothermic peaks can be observed at $T \approx 395\ ^\circ\text{C}$. For Test 2, there exist smaller peaks indicating chemical reactions within the temperature range of $75\ ^\circ\text{C} < T < 155\ ^\circ\text{C}$.

In conclusion, the results show that the specific heat capacity of the jelly roll remains depends on the position within the jelly roll. The specific heat capacity measurements of Position 1 (underneath the vent) and Position 2 samples (close to the nail) delivered comparable results, but there exist significant differences from Position 3 (positive terminal side) and Position 4 (negative terminal side) samples. The latter show a strong endothermic peak at $T \approx 395\ ^\circ\text{C}$. Based on the data available from this study, it is unfortunately not

possible to analyze the exact causes of these differences. Further research is therefore recommended in this context.

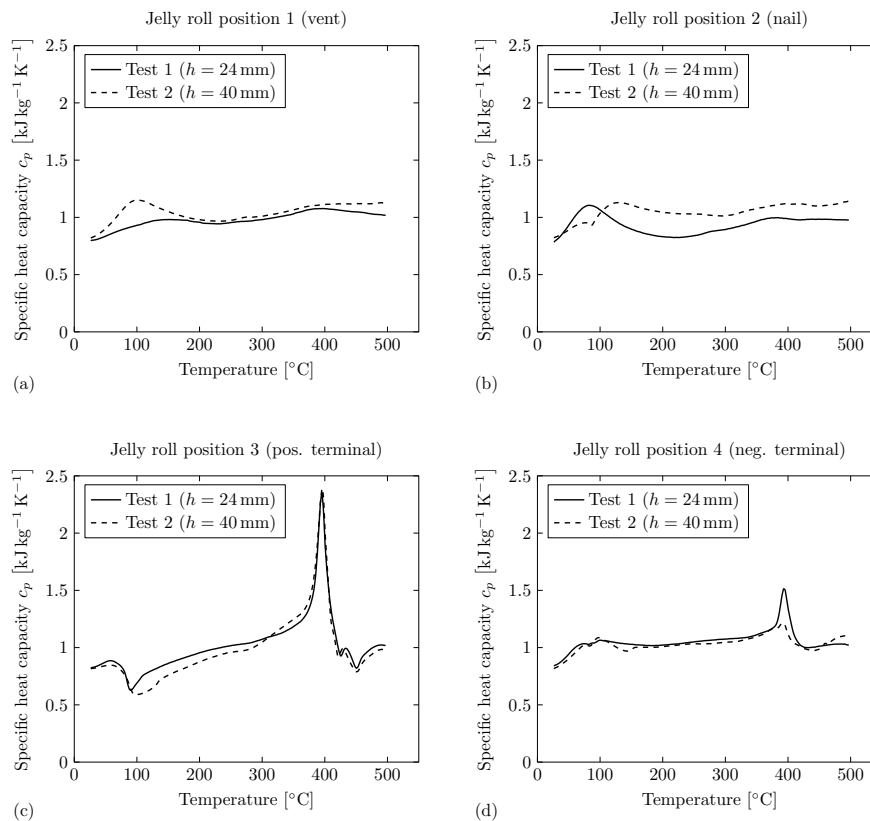


Figure 10. Specific heat capacity of the jelly roll remains for both tests measured via DSC. The shown curves are the mean values of three probes measured for each position (compare to Figure 3). (a) Sample extracted from Position 1 (vent), (b) Sample extracted from Position 2 (nail), (c) Sample extracted from Position 3 (pos. terminal), (d) Sample extracted from Position 4 (neg. terminal).

Figure 11 shows the specific heat capacity curves over temperature of the collected particles (solid lines) as well as the jelly roll remains (dashed lines) measured via DSC over temperature for Test 1 (black) and Test 2 (red). The shown curves are the mean values of all four particle sizes and all four jelly roll positions from Figure 9 and Figure 10, respectively.

The specific heat capacity measurements deliver comparable values for the particles ejected in both tests (solid lines). Therefore, it is concluded that there is a negligible dependence between the ejected particle’s specific heat capacity and the distance between cell vent and cover. In addition, there is no significant influence of the particle size on the specific heat capacity, as shown in Figure 9. The particle’s specific heat capacity can be set independently of the particle size and the battery’s installation case within simulation models, which is an important finding. For the jelly roll remains (dashed lines), the specific heat capacity measurements also deliver comparable values in both tests. It is concluded that there is a negligible dependence between the jelly roll remains’ specific heat capacity and the distance between cell vent and cover. However, there is an influence of the position within the jelly roll remains on the specific heat capacity, as shown in Figure 10.

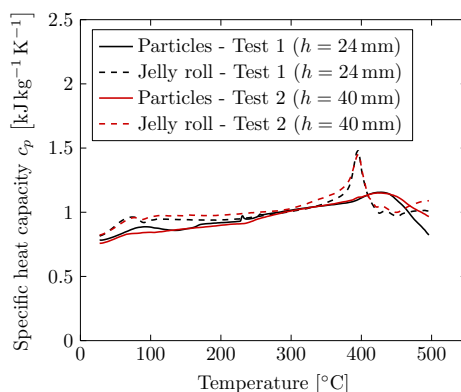


Figure 11. Specific heat capacity of the collected particles depositing on the weighing plates as well as the jelly roll remains for both tests measured via DSC. The shown curves are the mean values of all four particle sizes and all four jelly roll positions from Figure 9 and Figure 10, respectively.

Comparison of the specific heat capacity measurements of the ejected particles with the measurements of the jelly roll remains shows that the jelly roll remains have a slightly higher specific heat capacity. In addition, the occurrence of the endothermic peak at $T \approx 395$ °C for the jelly roll remains is a significant difference from the behavior of ejected particles. In this context, further investigations are recommended.

3.4. Suggestions for Further Improvement of the Proposed Setup

Based on the results of the proof-of-concept study presented here, the following suggestions for improvement are recommended for future research:

- As only a small fraction of the total ejected particle mass deposits on the weighing plates, it is recommended to extend the intermediate sheet metal. However, this can also result in higher time consumption for test preparation and evaluation.
- Determining the time-dependent particle deposition on the weighing plates, e.g., by implementing miniature load cells may provide further insights into the particle ejection process. This can also result in a more accurate weight measurement and lesser effort for post-test analysis.
- It is recommended to also collect particles that deposit within the steel box. This can offer further insights into the particle size distribution of all ejected particles.
- The milling process might be improved. There were still Cu particles that were not finely shredded with the method used in this study.
- Further findings could be obtained through the determination of the chemical composition for both ejected particles and jelly roll remains, for example, with inductively coupled plasma optical emission spectroscopy (ICP-OES).
- The presented results serve as proof of concept in the first place. Further tests must be carried out in order to quantify statistical deviations.

4. Conclusions

The presented study proposes a novel experimental setup to quantify the particle deposition during a lithium-ion battery TR. The setup integrates a single prismatic battery cell into an environment representing similar conditions as found for battery modules in EV battery packs. Within the flow path of the vented gas and particles, there are several weighing plates that can be individually removed from the setup in order to determine particle deposition. Two proof-of-concept experiments with a different distance between battery cell vent and cover are conducted. In addition, the size distribution of the vented particles is determined and specific heat capacity measurements are performed via DSC for both the vented particles and the jelly roll remains. The authors would like to point out

once again that the results of this study are based on just two proof-of-concept experiments and consequently the reliability of the statements made below is limited.

4.1. Particle Deposition

- The distance between cell vent and cover has a significant influence on the particle deposition on the weighing plates.
- With a 24 mm distance between cell vent and cover, particle accumulations concentrate at the side walls.
- With a 40 mm distance between cell vent and cover, particle accumulations are randomly distributed over the entire area. In addition, larger particles deposit on the weighing plates.

4.2. Particle Size Distribution

- The distance between cell vent and cover has an influence on the size distribution of particles depositing on the weighing plates.
- The mass percentage of small particles ($d < 80 \mu\text{m}$) is found to be nearly independent of the gas flow velocities.

4.3. Specific Heat Capacity Measurements

- The specific heat capacity measurements deliver comparable values for all four particle size ranges in both tests.
- The specific heat capacity measurements for the jelly roll remains indicate influence of the position within the jelly roll and the specific heat capacity.
- The influence of the distance between cell vent and cover on the specific heat capacity is negligible.

In summary, the proposed experimental setup is generally suitable to quantify the particle deposition during a lithium-ion battery TR. However, there is a need for further improvement in order to enhance the quality and reliability of the results. By additionally increasing the number of tests, the results may offer further insights into the particle ejection process during lithium-ion battery TRs. This is of utmost importance, as the ejected particles carry a significant amount of energy and can be responsible for causing short circuits during TR propagation within battery packs. Today, there is a lack of understanding of the role of ejected particles in TR propagation behavior, although they pose a safety risk. This study helps researches and engineers to gain a better understanding of the gas–particle flow occurring during TR. By implementing certain suggested improvements, the proposed experimental setup may in addition be used for simulation model validation. Crucial input parameters of such models are particle size distribution as well as the specific heat capacity of the particles; both are also provided within this study. Therefore, this study contributes to the improvement of battery pack design and safety.

Author Contributions: Conceptualization, S.H. and H.K.; methodology, S.H.; investigation, S.H. and H.K.; data curation, S.H.; writing—original draft preparation, S.H.; writing—review and editing, H.K., S.Z. and O.H.; visualization, S.H.; supervision, S.Z. and O.H. All authors have read and agreed to the published version of the manuscript.

Funding: This research received no external funding.

Data Availability Statement: The original contributions presented in the study are included in the article; further inquiries can be directed to the corresponding author.

Acknowledgments: The authors gratefully acknowledge the support of our BMW Group colleagues from the technology material and process analysis (TWA) in conducting the experiments and the support of our student Yunus Emir who took over a part of the CAD construction. In addition, S. Hoelle acknowledges the support of the TUM Graduate School.

Conflicts of Interest: Authors Sebastian Hoelle, Hyojeong Kim and Sascha Zimmermann were employed by the company BMW Group. The remaining authors declare that the research was

conducted in the absence of any commercial or financial relationships that could be construed as a potential conflict of interest.

Abbreviations and Symbols

The following abbreviations are used in this manuscript:

CCCV	constant current constant voltage
DSC	differential scanning calorimetry
DEC	diethyl carbonate
DMC	dimethyl carbonate
EC	ethylene carbonate
EMC	ethyl methyl carbonate
EV	electric vehicle
ICP-OES	inductively coupled plasma optical emission spectroscopy
LiPF ₆	lithium hexafluorophosphate
NMC	lithium nickel manganese cobalt oxide
SoC	state of charge
TR	thermal runaway

The following symbols are used in this manuscript:

A	flow path area, m ²
c_p	specific heat capacity, J kg ⁻¹ K ⁻¹
d	diameter, m
h	height between cell vent and cover of the test setup, m
m	mass, kg
Δ	difference, -
Indices:	
cell	index representing the full cell
i	index representing the weighing plate i
glas	index representing a glass (used for particle collection and weighing)
loose	index representing loose particles on a weighing plate
particles	index representing the particles vented during TR
postTR	index representing the state after TR
scraped	index representing particles that are scraped off from a weighing plate
stick	index representing sticking particles
total	index representing the total amount of particles on a weighing plate
TR	index representing the TR process

References

- Sun, P.; Bisschop, R.; Niu, H.; Huang, X. A Review of Battery Fires in Electric Vehicles. *Fire Technol.* **2020**, *56*, 1361–1410. [\[CrossRef\]](#)
- Huang, W.; Feng, X.; Han, X.; Zhang, W.; Jiang, F. Questions and Answers Relating to Lithium-Ion Battery Safety Issues. *Cell Rep. Phys. Sci.* **2021**, *2*, 100285. [\[CrossRef\]](#)
- Feng, X.; Ouyang, M.; Liu, X.; Lu, L.; Xia, Y.; He, X. Thermal runaway mechanism of lithium ion battery for electric vehicles: A review. *Energy Storage Mater.* **2018**, *10*, 246–267. [\[CrossRef\]](#)
- Liu, J.; Li, J.; Wang, J. In-depth analysis on thermal hazards related research trends about lithium-ion batteries: A bibliometric study. *J. Energy Storage* **2021**, *35*, 102253. [\[CrossRef\]](#)
- Jindal, P.; Bhattacharya, J. Review—Understanding the Thermal Runaway Behavior of Li-Ion Batteries through Experimental Techniques. *J. Electrochem. Soc.* **2019**, *166*, A2165–A2193. [\[CrossRef\]](#)
- Ouyang, D.; Chen, M.; Huang, Q.; Weng, J.; Wang, Z.; Wang, J. A Review on the Thermal Hazards of the Lithium-Ion Battery and the Corresponding Countermeasures. *Appl. Sci.* **2019**, *9*, 2483. [\[CrossRef\]](#)
- Wang, Q.; Mao, B.; Stolarov, S.I.; Sun, J. A review of lithium ion battery failure mechanisms and fire prevention strategies. *Prog. Energy Combust. Sci.* **2019**, *73*, 95–131. [\[CrossRef\]](#)
- Feng, X.; Ren, D.; He, X.; Ouyang, M. Mitigating Thermal Runaway of Lithium-Ion Batteries. *Joule* **2020**, *4*, 743–770. [\[CrossRef\]](#)
- Li, W.; Xue, Y.; Feng, X.; Rao, S.; Zhang, T.; Gao, Z.; Guo, Y.; Zhou, H.; Zhao, H.; Song, Z.; et al. Characteristics of particle emissions from lithium-ion batteries during thermal runaway: A review. *J. Energy Storage* **2024**, *78*, 109980. [\[CrossRef\]](#)
- Zou, K.; Chen, X.; Ding, Z.; Gu, J.; Lu, S. Jet behavior of prismatic lithium-ion batteries during thermal runaway. *Appl. Therm. Eng.* **2020**, *179*, 115745. [\[CrossRef\]](#)

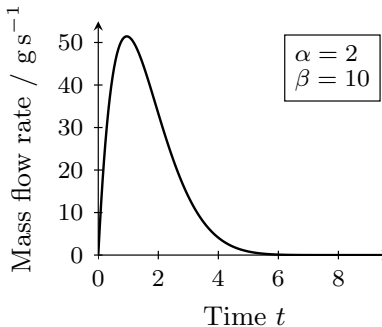
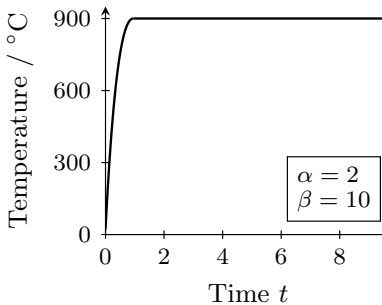
11. Garcia, A.; Monsalve-Serrano, J.; Sari, R.L.; Martinez-Boggio, S. An optical investigation of thermal runaway phenomenon under thermal abuse conditions. *Energy Convers. Manag.* **2021**, *246*, 114663. [CrossRef]
12. Wang, G.; Kong, D.; Ping, P.; Wen, J.; He, X.; Zhao, H.; He, X.; Peng, R.; Zhang, Y.; Dai, X. Revealing particle venting of lithium-ion batteries during thermal runaway: A multi-scale model toward multiphase process. *eTransportation* **2023**, *16*, 100237. [CrossRef]
13. Ding, C.; Zhu, N.; Yu, J.; Li, Y.; Sun, X.; Liu, C.; Huang, Q.; Wang, J. Experimental investigation of environmental pressure effects on thermal runaway properties of 21700 lithium-ion batteries with high energy density. *Case Stud. Therm. Eng.* **2022**, *38*, 102349. [CrossRef]
14. Liao, Z.; Zhang, S.; Li, K.; Zhao, M.; Qiu, Z.; Han, D.; Zhang, G.; Habetler, T.G. Hazard analysis of thermally abused lithium-ion batteries at different state of charges. *J. Energy Storage* **2022**, *27*, 101065. [CrossRef]
15. Essl, C.; Golubkov, A.W.; Gasser, E.; Nachtnebel, M.; Zankel, A.; Ewert, E.; Fuchs, A. Comprehensive Hazard Analysis of Failing Automotive Lithium-Ion Batteries in Overtemperature Experiments. *Batteries* **2020**, *6*, 30. [CrossRef]
16. Zhang, Y.; Wang, H.; Li, W.; Li, C. Quantitative identification of emissions from abused prismatic Ni-rich lithium-ion batteries. *eTransportation* **2019**, *2*, 100031. [CrossRef]
17. Zhang, Y.; Wang, H.; Li, W.; Li, C.; Ouyang, M. Size distribution and elemental composition of vent particles from abused prismatic Ni-rich automotive lithium-ion batteries. *J. Energy Storage* **2019**, *26*, 100991. [CrossRef]
18. Wang, Y.; Wang, H.; Zhang, Y.; Cheng, L.; Wu, Y.; Feng, X.; Lu, L.; Ouyang, M. Thermal oxidation characteristics for smoke particles from an abused prismatic Li(Ni_{0.6}Co_{0.2}Mn_{0.2})O₂ battery. *J. Energy Storage* **2021**, *39*, 102639. [CrossRef]
19. Premnath, V.; Wang, Y.; Wright, N.; Khalek, I.; Uribe, S. Detailed characterization of particle emissions from battery fires. *Aerosol Sci. Technol.* **2022**, *56*, 337–354. [CrossRef]
20. Chen, S.; Wang, Z.; Yan, W. Identification and characteristics analysis of powder ejected from a lithium ion battery during thermal runaway at elevated temperatures. *J. Hazard. Mater.* **2020**, *400*, 123169. [CrossRef]
21. Held, M.; Tuchschnid, M.; Zennegg, M.; Figi, R.; Schreiner, C.; Mellert, L.D.; Welte, U.; Kompatscher, M.; Hermann, M.; Nachev, L. Thermal runaway and fire of electric vehicle lithium-ion battery and contamination of infrastructure facility. *Renew. Sustain. Energy Rev.* **2022**, *165*, 112474. [CrossRef]
22. Wang, H.; Wang, Q.; Jin, C.; Xu, C.; Zhao, Y.; Li, Y.; Zhong, C.; Feng, X. Detailed characterization of particle emissions due to thermal failure of batteries with different cathodes. *J. Hazard. Mater.* **2023**, *458*, 131646. [CrossRef] [PubMed]
23. Coman, P.T.; Rayman, S.; White, R.E. A lumped model of venting during thermal runaway in a cylindrical Lithium Cobalt Oxide lithium-ion cell. *J. Power Sources* **2016**, *307*, 56–62. [CrossRef]
24. Coman, P.T.; Darcy, E.C.; White, R.E. Simplified Thermal Runaway Model for Assisting the Design of a Novel Safe Li-Ion Battery Pack. *J. Electrochem. Soc.* **2022**, *169*, 040516. [CrossRef]
25. Ostanek, J.K.; Li, W.; Mukherjee, P.P.; Crompton, K.R.; Hacker, C. Simulating onset and evolution of thermal runaway in Li-ion cells using a coupled thermal and venting model. *Appl. Energy* **2020**, *268*, 114972. [CrossRef]
26. Li, W.; Quiroga, V.L.; Crompton, K.R.; Ostanek, J.K. High Resolution 3-D Simulations of Venting in 18650 Lithium-Ion Cells. *Front. Energy Res.* **2021**, *9*, 788239. [CrossRef]
27. Kim, J.; Mallarapu, A.; Finegan, D.P.; Santhanagopalan, S. Modeling cell venting and gas-phase reactions in 18650 lithium ion batteries during thermal runaway. *J. Power Sources* **2021**, *489*, 229496. [CrossRef]
28. Citarella, M.; Suzzi, D.; Brunnsteiner, B.; Schiffbänker, P.; Maier, G.; Schneider, J. Computational Modelling of Thermal Runaway Propagation in Lithium-Ion Battery Systems. In Proceedings of the 2019 IEEE Transportation Electrification Conference (ITEC-India), Bengaluru, India, 17–19 December 2019. Available online: <https://ieeexplore.ieee.org/abstract/document/9080817> (accessed on 22 April 2024).
29. Mishra, D.; Shah, K.; Jain, A. Investigation of the Impact of Flow of Vented Gas on Propagation of Thermal Runaway in a Li-Ion Battery Pack. *J. Electrochem. Soc.* **2021**, *168*, 060555. [CrossRef]
30. Hoelle, S.; Scharner, S.; Asanin, S.; Hinrichsen, O. Analysis on Thermal Runaway Behavior of Prismatic Lithium-Ion Batteries with Autoclave Calorimetry. *J. Electrochem. Soc.* **2021**, *168*, 120515. [CrossRef]

Disclaimer/Publisher’s Note: The statements, opinions and data contained in all publications are solely those of the individual author(s) and contributor(s) and not of MDPI and/or the editor(s). MDPI and/or the editor(s) disclaim responsibility for any injury to people or property resulting from any ideas, methods, instructions or products referred to in the content.

Gas-particle-flow model As pointed out in section 1.5, the number of publications numerically investigating the gas-particle-flow during a lithium-ion cell TR is small. Wang et al. published one of the few studies proposing a fluid flow model that includes a phase for the vented particles during TR. Therefore, they used an Euler-Lagrange approach within the CFD framework of OpenFOAM.²⁶⁵ In the following, this approach is adopted to build a gas-particle-flow model of the particle deposition experiment described in the previous section within the 3D-CFD-framework of *Simcenter STAR-CCM+*[®]. For a detailed discussion on fundamentals of CFD or gas-particle-flow modeling, it is referred to Refs. [291–296].

Table 3.1 summarizes all relevant model parameters and boundary conditions used for the gas phase of the model. The gas phase is modeled as Eulerian flow field by solving the Reynolds-averaged Navier-Stokes equations with a $k-\varepsilon$ turbulence model. An ideal

Table 3.1: Model parameters and boundary conditions used for the gas phase of the particle-flow-model.

Parameter	Value	Source	
Gas components	Component	mole fraction	
	CO ₂	36.6 %	based on Ref. [168], fractions of C ₂ H ₆ and C ₃ H ₆ added to C ₂ H ₄
	CO	28.4 %	
	H ₂	22.3 %	
	C ₂ H ₄	7.4 %	
CH ₄	5.3 %		
Vented gas mass	$m_{\text{gas}} = 114.7 \text{ g}$	obtained from autoclave calorimetry experiments	
Venting duration	$t_{\text{venting}} = 9.5 \text{ s}$	observation during experiments	
Gas mass flow rate		empirical function (beta distribution), based on Refs. [262, 265]	
Gas temperature		empirical function (beta distribution) until maximum value, constant afterwards	

non-reacting multi-component gas consisting of CO_2 , CO , H_2 , C_2H_4 , and CH_4 is assumed to be vented out of the lithium-ion cell. The gas composition is based on the findings of Koch et al. in Ref. [168], the vented gas mass m_{gas} is obtained from autoclave calorimetry experiments, and the venting duration t_{venting} is chosen as observed during the particle deposition experiments. The gas mass flow rate and temperature are chosen empirically in accordance with previous studies.^{262,265}

Table 3.2 summarizes all relevant model parameters and boundary conditions used for the particle phase of the model. The particle phase is modeled as Lagrangian flow field containing ideally spherical solid particles with a constant density. As for the gas phase, the vented particle mass $m_{\text{particles}}$ is obtained from autoclave experiments. The particles are injected into the simulation domain by a cone injector with a cone angle of 10° and an aspect ratio of 14, which are both empirically chosen in accordance with the observations of Wang et al. in Ref. [265]. The particle mass flow rate and the particle velocity follow the same empirical function (beta distribution) as the gas mass flow rate. The maximum particle velocity is set to $v_{\text{particles,max}} = 14.5 \text{ m s}^{-1}$ as found in Ref. [265], the particle temperature is set equal to the gas temperature, and the particle size distribution is taken from Ref. [172]. In addition, two-way coupling is activated for the gas-particle-flow, i.e. the particles interact with the fluid flow and vice versa. Therefore, drag and shear lift forces are considered, as well as heat transfer between gas and particles. The drag coefficient is based on the Schiller-Naumann correlation, the shear lift coefficient on the Sommerfeld correlation, and the heat transfer on the Ranz-Marshall correlation.²⁹⁶ The particle-wall interaction is set as follows: particles impinging on a wall will rebound if their velocity magnitude is $\|\mathbf{v}_{\text{imp}}\| > 0.1 \text{ m s}^{-1}$. The rebound velocity \mathbf{v}_{reb} relative to the wall is defined by the wall-normal and tangential component of the impingement velocity ($v_{\text{imp,n}}$ and $v_{\text{imp,t}}$, respectively) and the corresponding restitution coefficients (e_n and e_t , respectively).²⁹⁶

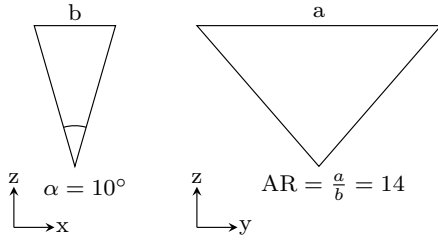
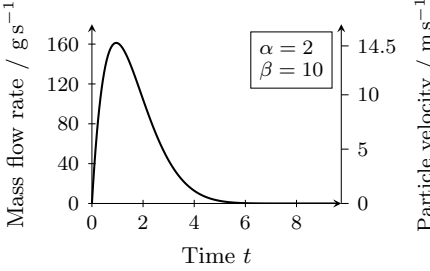
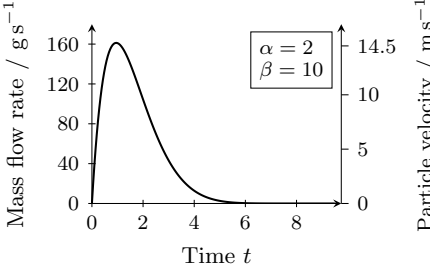
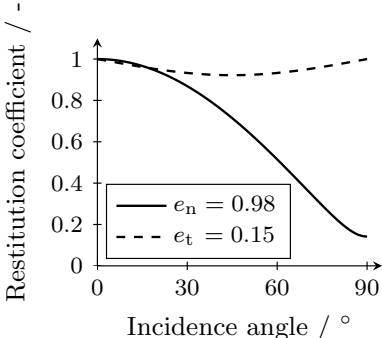
$$\mathbf{v}_{\text{reb}} = e_t v_{\text{imp,t}} - e_n v_{\text{imp,n}} . \quad (3.1)$$

The restitution coefficients are used as fitting parameters and depending on the impingement incidence angle.²⁹⁷

In order to reduce the necessary computational resources, the model domain is limited to the volume between weighing plates and module cover. Consequently, the steel box is not included in the model. Both experiments are modeled as transient simulation with a time step of $\Delta t = 0.001 \text{ s}$ and a total physical time of 10 s. This correlates to the venting duration of $t_{\text{venting}} = 9.5 \text{ s}$ that has been observed during the experiments. The initial temperature is set to $T_{\text{init}} = 21 \text{ }^\circ\text{C}$.

Figure 3.1 shows the experimentally measured and simulated mass distribution of deposited particles on the weighing plates. The case with 24 mm distance between cell vent and module cover is shown in Fig. 3.1a (experiment) and Fig. 3.1b (simulation). The case with 40 mm distance between cell vent and module cover is shown in Fig. 3.1c (experiment) and Fig. 3.1d (simulation).

Table 3.2: Model parameters and boundary conditions used for the particle phase of the particle-flow-model.

Parameter	Value	Source	
Particle density	$\rho_{\text{particles}} = 2233.6 \text{ kg m}^{-3}$	$\frac{m_{\text{JR}} - m_{\text{electrolyte}}}{V_{\text{JR}}}$	
Vented particle mass	$m_{\text{particles}} = 359.4 \text{ g}$	obtained from autoclave calorimetry experiments	
Particle cone injector		empirical, based on observations in Ref. [265]	
Particle mass flow rate		empirical function (beta distribution), based on Refs. [262, 265]	
Particle velocity			
Particle temperature	$T_{\text{particles}} = T_{\text{gas}}$	see Tab. 3.1	
Particle diameter	Size range / mm	fraction	Ref. [172]
	0.01 - 0.1	19.7 %	
	0.1 - 0.45	19.4 %	
	0.45 - 1.0	19.0 %	
	1.0 - 1.6	19.5 %	
1.6 - 2.0	22.4 %		
Gas-particle interaction	<ul style="list-style-type: none"> • drag force coefficient: Schiller-Naumann correlation • shear lift coefficient: Sommerfeld correlation • heat transfer: Ranz-Marshall correlation 	Ref. [296]	
Particle-wall interaction		fitting parameter, based on Ref. [297]	

3 Thermal Propagation Behavior of Lithium-Ion Battery Cell Stacks

For 24 mm distance, the experimental results show an accumulation of particles in the outer columns 1 and 6 (Fig. 3.1a). Especially for the rows around the cell (row 6 to 11), more than 1000 mg of particles deposit on several individual plates. The maximum mass of particles depositing on a single plate is 2710 mg (column 1, row 7). Within the columns 2 to 5, the mass depositing on single plates is below 141 mg. In total, 26.13 g of particles deposited on the weighing plates.

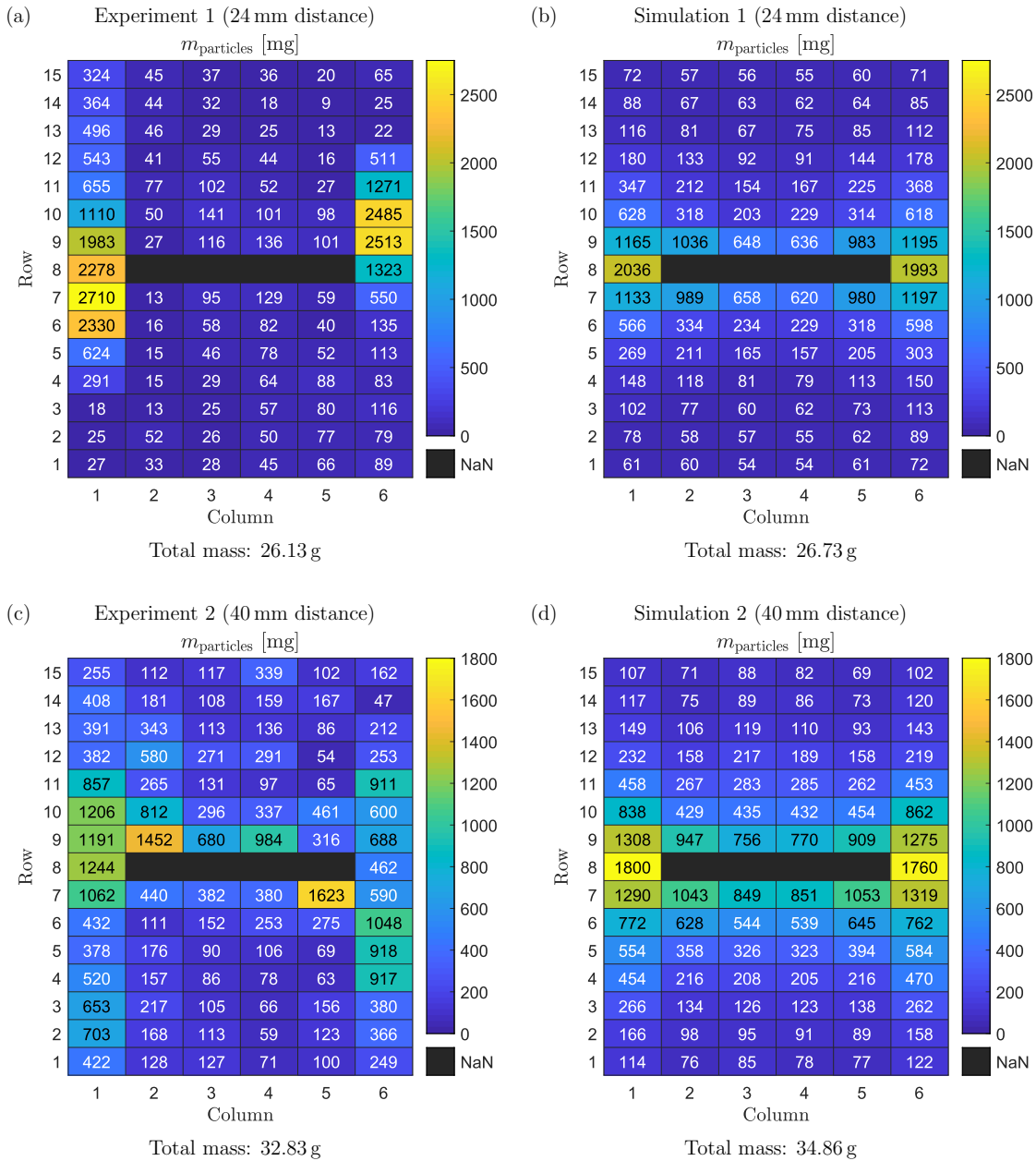


Figure 3.1: Mass of deposited particles on each weighing plate as determined in experiment 1 (a) and simulation 1 (b) for 24 mm distance between cell vent and module cover, as well as in experiment 2 (c) and simulation 2 (d) for 40 mm distance between cell vent and module cover.

The simulation model for 24 mm distance (Fig. 3.1b) is capable to reproduce the behavior of particle accumulation in the outer columns 1 and 6, but particles also aggregate on the

weighing plates in direct contact to the cell. Especially for columns 2 to 5 in row 7 and 9, the simulation model shows significant deviations from the experimental values. The maximum mass of particles depositing on a single plate is 2036 mg (column 1, row 8), which is lower than determined in the experiment. The total mass of particles depositing on the weighing plates (26.73 g), however, is in agreement with the experimental results.

For 40 mm distance, the experimental results also show an accumulation of particles in the outer columns 1 and 6 (Fig. 3.1c), but particles additionally aggregate within the inner columns 2 to 5 on weighing plates close to cell. The maximum mass of particles depositing on a single plate is also found in this area (1623 mg, column 5, row 7). In general, the mass is more evenly distributed in comparison to the lower distance between cell vent and module cover. In total, 32.83 g of particles deposited on the weighing plates.

The simulation model for 40 mm distance (Fig. 3.1d) shows a similar behavior. There are particle accumulations in the outer columns 1 and 6, but there is also more particle mass distributed within the inner columns 2 to 5. The maximum mass of particles depositing on a single plate is 1800 mg (column 1, row 8), which is higher than determined in the experiment. The total mass of particles depositing on the weighing plates is 34.86 g and therefore slightly higher compared to the experimental results.

There are several potential causes for the deviations between experimental and simulation results. First of all, the experimentally determined values are subject to uncertainties. The particle collection process, for example, causes inaccuracies, as particles may have moved during module cover removal or when the individual weighing plates were taken out of the test setup. In addition, only a single test per distance between cell vent and module cover was conducted. Therefore, statistical deviations cannot be quantified at this stage. A second reason for deviations is the potential choice of wrong input parameters for the simulation model. As mentioned before, some of the model parameters, such as the gas or particle mass flow rate or the restitution coefficients during particle-wall impingement, could not be derived from literature and hence had to be chosen empirically. During the model development, the following of these empirically chosen parameters showed a significant effect on the simulation results:

- gas mass flow rate,
- particle cone injector,
- particle mass flow rate,
- particle velocity, and
- particle-wall interaction.

For further improvement of the gas-particle-flow model, these unknown parameters need to be investigated in more detail.

4 Predictive Modeling of the Thermal Propagation Behavior

Satisfying both range and safety requirements of BEVs requires an extensive design and validation process that may be linked to high expenses. As OEMs rely on making a profit on the vehicles they sell, one of their objectives is to establish efficient experimental and numerical methods in order to reduce the costs related to battery pack design and validation. As pointed out in section 1.4, there exist various experimental methods on single and multiple cell level that aim to characterize lithium-ion cell TRs or their TP behavior within systems containing several battery cells. Within this context, additional effort is put into numerical methods that are capable of simulating these phenomena (see section 1.5). Most studies, however, focus only on experiments or modeling at either single or multiple cell level. Therefore, a multi-stage approach combining experimental and numerical methods on single and multiple cell level is necessary in order to enable an efficient assessment of the TP behavior.

In section 4.1, such an approach is presented for the application to a cell stack of prismatic lithium-ion cells by pointing out the interactions between the different experiments and simulation models introduced in section 2 and 3. Basically, the approach can be seen as workflow for the build-up of a predictive model for the TP behavior of lithium-ion battery cell stacks. Subsequently, in section 4.2, the resulting model is compared to experimental results of the cell stack experiment presented in section 3.2.1. In contrast to previous work, the proposed model considers all relevant aspects of the TP process, more precisely the model couples the solid body domain presented in section 3.1 with the gas-particle-flow domain presented in section 3.2.2. In particular, considering particles vented during TR of a lithium-ion cell was rarely done in the past (see section 1.5).

4.1 Multi-stage approach for efficient assessment of the thermal propagation behavior

In order to assess the TP behavior of lithium-ion batteries, experiments on multiple cell level are essential. Such experiments require special laboratories, instruments, and facilities, which cause high expenses. Testing of battery modules or packs is linked to additional costs, as they usually are only available when disassembled from an EV. Therefore, cell stack tests are widely used as low-cost alternative in order to investigate the TP behavior of lithium-ion batteries as pointed out in section 1.4. Simultaneously, numerical TP models are utilized as efficient and cost-effective tool to virtually develop and validate the design of battery packs with respect to safety (see section 1.5). In order to establish such

virtual methods it is necessary to determine, on the one hand, several input parameters by experiments. On the other hand, experimental data is required to validate the models. Figure 4.1 shows the schematic representation of a multi-stage approach that allows to efficiently assess the TP behavior in cell stacks of prismatic lithium-ion cells by combining both experimental and numerical methods. Experiments are shown as rectangle within the upper orange box, whilst simulation models are shown as circle (single domain) or as hexagon (coupling of domains) within the lower green box. Both experiments and simulation models are divided into three integration levels: there is the single cell level on the left and the multiple cell level on the right side. In addition, there is an “intermediate” level for the gas-particle-flow, as the corresponding particle deposition experiment is an experiment conducted with a single lithium-ion cell on the one hand, but on the other hand the experimental setup aims to represent battery module conditions and therefore the multiple cell level. Orange arrows indicate that parameters determined by experiments are used as input parameters for simulation models, whilst blue arrows indicate that experimental results are used to validate simulation models.

In order to determine necessary input parameters for a TR model within the solid body domain, two experiments are necessary: ARC and autoclave calorimetry. ARC experiments provide the TR trigger temperature T_{trigger} as well as the self-heating rate during TR dT/dt . As pointed out in section 2.2 and 3.1, a time-dependent function is recommended as modeling approach for the heat release during TR. This approach not necessarily requires dT/dt , which is indicated by brackets. Depending on the use case, however, other modeling approaches requiring the self-heating rate during TR may be more appropriate. Further necessary input parameters for the solid body TR model can be estimated by autoclave calorimetry experiments. The TR duration t_{TR} is necessary to derive the time-dependent function for heat release during TR, the mass of the cell after TR m_{remains} is necessary to consider the mass loss during TR by an adaption of the jelly roll density, and the fraction of heat released during TR remaining in the cell body Q_{remains} is necessary in order to fulfill the energy balance. The temperatures monitored during the experiment at several positions $T_i(t)$ can be used to validate the TR model.

The autoclave calorimetry experiment also provides input parameters for the gas-particle-flow model that accounts for the gas and particles vented during a lithium-ion cell TR. Necessary input parameters are the mass of vented gas m_{gas} , the mass of vented particles $m_{\text{particles}}$, the duration of venting t_{venting} , and the fraction of heat released during TR that is vented out of the cell body Q_{venting} . In order to validate the gas-particle-flow model, the mass distribution of vented particles obtained from the experiment presented in section 3.2.2 is used. The particle size distribution obtained from the experiment may be used as additional input parameter for the simulation model.

The temperatures monitored at several positions $T_i(t)$ during cell stack tests with an open setup, i.e. without any housing, and the propagation time are used to validate the TP model, resulting from transferring the TR model from single cell to multiple cell level. As the lithium-ion cells in the cell stack tests are exposed to different constraints compared to the autoclave calorimetry experiment, the mass of the cells after TR m_{remains} is adapted

4.1 Multi-stage approach for efficient assessment of the thermal propagation behavior

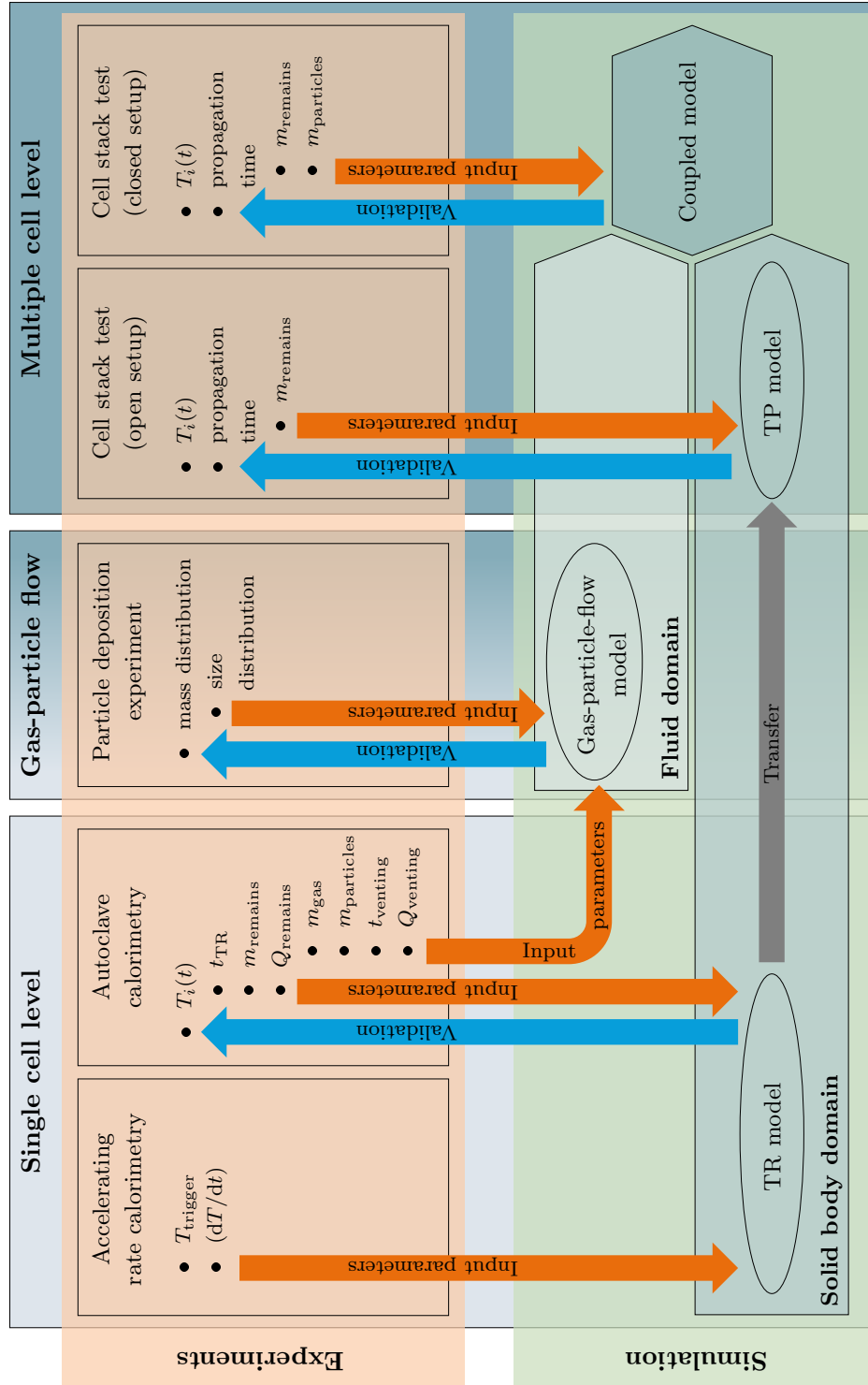


Figure 4.1: Schematic representation of a multi-stage approach that allows to efficiently assess the TP behavior of prismatic lithium-ion battery cell stacks.

according to the results of the cell stack experiment. As described in section 3.1, this also affects Q_{remains} , which consequently has to be adapted.

The coupled model combining both solid body (section 3.1) and fluid domain (section 3.2.2) is validated with experimental data from stack tests with a closed setup, i.e. the cell stack was integrated into a housing. As for the solid body TP model, temperatures monitored during the experiment at several positions $T_i(t)$ and the propagation time are used for this purpose. In addition, m_{remains} as well as $m_{\text{particles}}$ and hence Q_{remains} as well as Q_{venting} are adapted according to the test results.

4.2 Comparison of simulation and experiment

As shown in section 2.1, on average 44.7% of the heat released during a TR are transported out of the lithium-ion cell during the venting process in form of gas, liquid droplets and solid particles. This has a significant effect on the TP behavior within battery packs, where the ejected matter is for the most part kept within a housing. The comparison of TP experiments in an open and closed setup reveals, that the total propagation time of a cell stack consisting of five prismatic lithium-ion cells is reduced to 64.3% when the stack is integrated into a housing compared to a setup without housing (see section 3.2.1). In the following, the solid body domain TP model presented in section 3.1 is successively extended by a gas phase and a particle phase in order to assess the effect of considering Q_{venting} within TP simulations. Therefore, the gas-particle-flow model presented in section 3.2.2 is coupled with the solid body domain. For the simulation without particles, the Lagrangian phase of the gas-particle-flow model is deactivated.

In Fig. 4.2, the simulation results are compared to the experimental results for the total time of the experiment. Figure 4.2a shows the temperature sensor values on both sides of the thermal insulation material between cell 1 and 2 over time t since nail penetration of cell 1 for two experiments (black and gray) and the three simulations (colored). The two experiments were conducted with the same setup in order to cover a minimum statistical variance. The green curves represent the results of the solid body simulation without any additional gas or particle phase, the blue curves represent the solid body simulation coupled with a gas phase, and the red curves represent the fully coupled model, i.e. with consideration of gas and particles. Figure 4.2b-d show the temperature sensor values on both sides of the thermal insulation material between cell 2 and 3, cell 3 and 4, and cell 4 and 5, respectively.

Comparing the simulation results (colored curves) to the experimental results (black and grey curves) for the TP process from cell 1 to cell 2 (Fig. 4.2a) shows acceptable results for all simulation models. The difference in time of TR initiation in cell 2 between experiments and simulations is negligible small. It is concluded, that a coupling of the thermal model with a gas or a gas-particle-flow phase has a minor influence during this first phase of the TP process ($t < 172\text{s}$). In the further course, however, the influence of the vented gas and the vented particles becomes more significant (Fig. 4.2b-d). In

order to quantitatively determine this effect, Tab. 4.1 summarizes the time of TR initiation in each cell for both experiments and the three simulation models. The deviation between the thermal model (green curves) and the mean experimental value increases to 7.4% for cell 3 (Fig. 4.2b), 13.6% for cell 4 (Fig. 4.2c), and 14.2% for cell 5 (Fig. 4.2d). As expected, coupling the solid body domain with a gas phase (without particles - blue curves) accelerates the predicted TP process, but the time of TR in cell 5 still shows a deviation of 5.3% or 22 s. The coupled model considering not only gas but also vented particles (red curves) is capable of reducing this deviation to 0.7%. In sum, coupling the thermal model with a gas-particle-flow phase accelerated the TP process of the cell stack experiment investigated here by 57 s. For a larger number of cells within the cell stack, this effect is expected to become even more significant.

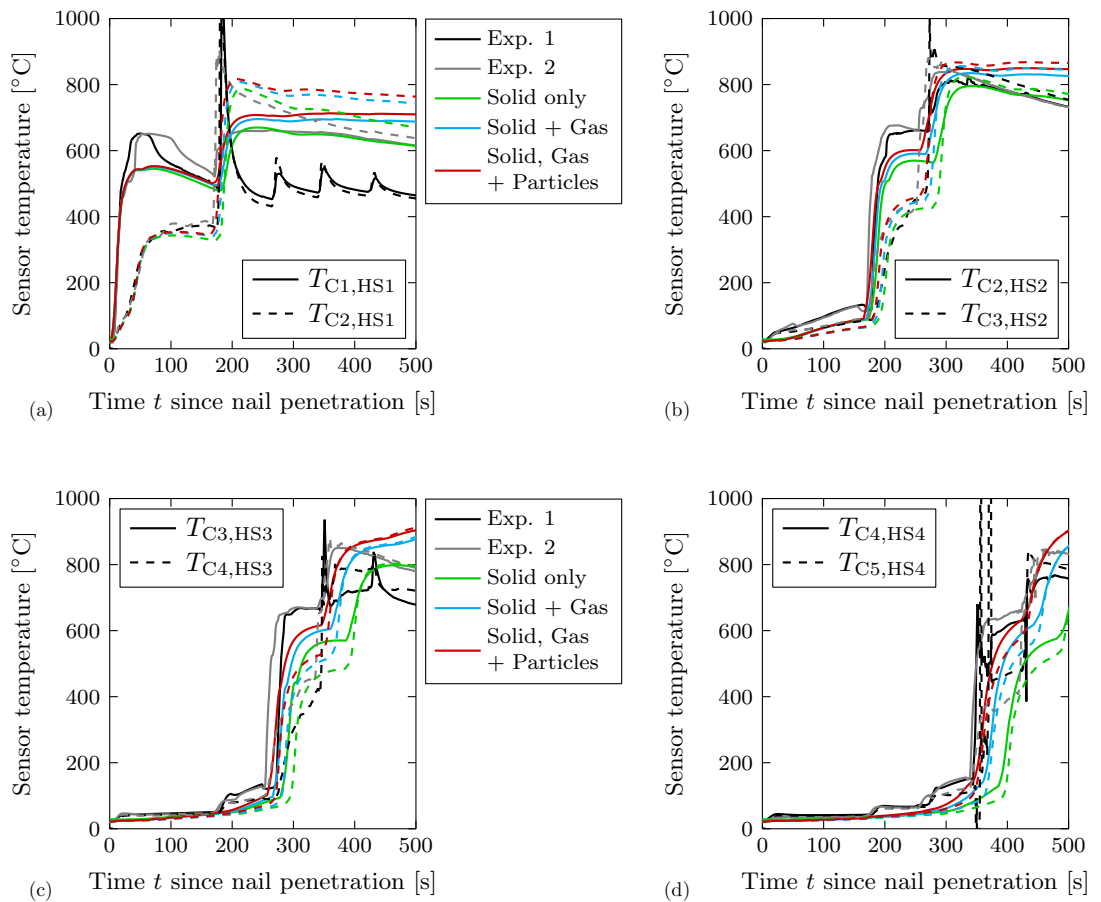


Figure 4.2: Sensor temperature on both sides of each thermal insulation material (heat-shield, subscript “HS”) in between the single cells over time t since nail penetration for both experiments (black and gray) and the three simulations (colored). (a) Sensor temperature on both sides of the thermal insulation material between cell 1 and 2. (b) Sensor temperature on both sides of the thermal insulation material between cell 2 and 3. (c) Sensor temperature on both sides of the thermal insulation material between cell 3 and 4. (d) Sensor temperature on both sides of the thermal insulation material between cell 4 and 5.

A possible explanation for these observations is as follows: during the venting process, the convective heat transfer to adjacent cells caused by the gas flow may result in significant heat transfer rates. The surface area being exposed to the gas flow, however, is small compared to the total surface of the cell. In addition, the duration of venting potentially is too short in order to transfer a considerable amount of heat. Therefore, the forced convection during venting is not considered to result in a significant acceleration of the TP process. After the venting process, however, the gas temperature within the housing will be at an elevated level compared to the initial state. This results in heat transfer via natural convection. As the heat transfer coefficient for natural convection is relatively low, the influence on the TP process is only noticeable for a longer duration. With every venting that occurs, the gas temperature within the housing will further increase and, hence, enhance heat transfer. Adding a particle phase to the model additionally contributes to an increase of the gas temperature within the housing. As known from section 2.1, the particles on average account for 70.9% of the total mass loss and, hence, 70.9% of Q_{venting} are allocated to these particles. Both experimental and numerical results show that most of the particles do not deposit on adjacent cells directly, but rather distribute on the housing's base plate. It is therefore concluded, that the acceleration of the TP process is caused by the enhancement of the natural convection due to particles transferring heat to the gas within the housing. On the one hand, this leads to higher gas temperatures, but also to the fact that these are present for a longer time.

Table 4.1: Time of TR initiation during experiment and simulation.

	Experiment			Simulation		
	No. 1	No. 2	mean	Solid only	Solid + gas	Solid + gas + particles
Cell 2	176 s	168 s	172 s	174 s / 1.0 %	169 s / -1.7 %	167 s / -3.3 %
Cell 3	267 s	251 s	259 s	278 s / 7.4 %	266 s / 2.6 %	257 s / -0.8 %
Cell 4	343 s	335 s	339 s	385 s / 13.6 %	359 s / 5.9 %	345 s / 1.8 %
Cell 5	424 s	418 s	421 s	481 s / 14.2 %	443 s / 5.3 %	424 s / 0.7 %

Taking into account that for the investigated cell stack experiment the majority of the vented particles do not deposit on adjacent cells, it is concluded that the coupled model delivers acceptable results for this case of application despite the limitations of the gas-particle-flow model discussed in section 3.2.2. Depending on the application case, however, a different conclusion may arise in which an improved accuracy of the gas-particle-flow model is necessary in order to obtain results with desired quality. In summary, the coupled model is capable of predicting the heat transfer mechanisms that occur during the investigated TP experiments with acceptable accuracy. At the same time, the following effects are not considered in the model and should be investigated in the future:

- direct coupling of mass loss within jelly roll and gas/particle ejection out of the cell,
- more realistic particle shape instead of ideally spherical particles,
- prediction of potential short circuits due to particle accumulations, and
- venting gas combustion.

5 Conclusions and Outlook

The shorter range of current BEVs compared to ICEVs is considered as one of their biggest disadvantages in public discussions. To address this issue, there is an ongoing demand within the automotive industry for ever increasing energy densities of lithium-ion battery packs. Unfortunately, increased energy densities also bear the risk of safety issues. Therefore, an extensive design and validation process, that may be linked to high expenses, is necessary to satisfy both range and safety requirements. As OEMs strive for optimized cost-benefit ratios on the vehicles they sell, one of their objectives is to establish efficient experimental and numerical methods within this context.

As shown in a comprehensive literature review at the beginning of this thesis, there already exists a variety of experimental and numerical methods in the context of lithium-ion battery safety. On single cell level, experimental methods such as ARC or autoclave experiments are readily available and widely applied to investigate the lithium-ion cell TR and assess its key characteristics. On multiple cell level, research focuses on cell stack tests that can be performed with reduced costs and less resource consumption compared to testing of battery modules or full battery packs. The problem with such cell stack tests, however, is that the experiments are often conducted in simplified setups. Hence, the boundary conditions are significantly different than in battery packs, where the battery cells are usually fixed in a module structure and integrated into a housing. Especially the effect of gas and particles vented during a TR on the TP process has not been fully understood until today. Accounting for vented gas and/or particles within numerical models is also rarely done so far. Last but not least, most studies only focus on experiments or modeling, at either single or multiple cell level, and consequently divide battery safety into individual disciplines.

Therefore, the aim of this thesis was to develop a multi-stage approach consisting of both experimental and numerical methods, that allows to efficiently assess the TP behavior in cell stacks of prismatic lithium-ion batteries. Due to the nature of a lithium-ion battery TR and TP, this work focused on accounting for all the three major heat transfer mechanisms defining this phenomenon: solid body heat conduction, heat transfer due to vented gas, and heat transfer due to vented particles.

The experimental assessment of several TR key characteristics on single cell level served as a starting point of this thesis. In total, 25 different types of prismatic lithium-ion cells with a capacity between 8 and 145 Ah were examined in an autoclave calorimetry experiment. Due to the wide capacity range, the analysis of the results allowed to derive empirical correlations for the mass loss and the heat released during TR. The results revealed that the mass loss during TR is distributed on average into 29.1 % gas and 70.9 %

5 Conclusions and Outlook

solid particles or liquid droplets. The average heat released during TR was found to be 41 % higher than the energy that was electrically stored within the lithium-ion cells.

In a next step, a simulation methodology was developed that is able to reproduce the solid body domain of a lithium-ion cell TR, more precisely the heat release during TR and the subsequent heat dissipation to contacting bodies. Therefore, the autoclave experiment conducted with a prismatic lithium-ion cell was simulated and three different modeling approaches for the heat release during TR were applied: a time-dependent function for heat release, a temperature-dependent heat release rate based on ARC data, and an empirical Arrhenius source term that allows to spatially resolve the TR reaction. In addition, the influence of the jelly roll density, specific heat capacity, and thermal conductivity on the simulation results were investigated. The comparison revealed that the modeling approaches have a major influence on the simulation results for the time range of the TR itself, whilst the effect for large time scales is negligible (time much larger as the TR duration). The lowest computational effort was found for the time-dependent function for heat release. The variation of the jelly roll density showed that the mass loss during TR has to be considered within the model in order to reproduce the experimental results with acceptable quality.

On multiple cell level, the first step was to transfer the single cell TR model to a cell stack experiment in order to identify a suitable modeling approach for TP simulation. Therefore, the modeling approaches for heat release during TR investigated on single cell level were not only evaluated with respect to their influence on the simulation results on multiple cell level, but also regarding computational resource consumption. In order to reproduce the experimental results, it was necessary to consider the mass loss during TR and a bulging of the cells due to electrolyte vaporization or gas generation. Therefore, the jelly roll density was adapted over the venting duration, and the formation of a gas layer between jelly roll and cell can was considered in form of a thermal resistance. The results showed that the modeling approaches have a significant effect on the simulation results. Whilst the temperature-dependent heat release rate based on ARC data was found to be not suitable for the investigated simulation case, both the time-dependent function for heat release and the empirical Arrhenius source term spatially resolving the TR reaction are capable of modeling the TP process. As on single cell level, however, the time-dependent approach was found to consume the lowest computational resources and was therefore identified as best option.

The next step was to identify the influence of vented gas and particles on the TP process. Therefore, different cell stack setups were compared in an experimental study. More precisely, the effect of components that are related to the integration of lithium-ion cells into a battery pack, such as cooler, module structure, or housing, on the TP behavior were evaluated in terms of propagation time. The attachment of a cooling plate reduced the total propagation time (time span between nail penetration of cell 1 and TR initiation in cell 5) to 52.4 % compared to the reference case, whereas additional side plates further reduced the total propagation time to 47.5 %. Within this comparison, vented

gas and particles played a minor role due to testing in an open setup. The integration of the cell stack into a housing reduced the total propagation time to 48.7% for the case without cooling and side plates. For the case with cooling and side plates, which is close to the conditions in a battery module, the comparison of open and closed setup resulted in a reduction of the total propagation time to 64.3%. In conclusion, the results showed that not only gas and particles, but also the module structure have a major influence on the TP process within a battery cell stack. On the one hand, this has to be considered when performing cell stack tests that aim to replace or reduce the number of experiments conducted on module or battery pack level. On the other hand, this underlines the importance of coupling solid body models with a fluid domain considering both vented gas and particles within TP simulations.

In order to develop such a coupled model, the characteristics of the gas-particle-flow occurring during a TR have to be fully understood. As there is a lack of experimental or numerical studies within this context, a novel experimental setup was developed in order to provide a basis for model development. The objective was to experimentally determine the particle deposition during the TR of a lithium-ion cell in a battery module. Therefore, a single prismatic lithium-ion cell was integrated into an environment representing battery module conditions with a defined flow path for the vented gas and particles and two nail penetration tests were performed with different distances between cell vent and module cover. In total, 86 weighing plates, positioned within the flow path, could be individually removed from the setup in order to determine the spatial mass distribution of deposited particles. The results revealed that the distance between cell vent and module cover has a major influence on the particle deposition. Whilst particle accumulations concentrated at the side walls for the lower distance, the particles were randomly distributed over the entire weighing plate area for the high distance between cell vent and module cover. Subsequently, these results were used to develop a gas-particle-flow model that is capable of reproducing the observed behavior.

In a last step, the interaction between the individual experimental and numerical methods used and developed within this thesis were combined to a multi-stage approach that allows to efficiently assess the TP behavior in cell stacks of prismatic lithium-ion cells. Basically, the approach can be seen as workflow for the build-up of a predictive model for the TP behavior. Comparing the experimental results obtained in cell stack experiments with the simulation results of the coupled model showed that the consideration of gas and particles is of utmost importance for applications where the TP process happens within a closed environment such as a housing. For the cell stack experiment investigated in this thesis, the time of TR initiation in the fifth cell is shifted by 38s when the solid body domain is coupled with a gas phase model. The additional consideration of particles led to a shift of 57s compared to the model considering solid body heat conduction only.

Whilst important insights into the TP phenomenon are provided in this thesis, the shown multi-stage approach and its single components have still potential for further optimiza-

5 Conclusions and Outlook

tion. From the author's point of view, in particular, the following topics are worth further investigation in the future:

- validation of the estimation for Q_{venting} within autoclave calorimetry experiments,
- measurement/determination of material parameters such as specific heat capacity and thermal conductivity within the temperature range of a TR,
- investigation on additional heat sources occurring during a TP such as electrical short circuits within parallel connections,
- measurement/determination of the (time-dependent) gas and particle mass flow rate during a TR,
- consideration of melting and/or combustion effects within modeling, and
- transfer of the methods to cylindrical and pouch cell format.

In conclusion, the multi-stage approach presented in this thesis combines experimental and numerical methods on both single and multiple cell level, allowing to efficiently assess the TP behavior in cell stacks of prismatic lithium-ion batteries. The potential application of the approach to other cell formats or higher integration levels, such as battery modules or packs, enables to satisfy both range and safety requirements of current and future battery packs for EVs.

Bibliography

- [1] European Parliament and Council, *Regulation (EU) 2023/851*, 2023.
- [2] European Parliament, *Fit for 55: Zero CO₂ emissions for new cars and vans in 2035*, 2023. [Online]. Available: <https://www.europarl.europa.eu/news/en/press-room/20230210IPR74715/fit-for-55-zero-co2-emissions-for-new-cars-and-vans-in-2035> (visited on 05/15/2023).
- [3] European Commission, *Zero emission vehicles: First 'Fit for 55' deal will end the sale of new CO₂ emitting cars in Europe by 2035 (IP/22/6462)*, 2022. [Online]. Available: https://ec.europa.eu/commission/presscorner/api/files/document/print/en/ip_22_6462/IP_22_6462_EN.pdf (visited on 05/15/2023).
- [4] P. Mock and J. Dornoff, *E-FUELS: THE MAGIC LOLLIPOP TO KEEP COMBUSTION ENGINES ALIVE (OR NOT)*, 2022. [Online]. Available: <https://theicct.org/e-fuels-eu-co2-standards-jun22/> (visited on 05/08/2023).
- [5] K. Abnett, *EU countries approve 2035 phaseout of CO₂-emitting cars*, 2023. [Online]. Available: <https://www.reuters.com/business/autos-transportation/eu-countries-poised-approve-2035-phaseout-co2-emitting-cars-2023-03-28/> (visited on 05/08/2023).
- [6] T. J. Wallington, J. E. Anderson, D. J. Siegel, M. A. Tamor, S. A. Mueller, S. L. Winkler, and O. J. Nielsen, "Sustainable Mobility, Future Fuels, and the Periodic Table", *Journal of Chemical Education*, vol. 90, no. 4, pp. 440–445, 2013. DOI: 10.1021/ed3004269.
- [7] J. M. Bergthorson, "Recyclable metal fuels for clean and compact zero-carbon power", *Progress in Energy and Combustion Science*, vol. 68, pp. 169–196, 2018. DOI: 10.1016/j.pecs.2018.05.001.
- [8] H. Kobayashi, A. Hayakawa, K. K. A. Somarathne, and E. C. Okafor, "Science and technology of ammonia combustion", *Proceedings of the Combustion Institute*, vol. 37, no. 1, pp. 109–133, 2019. DOI: 10.1016/j.proci.2018.09.029.
- [9] S. J. Curran, R. M. Wagner, R. L. Graves, M. Keller, and J. B. Green, "Well-to-wheel analysis of direct and indirect use of natural gas in passenger vehicles", *Energy*, vol. 75, pp. 194–203, 2014. DOI: 10.1016/j.energy.2014.07.035.
- [10] A. Albatayneh, M. N. Assaf, D. Alterman, and M. Jaradat, "Comparison of the Overall Energy Efficiency for Internal Combustion Engine Vehicles and Electric Vehicles", *Environmental and Climate Technologies*, vol. 24, no. 1, pp. 669–680, 2020. DOI: 10.2478/rtuect-2020-0041.

- [11] E. Lindstad, T. Ø. Ask, P. Cariou, G. S. Eskeland, and A. Rialland, “Wise use of renewable energy in transport”, *Transportation Research Part D: Transport and Environment*, vol. 119, p. 103–113, 2023. DOI: 10.1016/j.trd.2023.103713.
- [12] S. Brynolf, J. Hansson, J. E. Anderson, I. R. Skov, T. J. Wallington, M. Grahn, A. D. Korberg, E. Malmgren, and M. Taljegård, “Review of electrofuel feasibility—prospects for road, ocean, and air transport”, *Progress in Energy*, vol. 4, no. 4, p. 042007, 2022. DOI: 10.1088/2516-1083/ac8097.
- [13] M. Fischer, M. Werber, and P. V. Schwartz, “Batteries: Higher energy density than gasoline?”, *Energy Policy*, vol. 37, no. 7, pp. 2639–2641, 2009. DOI: 10.1016/j.enpol.2009.02.030.
- [14] International Energy Agency (IEA), *Global EV Outlook 2023: Catching up with climate ambitions*, 2023.
- [15] A. Mahmoudzadeh Andwari, A. Pesiridis, S. Rajoo, R. Martinez-Botas, and V. Esfahanian, “A review of Battery Electric Vehicle technology and readiness levels”, *Renewable and Sustainable Energy Reviews*, vol. 78, pp. 414–430, 2017. DOI: 10.1016/j.rser.2017.03.138.
- [16] W. Huang, X. Feng, X. Han, W. Zhang, and F. Jiang, “Questions and Answers Relating to Lithium-Ion Battery Safety Issues”, *Cell Reports Physical Science*, vol. 2, no. 1, p. 100285, 2021. DOI: 10.1016/j.xcrp.2020.100285.
- [17] X. Feng, M. Ouyang, X. Liu, L. Lu, Y. Xia, and X. He, “Thermal runaway mechanism of lithium ion battery for electric vehicles: A review”, *Energy Storage Materials*, vol. 10, pp. 246–267, 2018. DOI: 10.1016/j.ensm.2017.05.013.
- [18] J. Lamb, L. Torres-Castro, J. C. Hewson, R. C. Shurtz, and Y. Preger, “Investigating the Role of Energy Density in Thermal Runaway of Lithium-Ion Batteries with Accelerating Rate Calorimetry”, *Journal of The Electrochemical Society*, vol. 168, no. 6, p. 060516, 2021. DOI: 10.1149/1945-7111/ac0699.
- [19] P. Lamp, “Requirements for batteries used in electric mobility applications”, in *Lithium-Ion Batteries: Basics and Applications*, R. Korthauer, Ed., Berlin, Heidelberg: Springer Berlin Heidelberg, 2018, pp. 371–391. DOI: 10.1007/978-3-662-53071-9_31.
- [20] M. Sterner and F. Bauer, “Definition und Klassifizierung von Energiespeichern”, in *Energiespeicher - Bedarf, Technologien, Integration*, M. Sterner and I. Stadler, Eds., Berlin, Heidelberg: Springer Berlin Heidelberg, 2017, pp. 25–49. DOI: 10.1007/978-3-662-48893-5_2.
- [21] A. Masias, “Lithium-Ion Battery Design for Transportation”, in *Behaviour of Lithium-Ion Batteries in Electric Vehicles*, G. Pistoia and B. Liaw, Eds., Cham: Springer International Publishing, 2018, pp. 1–33. DOI: 10.1007/978-3-319-69950-9_1.

- [22] K.-H. Pettinger, A. Kampker, C.-R. Hohenthanner, C. Deutskens, H. Heimes, and A. Vom Hemdt, “Lithium-ion cell and battery production processes”, in *Lithium-Ion Batteries: Basics and Applications*, R. Korthauer, Ed., Berlin, Heidelberg: Springer Berlin Heidelberg, 2018, pp. 211–226. DOI: 10.1007/978-3-662-53071-9_17.
- [23] Z. Drori, *We have begun regular production of the Tesla Roadster*, 2008. [Online]. Available: <https://www.tesla.com/blog/we-have-begun-regular-production-tesla-roadster> (visited on 12/14/2022).
- [24] E. Toomre, *The Most Coddled Automotive Battery Ever?*, 2007. [Online]. Available: <https://www.tesla.com/blog/most-coddled-automotive-battery-ever> (visited on 12/14/2022).
- [25] Y. Chen, “The Impact of Strategic Alliance on Corporate Performance: Evidence from Tesla”, in *2022 2nd International Conference on Enterprise Management and Economic Development (ICEMED 2022)*, 2022. DOI: 10.2991/aebmr.k.220603.036.
- [26] E. Musk and D. Baglino, *Tesla Battery Day*, 2020. [Online]. Available: <https://tesla-share.thron.com/content/?id=96ea71cf-8fda-4648-a62c-753af436c3b6&pkey=S1dbei4> (visited on 12/14/2022).
- [27] Samsung SDI, *Samsung SDI introduces a Lineup of Various High-Performance Batteries*, 2017. [Online]. Available: <https://www.samsungsdi.com/sdi-news/1761.html> (visited on 12/14/2022).
- [28] C. Ruoff, “Q&A with Rivian’s VP of propulsion Richard Farquhar”, *Charged Electric Vehicles Magazine*, vol. 46, no. Nov/Dec, pp. 36–44, 2019. [Online]. Available: https://issuu.com/chargedevs/docs/iss.46_issuu.com.v2.
- [29] LG Chem, *LG Chem to Supply Next-Generation Cylindrical Batteries to Lucid Motors of the US*, 2020. [Online]. Available: <https://www.lgcorp.com/media/release/21602> (visited on 12/15/2022).
- [30] J. Frazelle, “Battery Day: A closer look at the technology that makes portable electronics possible”, *Queue*, vol. 18, no. 5, pp. 5–25, 2020. DOI: 10.1145/3434571.3439415.
- [31] H. Löbberding, S. Wessel, C. Offermanns, M. Kehrer, J. Rother, H. Heimes, and A. Kampker, “From Cell to Battery System in BEVs: Analysis of System Packing Efficiency and Cell Types”, *World Electric Vehicle Journal*, vol. 11, no. 4, p. 77, 2020. DOI: 10.3390/wevj11040077.
- [32] G. Harper, R. Sommerville, E. Kendrick, L. Driscoll, P. Slater, R. Stolkin, A. Walton, P. Christensen, O. Heidrich, S. Lambert, A. Abbott, K. Ryder, L. Gaines, and P. Anderson, “Recycling lithium-ion batteries from electric vehicles”, *Nature*, vol. 575, no. 7781, pp. 75–86, 2019. DOI: 10.1038/s41586-019-1682-5.
- [33] BMW Media Information, *Technical Specifications. BMW i3*, 2014. [Online]. Available: <https://www.press.bmwgroup.com/global/article/detail/T0189822EN/specifications-of-the-bmw-i3-valid-from-03/2014> (visited on 12/19/2022).

- [34] BMW Media Information, *Technical Specifications. BMW i3 94 Ah*, 2016. [Online]. Available: <https://www.press.bmwgroup.com/global/article/detail/T0259598EN/technical-specifications-for-the-bmw-i3-94ah-valid-from-07/2016> (visited on 12/19/2022).
- [35] BMW Media Information, *Technical Specifications. The new BMW i3*, 2017. [Online]. Available: <https://www.press.bmwgroup.com/global/article/detail/T0280411EN/technical-specifications-of-the-new-bmw-i3-and-the-new-bmw-i3s-valid-from-11/2017> (visited on 12/19/2022).
- [36] BMW Media Information, *Technical Specifications. BMW i3 (120 Ah)*, 2018. [Online]. Available: <https://www.press.bmwgroup.com/global/article/detail/T0285608EN/technical-specifications-of-the-bmw-i3-120-ah-and-the-bmw-i3s-120-ah-valid-from-11/2018> (visited on 12/19/2022).
- [37] DIN-91252:2016-11, *Elektrische Straßenfahrzeuge - Batteriesysteme - Anforderungen an die Gestaltung von Lithium-Ionen-Batteriezellen*, 2016.
- [38] SVOLT Energy Technology, *Completely Cobalt-free battery cells from SVOLT available for order now*, 2021. [Online]. Available: https://svolt-eu.com/wp-content/uploads/2021/02/2021-02_01_SVOLT_NMX_EN_final.pdf (visited on 12/17/2022).
- [39] F. Qu, H. Zhang, B. Weng, and X. Tian, “Battery pack”, Patent CN111430621A, 2020.
- [40] C. Wang, L. He, H. Sun, X. Wang, and Y. Zhu, “Power Battery Pack and Electric Vehicle”, Patent CN110165116A, 2019.
- [41] E. Gerlitz, D. Botzem, H. Weinmann, J. Ruhland, and J. Fleischer, “Cell-to-Pack-Technologie für Li-Ionen-Batterien: Aktueller Entwicklungsstand, Marktakteure in der Automobilindustrie und Auswirkungen auf eine nachhaltige Produktionstechnik unter dem Aspekt der Kreislaufwirtschaft”, *Zeitschrift für wirtschaftlichen Fabrikbetrieb*, vol. 116, no. 10, pp. 689–694, 2021. DOI: 10.1515/zwf-2021-0146.
- [42] X. Li, S. Wang, X. Wu, H. Yang, M. Zheng, and Z. Lu, “Battery pack”, Patent CN111384327A, 2020.
- [43] J. Wang, F. Qu, H. Zhang, C. Kang, Z. Zhou, J. Li, Y. Wei, and X. Tian, “Battery pack and vehicle”, Patent CN110504395A, 2019.
- [44] T. Woehrle, “Lithium-ion cell”, in *Lithium-Ion Batteries: Basics and Applications*, R. Korthauer, Ed., Berlin, Heidelberg: Springer Berlin Heidelberg, 2018, pp. 101–111. DOI: 10.1007/978-3-662-53071-9_9.
- [45] K. Vuorilehto, “Materials and function”, in *Lithium-Ion Batteries: Basics and Applications*, R. Korthauer, Ed., Berlin, Heidelberg: Springer Berlin Heidelberg, 2018, pp. 21–28. DOI: 10.1007/978-3-662-53071-9_3.
- [46] M. S. E. Houache, C.-H. Yim, Z. Karkar, and Y. Abu-Lebdeh, “On the Current and Future Outlook of Battery Chemistries for Electric Vehicles—Mini Review”, *Batteries*, vol. 8, no. 7, p. 70, 2022. DOI: 10.3390/batteries8070070.

- [47] N. Wassiliadis, M. Steinsträter, M. Schreiber, P. Rosner, L. Nicoletti, F. Schmid, M. Ank, O. Teichert, L. Wildfeuer, J. Schneider, A. Koch, A. König, A. Glatz, J. Gandlgruber, T. Kröger, X. Lin, and M. Lienkamp, “Quantifying the state of the art of electric powertrains in battery electric vehicles: Range, efficiency, and lifetime from component to system level of the Volkswagen ID.3”, *eTransportation*, vol. 12, p. 100167, 2022. DOI: 10.1016/j.etrans.2022.100167.
- [48] H. Manz, *Future Trends on Battery Systems - ready for the next Generation*, 2021. [Online]. Available: https://www.volkswagenag.com/presence/investorrelation/publications/presentations/2021/03/2021-03-04_VWAG_UBS_MEB_Battery.pdf (visited on 12/17/2022).
- [49] K. Brandt and J. Garche, “General Overview of Li-Secondary Battery Safety Issues”, in *Electrochemical Power Sources: Fundamentals, Systems, and Applications : Li-Battery Safety*. Ser. Electrochemical Power Sources: Fundamentals, Systems, and Applications, J. Garche and K. Brandt, Eds., Elsevier, 2019, pp. 127–141. DOI: 10.1016/B978-0-444-63777-2.00006-2.
- [50] L. Spitthoff, P. R. Shearing, and O. S. Burheim, “Temperature, Ageing and Thermal Management of Lithium-Ion Batteries”, *Energies*, vol. 14, no. 5, p. 1248, 2021. DOI: 10.3390/en14051248.
- [51] N. Nitta, F. Wu, J. T. Lee, and G. Yushin, “Li-ion battery materials: Present and future”, *Materials Today*, vol. 18, no. 5, pp. 252–264, 2015. DOI: 10.1016/j.mattod.2014.10.040.
- [52] J. Dahn and G. M. Ehrlich, “Lithium-Ion Batteries”, in *Linden’s Handbook of Batteries*, T. B. Reddy and D. Linden, Eds., 4th ed, New York: McGraw-Hill, 2011, ISBN: 978-0-07-162419-0.
- [53] C. Lyness, “Lithium-Secondary Cell: Sources of Risks and Their Effects - Sources of Risk”, in *Electrochemical Power Sources: Fundamentals, Systems, and Applications : Li-Battery Safety*. Ser. Electrochemical Power Sources: Fundamentals, Systems, and Applications, J. Garche and K. Brandt, Eds., Elsevier, 2019, pp. 143–266. DOI: 10.1016/B978-0-444-63777-2.00007-4.
- [54] K. Brandt and J. Garche, “General Battery Safety Considerations”, in *Electrochemical Power Sources: Fundamentals, Systems, and Applications : Li-Battery Safety*. Ser. Electrochemical Power Sources: Fundamentals, Systems, and Applications, J. Garche and K. Brandt, Eds., Elsevier, 2019, pp. 1–19. DOI: 10.1016/B978-0-444-63777-2.00001-3.
- [55] E. J. Spek, “Safety of Secondary-Lithium Batteries”, in *Electrochemical Power Sources: Fundamentals, Systems, and Applications : Li-Battery Safety*. Ser. Electrochemical Power Sources: Fundamentals, Systems, and Applications, J. Garche and K. Brandt, Eds., Elsevier, 2019, pp. 113–126. DOI: 10.1016/B978-0-444-63777-2.00005-0.

- [56] M. Fleischhammer, “Lithium-Secondary Cell: Sources of Risks and Their Effects - Risk Potential by Materials”, in *Electrochemical Power Sources: Fundamentals, Systems, and Applications: Li-Battery Safety*. Ser. Electrochemical Power Sources: Fundamentals, Systems, and Applications, J. Garche and K. Brandt, Eds., Elsevier, 2019, pp. 143–266. DOI: 10.1016/B978-0-444-63777-2.00007-4.
- [57] G. E. Gorbett and S. P. Kozhumal, “Fire Fundamentals”, in *Handbook of Fire and the Environment*, B. J. Meacham and M. McNamee, Eds., Cham: Springer International Publishing, 2023, pp. 55–100. DOI: 10.1007/978-3-030-94356-1_3.
- [58] D. Doughty and E. P. Roth, “A General Discussion of Li Ion Battery Safety”, *The Electrochemical Society Interface*, 2012.
- [59] J. A. G. Rheinfeld, “Performance and Safety of Lithium-Ion Electrodes and Cells: Modeling, Simulation, and Validation at Elevated Temperatures and Currents”, Ph.D. dissertation, Technical University of Munich, Germany, 2019.
- [60] M. N. Richard and J. R. Dahn, “Accelerating Rate Calorimetry Study on the Thermal Stability of Lithium Intercalated Graphite in Electrolyte. I. Experimental”, *Journal of The Electrochemical Society*, vol. 146, no. 6, pp. 2068–2077, 1999. DOI: 10.1149/1.1391893.
- [61] D. D. MacNeil, D. Larcher, and J. R. Dahn, “Comparison of the Reactivity of Various Carbon Electrode Materials with Electrolyte at Elevated Temperature”, *Journal of The Electrochemical Society*, vol. 146, no. 10, pp. 3596–3602, 1999. DOI: 10.1149/1.1392520.
- [62] Q. Wang, J. Sun, X. Yao, and C. Chen, “Thermal Behavior of Lithiated Graphite with Electrolyte in Lithium-Ion Batteries”, *Journal of The Electrochemical Society*, vol. 153, no. 2, A329, 2006. DOI: 10.1149/1.2139955.
- [63] A. D. Pasquier, F. Disma, T. Bowmer, A. S. Gozdz, G. Amatucci, and J.-M. Tarascon, “Differential Scanning Calorimetry Study of the Reactivity of Carbon Anodes in Plastic Li-Ion Batteries”, *Journal of The Electrochemical Society*, vol. 145, no. 2, pp. 472–477, 1998. DOI: 10.1149/1.1838287.
- [64] P. Biensan, B. Simon, J. Pérès, A. de Guibert, M. Broussely, J. Bodet, and F. Perton, “On safety of lithium-ion cells”, *Journal of Power Sources*, vol. 81–82, pp. 906–912, 1999. DOI: 10.1016/S0378-7753(99)00135-4.
- [65] Z. Zhang, D. Fouchard, and J. Rea, “Differential scanning calorimetry material studies: Implications for the safety of lithium-ion cells”, *Journal of Power Sources*, vol. 70, no. 1, pp. 16–20, 1998. DOI: 10.1016/S0378-7753(97)02611-6.
- [66] D. D. MacNeil and J. R. Dahn, “The Reaction of Charged Cathodes with Non-aqueous Solvents and Electrolytes: I. $\text{Li}_{0.5}\text{CoO}_2$ ”, *Journal of The Electrochemical Society*, vol. 148, no. 11, A1205, 2001. DOI: 10.1149/1.1407245.
- [67] D. D. MacNeil and J. R. Dahn, “The Reactions of $\text{Li}_{0.5}\text{CoO}_2$ with Nonaqueous Solvents at Elevated Temperatures”, *Journal of The Electrochemical Society*, 2002. DOI: 10.1149/1.1483865.

- [68] Y. Baba, “Thermal stability of Li_xCoO_2 cathode for lithium ion battery”, *Solid State Ionics*, vol. 148, no. 3-4, pp. 311–316, 2002. DOI: 10.1016/S0167-2738(02)00067-X.
- [69] S. K. Martha, O. Haik, E. Zinigrad, I. Exnar, T. Drezen, J. H. Miners, and D. Aurbach, “On the Thermal Stability of Olivine Cathode Materials for Lithium-Ion Batteries”, *Journal of The Electrochemical Society*, vol. 158, no. 10, A1115, 2011. DOI: 10.1149/1.3622849.
- [70] Q. Wang, J. Sun, and C. Chen, “Thermal Stability of Delithiated LiMn_2O_4 with Electrolyte for Lithium-Ion Batteries”, *Journal of The Electrochemical Society*, 2007. DOI: 10.1149/1.2433698.
- [71] J. Jiang and J. Dahn, “ARC studies of the thermal stability of three different cathode materials: LiCoO_2 ; $\text{Li}[\text{Ni}_{0.1}\text{Co}_{0.8}\text{Mn}_{0.1}]\text{O}_2$; and LiFePO_4 , in LiPF_6 and LiBoB EC/DEC electrolytes”, *Electrochemistry Communications*, vol. 6, no. 1, pp. 39–43, 2004. DOI: 10.1016/j.elecom.2003.10.011.
- [72] J. Dahn, E. Fuller, M. Obrovac, and U. Vonsacken, “Thermal stability of Li_xCoO_2 , Li_xNiO_2 and $\lambda\text{-MnO}_2$ and consequences for the safety of Li-ion cells”, *Solid State Ionics*, vol. 69, no. 3-4, pp. 265–270, 1994. DOI: 10.1016/0167-2738(94)90415-4.
- [73] K.-W. Nam, S.-M. Bak, E. Hu, X. Yu, Y. Zhou, X. Wang, L. Wu, Y. Zhu, K.-Y. Chung, and X.-Q. Yang, “Combining In Situ Synchrotron X-Ray Diffraction and Absorption Techniques with Transmission Electron Microscopy to Study the Origin of Thermal Instability in Overcharged Cathode Materials for Lithium-Ion Batteries”, *Advanced Functional Materials*, vol. 23, no. 8, pp. 1047–1063, 2013. DOI: 10.1002/adfm.201200693.
- [74] I. Belharouak, D. Vissers, and K. Amine, “Thermal Stability of the $\text{Li}(\text{Ni}_{0.8}\text{Co}_{0.15}\text{Al}_{0.05})\text{O}_2$ Cathode in the Presence of Cell Components”, *Journal of The Electrochemical Society*, vol. 153, no. 11, A2030, 2006. DOI: 10.1149/1.2336994.
- [75] W.-S. Yoon, M. Balasubramanian, X.-Q. Yang, J. McBreen, and J. Hanson, “Time-Resolved XRD Study on the Thermal Decomposition of $\text{Li}_{1-x}\text{Ni}_{0.8}\text{Co}_{0.15}\text{Al}_{0.05}\text{O}_2$ Cathode Materials for Li-Ion Batteries”, *Electrochemical and Solid-State Letters*, vol. 8, no. 2, A83, 2005. DOI: 10.1149/1.1846714.
- [76] Y. Huang, Y.-C. Lin, D. M. Jenkins, N. A. Chernova, Y. Chung, B. Radhakrishnan, I.-H. Chu, J. Fang, Q. Wang, F. Omenya, S. P. Ong, and M. S. Whittingham, “Thermal Stability and Reactivity of Cathode Materials for Li-Ion Batteries”, *ACS Applied Materials & Interfaces*, vol. 8, no. 11, pp. 7013–7021, 2016. DOI: 10.1021/acsami.5b12081.
- [77] K. Zaghib, J. Dubé, A. Dallaire, K. Galoustov, A. Guerfi, M. Ramanathan, A. Benmayza, J. Prakash, A. Mauger, and C. Julien, “Enhanced thermal safety and high power performance of carbon-coated LiFePO_4 olivine cathode for Li-ion batteries”, *Journal of Power Sources*, vol. 219, pp. 36–44, 2012. DOI: 10.1016/j.jpowsour.2012.05.018.

- [78] I. Belharouak, Y.-K. Sun, J. Liu, and K. Amine, “Li(Ni_{1/3}Co_{1/3}Mn_{1/3})O₂ as a suitable cathode for high power applications”, *Journal of Power Sources*, vol. 123, no. 2, pp. 247–252, 2003. DOI: 10.1016/S0378-7753(03)00529-9.
- [79] P. Röder, N. Baba, and H.-D. Wiemhöfer, “A detailed thermal study of a Li[Ni_{0.33}Co_{0.33}Mn_{0.33}]O₂ / LiMn₂O₄-based lithium ion cell by accelerating rate and differential scanning calorimetry”, *Journal of Power Sources*, vol. 248, pp. 978–987, 2014. DOI: 10.1016/j.jpowsour.2013.09.146.
- [80] S.-M. Bak, E. Hu, Y. Zhou, X. Yu, S. D. Senanayake, S.-J. Cho, K.-B. Kim, K. Y. Chung, X.-Q. Yang, and K.-W. Nam, “Structural Changes and Thermal Stability of Charged LiNi_xMn_yCo_zO₂ Cathode Materials Studied by Combined *In Situ* Time-Resolved XRD and Mass Spectroscopy”, *ACS Applied Materials & Interfaces*, vol. 6, no. 24, pp. 22 594–22 601, 2014. DOI: 10.1021/am506712c.
- [81] A. Kriston, I. Adanouj, V. Ruiz, and A. Pfrang, “Quantification and simulation of thermal decomposition reactions of Li-ion battery materials by simultaneous thermal analysis coupled with gas analysis”, *Journal of Power Sources*, vol. 435, p. 226 774, 2019. DOI: 10.1016/j.jpowsour.2019.226774.
- [82] A. K. Padhi, K. S. Nanjundaswamy, and J. B. Goodenough, “Phospho-olivines as Positive-Electrode Materials for Rechargeable Lithium Batteries”, *Journal of The Electrochemical Society*, vol. 144, no. 4, pp. 1188–1194, 1997. DOI: 10.1149/1.1837571.
- [83] M. Takahashi, “Reaction behavior of LiFePO₄ as a cathode material for rechargeable lithium batteries”, *Solid State Ionics*, vol. 148, no. 3-4, pp. 283–289, 2002. DOI: 10.1016/S0167-2738(02)00064-4.
- [84] C. Delacourt, P. Poizot, J.-M. Tarascon, and C. Masquelier, “The existence of a temperature-driven solid solution in Li_xFePO₄ for 0 ≤ x ≤ 1”, *Nature Materials*, vol. 4, no. 3, pp. 254–260, 2005. DOI: 10.1038/nmat1335.
- [85] H. Joachin, T. D. Kaun, K. Zaghbi, and J. Prakash, “Electrochemical and Thermal Studies of Carbon-Coated LiFePO₄ Cathode”, *Journal of The Electrochemical Society*, vol. 156, no. 6, A401, 2009. DOI: 10.1149/1.3106121.
- [86] A. Yamada, S. C. Chung, and K. Hinokuma, “Optimized LiFePO₄ for Lithium Battery Cathodes”, *Journal of The Electrochemical Society*, vol. 148, no. 3, A224, 2001. DOI: 10.1149/1.1348257.
- [87] H.-J. Noh, S. Youn, C. S. Yoon, and Y.-K. Sun, “Comparison of the structural and electrochemical properties of layered Li[Ni_xCo_yMn_z]O₂ (x = 1/3, 0.5, 0.6, 0.7, 0.8 and 0.85) cathode material for lithium-ion batteries”, *Journal of Power Sources*, vol. 233, pp. 121–130, 2013. DOI: 10.1016/j.jpowsour.2013.01.063.
- [88] P. Huang, P. Ping, K. Li, H. Chen, Q. Wang, J. Wen, and J. Sun, “Experimental and modeling analysis of thermal runaway propagation over the large format energy storage battery module with Li₄Ti₅O₁₂ anode”, *Applied Energy*, vol. 183, pp. 659–673, 2016. DOI: 10.1016/j.apenergy.2016.08.160.

- [89] Y. Ding, Z. P. Cano, A. Yu, J. Lu, and Z. Chen, “Automotive Li-Ion Batteries: Current Status and Future Perspectives”, *Electrochemical Energy Reviews*, vol. 2, no. 1, pp. 1–28, 2019. DOI: 10.1007/s41918-018-0022-z.
- [90] P. Arora and Z. J. Zhang, “Battery Separators”, *Chemical Reviews*, vol. 104, no. 10, pp. 4419–4462, 2004. DOI: 10.1021/cr020738u.
- [91] B. N. Pinnangudi, S. B. Dalal, N. K. Medora, A. Arora, and J. Swart, “Thermal shutdown characteristics of insulating materials used in lithium ion batteries”, in *2010 IEEE Symposium on Product Compliance Engineering Proceedings*, IEEE, 2010, pp. 1–5. DOI: 10.1109/PSES.2010.5636859.
- [92] C. J. Orendorff, “The Role of Separators in Lithium-Ion Cell Safety”, *Interface magazine*, vol. 21, no. 2, pp. 61–65, 2012. DOI: 10.1149/2.F07122if.
- [93] X. Huang, “Separator technologies for lithium-ion batteries”, *Journal of Solid State Electrochemistry*, vol. 15, no. 4, pp. 649–662, 2011. DOI: 10.1007/s10008-010-1264-9.
- [94] G. Venugopal, J. Moore, J. Howard, and S. Pandalwar, “Characterization of microporous separators for lithium-ion batteries”, *Journal of Power Sources*, vol. 77, no. 1, pp. 34–41, 1999. DOI: 10.1016/S0378-7753(98)00168-2.
- [95] X. Feng, M. Fang, X. He, M. Ouyang, L. Lu, H. Wang, and M. Zhang, “Thermal runaway features of large format prismatic lithium ion battery using extended volume accelerating rate calorimetry”, *Journal of Power Sources*, vol. 255, pp. 294–301, 2014. DOI: 10.1016/j.jpowsour.2014.01.005.
- [96] C. F. J. Francis, I. L. Kyratzis, and A. S. Best, “Lithium-Ion Battery Separators for Ionic-Liquid Electrolytes: A Review”, *Advanced Materials*, vol. 32, no. 18, p. 1904205, 2020. DOI: 10.1002/adma.201904205.
- [97] J. S. Gnanaraj, E. Zinigrad, L. Asraf, H. E. Gottlieb, M. Sprecher, M. Schmidt, W. Geissler, and D. Aurbach, “A Detailed Investigation of the Thermal Reactions of LiPF₆ Solution in Organic Carbonates Using ARC and DSC”, *Journal of The Electrochemical Society*, vol. 150, no. 11, A1533, 2003. DOI: 10.1149/1.1617301.
- [98] B. Ravdel, K. Abraham, R. Gitzendanner, J. DiCarlo, B. Lucht, and C. Campion, “Thermal stability of lithium-ion battery electrolytes”, *Journal of Power Sources*, vol. 119–121, pp. 805–810, 2003. DOI: 10.1016/S0378-7753(03)00257-X.
- [99] G. G. Botte, R. E. White, and Z. Zhang, “Thermal stability of LiPF₆–EC:EMC electrolyte for lithium ion batteries”, *Journal of Power Sources*, vol. 97–98, pp. 570–575, 2001. DOI: 10.1016/S0378-7753(01)00746-7.
- [100] T. Kawamura, A. Kimura, M. Egashira, S. Okada, and J.-I. Yamaki, “Thermal stability of alkyl carbonate mixed-solvent electrolytes for lithium ion cells”, *Journal of Power Sources*, vol. 104, no. 2, pp. 260–264, 2002. DOI: 10.1016/S0378-7753(01)00960-0.

- [101] K. Xu, “Nonaqueous Liquid Electrolytes for Lithium-Based Rechargeable Batteries”, *Chemical Reviews*, vol. 104, no. 10, pp. 4303–4418, 2004. DOI: 10.1021/cr030203g.
- [102] P. Ribière, S. Grugeon, M. Morcrette, S. Boyanov, S. Laruelle, and G. Marlair, “Investigation on the fire-induced hazards of Li-ion battery cells by fire calorimetry”, *Energy & Environmental Science*, vol. 5, no. 1, pp. 5271–5280, 2012. DOI: 10.1039/C1EE02218K.
- [103] G. G. Eshetu, S. Grugeon, S. Laruelle, S. Boyanov, A. Lecocq, J.-P. Bertrand, and G. Marlair, “In-depth safety-focused analysis of solvents used in electrolytes for large scale lithium ion batteries”, *Physical Chemistry Chemical Physics*, vol. 15, no. 23, p. 9145, 2013. DOI: 10.1039/c3cp51315g.
- [104] J. Kalhoff, G. G. Eshetu, D. Bresser, and S. Passerini, “Safer Electrolytes for Lithium-Ion Batteries: State of the Art and Perspectives”, *ChemSusChem*, vol. 8, no. 13, pp. 2154–2175, 2015. DOI: 10.1002/cssc.201500284.
- [105] X. Feng, S. Zheng, D. Ren, X. He, L. Wang, H. Cui, X. Liu, C. Jin, F. Zhang, C. Xu, H. Hsu, S. Gao, T. Chen, Y. Li, T. Wang, H. Wang, M. Li, and M. Ouyang, “Investigating the thermal runaway mechanisms of lithium-ion batteries based on thermal analysis database”, *Applied Energy*, vol. 246, pp. 53–64, 2019. DOI: 10.1016/j.apenergy.2019.04.009.
- [106] X. Feng, S. Zheng, X. He, L. Wang, Y. Wang, D. Ren, and M. Ouyang, “Time Sequence Map for Interpreting the Thermal Runaway Mechanism of Lithium-Ion Batteries With $\text{LiNi}_x\text{Co}_y\text{Mn}_z\text{O}_2$ Cathode”, *Frontiers in Energy Research*, vol. 6, p. 126, 2018. DOI: 10.3389/fenrg.2018.00126.
- [107] X. Liu, D. Ren, H. Hsu, X. Feng, G.-L. Xu, M. Zhuang, H. Gao, L. Lu, X. Han, Z. Chu, J. Li, X. He, K. Amine, and M. Ouyang, “Thermal Runaway of Lithium-Ion Batteries without Internal Short Circuit”, *Joule*, vol. 2, no. 10, pp. 2047–2064, 2018. DOI: 10.1016/j.joule.2018.06.015.
- [108] Q. Wang, B. Mao, S. I. Stolarov, and J. Sun, “A review of lithium ion battery failure mechanisms and fire prevention strategies”, *Progress in Energy and Combustion Science*, vol. 73, pp. 95–131, 2019. DOI: 10.1016/j.pecs.2019.03.002.
- [109] X. Feng, D. Ren, X. He, and M. Ouyang, “Mitigating Thermal Runaway of Lithium-Ion Batteries”, *Joule*, vol. 4, no. 4, pp. 743–770, 2020. DOI: 10.1016/j.joule.2020.02.010.
- [110] M. Yacoub Al Shdaifat, R. Zulkifli, K. Sopian, and A. Adel Salih, “Basics, properties, and thermal issues of EV battery and battery thermal management systems: Comprehensive review”, *Proceedings of the Institution of Mechanical Engineers, Part D: Journal of Automobile Engineering*, vol. 237, no. 2-3, pp. 295–311, 2023. DOI: 10.1177/09544070221079195.

- [111] S. Shahid and M. Agelin-Chaab, “A review of thermal runaway prevention and mitigation strategies for lithium-ion batteries”, *Energy Conversion and Management: X*, vol. 16, p. 100310, 2022. DOI: 10.1016/j.ecmx.2022.100310.
- [112] UN-R 100.03, *Uniform provisions concerning the approval of vehicles with regard to specific requirements for the electric power train [2021/2190]*, 2021.
- [113] GB 38031-2020, *Electric vehicles traction battery safety requirements*, 2020.
- [114] A. Pfrang, A. Kriston, V. Ruiz, N. Lebedeva, and F. Di Persio, “Safety of Rechargeable Energy Storage Systems with a focus on Li-ion Technology”, in *Emerging Nanotechnologies in Rechargeable Energy Storage Systems*, Elsevier, 2017, pp. 253–290. DOI: 10.1016/B978-0-323-42977-1.00008-X.
- [115] Z. J. Zhang, P. Ramadass, and W. Fang, “Safety of Lithium-Ion Batteries”, in *Lithium-Ion Batteries*, Elsevier, 2014, pp. 409–435. DOI: 10.1016/B978-0-444-59513-3.00018-2.
- [116] Q. Wang, P. Ping, X. Zhao, G. Chu, J. Sun, and C. Chen, “Thermal runaway caused fire and explosion of lithium ion battery”, *Journal of Power Sources*, vol. 208, pp. 210–224, 2012. DOI: 10.1016/j.jpowsour.2012.02.038.
- [117] B. Liu, Y. Jia, C. Yuan, L. Wang, X. Gao, S. Yin, and J. Xu, “Safety issues and mechanisms of lithium-ion battery cell upon mechanical abusive loading: A review”, *Energy Storage Materials*, vol. 24, pp. 85–112, 2020. DOI: 10.1016/j.ensm.2019.06.036.
- [118] K. Kitoh and H. Nemoto, “100 Wh Large size Li-ion batteries and safety tests”, *Journal of Power Sources*, vol. 81–82, pp. 887–890, 1999. DOI: 10.1016/S0378-7753(99)00125-1.
- [119] S.-i. Tobishima, K. Takei, Y. Sakurai, and J.-i. Yamaki, “Lithium ion cell safety”, *Journal of Power Sources*, vol. 90, no. 2, pp. 188–195, 2000. DOI: 10.1016/S0378-7753(00)00409-2.
- [120] H. Maleki and J. N. Howard, “Internal short circuit in Li-ion cells”, *Journal of Power Sources*, vol. 191, no. 2, pp. 568–574, 2009. DOI: 10.1016/j.jpowsour.2009.02.070.
- [121] J. Lamb and C. J. Orendorff, “Evaluation of mechanical abuse techniques in lithium ion batteries”, *Journal of Power Sources*, vol. 247, pp. 189–196, 2014. DOI: 10.1016/j.jpowsour.2013.08.066.
- [122] D. P. Finegan, B. Tjaden, T. M. M. Heenan, R. Jervis, M. D. Michiel, A. Rack, G. Hinds, D. J. L. Brett, and P. R. Shearing, “Tracking Internal Temperature and Structural Dynamics during Nail Penetration of Lithium-Ion Cells”, *Journal of The Electrochemical Society*, vol. 164, no. 13, A3285–A3291, 2017. DOI: 10.1149/2.1501713jes.

- [123] B. Mao, H. Chen, Z. Cui, T. Wu, and Q. Wang, “Failure mechanism of the lithium ion battery during nail penetration”, *International Journal of Heat and Mass Transfer*, vol. 122, pp. 1103–1115, 2018. DOI: 10.1016/j.ijheatmasstransfer.2018.02.036.
- [124] C. Essl, A. W. Golubkov, and A. Fuchs, “Comparing Different Thermal Runaway Triggers for Two Automotive Lithium-Ion Battery Cell Types”, *Journal of The Electrochemical Society*, vol. 167, no. 13, p. 130 542, 2020. DOI: 10.1149/1945-7111/abbe5a.
- [125] X. Qi, B. Liu, J. Pang, F. Yun, R. Wang, Y. Cui, C. Wang, K. Doyle-Davis, C. Xing, S. Fang, W. Quan, B. Li, Q. Zhang, S. Wu, S. Liu, J. Wang, and X. Sun, “Unveiling micro internal short circuit mechanism in a 60 Ah high-energy-density Li-ion pouch cell”, *Nano Energy*, vol. 84, p. 105 908, 2021. DOI: 10.1016/j.nanoen.2021.105908.
- [126] M. Sharp, J. J. Darst, P. Hughes, J. Billman, M. Pham, D. Petrushenko, T. M. M. Heenan, R. Jervis, R. Owen, D. Patel, D. Wenjia, H. Michael, A. Rack, O. V. Magdysyuk, T. Connolley, D. J. L. Brett, G. Hinds, M. Keyser, E. Darcy, P. R. Shearing, W. Walker, and D. P. Finegan, “Thermal Runaway of Li-Ion Cells: How Internal Dynamics, Mass Ejection, and Heat Vary with Cell Geometry and Abuse Type”, *Journal of The Electrochemical Society*, vol. 169, no. 2, p. 020 526, 2022. DOI: 10.1149/1945-7111/ac4fef.
- [127] D. P. Finegan, M. Scheel, J. B. Robinson, B. Tjaden, M. Di Michiel, G. Hinds, D. J. L. Brett, and P. R. Shearing, “Investigating lithium-ion battery materials during overcharge-induced thermal runaway: An operando and multi-scale X-ray CT study”, *Physical Chemistry Chemical Physics*, vol. 18, no. 45, pp. 30 912–30 919, 2016. DOI: 10.1039/C6CP04251A.
- [128] J. Ye, H. Chen, Q. Wang, P. Huang, J. Sun, and S. Lo, “Thermal behavior and failure mechanism of lithium ion cells during overcharge under adiabatic conditions”, *Applied Energy*, vol. 182, pp. 464–474, 2016. DOI: 10.1016/j.apenergy.2016.08.124.
- [129] Y. Fernandes, A. Bry, and S. De Persis, “Identification and quantification of gases emitted during abuse tests by overcharge of a commercial Li-ion battery”, *Journal of Power Sources*, vol. 389, pp. 106–119, 2018. DOI: 10.1016/j.jpowsour.2018.03.034.
- [130] D. P. Finegan, M. Scheel, J. B. Robinson, B. Tjaden, I. Hunt, T. J. Mason, J. Millichamp, M. Di Michiel, G. J. Offer, G. Hinds, D. J. Brett, and P. R. Shearing, “In-operando high-speed tomography of lithium-ion batteries during thermal runaway”, *Nature Communications*, vol. 6, no. 1, p. 6924, 2015. DOI: 10.1038/ncomms7924.
- [131] W. Li, H. Wang, Y. Zhang, and M. Ouyang, “Flammability characteristics of the battery vent gas: A case of NCA and LFP lithium-ion batteries during external heating abuse”, *Journal of Energy Storage*, vol. 24, p. 100 775, 2019. DOI: 10.1016/j.est.2019.100775.

- [132] H. Chen, J. E. Buston, J. Gill, D. Howard, R. C. Williams, C. M. Rao Vendra, A. Shelke, and J. X. Wen, “An experimental study on thermal runaway characteristics of lithium-ion batteries with high specific energy and prediction of heat release rate”, *Journal of Power Sources*, vol. 472, p. 228 585, 2020. DOI: 10.1016/j.jpowsour.2020.228585.
- [133] K. Zou, X. Chen, Z. Ding, J. Gu, and S. Lu, “Jet behavior of prismatic lithium-ion batteries during thermal runaway”, *Applied Thermal Engineering*, vol. 179, p. 115 745, 2020. DOI: 10.1016/j.applthermaleng.2020.115745.
- [134] P. Ramadass, W. Fang, and Z. J. Zhang, “Study of internal short in a Li-ion cell I. Test method development using infra-red imaging technique”, *Journal of Power Sources*, vol. 248, pp. 769–776, 2014. DOI: 10.1016/j.jpowsour.2013.09.145.
- [135] P. Jindal and J. Bhattacharya, “Review—Understanding the Thermal Runaway Behavior of Li-Ion Batteries through Experimental Techniques”, *Journal of The Electrochemical Society*, vol. 166, no. 10, A2165–A2193, 2019. DOI: 10.1149/2.1381910jes.
- [136] Thermal Hazard Technology (THT), *Accelerating Rate Calorimeter - product brochure*, 2023. [Online]. Available: <https://www.thermalhazardtechnology.com/contentfiles/downloads/38.pdf> (visited on 04/22/2023).
- [137] S. Hildebrand, A. Rheinfeld, A. Friesen, J. Haetge, F. M. Schappacher, A. Jossen, and M. Winter, “Thermal Analysis of $\text{LiNi}_{0.4}\text{Co}_{0.2}\text{Mn}_{0.4}\text{O}_2$ /Mesocarbon Microbeads Cells and Electrodes: State-of-Charge and State-of-Health Influences on Reaction Kinetics”, *Journal of The Electrochemical Society*, vol. 165, no. 2, A104–A117, 2018. DOI: 10.1149/2.0361802jes.
- [138] E. P. Roth, “Abuse Response of 18650 Li-Ion Cells with different cathodes using EC:EMC/LiPF₆ and EC:PC:DMC/LiPF₆ Electrolytes”, *ECS Transactions*, vol. 11, no. 19, pp. 19–41, 2008. DOI: 10.1149/1.2897969.
- [139] E. Roth and D. Doughty, “Thermal abuse performance of high-power 18650 Li-ion cells”, *Journal of Power Sources*, vol. 128, no. 2, pp. 308–318, 2004. DOI: 10.1016/j.jpowsour.2003.09.068.
- [140] D. Ren, H. Hsu, R. Li, X. Feng, D. Guo, X. Han, L. Lu, X. He, S. Gao, J. Hou, Y. Li, Y. Wang, and M. Ouyang, “A comparative investigation of aging effects on thermal runaway behavior of lithium-ion batteries”, *eTransportation*, vol. 2, p. 100 034, 2019. DOI: 10.1016/j.etrans.2019.100034.
- [141] S. Liu, T. Ma, Z. Wei, G. Bai, H. Liu, D. Xu, Z. Shan, and F. Wang, “Study about thermal runaway behavior of high specific energy density Li-ion batteries in a low state of charge”, *Journal of Energy Chemistry*, vol. 52, pp. 20–27, 2021. DOI: 10.1016/j.jechem.2020.03.029.

- [142] D. Abraham, E. Roth, R. KostECKI, K. McCarthy, S. MacLaren, and D. Doughty, “Diagnostic examination of thermally abused high-power lithium-ion cells”, *Journal of Power Sources*, vol. 161, no. 1, pp. 648–657, 2006. DOI: 10.1016/j.jpowsour.2006.04.088.
- [143] L. Yuan, T. Dubaniewicz, I. Zlochower, R. Thomas, and N. Rayyan, “Experimental study on thermal runaway and vented gases of lithium-ion cells”, *Process Safety and Environmental Protection*, vol. 144, pp. 186–192, 2020. DOI: 10.1016/j.psep.2020.07.028.
- [144] K. Zou, S. Lu, X. Chen, E. Gao, Y. Cao, and Y. Bi, “Thermal and gas characteristics of large-format $\text{LiNi}_{0.8}\text{Co}_{0.1}\text{Mn}_{0.1}\text{O}_2$ pouch power cell during thermal runaway”, *Journal of Energy Storage*, vol. 39, p. 102609, 2021. DOI: 10.1016/j.est.2021.102609.
- [145] A. W. Golubkov, D. Fuchs, J. Wagner, H. Wiltsche, C. Stangl, G. Fauler, G. Voitic, A. Thaler, and V. Hacker, “Thermal-runaway experiments on consumer Li-ion batteries with metal-oxide and olivin-type cathodes”, *RSC Adv.*, vol. 4, no. 7, pp. 3633–3642, 2014. DOI: 10.1039/C3RA45748F.
- [146] A. W. Golubkov, S. Scheickl, R. Planteu, G. Voitic, H. Wiltsche, C. Stangl, G. Fauler, A. Thaler, and V. Hacker, “Thermal runaway of commercial 18650 Li-ion batteries with LFP and NCA cathodes – impact of state of charge and overcharge”, *RSC Advances*, vol. 5, no. 70, pp. 57171–57186, 2015. DOI: 10.1039/C5RA05897J.
- [147] S. Zheng, L. Wang, X. Feng, and X. He, “Probing the heat sources during thermal runaway process by thermal analysis of different battery chemistries”, *Journal of Power Sources*, vol. 378, pp. 527–536, 2018. DOI: 10.1016/j.jpowsour.2017.12.050.
- [148] C. Xu, X. Feng, W. Huang, Y. Duan, T. Chen, S. Gao, L. Lu, F. Jiang, and M. Ouyang, “Internal temperature detection of thermal runaway in lithium-ion cells tested by extended-volume accelerating rate calorimetry”, *Journal of Energy Storage*, vol. 31, p. 101670, 2020. DOI: 10.1016/j.est.2020.101670.
- [149] D. Ren, X. Feng, L. Liu, H. Hsu, L. Lu, L. Wang, X. He, and M. Ouyang, “Investigating the relationship between internal short circuit and thermal runaway of lithium-ion batteries under thermal abuse condition”, *Energy Storage Materials*, vol. 34, pp. 563–573, 2021. DOI: 10.1016/j.ensm.2020.10.020.
- [150] X. Tang, G. Zhang, X. Wang, G. Wei, G. Han, J. Zhu, X. Wei, and H. Dai, “Investigating the critical characteristics of thermal runaway process for LiFePO_4 / graphite batteries by a ceased segmented method”, *iScience*, vol. 24, no. 10, p. 103088, 2021. DOI: 10.1016/j.isci.2021.103088.
- [151] S. Yayathi, W. Walker, D. Doughty, and H. Ardebili, “Energy distributions exhibited during thermal runaway of commercial lithium ion batteries used for human spaceflight applications”, *Journal of Power Sources*, vol. 329, pp. 197–206, 2016. DOI: 10.1016/j.jpowsour.2016.08.078.

- [152] C. Zhao, J. Sun, and Q. Wang, “Thermal runaway hazards investigation on 18650 lithium-ion battery using extended volume accelerating rate calorimeter”, *Journal of Energy Storage*, vol. 28, p. 101 232, 2020. DOI: 10.1016/j.est.2020.101232.
- [153] X. He, C. Zhao, Z. Hu, F. Restuccia, F. Richter, Q. Wang, and G. Rein, “Heat transfer effects on accelerating rate calorimetry of the thermal runaway of Lithium-ion batteries”, *Process Safety and Environmental Protection*, vol. 162, pp. 684–693, 2022. DOI: 10.1016/j.psep.2022.04.028.
- [154] Fauske, “Vent sizing package”, *Chemical Health & Safety*, vol. 6, no. 2, pp. 47–47, 1999. DOI: 10.1016/S1074-9098(00)80023-4.
- [155] C.-Y. Jhu, Y.-W. Wang, C.-Y. Wen, C.-C. Chiang, and C.-M. Shu, “Self-reactive rating of thermal runaway hazards on 18650 lithium-ion batteries”, *Journal of Thermal Analysis and Calorimetry*, vol. 106, no. 1, pp. 159–163, 2011. DOI: 10.1007/s10973-011-1452-6.
- [156] C.-Y. Jhu, Y.-W. Wang, C.-M. Shu, J.-C. Chang, and H.-C. Wu, “Thermal explosion hazards on 18650 lithium ion batteries with a VSP2 adiabatic calorimeter”, *Journal of Hazardous Materials*, S0304389411005358, 2011. DOI: 10.1016/j.jhazmat.2011.04.097.
- [157] C.-Y. Jhu, Y.-W. Wang, C.-Y. Wen, and C.-M. Shu, “Thermal runaway potential of LiCoO_2 and $\text{LiNi}_{1/3}\text{Co}_{1/3}\text{Mn}_{1/3}\text{O}_2$ batteries determined with adiabatic calorimetry methodology”, *Applied Energy*, vol. 100, pp. 127–131, 2012. DOI: 10.1016/j.apenergy.2012.05.064.
- [158] C.-Y. Wen, C.-Y. Jhu, Y.-W. Wang, C.-C. Chiang, and C.-M. Shu, “Thermal runaway features of 18650 lithium-ion batteries for LiFePO_4 cathode material by DSC and VSP2”, *Journal of Thermal Analysis and Calorimetry*, vol. 109, no. 3, pp. 1297–1302, 2012. DOI: 10.1007/s10973-012-2573-2.
- [159] T.-Y. Lu, C.-C. Chiang, S.-H. Wu, K.-C. Chen, S.-J. Lin, C.-Y. Wen, and C.-M. Shu, “Thermal hazard evaluations of 18650 lithium-ion batteries by an adiabatic calorimeter”, *Journal of Thermal Analysis and Calorimetry*, vol. 114, no. 3, pp. 1083–1088, 2013. DOI: 10.1007/s10973-013-3137-9.
- [160] X. Liu, S. I. Stoliarov, M. Denlinger, A. Masias, and K. Snyder, “Comprehensive calorimetry of the thermally-induced failure of a lithium ion battery”, *Journal of Power Sources*, vol. 280, pp. 516–525, 2015. DOI: 10.1016/j.jpowsour.2015.01.125.
- [161] X. Liu, Z. Wu, S. I. Stoliarov, M. Denlinger, A. Masias, and K. Snyder, “Heat release during thermally-induced failure of a lithium ion battery: Impact of cathode composition”, *Fire Safety Journal*, vol. 85, pp. 10–22, 2016. DOI: 10.1016/j.firesaf.2016.08.001.
- [162] P. Liu, C. Liu, K. Yang, M. Zhang, F. Gao, B. Mao, H. Li, Q. Duan, and Q. Wang, “Thermal runaway and fire behaviors of lithium iron phosphate battery induced by over heating”, *Journal of Energy Storage*, vol. 31, p. 101 714, 2020. DOI: 10.1016/j.est.2020.101714.

- [163] R. E. Lyon and R. N. Walters, “Energetics of lithium ion battery failure”, *Journal of Hazardous Materials*, vol. 318, pp. 164–172, 2016. DOI: 10.1016/j.jhazmat.2016.06.047.
- [164] W. Q. Walker, J. J. Darst, D. P. Finegan, G. A. Bayles, K. L. Johnson, E. C. Darcy, and S. L. Rickman, “Decoupling of heat generated from ejected and non-ejected contents of 18650-format lithium-ion cells using statistical methods”, *Journal of Power Sources*, vol. 415, pp. 207–218, 2019. DOI: 10.1016/j.jpowsour.2018.10.099.
- [165] C. Essl, A. W. Golubkov, E. Gasser, M. Nachtnebel, A. Zankel, E. Ewert, and A. Fuchs, “Comprehensive Hazard Analysis of Failing Automotive Lithium-Ion Batteries in Overtemperature Experiments”, *Batteries*, vol. 6, no. 2, p. 30, 2020. DOI: 10.3390/batteries6020030.
- [166] Z. Liao, S. Zhang, K. Li, M. Zhao, Z. Qiu, D. Han, G. Zhang, and T. G. Habetler, “Hazard analysis of thermally abused lithium-ion batteries at different state of charges”, *Journal of Energy Storage*, vol. 27, p. 101065, 2020. DOI: 10.1016/j.est.2019.101065.
- [167] V. Somandepalli, K. Marr, and Q. Horn, “Quantification of Combustion Hazards of Thermal Runaway Failures in Lithium-Ion Batteries”, *SAE International Journal of Alternative Powertrains*, vol. 3, no. 1, pp. 98–104, 2014. DOI: 10.4271/2014-01-1857.
- [168] S. Koch, A. Fill, and K. P. Birke, “Comprehensive gas analysis on large scale automotive lithium-ion cells in thermal runaway”, *Journal of Power Sources*, vol. 398, pp. 106–112, 2018. DOI: 10.1016/j.jpowsour.2018.07.051.
- [169] A. W. Golubkov, R. Planteu, P. Krohn, B. Rasch, B. Brunnsteiner, A. Thaler, and V. Hacker, “Thermal runaway of large automotive Li-ion batteries”, *RSC Advances*, vol. 8, no. 70, pp. 40172–40186, 2018. DOI: 10.1039/C8RA06458J.
- [170] Y. Zhang, H. Wang, W. Li, and C. Li, “Quantitative identification of emissions from abused prismatic Ni-rich lithium-ion batteries”, *eTransportation*, vol. 2, p. 100031, 2019. DOI: 10.1016/j.etrans.2019.100031.
- [171] Y. Zhang, H. Wang, W. Li, C. Li, and M. Ouyang, “Size distribution and elemental composition of vent particles from abused prismatic Ni-rich automotive lithium-ion batteries”, *Journal of Energy Storage*, vol. 26, p. 100991, 2019. DOI: 10.1016/j.est.2019.100991.
- [172] Y. Wang, H. Wang, Y. Zhang, L. Cheng, Y. Wu, X. Feng, L. Lu, and M. Ouyang, “Thermal oxidation characteristics for smoke particles from an abused prismatic $\text{LiNi}_{0.6}\text{Co}_{0.2}\text{Mn}_{0.2}\text{O}_2$ battery”, *Journal of Energy Storage*, vol. 39, p. 102639, 2021. DOI: 10.1016/j.est.2021.102639.
- [173] D. P. Finegan, E. Darcy, M. Keyser, B. Tjaden, T. M. M. Heenan, R. Jervis, J. J. Bailey, R. Malik, N. T. Vo, O. V. Magdysyuk, R. Atwood, M. Drakopoulos, M. DiMichiel, A. Rack, G. Hinds, D. J. L. Brett, and P. R. Shearing, “Characterising thermal runaway within lithium-ion cells by inducing and monitoring internal short

- circuits”, *Energy & Environmental Science*, vol. 10, no. 6, pp. 1377–1388, 2017. DOI: 10.1039/C7EE00385D.
- [174] C. Ding, N. Zhu, J. Yu, Y. Li, X. Sun, C. Liu, Q. Huang, and J. Wang, “Experimental investigation of environmental pressure effects on thermal runaway properties of 21700 lithium-ion batteries with high energy density”, *Case Studies in Thermal Engineering*, vol. 38, p. 102349, 2022. DOI: 10.1016/j.csite.2022.102349.
- [175] A. García, J. Monsalve-Serrano, R. Lago Sari, and S. Martinez-Boggio, “An optical investigation of thermal runaway phenomenon under thermal abuse conditions”, *Energy Conversion and Management*, vol. 246, p. 114663, 2021. DOI: 10.1016/j.enconman.2021.114663.
- [176] H. Matsumura, S. Itoh, and K. Ando, “Basic Study on Thermal Runaway Propagation through Lithium Ion Cells”, *SAE International Journal of Passenger Cars - Mechanical Systems*, vol. 8, no. 2, pp. 546–555, 2015. DOI: 10.4271/2015-01-1379.
- [177] L. Torres-Castro, A. Kurzawski, J. Hewson, and J. Lamb, “Passive Mitigation of Cascading Propagation in Multi-Cell Lithium Ion Batteries”, *Journal of The Electrochemical Society*, vol. 167, no. 9, p. 090515, 2020. DOI: 10.1149/1945-7111/ab84fa.
- [178] J. Lamb, C. J. Orendorff, L. A. M. Steele, and S. W. Spangler, “Failure propagation in multi-cell lithium ion batteries”, *Journal of Power Sources*, vol. 283, pp. 517–523, 2015. DOI: 10.1016/j.jpowsour.2014.10.081.
- [179] D. Becher, M. Bauer, H. Döring, O. Böse, B. Friess, and M. A. Danzer, “Preventing thermal propagation in battery packs using enthalpy supported thermal barriers”, *Journal of Energy Storage*, vol. 42, p. 103057, 2021. DOI: 10.1016/j.est.2021.103057.
- [180] X. Feng, J. Sun, M. Ouyang, F. Wang, X. He, L. Lu, and H. Peng, “Characterization of penetration induced thermal runaway propagation process within a large format lithium ion battery module”, *Journal of Power Sources*, vol. 275, pp. 261–273, 2015. DOI: 10.1016/j.jpowsour.2014.11.017.
- [181] H. Niu, C. Chen, D. Ji, L. Li, Z. Li, Y. Liu, and X. Huang, “Thermal-Runaway Propagation over a Linear Cylindrical Battery Module”, *Fire Technology*, vol. 56, no. 6, pp. 2491–2507, 2020. DOI: 10.1007/s10694-020-00976-0.
- [182] Z. Wang, T. He, H. Bian, F. Jiang, and Y. Yang, “Characteristics of and factors influencing thermal runaway propagation in lithium-ion battery packs”, *Journal of Energy Storage*, vol. 41, p. 102956, 2021. DOI: 10.1016/j.est.2021.102956.
- [183] Z. Wang, N. Mao, and F. Jiang, “Study on the effect of spacing on thermal runaway propagation for lithium-ion batteries”, *Journal of Thermal Analysis and Calorimetry*, vol. 140, no. 6, pp. 2849–2863, 2020. DOI: 10.1007/s10973-019-09026-6.
- [184] C. F. Lopez, J. A. Jeevarajan, and P. P. Mukherjee, “Experimental Analysis of Thermal Runaway and Propagation in Lithium-Ion Battery Modules”, *Journal of The Electrochemical Society*, vol. 162, no. 9, A1905–A1915, 2015. DOI: 10.1149/2.0921509jes.

- [185] D. Ouyang, J. Liu, M. Chen, J. Weng, and J. Wang, “An Experimental Study on the Thermal Failure Propagation in Lithium-Ion Battery Pack”, *Journal of The Electrochemical Society*, vol. 165, no. 10, A2184–A2193, 2018. DOI: 10.1149/2.0721810jes.
- [186] G. Zhong, H. Li, C. Wang, K. Xu, and Q. Wang, “Experimental Analysis of Thermal Runaway Propagation Risk within 18650 Lithium-Ion Battery Modules”, *Journal of The Electrochemical Society*, vol. 165, no. 9, A1925–A1934, 2018. DOI: 10.1149/2.0461809jes.
- [187] T. Liu, C. Tao, and X. Wang, “Cooling control effect of water mist on thermal runaway propagation in lithium ion battery modules”, *Applied Energy*, vol. 267, p. 115087, 2020. DOI: 10.1016/j.apenergy.2020.115087.
- [188] M. Chen, J. Liu, Y. He, R. Yuen, and J. Wang, “Study of the fire hazards of lithium-ion batteries at different pressures”, *Applied Thermal Engineering*, vol. 125, pp. 1061–1074, 2017. DOI: 10.1016/j.applthermaleng.2017.06.131.
- [189] P. Ping, Q. Wang, P. Huang, K. Li, J. Sun, D. Kong, and C. Chen, “Study of the fire behavior of high-energy lithium-ion batteries with full-scale burning test”, *Journal of Power Sources*, vol. 285, pp. 80–89, 2015. DOI: 10.1016/j.jpowsour.2015.03.035.
- [190] H. Li, Q. Duan, C. Zhao, Z. Huang, and Q. Wang, “Experimental investigation on the thermal runaway and its propagation in the large format battery module with $\text{Li}(\text{Ni}_{1/3}\text{Co}_{1/3}\text{Mn}_{1/3})\text{O}_2$ as cathode”, *Journal of Hazardous Materials*, vol. 375, pp. 241–254, 2019. DOI: 10.1016/j.jhazmat.2019.03.116.
- [191] L. Li, C. Xu, R. Chang, C. Yang, C. Jia, L. Wang, J. Song, Z. Li, F. Zhang, B. Fang, X. Wei, H. Wang, Q. Wu, Z. Chen, X. He, X. Feng, H. Wu, and M. Ouyang, “Thermal-responsive, super-strong, ultrathin firewalls for quenching thermal runaway in high-energy battery modules”, *Energy Storage Materials*, vol. 40, pp. 329–336, 2021. DOI: 10.1016/j.ensm.2021.05.018.
- [192] Z. Huang, C. Zhao, H. Li, W. Peng, Z. Zhang, and Q. Wang, “Experimental study on thermal runaway and its propagation in the large format lithium ion battery module with two electrical connection modes”, *Energy*, vol. 205, p. 117906, 2020. DOI: 10.1016/j.energy.2020.117906.
- [193] Z. Huang, X. Li, Q. Wang, Q. Duan, Y. Li, L. Li, and Q. Wang, “Experimental investigation on thermal runaway propagation of large format lithium ion battery modules with two cathodes”, *International Journal of Heat and Mass Transfer*, vol. 172, p. 121077, 2021. DOI: 10.1016/j.ijheatmasstransfer.2021.121077.
- [194] S. Gao, X. Feng, L. Lu, N. Kamyab, J. Du, P. Coman, R. E. White, and M. Ouyang, “An experimental and analytical study of thermal runaway propagation in a large format lithium ion battery module with NCM pouch-cells in parallel”, *International Journal of Heat and Mass Transfer*, vol. 135, pp. 93–103, 2019. DOI: 10.1016/j.ijheatmasstransfer.2019.01.125.

- [195] J. Weng, D. Ouyang, Y. Liu, M. Chen, Y. Li, X. Huang, and J. Wang, “Alleviation on battery thermal runaway propagation: Effects of oxygen level and dilution gas”, *Journal of Power Sources*, vol. 509, p. 230 340, 2021. DOI: 10.1016/j.jpowsour.2021.230340.
- [196] W. Yan, Z. Wang, and S. Chen, “Quantitative analysis on the heat transfer modes in the process of thermal runaway propagation in lithium-ion battery pack under confined and semi-confined space”, *International Journal of Heat and Mass Transfer*, vol. 176, p. 121 483, 2021. DOI: 10.1016/j.ijheatmasstransfer.2021.121483.
- [197] E. Archibald, R. Kennedy, K. Marr, J. Jeevarajan, and O. Ezekoye, “Characterization of Thermally Induced Runaway in Pouch Cells for Propagation”, *Fire Technology*, vol. 56, no. 6, pp. 2467–2490, 2020. DOI: 10.1007/s10694-020-00974-2.
- [198] R. W. Kennedy, K. C. Marr, and O. A. Ezekoye, “Gas release rates and properties from Lithium Cobalt Oxide lithium ion battery arrays”, *Journal of Power Sources*, vol. 487, p. 229 388, 2021. DOI: 10.1016/j.jpowsour.2020.229388.
- [199] C. Xu, F. Zhang, X. Feng, F. Jiang, D. Ren, L. Lu, Y. Yang, G. Liu, X. Han, B. Friess, and M. Ouyang, “Experimental study on thermal runaway propagation of lithium-ion battery modules with different parallel-series hybrid connections”, *Journal of Cleaner Production*, vol. 284, p. 124 749, 2021. DOI: 10.1016/j.jclepro.2020.124749.
- [200] X. Lai, S. Wang, H. Wang, Y. Zheng, and X. Feng, “Investigation of thermal runaway propagation characteristics of lithium-ion battery modules under different trigger modes”, *International Journal of Heat and Mass Transfer*, vol. 171, p. 121 080, 2021. DOI: 10.1016/j.ijheatmasstransfer.2021.121080.
- [201] X. Yang, Y. Duan, X. Feng, T. Chen, C. Xu, X. Rui, M. Ouyang, L. Lu, X. Han, D. Ren, Z. Zhang, C. Li, and S. Gao, “An Experimental Study on Preventing Thermal Runaway Propagation in Lithium-Ion Battery Module Using Aerogel and Liquid Cooling Plate Together”, *Fire Technology*, vol. 56, no. 6, pp. 2579–2602, 2020. DOI: 10.1007/s10694-020-00995-x.
- [202] X. Rui, X. Feng, H. Wang, H. Yang, Y. Zhang, M. Wan, Y. Wei, and M. Ouyang, “Synergistic effect of insulation and liquid cooling on mitigating the thermal runaway propagation in lithium-ion battery module”, *Applied Thermal Engineering*, vol. 199, p. 117 521, 2021. DOI: 10.1016/j.applthermaleng.2021.117521.
- [203] H. Wang, Z. Du, X. Rui, S. Wang, C. Jin, L. He, F. Zhang, Q. Wang, and X. Feng, “A comparative analysis on thermal runaway behavior of Li ($\text{Ni}_x\text{Co}_y\text{Mn}_z$) O_2 battery with different nickel contents at cell and module level”, *Journal of Hazardous Materials*, vol. 393, p. 122 361, 2020. DOI: 10.1016/j.jhazmat.2020.122361.
- [204] S. Wilke, B. Schweitzer, S. Khateeb, and S. Al-Hallaj, “Preventing thermal runaway propagation in lithium ion battery packs using a phase change composite

- material: An experimental study”, *Journal of Power Sources*, vol. 340, pp. 51–59, 2017. DOI: 10.1016/j.jpowsour.2016.11.018.
- [205] V. Premnath, Y. Wang, N. Wright, I. Khalek, and S. Uribe, “Detailed characterization of particle emissions from battery fires”, *Aerosol Science and Technology*, vol. 56, no. 4, pp. 337–354, 2022. DOI: 10.1080/02786826.2021.2018399.
- [206] P. Christensen, Z. Milojevic, M. Wise, M. Ahmeid, P. Attidekou, W. Mrozik, N. Dickmann, F. Restuccia, S. Lambert, and P. Das, “Thermal and mechanical abuse of electric vehicle pouch cell modules”, *Applied Thermal Engineering*, vol. 189, p. 116 623, 2021. DOI: 10.1016/j.applthermaleng.2021.116623.
- [207] M. Held, M. Tuchschnid, M. Zennegg, R. Figi, C. Schreiner, L. D. Mellert, U. Welte, M. Kompatscher, M. Hermann, and L. Nachef, “Thermal runaway and fire of electric vehicle lithium-ion battery and contamination of infrastructure facility”, *Renewable and Sustainable Energy Reviews*, vol. 165, p. 112 474, 2022. DOI: 10.1016/j.rser.2022.112474.
- [208] C. Chen, L. Guo, N. Huichang, Z. Li, S. Mo, P. Sun, and X. Huang, “Characteristics of Thermal Runaway Propagation of Lithium Ion Battery Module Induced by Thermal Abuses in Enclosure Space”, in *The Proceedings of 11th Asia-Oceania Symposium on Fire Science and Technology*, G.-Y. Wu, K.-C. Tsai, and W. K. Chow, Eds., Singapore: Springer Singapore, 2020, pp. 667–676. DOI: 10.1007/978-981-32-9139-3_48.
- [209] Cheng, Li, Ruan, and Wang, “Thermal Runaway Characteristics of a Large Format Lithium-Ion Battery Module”, *Energies*, vol. 12, no. 16, p. 3099, 2019. DOI: 10.3390/en12163099.
- [210] S. Gao, X. Feng, L. Lu, M. Ouyang, and D. Ren, “A Test Approach for Evaluating the Safety Considering Thermal Runaway Propagation within the Battery Pack”, *ECS Transactions*, vol. 77, no. 11, pp. 225–236, 2017. DOI: 10.1149/07711.0225ecst.
- [211] S. Gao, L. Lu, M. Ouyang, Y. Duan, X. Zhu, C. Xu, B. Ng, N. Kamyab, R. E. White, and P. T. Coman, “Experimental Study on Module-to-Module Thermal Runaway-Propagation in a Battery Pack”, *Journal of The Electrochemical Society*, vol. 166, no. 10, A2065–A2073, 2019. DOI: 10.1149/2.1011910jes.
- [212] J. Deng, C. Bae, A. Denlinger, and T. Miller, “Progress in battery safety modeling”, *Progress in Energy*, vol. 4, no. 4, p. 043 001, 2022. DOI: 10.1088/2516-1083/ac8333.
- [213] S. Abada, G. Marlair, A. Lecocq, M. Petit, V. Sauvante-Moynot, and F. Huet, “Safety focused modeling of lithium-ion batteries: A review”, *Journal of Power Sources*, vol. 306, pp. 178–192, 2016. DOI: 10.1016/j.jpowsour.2015.11.100.
- [214] J. Zhu, T. Wierzbicki, and W. Li, “A review of safety-focused mechanical modeling of commercial lithium-ion batteries”, *Journal of Power Sources*, vol. 378, pp. 153–168, 2018. DOI: 10.1016/j.jpowsour.2017.12.034.

- [215] M. N. Richard and J. R. Dahn, “Accelerating Rate Calorimetry Study on the Thermal Stability of Lithium Intercalated Graphite in Electrolyte. II. Modeling the Results and Predicting Differential Scanning Calorimeter Curves”, *Journal of The Electrochemical Society*, vol. 146, no. 6, pp. 2078–2084, 1999. DOI: 10.1149/1.1391894.
- [216] C. H. Lee, S. J. Bae, and M. Jang, “A study on effect of lithium ion battery design variables upon features of thermal-runaway using mathematical model and simulation”, *Journal of Power Sources*, vol. 293, pp. 498–510, 2015. DOI: 10.1016/j.jpowsour.2015.05.095.
- [217] S. Santhanagopalan, P. Ramadass, and J. Z. Zhang, “Analysis of internal short-circuit in a lithium ion cell”, *Journal of Power Sources*, vol. 194, no. 1, pp. 550–557, 2009. DOI: 10.1016/j.jpowsour.2009.05.002.
- [218] Y. Zhang, W. Mei, P. Qin, Q. Duan, and Q. Wang, “Numerical modeling on thermal runaway triggered by local overheating for lithium iron phosphate battery”, *Applied Thermal Engineering*, vol. 192, p. 116–128, 2021. DOI: 10.1016/j.applthermaleng.2021.116928.
- [219] K.-C. Chiu, C.-H. Lin, S.-F. Yeh, Y.-H. Lin, and K.-C. Chen, “An electrochemical modeling of lithium-ion battery nail penetration”, *Journal of Power Sources*, vol. 251, pp. 254–263, 2014. DOI: 10.1016/j.jpowsour.2013.11.069.
- [220] G. Liang, Y. Zhang, Q. Han, Z. Liu, Z. Jiang, and S. Tian, “A novel 3D-layered electrochemical-thermal coupled model strategy for the nail-penetration process simulation”, *Journal of Power Sources*, vol. 342, pp. 836–845, 2017. DOI: 10.1016/j.jpowsour.2017.01.005.
- [221] T. Yamanaka, Y. Takagishi, Y. Tozuka, and T. Yamaue, “Modeling lithium ion battery nail penetration tests and quantitative evaluation of the degree of combustion risk”, *Journal of Power Sources*, vol. 416, pp. 132–140, 2019. DOI: 10.1016/j.jpowsour.2019.01.055.
- [222] M. Ye, G. Hu, F. Guo, W. Huang, Z. Wang, X. Zhao, and Y. Li, “A novel semi-analytical solution for calculating the temperature distribution of the lithium-ion batteries during nail penetration based on Green’s function method”, *Applied Thermal Engineering*, vol. 174, p. 115–129, 2020. DOI: 10.1016/j.applthermaleng.2020.115129.
- [223] X. Liu, Z. Zhou, W. Wu, L. Gao, Y. Li, H. Huang, Z. Huang, Y. Li, and Y. Song, “Three-Dimensional Modeling for the Internal Shorting Caused Thermal Runaway Process in 20Ah Lithium-Ion Battery”, *Energies*, vol. 15, no. 19, p. 6868, 2022. DOI: 10.3390/en15196868.
- [224] D. Kong, G. Wang, P. Ping, and J. Wen, “Numerical investigation of thermal runaway behavior of lithium-ion batteries with different battery materials and heating conditions”, *Applied Thermal Engineering*, vol. 189, p. 116–161, 2021. DOI: 10.1016/j.applthermaleng.2021.116661.

- [225] D. Ren, X. Feng, L. Lu, M. Ouyang, S. Zheng, J. Li, and X. He, “An electrochemical-thermal coupled overcharge-to-thermal-runaway model for lithium ion battery”, *Journal of Power Sources*, vol. 364, pp. 328–340, 2017. DOI: 10.1016/j.jpowsour.2017.08.035.
- [226] R. Spotnitz and J. Franklin, “Abuse behavior of high-power, lithium-ion cells”, *Journal of Power Sources*, vol. 113, no. 1, pp. 81–100, 2003. DOI: 10.1016/S0378-7753(02)00488-3.
- [227] A. Melcher, C. Ziebert, M. Rohde, and H. Seifert, “Modeling and Simulation of the Thermal Runaway Behavior of Cylindrical Li-Ion Cells—Computing of Critical Parameters”, *Energies*, vol. 9, no. 4, p. 292, 2016. DOI: 10.3390/en9040292.
- [228] L. Zhang, P. Zhao, M. Xu, and X. Wang, “Computational identification of the safety regime of Li-ion battery thermal runaway”, *Applied Energy*, vol. 261, p. 114 440, 2020. DOI: 10.1016/j.apenergy.2019.114440.
- [229] J.-H. Kim, E. Kwak, J. Jeong, and K.-Y. Oh, “Versatile multiphysics model for thermal runaway estimation of a lithium-ion battery”, *International Journal of Energy Research*, vol. 46, no. 12, pp. 16 550–16 575, 2022. DOI: 10.1002/er.8317.
- [230] J. Xu and C. Hendricks, “An Electrochemical-thermal Coupled Gas Generation and Overcharge-to-thermal-runaway Model for Large-format Lithium Ion Battery”, in *2020 19th IEEE Intersociety Conference on Thermal and Thermomechanical Phenomena in Electronic Systems (ITherm)*, IEEE, 2020, pp. 597–603. DOI: 10.1109/ITherm45881.2020.9190182.
- [231] J. Xu and C. Hendricks, “A Multiphysics Simulation of the Thermal Runaway in Large-Format Lithium-ion Batteries”, in *2019 18th IEEE Intersociety Conference on Thermal and Thermomechanical Phenomena in Electronic Systems (ITherm)*, IEEE, 2019, pp. 815–821. DOI: 10.1109/ITHERM.2019.8757424.
- [232] P. T. Coman, S. Rayman, and R. E. White, “A lumped model of venting during thermal runaway in a cylindrical Lithium Cobalt Oxide lithium-ion cell”, *Journal of Power Sources*, vol. 307, pp. 56–62, 2016. DOI: 10.1016/j.jpowsour.2015.12.088.
- [233] T. Cai, A. G. Stefanopoulou, and J. B. Siegel, “Modeling Li-Ion Battery Temperature and Expansion Force during the Early Stages of Thermal Runaway Triggered by Internal Shorts”, *Journal of The Electrochemical Society*, vol. 166, no. 12, A2431–A2443, 2019. DOI: 10.1149/2.1561910jes.
- [234] B. Wang, C. Ji, S. Wang, and S. Pan, “A Detailed Finite Element Model of Internal Short Circuit and Venting During Thermal Runaway in a 32650 Lithium-Ion Battery”, *Fire Technology*, vol. 56, no. 6, pp. 2525–2544, 2020. DOI: 10.1007/s10694-020-00978-y.
- [235] J. K. Ostanek, W. Li, P. P. Mukherjee, K. Crompton, and C. Hacker, “Simulating onset and evolution of thermal runaway in Li-ion cells using a coupled thermal and venting model”, *Applied Energy*, vol. 268, p. 114 972, 2020. DOI: 10.1016/j.apenergy.2020.114972.

- [236] F. Baakes, M. Lütke, M. Gerasimov, V. Laue, F. Röder, P. Balbuena, and U. Krewer, “Unveiling the interaction of reactions and phase transition during thermal abuse of Li-ion batteries”, *Journal of Power Sources*, vol. 522, p. 230 881, 2022. DOI: 10.1016/j.jpowsour.2021.230881.
- [237] P. T. Coman, E. C. Darcy, C. T. Veje, and R. E. White, “Modelling Li-Ion Cell Thermal Runaway Triggered by an Internal Short Circuit Device Using an Efficiency Factor and Arrhenius Formulations”, *Journal of The Electrochemical Society*, vol. 164, no. 4, A587–A593, 2017. DOI: 10.1149/2.0341704jes.
- [238] S. Wu, Y. Bai, W. Luan, Y. Wang, W. Li, L. Wang, and S. Lu, “Thermal runaway model of high-nickel large format lithium-ion battery under thermal abuse conditions”, *IOP Conference Series: Earth and Environmental Science*, vol. 844, no. 1, p. 012 009, 2021. DOI: 10.1088/1755-1315/844/1/012009.
- [239] X. Feng, X. He, M. Ouyang, L. Wang, L. Lu, D. Ren, and S. Santhanagopalan, “A Coupled Electrochemical-Thermal Failure Model for Predicting the Thermal Runaway Behavior of Lithium-Ion Batteries”, *Journal of The Electrochemical Society*, vol. 165, no. 16, A3748–A3765, 2018. DOI: 10.1149/2.0311816jes.
- [240] A. V. Shelkea, J. E. Buston, J. Gill, D. Howard, R. C. Williams, E. Read, A. Abaza, B. Cooper, P. Richards, and J. X. Wen, “Combined numerical and experimental studies of 21700 lithium-ion battery thermal runaway induced by different thermal abuse”, *International Journal of Heat and Mass Transfer*, vol. 194, p. 123 099, 2022. DOI: 10.1016/j.ijheatmasstransfer.2022.123099.
- [241] P. Ping, Q. Wang, Y. Chung, and J. Wen, “Modelling electro-thermal response of lithium-ion batteries from normal to abuse conditions”, *Applied Energy*, vol. 205, pp. 1327–1344, 2017. DOI: 10.1016/j.apenergy.2017.08.073.
- [242] I. Lalinde, A. Berrueta, P. Sanchis, and A. Ursua, “Applied method to model the thermal runaway of lithium-ion batteries”, in *2021 IEEE International Conference on Environment and Electrical Engineering and 2021 IEEE Industrial and Commercial Power Systems Europe (EEEIC / I&CPS Europe)*, IEEE, 2021, pp. 1–6. DOI: 10.1109/EEEIC/ICPSEurope51590.2021.9584560.
- [243] H. Chen, J. E. H. Buston, J. Gill, D. Howard, R. C. E. Williams, E. Read, A. Abaza, B. Cooper, and J. X. Wen, “A Simplified Mathematical Model for Heating-Induced Thermal Runaway of Lithium-Ion Batteries”, *Journal of The Electrochemical Society*, vol. 168, no. 1, p. 010 502, 2021. DOI: 10.1149/1945-7111/abd64c.
- [244] C. Jin, Y. Sun, H. Wang, X. Lai, S. Wang, S. Chen, X. Rui, Y. Zheng, X. Feng, H. Wang, and M. Ouyang, “Model and experiments to investigate thermal runaway characterization of lithium-ion batteries induced by external heating method”, *Journal of Power Sources*, vol. 504, p. 230 065, 2021. DOI: 10.1016/j.jpowsour.2021.230065.

- [245] F. Zhang, X. Feng, C. Xu, F. Jiang, and M. Ouyang, “Thermal runaway front in failure propagation of long-shape lithium-ion battery”, *International Journal of Heat and Mass Transfer*, vol. 182, p. 121 928, 2022. DOI: 10.1016/j.ijheatmasstransfer.2021.121928.
- [246] T. D. Hatchard, D. D. MacNeil, A. Basu, and J. R. Dahn, “Thermal Model of Cylindrical and Prismatic Lithium-Ion Cells”, *Journal of The Electrochemical Society*, vol. 148, no. 7, A755, 2001. DOI: 10.1149/1.1377592.
- [247] G.-H. Kim, A. Pesaran, and R. Spotnitz, “A three-dimensional thermal abuse model for lithium-ion cells”, *Journal of Power Sources*, vol. 170, no. 2, pp. 476–489, 2007. DOI: 10.1016/j.jpowsour.2007.04.018.
- [248] C. F. Lopez, J. A. Jeevarajan, and P. P. Mukherjee, “Characterization of Lithium-Ion Battery Thermal Abuse Behavior Using Experimental and Computational Analysis”, *Journal of The Electrochemical Society*, vol. 162, no. 10, A2163–A2173, 2015. DOI: 10.1149/2.0751510jes.
- [249] P. Peng and F. Jiang, “Thermal safety of lithium-ion batteries with various cathode materials: A numerical study”, *International Journal of Heat and Mass Transfer*, vol. 103, pp. 1008–1016, 2016. DOI: 10.1016/j.ijheatmasstransfer.2016.07.088.
- [250] M. Parhizi, M. Ahmed, and A. Jain, “Determination of the core temperature of a Li-ion cell during thermal runaway”, *Journal of Power Sources*, vol. 370, pp. 27–35, 2017. DOI: 10.1016/j.jpowsour.2017.09.086.
- [251] Y. Lai, K. Yang, H. Liu, F. Gao, M. Zhang, and W. Xu, “A Probe into the Accuracy of Thermal Runaway Simulation Model of Lithium-ion Battery under Adiabatic Condition”, *IOP Conference Series: Earth and Environmental Science*, vol. 680, no. 1, p. 012 009, 2021. DOI: 10.1088/1755-1315/680/1/012009.
- [252] M. P. Macdonald, S. Chandrasekaran, S. Garimella, and T. F. Fuller, “Thermal runaway in a prismatic lithium ion cell triggered by a short circuit”, *Journal of Energy Storage*, vol. 40, p. 102 737, 2021. DOI: 10.1016/j.est.2021.102737.
- [253] D. Ren, X. Liu, X. Feng, L. Lu, M. Ouyang, J. Li, and X. He, “Model-based thermal runaway prediction of lithium-ion batteries from kinetics analysis of cell components”, *Applied Energy*, vol. 228, pp. 633–644, 2018. DOI: 10.1016/j.apenergy.2018.06.126.
- [254] K. Jiang, T. Wang, X. Li, B. Duan, and C. Zhang, “Simulation of thermal runaway prediction model for nickel-rich Lithium ion batteries”, in *2020 Chinese Automation Congress (CAC)*, IEEE, 2020, pp. 1293–1297. DOI: 10.1109/CAC51589.2020.9326525.
- [255] D. D. MacNeil, L. Christensen, J. Landucci, J. M. Paulsen, and J. R. Dahn, “An Autocatalytic Mechanism for the Reaction of Li_xCoO_2 in Electrolyte at Elevated Temperature”, *Journal of The Electrochemical Society*, vol. 147, no. 3, p. 970, 2000. DOI: 10.1149/1.1393299.

- [256] D. D. MacNeil and J. R. Dahn, “The Reaction of Charged Cathodes with Non-aqueous Solvents and Electrolytes: I. $\text{Li}_{0.5}\text{CoO}_2$ ”, *Journal of The Electrochemical Society*, vol. 148, no. 11, A1205, 2001. DOI: 10.1149/1.1407245.
- [257] D. D. MacNeil and J. R. Dahn, “Test of Reaction Kinetics Using Both Differential Scanning and Accelerating Rate Calorimetries As Applied to the Reaction of Li_xCoO_2 in Non-aqueous Electrolyte”, *The Journal of Physical Chemistry A*, vol. 105, no. 18, pp. 4430–4439, 2001. DOI: 10.1021/jp001187j.
- [258] S. Abada, M. Petit, A. Lecocq, G. Marlair, V. Sauvant-Moynot, and F. Huet, “Combined experimental and modeling approaches of the thermal runaway of fresh and aged lithium-ion batteries”, *Journal of Power Sources*, vol. 399, pp. 264–273, 2018. DOI: 10.1016/j.jpowsour.2018.07.094.
- [259] E. Kwak, J.-h. Kim, S. H. Hong, and K.-Y. Oh, “Detailed modeling investigation of thermal runaway pathways of a lithium iron phosphate battery”, *International Journal of Energy Research*, vol. 46, no. 2, pp. 1146–1167, 2022. DOI: 10.1002/er.7235.
- [260] C. Liu, H. Li, X. Kong, and J. Zhao, “Modeling analysis of the effect of battery design on internal short circuit hazard in $\text{LiNi}_{0.8}\text{Co}_{0.1}\text{Mn}_{0.1}\text{O}_2/\text{SiO}_x$ -graphite lithium ion batteries”, *International Journal of Heat and Mass Transfer*, vol. 153, p. 119 590, 2020. DOI: 10.1016/j.ijheatmasstransfer.2020.119590.
- [261] P. T. Coman, S. Mátéfi-Tempfli, C. T. Veje, and R. E. White, “Modeling Vaporization, Gas Generation and Venting in Li-Ion Battery Cells with a Dimethyl Carbonate Electrolyte”, *Journal of The Electrochemical Society*, vol. 164, no. 9, A1858–A1865, 2017. DOI: 10.1149/2.0631709jes.
- [262] J. Kim, A. Mallarapu, D. P. Finegan, and S. Santhanagopalan, “Modeling cell venting and gas-phase reactions in 18650 lithium ion batteries during thermal runaway”, *Journal of Power Sources*, vol. 489, p. 229 496, 2021. DOI: 10.1016/j.jpowsour.2021.229496.
- [263] R. Srinivasan, M. E. Thomas, M. B. Airola, B. G. Carkhuff, L. J. Frizzell-Makowski, H. Alkandry, J. G. Reuster, H. N. Oguz, P. W. Green, J. La Favors, L. J. Currano, and P. A. Demirev, “Preventing Cell-to-Cell Propagation of Thermal Runaway in Lithium-Ion Batteries”, *Journal of The Electrochemical Society*, vol. 167, no. 2, p. 020 559, 2020. DOI: 10.1149/1945-7111/ab6ff0.
- [264] W. Li, V. León Quiroga, K. R. Crompton, and J. K. Ostanek, “High Resolution 3-D Simulations of Venting in 18650 Lithium-Ion Cells”, *Frontiers in Energy Research*, vol. 9, p. 788 239, 2021. DOI: 10.3389/fenrg.2021.788239.
- [265] G. Wang, D. Kong, P. Ping, J. Wen, X. He, H. Zhao, X. He, R. Peng, Y. Zhang, and X. Dai, “Revealing particle venting of lithium-ion batteries during thermal runaway: A multi-scale model toward multiphase process”, *eTransportation*, vol. 16, p. 100 237, 2023. DOI: 10.1016/j.etrans.2023.100237.

- [266] Y. Jia and J. Xu, “Modeling of Thermal Propagation Based on Two Cylindrical Lithium-Ion Cells”, *Journal of Electrochemical Energy Conversion and Storage*, vol. 17, no. 2, p. 021 105, 2020. DOI: 10.1115/1.4045199.
- [267] P. T. Coman, E. C. Darcy, C. T. Veje, and R. E. White, “Numerical analysis of heat propagation in a battery pack using a novel technology for triggering thermal runaway”, *Applied Energy*, vol. 203, pp. 189–200, 2017. DOI: 10.1016/j.apenergy.2017.06.033.
- [268] A. Kurzawski, L. Torres-Castro, R. Shurtz, J. Lamb, and J. C. Hewson, “Predicting cell-to-cell failure propagation and limits of propagation in lithium-ion cell stacks”, *Proceedings of the Combustion Institute*, vol. 38, no. 3, pp. 4737–4745, 2021. DOI: 10.1016/j.proci.2020.06.270.
- [269] C. Yuan, Q. Wang, Y. Wang, and Y. Zhao, “Inhibition effect of different interstitial materials on thermal runaway propagation in the cylindrical lithium-ion battery module”, *Applied Thermal Engineering*, vol. 153, pp. 39–50, 2019. DOI: 10.1016/j.applthermaleng.2019.02.127.
- [270] P. J. Bugryniec, J. N. Davidson, and S. F. Brown, “Computational modelling of thermal runaway propagation potential in lithium iron phosphate battery packs”, *Energy Reports*, vol. 6, pp. 189–197, 2020. DOI: 10.1016/j.egy.2020.03.024.
- [271] D. Mishra, K. Shah, and A. Jain, “Investigation of the Impact of Flow of Vented Gas on Propagation of Thermal Runaway in a Li-Ion Battery Pack”, *Journal of The Electrochemical Society*, vol. 168, no. 6, p. 060 555, 2021. DOI: 10.1149/1945-7111/ac0a20.
- [272] D. Mishra, K. Shah, and A. Jain, “Investigation of the Impact of Radiative Shielding by Internal Partitions Walls on Propagation of Thermal Runaway in a Matrix of Cylindrical Li-Ion Cells”, *Journal of The Electrochemical Society*, vol. 168, no. 12, p. 120 507, 2021. DOI: 10.1149/1945-7111/ac3715.
- [273] D. Mishra and A. Jain, “Multi-Mode Heat Transfer Simulations of the Onset and Propagation of Thermal Runaway in a Pack of Cylindrical Li-Ion Cells”, *Journal of The Electrochemical Society*, vol. 168, no. 2, p. 020 504, 2021. DOI: 10.1149/1945-7111/abdc7b.
- [274] Y. Li, G. Liu, and Z. Li, “Numerical modeling of thermal runaway in high-energy lithium-ion battery packs induced by multipoint heating”, *Case Studies in Thermal Engineering*, vol. 38, p. 102 335, 2022. DOI: 10.1016/j.csite.2022.102335.
- [275] K. Shen, Y. Mao, Y. Zheng, W. Yang, and B. Wu, “One-Dimensional Modeling and Experimental Analysis of Nail Penetration Thermal Runaway for Large Capacity Li-Ion Power Battery”, *Journal of The Electrochemical Society*, vol. 169, no. 4, p. 040 502, 2022. DOI: 10.1149/1945-7111/ac5cf0.
- [276] P. Vyroubal, T. Kazda, and M. Mačák, “The Numerical Simulation of Thermal Abuse and Runaway in Lithium Ion Battery Pack”, *ECS Transactions*, vol. 105, no. 1, pp. 549–559, 2021. DOI: 10.1149/10501.0549ecst.

- [277] Y. Jia, M. Uddin, Y. Li, and J. Xu, “Thermal runaway propagation behavior within 18,650 lithium-ion battery packs: A modeling study”, *Journal of Energy Storage*, vol. 31, p. 101 668, 2020. DOI: 10.1016/j.est.2020.101668.
- [278] W. Zhang, Z. Liang, X. Yin, and G. Ling, “Avoiding thermal runaway propagation of lithium-ion battery modules by using hybrid phase change material and liquid cooling”, *Applied Thermal Engineering*, vol. 184, p. 116 380, 2021. DOI: 10.1016/j.applthermaleng.2020.116380.
- [279] P. Jindal, B. S. Kumar, and J. Bhattacharya, “Coupled electrochemical-abuse-heat-transfer model to predict thermal runaway propagation and mitigation strategy for an EV battery module”, *Journal of Energy Storage*, vol. 39, p. 102 619, 2021. DOI: 10.1016/j.est.2021.102619.
- [280] X. Feng, X. He, M. Ouyang, L. Lu, P. Wu, C. Kulp, and S. Prasser, “Thermal runaway propagation model for designing a safer battery pack with 25 Ah $\text{LiNi}_x\text{Co}_y\text{Mn}_z\text{O}_2$ large format lithium ion battery”, *Applied Energy*, vol. 154, pp. 74–91, 2015. DOI: 10.1016/j.apenergy.2015.04.118.
- [281] J. Chen, D. Ren, H. Hsu, L. Wang, X. He, C. Zhang, X. Feng, and M. Ouyang, “Investigating the thermal runaway features of lithium-ion batteries using a thermal resistance network model”, *Applied Energy*, vol. 295, p. 117 038, 2021. DOI: 10.1016/j.apenergy.2021.117038.
- [282] X. Liu, Z. Wu, S. I. Stoliarov, M. Denlinger, A. Masias, and K. Snyder, “A Thermo-Kinetic Model of Thermally-Induced Failure of a Lithium Ion Battery: Development, Validation and Application”, *Journal of The Electrochemical Society*, vol. 165, no. 11, A2909–A2918, 2018. DOI: 10.1149/2.0111813jes.
- [283] X. Feng, L. Lu, M. Ouyang, J. Li, and X. He, “A 3D thermal runaway propagation model for a large format lithium ion battery module”, *Energy*, vol. 115, pp. 194–208, 2016. DOI: 10.1016/j.energy.2016.08.094.
- [284] C. Xu, H. Wang, F. Jiang, X. Feng, L. Lu, C. Jin, F. Zhang, W. Huang, M. Zhang, and M. Ouyang, “Modelling of thermal runaway propagation in lithium-ion battery pack using reduced-order model”, *Energy*, vol. 268, p. 126 646, 2023. DOI: 10.1016/j.energy.2023.126646.
- [285] D. Grimmeisen and M. S. Schneider, “Numerical Simulation of Cell Venting within a Simplified 18650 Li-Ion Battery Pack”, 2021.
- [286] J. Qin, S. Zhao, X. Liu, and Y. Liu, “Simulation study on thermal runaway suppression of 18650 lithium battery”, *Energy Sources, Part A: Recovery, Utilization, and Environmental Effects*, pp. 1–13, 2020. DOI: 10.1080/15567036.2020.1817189.
- [287] M. Citarella, D. Suzzi, B. Brunnsteiner, P. Schiffbanker, G. Maier, and J. Schneider, “Computational Modelling of Thermal Runaway Propagation in Lithium-Ion Battery Systems”, in *2019 IEEE Transportation Electrification Conference (ITEC-India)*, IEEE, 2019, pp. 1–4. DOI: 10.1109/ITEC-India48457.2019.ITECINDIA2019-274.

- [288] K. F. Yeow and H. Teng, “Characterizing Thermal Runaway of Lithium-ion Cells in a Battery System Using Finite Element Analysis Approach”, *SAE International Journal of Alternative Powertrains*, vol. 2, no. 1, pp. 179–186, 2013. DOI: 10.4271/2013-01-1534.
- [289] P. T. Coman, E. C. Darcy, and R. E. White, “Simplified Thermal Runaway Model for Assisting the Design of a Novel Safe Li-Ion Battery Pack”, *Journal of The Electrochemical Society*, vol. 169, no. 4, p. 040 516, 2022. DOI: 10.1149 / 1945-7111/ac62bd.
- [290] S. Bilyaz, K. C. Marr, and O. A. Ezekoye, “Modeling of Thermal Runaway Propagation in a Pouch Cell Stack”, *Fire Technology*, vol. 56, no. 6, pp. 2441–2466, 2020. DOI: 10.1007/s10694-020-00970-6.
- [291] H. Lomax, T. H. Pulliam, and D. W. Zingg, *Fundamentals of Computational Fluid Dynamics* (Scientific Computation). Berlin, Heidelberg: Springer Berlin Heidelberg, 2001. DOI: 10.1007/978-3-662-04654-8.
- [292] C. Hirsch, *Numerical Computation of Internal and External Flows: Fundamentals of Computational Fluid Dynamics*, 2nd ed. Oxford; Burlington: Elsevier / Butterworth-Heinemann, 2007, ISBN: 978-0-7506-6594-0.
- [293] J. H. Ferziger, M. Perić, and R. L. Street, *Computational Methods for Fluid Dynamics*. Cham: Springer International Publishing, 2020. DOI: 10.1007/978-3-319-99693-6.
- [294] A. Prosperetti and G. Tryggvason, *Computational Methods for Multiphase Flow*. Cambridge: Cambridge University Press, 2007, ISBN: 978-0-511-29611-6.
- [295] M. Ishii and T. Hibiki, *Thermo-Fluid Dynamics of Two-Phase Flow*. New York, NY: Springer New York, 2011. DOI: 10.1007/978-1-4419-7985-8.
- [296] Siemens Digital Industries Software, *Simcenter Star-CCM+ Documentation. Version 2021.3*, 2021.
- [297] A. Illyés and H. Bauer, *Die Energiewandlung bei ein- und mehrmaligem Stoß einer Partikel gegen eine feste Wand* (VDI-Forschungsheft / Verein Deutscher Ingenieure 640). Düsseldorf: VDI-Verl, 1987, ISBN: 978-3-18-850640-3.

Scientific Contributions

- **S. Hoelle**, H. Kim, S. Zimmermann, and O. Hinrichsen. “Lithium-Ion Battery Thermal Runaway: Experimental Analysis of Particle Deposition in Battery Module Environment”, *Batteries*, vol. 10, no. 6, p. 173, 2024. DOI: 10.3390/batteries10060173.
- **S. Hoelle**, S. Zimmermann, and O. Hinrichsen. “3D Thermal Simulation of Thermal Runaway Propagation in Lithium-Ion Battery Cell Stack - Review and Comparison of Modeling Approaches”, *Journal of The Electrochemical Society*, vol. 170, no. 6, p. 060516, 2023. DOI: 10.1149/1945-7111/acd966.
- **S. Hoelle**, F. Dengler, S. Zimmermann, and O. Hinrichsen. “3D Thermal Simulation of Lithium-Ion Battery Thermal Runaway in Autoclave Calorimetry: Development and Comparison of Modeling Approaches”, *Journal of The Electrochemical Society*, vol. 170, no. 1, p. 010509, 2023. DOI: 10.1149/1945-7111/acac06.
- **S. Hoelle**, S. Haberl, A. Rheinfeld, P. Osswald, S. Zimmermann, and O. Hinrichsen. “Experimental Investigation on Thermal Runaway Propagation in Lithium-Ion Battery Cell Stack”, *2022 IEEE Transportation Electrification Conference & Expo (ITEC) (2022)*, pp. 1174–1179. DOI: 10.1109/ITEC53557.2022.9813813.
- **S. Hoelle**, S. Scharner, S. Asanin, and O. Hinrichsen. “Analysis on Thermal Runaway Behavior of Prismatic Lithium-Ion Batteries with Autoclave Calorimetry”, *Journal of The Electrochemical Society*, vol. 168, no. 12, p. 120515, 2021. DOI: 10.1149/1945-7111/ac3c27.